Highly Ordered Surface Roughness Effects on Turbulent Boundary Layers

by

Bagus Nugroho

Submitted in total fulfillment of the requirements
of the degree of Doctor of Philosophy

The Department of Mechanical Engineering
The University of Melbourne

September 4, 2015

Abstract

The effects of highly ordered riblet type surface roughness with converging-diverging/herringbone pattern in zero pressure gradient (ZPG) turbulent boundary layers are investigated experimentally. The study is based on a novel investigation by Koeltzsch et al. (2002), where a new class of riblet type surface roughness with converging-diverging/herringbone riblet pattern is applied inside the surface of fully-developed turbulent pipe-flow. Their experimental results show that the unique pattern generates a large-scale azimuthal variation in the mean velocity and turbulence intensity. Inspired by these results we intend to extend their study and investigate it in more detail, particularly in zero pressure gradient (ZPG) turbulent boundary layers.

The general results from the present study show that the converging region forms a common-flow-up that transfers the highly turbulent and slower near-wall fluid away from the surface, resulting in a low local mean velocity and high local turbulence intensity. The low momentum over the converging region results in a thicker turbulent boundary layer. Over the diverging region the opposite situation occurs, the diverging pattern forms a common-flow-down that forces the faster and less turbulent fluid that originally resides further from the wall to move towards the surface, resulting in a high local mean velocity and low local turbulence intensity. The high local mean velocity over the diverging region results in a thinner turbulent boundary layer. For certain cases, the spanwise variation in boundary layer thickness between the converging and diverging region is almost double. Such large and aggressive variation is uncommon considering that the height of the riblets is $\approx 1\%$ of the boundary layer thickness. The combination of the

iv

common-flow-up and common-flow-down regions forms a large scale counter rotating vortices that dominate the entire boundary layer. The resulting magnitude of maximum spanwise and wall-normal velocity components of the counter-rotating vortices are $\approx 2 - 3\%$ of U_∞, which is comparable to the lower end strength of typical vortex generators for turbulent flow. Our study reveals that the strength of the spanwise variation depends on several parameters, namely : yaw angle (α), viscous-scaled riblet height (h^+), streamwise fetch/development length over the rough surface (F_x), and relaxation distance/development length over the smooth surface (r_s). The riblet pattern may offer a unique technique to generate counter-rotating roll-modes within turbulent boundary layers and act as a low-profile flow control mechanism.

Analysis of the pre-multiplied energy spectra suggests that the converging and diverging pattern has redistributed the large-scale turbulent features. Over the converging region the large-scales are found to be very dominant in the logarithmic region, which closely resembles the recently discovered 'superstructures' by Hutchins and Marusic (2007a,b). The highly ordered surface roughness pattern seems to preferentially arrange and lock the largest scales over the converging region. Further examination of the three-dimensional conditional structures strengthen this view. The conditionally averaged large-scale low-speed feature over the converging region is wider in size and has a stronger magnitude than the equivalent feature over the diverging region.

We also look into amplitude modulation over the converging and diverging pattern. Recent reports by Hutchins and Marusic (2007b); Mathis et al. (2009a,b); Marusic et al. (2010b); Chung and McKeon (2010a); Ganapathisubramani et al. (2012) reveal that large-scale structures in turbulent boundary layers modulate the amplitude and frequency of the small-scale energy. The amplitude and frequency magnitude of the near-wall small-scale structures are found to be reduced when low-speed large-scale features are detected. Our analyses show that over the converging region, the reduction in the conditioned small-scale variance/small-scale energy is stronger than over the diverging region. This finding further strengthens our previous observation that the highly ordered riblet pattern preferentially arranges and locks the largest scales over the converging region.

Finally, we look into the turbulent and non-turbulent interface (TNTI) of

the converging and diverging pattern and found that the interface location experiencing spanwise variation in the same manner as the boundary layer thickness. Furthermore, there are not many differences in the TNTI properties (i.e. interface position and width) between the smooth wall case, converging region, and diverging region when they are scaled with their respective boundary layer thickness.

Declaration of Authorship

I, Bagus Nugroho, declare that this thesis titled, 'Highly Ordered Surface Roughness Effects on Turbulent Boundary Layers' and the work presented in it are my own. I confirm that :

- This work was done wholly or mainly while in candidature for a research degree at this University.

- Where any part of this thesis has previously been submitted for a degree or any other qualification at this University or any other institution, this has been clearly stated.

- Where I have consulted the published work of others, this is always clearly attributed.

- Where I have quoted from the work of others, the source is always given. With the exception of such quotations, this thesis is entirely my own work.

- I have acknowledged all main sources of help.

- Where the thesis is based on work done by myself jointly with others, I have made clear exactly what was done by others and what I have contributed myself.

Signed / Date:

Acknowledgements

Firstly, I would like to express my sincere gratitude and appreciation to my advisors, A/Prof Jason Monty and A/Prof Nicholas Hutchins for their support during my PhD candidature, for their enthusiasm, patience, trust, and motivation. Their guidance and wealth of knowledge have helped me immensely in the past five years. They have sent me to many corners of the planet and have allowed me to see the world. I really enjoy our light talk during lunch in the office and discussions about European football. I cannot think of any other supervisors who allow their students to set up projectors in the office for the football World Cup. I am very grateful to have such excellent supervisors.

I would like to thank my PhD committee, Prof Ivan Marusic and Prof Andrew Ooi for their, support, encouragement, ideas, and comments during my candidature. I also thank Prof Joe Klewicki for his opinions and discussion regarding turbulent structures. My gratitude also to Prof Min Chong who always spares his time when I need to talk about fluid mechanics and life in general; his experience has been very inspirational. I also really enjoy his hospitality every time we watch European football at his wonderful place. I also appreciate the help from Prof Doreen Thomas, Head of Department of Mechanical Engineering, as a non Australian passport holder, without her reference letter I would not have been able to periodically attend conferences overseas. Special thanks to the late Dr Tim Nickels for his hospitality during my short visit to Cambridge University.

My sincere thanks goes to Dr Romain Mathis, Dr Ebenezer Gnanamanickam, Dr Kapil Chauhan, Dr John Elsnab, Dr Honglei Bai, Dr Woutijn

Thesis dedication

In loving memory of my father, Hari Rahardjo (1955 – 2005).

Contents

List of Figures

List of Tables

Nomenclature

x Streamwise direction/distance, m

y Spanwise direction/distance, m

z Wall-normal direction/distance, m

τ Frictional wall shear stress, N/m^2

$\Delta\tau$ Change in wall shear stress, N/m^2

τ_0 Reference wall shear stress, N/m^2

L Characteristic length scale, m

$\breve{u}$ Instantaneous streamwise velocity , m/s

$\overline{u^2}$ Turbulence intensity, m^2/s^2

$\overline{u^2}_{sa}$ Spanwise averaged turbulence intensity, m^2/s^2

u Fluctuations of streamwise velocity, m/s

u_{hf} Filtered fluctuations of streamwise velocity from hot-films, m/s

$\tilde{u}$ Conditionally averaged streamwise velocity fluctuations, m/s

u_s Small-scale component of velocity fluctuations, m/s

u_l Large-scale component of velocity fluctuations, m/s

$\mathrm{hf_c}$ Hot-film over converging region

$\mathrm{hf_d}$ Hot-film over diverging region

U Mean streamwise velocity, m/s

U_c Convection velocity velocity, m/s

U_∞ Free-stream velocity, m/s

U_τ Skin-friction velocity, m/s

U_{τ_s} Skin-friction velocity over smooth-wall, m/s

U_{τ_r} Skin-friction velocity over rough-wall, m/s

$U_{\tau_{sa}}$ Spanwise averaged skin friction velocity, m/s

U_{sa} Spanwise averaged mean velocity, m/s

δ	Boundary layer thickness, m
δ_s	Boundary layer thickness over smooth-wall, m
δ_r	Boundary layer thickness over rough surface, m
δ_{sa}	Boundary layer thickness averaged over one spanwise wavelength, m
δ_{r_s}	Boundary layer over rough to smooth case, m
ν	Kinematic viscosity, m^2/s
Re	Reynolds number
Re_τ	Friction Reynolds number
Re_θ	Momentum thickness Reynolds number
A	Log law constant
B	Velocity defect constant
$k_x\phi_{uu}$	Pre-multiplied streamwise energy spectra, m^2/s^2
k_x	Streamwise wave number, 1/m
ϕ_{uu}	Spectral density of the streamwise velocity fluctuations, m^3/s^2
λ_x	Streamwise length-scale
α	Riblet yaw angle, °
β	Riblet tip angle, °
r_s	Separation distance from rough to smooth-wall, m
s	Riblet spacing, mm
s^+	Viscous-scaled riblet spacing
h	Riblet height, mm
h^+	Viscous-scaled riblet height
h_{pl}	Longitudinal protrusion height, mm
h_{pc}	Crossflow protrusion height, mm
Λ	One spanwise length, mm
F_x	Fetch distance, m
l	Hot-wire etched length, mm
l^+	Hot-wire etched viscous-scaled length
d	Hot-wire etched diameter, mm
Cp	Coefficient of pressure
H	Shape factor
γ	intermittency

lc Low speed event over converging region

ld Low speed event over diverging region

Π Wake parameter

T_a Ambient temperature, K

f_s Sampling frequency, Hz

D Pipe Diameter, m

t Time, s

t^+ Viscous scaled time

S_u Skewness

F_u Kurtosis

Ω_x Streamwise vorticity

Υ Intermittency detector function

Abbreviations

ZPG	Zero Pressure Gradient
HWA	Hot-Wire Anemometer
CTA	Constant Temperature Anemometry
DNS	Direct Numerical Simulation
LES	Large Eddy Simulation
RMS	Root Mean Square
MUCTA	Melbourne University Constant Temperature Anemometer
LDA	Laser Doppler Anemometry
PIV	Particle Image Velocimetry
NPL	National Physical Laboratory
DAQ	Data Acquisition
CAD	Computer Aided Design
HRNBLWT	High Reynolds Number Boundary Layer Wind Tunnel
VLSM	Very Large Scale Motions
VITA	Variable Interval Time Averaging
VISA	Variable Interval Space Averaging
TNTI	Turbulent and Non-Turbulent Interface

Chapter 1

Introduction

An experimental study has been performed with the aim of modifying a zero pressure gradient (ZPG) turbulent boundary layer using a highly ordered riblet-type surface roughness arranged in a converging-diverging ('herringbone') pattern. Riblets are small longitudinal grooves on a surface that are aligned with the flow direction. The main idea of the experiment is to have a detailed comparison between a ZPG turbulent boundary over a smooth-wall and a boundary layer that has been modified by this surface roughness type. The study is particularly concerned with the large-scale spanwise modification of the boundary layer parameters (i.e. mean velocity, turbulence intensity, boundary layer thickness) and its effects on the large-scale structure. Furthermore, we are also interested in the possibility of using the riblet-type surface roughness as a 'low profile' flow control and drag reduction technique. This work is inspired by the study of Koeltzsch et al. (2002), where a converging-diverging riblet-type surface roughness is applied inside the surface of fully-developed turbulent pipe-flow. To the best of our knowledge, this novel and remarkable riblets experiment is yet to be studied in more detail (i.e. looking at different riblet parameters) or extended to other types of canonical wall bounded flow (such as Channel flow and ZPG turbulent boundary layer). The current study seeks to revisit this unique surface roughness pattern and perform accurate parametric studies using hot-wire anemometry (both single- and cross-wire) and hot-films in a ZPG turbulent boundary layer.

1

1.1   Motivation and background

Global warming and the rising cost of fuel have sparked much interest in finding better ways to reduce energy consumption. This is reflected in the 2005 European Commission Emission Trading System (ETS) that aims to help all 25 European Union (EU) members reduce carbon emissions by 21% by 2020. This is currently the world's largest emission trading scheme (Ellerman and Buchner, 2007). The scheme affects transportation sectors heavily and forces industries such as automotive (Michaelis and Zerle, 2006), naval (Davies, 2006; Longva et al., 2010), and aerospace (Preston et al., 2012; Kopsch, 2012; Malina et al., 2012) to adopt a more sustainable, energy efficient, and low running cost products. Faced with these challenges, several automotive companies have tried to create environmentally friendly and energy efficient vehicles by employing hybrid technology, using electric motors and hydrogen fuel cells. Aerospace companies such as Boeing, Bombardier, Rolls-Royce, General Electric, and Airbus are implementing lighter composite materials and more fuel efficient jet engines. And naval companies are installing sulphur fuel abatement technology. Although those efforts are beneficial in reducing fuel consumption, one of the main energy usage in transport vehicles is to overcome *skin-friction drag* from the *turbulent boundary layer.*

Skin-friction drag originates from the thin region of slow moving fluid immediately adjacent to a solid surface. This small region of shear (which is commonly called the boundary layer, with certain thickness δ) arises from the no-slip condition at the solid boundary, where the velocity gradients generate tangential shear stress or skin-friction drag. Skin-friction drag is the force that aircraft and ship propulsion systems must overcome to propel themselves. In the piping or air ducting industries, the skin-friction drag causes pressure loss, which again must be compensated for by pumps or compressors. Energy consumption to overcome skin-friction drag is relatively costly, e.g. around 50% of the total drag in modern aircraft is caused by skin-friction drag (Saric et al., 2011; Lee et al., 2011; Marusic, 2009), in large ships such as container ships or Very Large Crude Carriers (VLCC) this figure can be up to 80%, and for pipes and ducts it is close to 100%. Hence a large volume of fuel (or in many cases, the majority) is used to overcome skin-friction drag. In large engineering applications (where the Reynolds number is large) such as aircraft, the motions within the thin

shear layer (or boundary layer) that gives rise to skin-friction drag, are highly turbulent, complex and seemingly random swirling motions (vortical motions). Hence the term turbulent boundary layer is used to describe this region.

In the study of fluid mechanics, one of the most important non-dimensional parameters is the *Reynolds number* $Re = UL/\nu$, where U is mean streamwise velocity, ν is kinematic viscosity, and L is characteristic length scale. UL/ν represents the ratio of inertial to viscous force. In high performance engineering applications, such as aerofoils of an aircraft or hulls of large ships, the Reynolds number represents distance downstream from the leading edge or the beginning of the boundary layer (which is generally turbulent). Several basic fluid mechanics text books define turbulent flow as $Re > 2 \times 10^3$ (Fox and McDonald, 1998). Typical large container and VLCC ships, with hull lengths of 100 to 300 m and average cruising speed of 5 to 10 m/s, will generate very large Reynolds numbers of the order of 10^9 (Kodama et al., 2000). Smaller engineering systems such as cars with a length of 4 m and a velocity of 20 m/s will have Reynolds numbers of the order of 10^6. Larger Reynolds numbers results in a more turbulent flow and higher skin-friction drag which inevitably requires more energy to overcome (Smits and Marusic, 2013). For canonical wall bounded turbulent flow (i.e. channel flow, pipe flow and ZPG turbulent boundary layer flow), it is common to use the Friction Reynolds number (or commonly called Kármán number), $Re_\tau = U_\tau \delta/\nu$, that represents the ratio of scales in a turbulent flow. Here U_τ is skin-friction velocity and δ is boundary layer thickness. The skin-friction velocity is proportional to the skin-friction drag, hence higher skin-friction velocity translates to higher skin-friction drag.

In addition to the challenges associated with viscous drag at high Reynolds numbers, another important consideration in the study of turbulent boundary layers is *surface roughness*. Visually, the surface of a commercial aircraft's fuselage and wings and the hull of a large ship seem smooth, however, this is generally not so from the perspective of the flow. The flow starts to interact with surface irregularities when the height of these irregularities becomes appreciable in term of viscous length scales. A surface is considered smooth with no extra drag penalty when the roughness height k^+ is < 5, where $k^+ = U_\tau k/\nu$. This means that for a ship or aircraft moving at their cruising speed with Re_τ in the order of 10^5, the maximum admissible physical roughness height is $k \approx 1 - 10$ μm. According to Jiménez

(2004), the root-mean square roughness of a machined surface is between 0.05 μm and 25 μm. However, considering construction irregularities such as welding, rivets, painting, and bio-fouling (in ships), the roughness may be greater than this range. Hence seemingly smooth surfaces are in fact rough, and rough surfaces increase skin-friction drag (Schultz and Swain, 2000; Schultz, 2007).

Another challenge in studying turbulent flow is the seemingly complex and quasi-random vortical motions inside the turbulent boundary layer. Earlier studies by Kline et al. (1967) hypothesised that small-scale near-wall structures dominate turbulent production. However, more recent studies at higher Reynolds number have challenged this view. As the Reynolds number increases, small-scale structures are increasingly eclipsed by large-scale features that reside further away from the wall (see figure 1.2) (Marusic, 2009; Marusic et al., 2010a,c; Smits et al., 2011a; Smits and Marusic, 2013). It is believed that large features may influence the near-wall structures, which are directly correlated to the skin friction drag.

Considering many important engineering applications operate in a high Reynolds number environment, it is easy to appreciate that skin-friction drag from turbulent boundary layers is responsible for a significant proportion of the world's energy consumption. Consequently turbulent boundary layers indirectly contribute to pollution emissions (CO_2, CO, and other harmful substances). Thus it is crucial to understand high Reynolds number turbulent boundary layers and how to control them.

Over the past few decades there have been many efforts to control turbulent boundary layers and to reduce skin-friction drag. Some of these efforts involve a large number of institutions from several different countries. One of the largest is the European Research Community on Flow, Turbulence and Combustion (ERCOFTAC), which has conducted around ten specialised meetings on drag reduction research since the mid 1980s (Choi, 2000). According to Bushnell (1983) and Luchini et al. (1991) the three most common drag reduction techniques are injection or suction of fluid to delay separation (Collis et al., 2004; Messing and Kloker, 2010; Friederich and Kloker, 2012; Cadirci et al., 2013), changing the viscosity of fluid by adding a different type of fluid (White and Mungal, 2008; Woodcock et al., 2010; Yang and Dou, 2010), and suppressing the near-wall cycle of streaks and quasi streamwise vortices through surface modification (Choi, 1989; Bechert et al.,

1997; Karniadakis and Choi, 2003).

Progress in the understanding of turbulence structure has shown that around 80% of the turbulent energy is produced by sweeps (transport of high speed fluid towards wall) and ejections (transport of low speed fluid away from the wall) very close to the surface (Wallace and Eckelmann, 1972; Lu and Willmarth, 1973; Falco, 1977). Furthermore, numerical studies by Orlandi and Jiménez (1994) show that sweep event are more important because of their primary role in the production of turbulent wall shear-stress. Thus, targeting and suppressing the near-wall events will result in effective flow control and drag reduction (Choi, 1989; Jiménez, 1994; Karniadakis and Choi, 2003). There are several possible methods to manipulate the near-wall structures, namely through riblets (Walsh, 1982, 1983; Bechert et al., 1997), compliant surface (Lucey and Carpenter, 1995; Choi et al., 1997), spanwise wall oscillations (Jung et al., 1993; Laadhari et al., 1994; Choi and M, 1998; Choi and Clayton, 2001), spanwise travelling waves (Du and Karniadakis, 2000; Du et al., 2002; Karniadakis and Choi, 2003) and micro-electromechanical systems (MEMS), which involve complex feedback control mechanism with small sensors and actuators (Ho and Tai, 1998; Kasagi et al., 2009).

Modifying the near-wall structures through corrugated surfaces or riblets (see figure 1.1) is seen by many as a very promising flow control and drag reduction technique. Its main advantage is the ability to manipulate turbulent boundary layer properties and reduce skin-friction drag passively ($\approx 7 - 10\%$) without generating additional form drag (see Walsh (1982, 1983); Bechert et al. (1997, 2000a)). However, this potential technique is rarely applied in real engineering applications. According to Spalart and McLean (2011), the main challenges in employing riblets as a flow control or drag reduction mechanism in commercial engineering applications, such as aircraft or ships, are production and labour costs. Furthermore, riblets are prone to erosion due to dramatic changes in pressure, temperature, and from dirt. Thus the current problem does not lies on the fluid mechanics side, rather it is in other fields of engineering, such as; painting technique, materials, and manufacturing (Spalart and McLean, 2011). Recently however, significant progress in riblet manufacturing and material has been achieved, and with very promising results (Gruneberger and Hage, 2010; Stenzel et al., 2011).
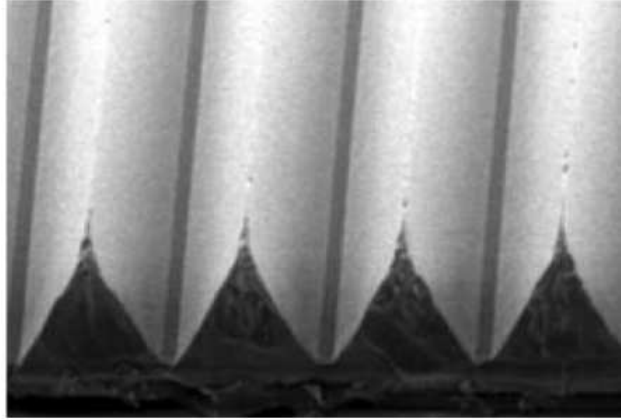
Figure 1.1: Riblets surface (Koeltzsch et al., 2002)

Although many of the aforementioned flow control techniques provide excellent results, most of these studies are from low or moderate Reynolds number and very few attempt to account for the very pronounced changes in turbulence structure that occur as Re increases. Furthermore, the studies generally targeted the near-wall small-scale events, and one should take into consideration that as Re increases, large-scale events play an increasing role in the turbulent production.

A new class of riblet-type surface roughness has been reported by Koeltzsch et al. (2002). In this unique, yet rarely referenced study, a pattern of converging and diverging riblets (or 'herringbone' riblet) is applied inside the surface of a pipe. The results show that this unconventional riblet pattern is able to force fluid flow to move in an azimuthal direction and causes a large scale azimuthal variation in mean velocity, turbulence intensity, and boundary layer thickness. Closer inspection suggests that the converging and diverging surface pattern imposes large scale roll-modes into the turbulent boundary layer. However, the lack of cross-wire or Particle Image Velocimetry (PIV) data prevents Koeltzsch et al. (2002) from reaching this conclusion. To the best of our knowledge it is the first riblets experiment where such a strong large-scale perturbation could be generated. It is also one of the few surface roughnesses investigated, where very small surface perturbations are able to generate large-scale modifications to the layer. The result of their study may have important engineering implications, such as low profile vortex generators.
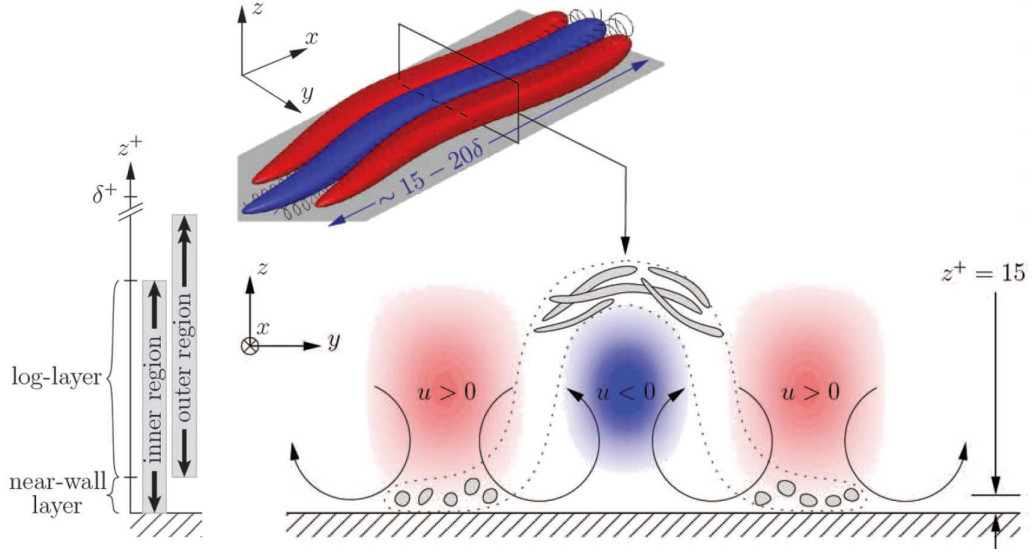
Figure 1.2: Cross-section of superstructures (Marusic et al., 2010b)

Furthermore, the herringbone arranged surface roughness could be applied as a means to generate very large-scale modes which can affect the recently discovered *Very Large Scale Motions (VLSM)* and *superstructures* (Kim and Adrian, 1999; Guala et al., 2006; Balakumar and Adrian, 2007; Hutchins and Marusic, 2007a; Monty et al., 2007). In the last decade, VLSM (for pipe-flow and channel-flow) and superstructures (for ZPG turbulent boundary layers) have attracted plenty of attention. They are known to consist of long $(15 - 20\delta)$ meandering positive and negative velocity fluctuations (Hutchins and Marusic, 2007a; Monty et al., 2007; Dennis and Nickels, 2011) which modulate near wall turbulence (Ganapathisubramani et al., 2012) and contribute substantially to Reynolds shear stress and turbulence production (Mathis et al., 2009a). The features are demonstrated to leave a large scale skin-friction footprint at the wall (Hutchins and Marusic, 2007b), and have accompanying large-scale roll-modes (Chung and McKeon, 2010a). Figure 1.2 shows the cross section of a superstructure event with high (red) and low (blue) velocity fluctuations accompanied by large scale counter rotating modes. So far very few studies have investigated surface roughness as a means to modify the superstructures. To the best of our knowledge, the only study is that of Monty et al. (2011a), where they have shown the ability of braille dot surface roughness to attenuate the energy in superstructures. Therefore, there may be a benefit in exploring control strategies (such as from the herringbone surface pattern) that target superstructures.

Looking at the potential of the herringbone pattern riblet-type surface roughness, it is surprising that the findings of Koeltzsch et al. (2002) are yet to be investigated further or repeated for different types of flow (such as channel flow and the ZPG turbulent boundary layer). The herringbone shaped riblets are different from the conventional riblets. In the conventional riblets, it controls the near-wall structures in a manner that reduces skin friction (Choi, 1989; Bechert et al., 1997). On the other hand, the converging-diverging pattern from the herringbone riblets introduces large-scale flow features with an unknown effect on the near-wall structures. Inspired by Koeltzsch et al. (2002) work, in this study we extend their investigation for ZPG turbulent boundary layers.

1.2   Aims of the current investigation

1. To investigate the effect of converging-diverging riblet-type surface roughness on zero pressure gradient turbulent boundary layers.

2. Confirm Koeltzsch et al. (2002) hypothesis that converging-diverging riblets generate large-scale counter-rotating vortices.

3. Analyze different parameters of the converging-diverging riblets:

   a) converging-diverging riblet yaw angle, α.

   b) viscous-scaled riblet height, h^+.

   c) streamwise fetch or development length over the rough surface, F_x.

   d) relaxation distance or development length over the smooth surface r_s

4. To investigate the effect of the surface roughness on the large-scale features.

5. To see the effect of the surface roughness on the turbulent and non-turbulent interface (TNTI)

1.3 Thesis Outline

Chapter 2 presents a review of literature from previous studies which are related to the current investigations. Here we examine two important topics, namely, coherent structures, and riblets. The complexity and breadth of these topics are reflected in the sheer number of studies that have been reported in the last five decades. Here we do not intend to present a full historical review or comprehensively compile the work undertaken on these topics. The aim is to provide an introduction of earlier studies done and provide a foundation for the current investigation.

The experimental apparatus and measurement technique used throughout this study are explained in Chapter 3. These include wind-tunnel setting, in-house-built apparatus, calibration procedure, data collection technique and data processing method. Throughout the current investigation, the flow is measured using single-normal hot-wire, cross-wire and hot-film. We have extensively modified and refurbished the wind tunnel to accommodate new equipment, such as a two-dimensional traversing system that rests on a rail above the tunnel and is able to move upstream and downstream freely. The roof and the floor of the wind tunnel are fully adjustable, which significantly improves its capability and versatility. Various measurement apparatus such as hot-wires, hot-films, pitot tubes, temperature sensors, and atmospheric pressure sensors are discussed in detail. In this chapter 3, we also explain the manufacturing process for the converging-diverging surface roughness. The roughness is made of polyurethane plates with herringbone patterns on the surface. In total there are 30 tiles covering the wind tunnel floor for each study case. Three sets of tiles with different yaw angle α are used throughout this study. The production methods involve two steps, cutting the master tile using the CNC-machine and creating the replica through silicone rubber molding and polyurethane casting. The procedures are labour intensive and take about 30 days to manufacture. This chapter also report flow validation and the smooth wall case results.

Chapter 4 discusses the parametric study results by analysing the mean velocity and turbulence intensity spanwise variation. Data from single-normal hot-wire and cross-wire experiments are presented and discussed in detail. Here we look at four different parameters, namely : converging - diverging riblet yaw angle α, viscous-scaled riblet height h^+, streamwise

fetch F_x, and relaxation distance r_s.

Recent studies have shown the importance of scaling in the study of wall bounded turbulent flow, particularly at high Reynolds number (Marusic, 2009; Marusic et al., 2010a,c; Smits et al., 2011a; Smits and Marusic, 2013). The issue of scaling in turbulent flow is closely connected to the recently discovered Very Large Scale Motions (VLSMs) and superstructures that have attracted plenty of attention in the last decade. However, most reports in the literature are concerned with canonical turbulent wall-bounded smooth-wall flows. There are very few studies that investigate the effect of surface roughness on scaling, VLSMs, and superstructures. To this end, in Chapter 5 we discuss the importance of having velocity and length scales based on the wall shear-stress, here we present methods of finding the skin-friction velocity U_τ (where $U_\tau = \sqrt{\tau_w/\rho}$, τ_w is wall shear stress and ρ is fluid density) through Clauser (for smooth-wall case) and modified Clauser (for rough-wall case) methods. This chapter also show the effects of converging-diverging surface roughness on the aforementioned subjects by analysing the energy spectra. Chapter 6 extends the results from Chapter 5 and look into the three-dimensional conditional structure and amplitude modulation of turbulent boundary layers over the converging and diverging regions.

Chapter 7 concern with the turbulent and non-turbulent Interface (TNTI) over the converging and diverging surface. There are very few studies that look into the TNTI of rough surface, so far the majority of TNTI studies in the literature are mainly in canonical wall bounded flows and jets. For this analysis we look at several general features of TNTI, such as interface position and interface width for three different surfaces, namely: smooth, converging, and diverging region at similar freestream velocity and stream-wise velocity.

The conclusion of this thesis will be discussed in Chapter 8, which summarises the key findings from this investigation. Considering that this is the first time that this new class of surface roughness is studied parametrically, there is much scope for further investigations using different type of measurements techniques. Finally, Chapter 9 will discuss possible future work which the author may pursue after the completion of the PhD study.

Chapter 2

Literature review

This literature review comprises two sections :

1. Coherent structures

2. Riblets

The aim of this review is to introduce the necessary background in order to provide a solid foundation and better understanding of the current investigation. It presents an outline of the previous studies and developments in turbulent boundary layer structures and riblets. Considering the wide scope within each of the topics, the review focuses solely on the issues that are relevant to this study. Other less relevant cases are only mentioned briefly and the reader is referred to the appropriate source.

2.1 Coherent structures

In the last few decades the study of coherent structures or organised motion is at the cornerstone of understanding the complexity of wall bounded fluid flow. In his review, Robinson (1991) defines coherent motions as 'a

three-dimensional region of the flow over which at least one fundamental flow variable (velocity component, density, temperature, etc.) exhibits significant correlation with itself or with another variable over a range of space and/or time that is significantly larger than the smallest local scales of the flow'. Smits et al. (2011b) identifies coherent structures into four different classes, namely, the near-wall cycle of quasi-streamwise vortices (Kline et al., 1967), horse shoe/hairpin vortices (Head and Bandyopadhyay, 1981; Robinson, 1991), 'Large-Scale Motions', and 'Very Large-Scale Motions' (VLSM) or 'superstructures' that reside in the logarithmic region (Kim and Adrian, 1999; Guala et al., 2006; Balakumar and Adrian, 2007; Hutchins and Marusic, 2007a; Monty et al., 2007).

These 'internal structures' are believed to be the driving force of turbulent boundary layers where kinetic energy from the free-stream becomes turbulent fluctuations and internal energy through the action of viscous force (Robinson, 1991). This process is believed to be self-sustaining (i.e. continuous) (Robinson, 1991; Panton, 2001a,b). The earliest explanation and hypothesis of coherent structures were put forth by two giants of classical fluid mechanics, Theodorsen (1952) and Townsend (1956), in which the latter extended his works in Townsend (1961, 1976). Both Theodorsen's and Townsend's work are discussed in more detail in section 2.1.2. Robinson (1991) divided coherent motion studies into several different periods, namely: *the discovery era (1932 - 1959), the flow-visualisation era (1960 - 1971), the conditional-sampling era (1972 - 1979),* and *the computer simulation era (1980 - present).* However, the 'present' era ends with Robinson (1991) more than 20 years ago. Since then there have been more developments in the study of coherent structures, for example : particle image velocimetry (PIV) and the discovery of very large scale motions and superstructures.

Following the identification classes of coherent structures by Smits et al. (2011b), here we divide the review of coherent structures into three different categories, namely:

1. Near-wall structures.

2. Hairpin vortices.

3. Large and very-large structures.

In this chapter we concentrate our attention on the coherent structures of the canonical turbulent flows of incompressible fluids, namely turbulent pipe flow, channel flow and zero pressure gradient (ZPG) turbulent boundary layers.

2.1.1 Near-wall structures

The near-wall structures started to gain a lot of attention between 1960 and 1971, in a period which Robinson (1991) calls *the flow-visualisation era.* This was an era where the understanding of coherent-structures was still in its infancy and technology in fluid flow experiments was beginning to advance (particularly in electronics) and become more affordable. The pursuit to understand near-wall structures continued in the 1970's, Robinson (1991) called it *the conditional-sampling era.* It was an era where digital computers became more affordable and revolutionised the way fluid-mechanics research was conducted. The early studies of near-wall structures (especially in flow-visualisation) were dominated by Kline and co-workers from the Stanford group and Brodkey and co-workers from the Ohio state group. In this report we combine the two eras (the flow-visualisation and conditional-sampling era) into one section and discuss it simultaneously, as there are many aspects of near-wall structures investigations that are connected and overlapped between the two periods.

Near-wall turbulence production

Although the study of near-wall structures began during *the discovery era* of $1932 - 1959$ (Robinson, 1991), it was not until the late 1960's that a breakthrough was achieved through the seminal work of Kline et al. (1967). The near-wall region can be defined as a region between the wall and the lower end of the logarithmic profile $0 < z^+ < 15$, although some may argue that the upper limit is higher (i.e $z^+ = 50$ by Jiménez (1994)). According to Jiménez (1994) it is a region where turbulent energy production has the largest rate and a location where viscosity is dominant and interacts with the turbulence strongly. Kline et al. (1967) reported the presence of well-organized spatially and temporally dependent motions within the near-wall region using Hydrogen bubble flow visualisation technique. These

motions result in low-velocity streaks that gradually lift-up, then oscillate, burst and eject/grow away from the surface due to vortex stretching. The streaks/elongated structures are also known to move away from the wall at a certain angle and convection velocity relative to the mean flow. The visualised streakiness is now known as the *near-wall cycle of quasi-streamwise vortices*, which play a central role in generating and sustaining turbulent production processes. The streaks are found to have width $\Delta y^+ \approx 80 - 100$ and length $\Delta x^+ \approx 1000$ and located at $z^+ < 40 - 50$ (see figure 2.1) (Kline et al., 1967; Panton, 2001b). The mechanics of streak formation and breakup is visualised in figure 2.2.
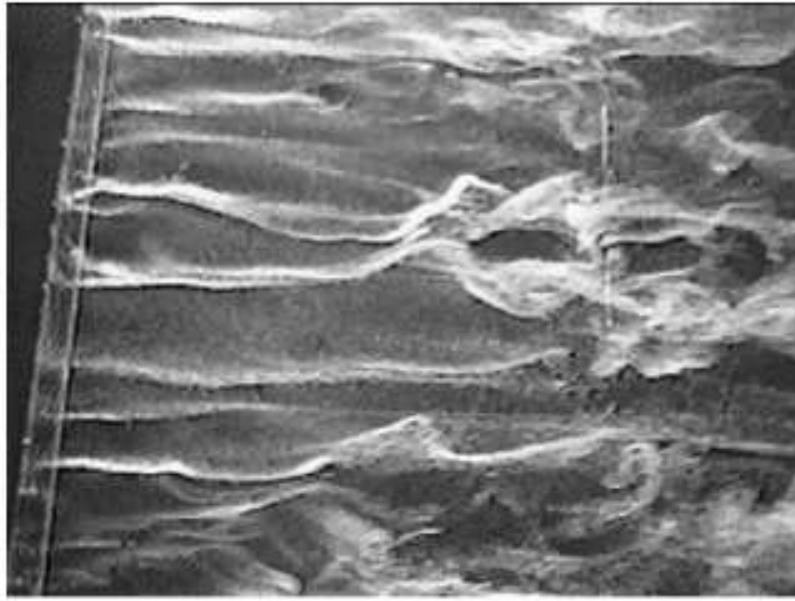
Figure 2.1: Image of low-speed streaks (Panton, 2001b).

The bursting process which Kline et al. (1967) refer to as a violent breakup of a low-velocity streak after lifting, is often interpreted differently. Bogard and Tiederman (1987) and Panton (2001b) define bursts as several ejections coming from one streak. Indeed there is no universal agreement on the precise definition of the term burst or bursting. Robinson (1991) indicates that there are at least five different definitions of burst from various reports. However, he summarizes it into two :

1. *'A violent, temporally intermittent eruption of fluid away from the wall, in which a form of local instability is often implied.'*

2. *'A localized ejection of fluid from the wall, caused by the passage of one or more tilted, quasi-stream wise vortices, which persist for considerably longer time scales than do the observed ejection motions.'*
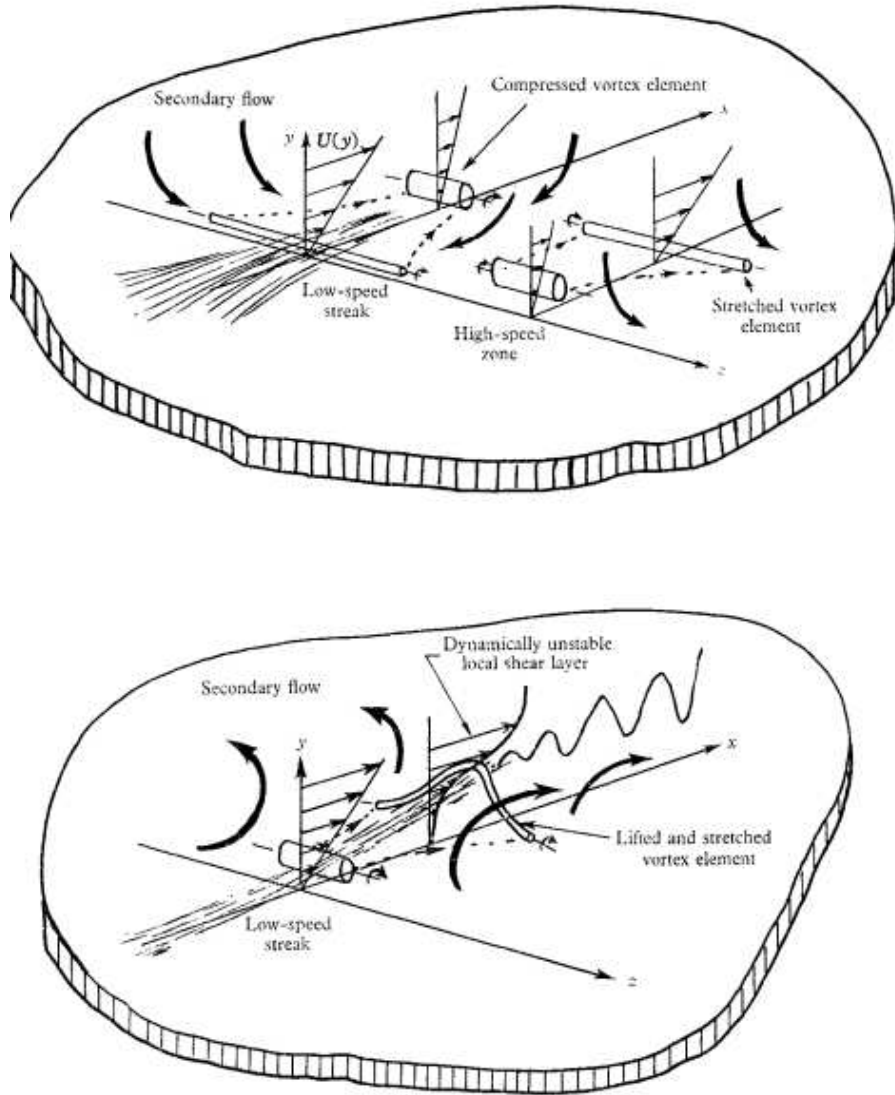
Figure 2.2: The mechanics of streak formation (top figure) and breakup (bottom figure) (Kline et al., 1967).

Corino and Brodkey (1969) from the Ohio State group performed a slightly more sophisticated method of a visual-photographic technique using colloidal particles as tracers, an early version of the Particle Image Velocimetry (PIV) technique. They have extended the findings of Kline et al. (1967) by

showing the ejection/bursting sequence in more detail, involving deceleration and acceleration of the fluid flow. Their results indicate that ejection occurs $\approx 18\%$ of the time and accounts for $50 - 70\%$ of turbulence production. Corino and Brodkey (1969) introduced another coherent motion event following the ejection, namely *sweep*, which is a condition where fluid from a higher region accelerates and moves towards the wall. The sequence of ejection followed by sweep is believed to play a major role in the Reynolds stresses.

Kline and co-workers extended their earlier experiments on the near-wall turbulent flow by combining hot-wire with dye visualisation complementing the Hydrogen-bubble measurements (Kim et al., 1971). In this report, they seem to have paid more attention to the bursting event and recognised its importance. Furthermore, they reported that practically all of the turbulence production occurs at $0 < z^+ < 100$ during a bursting event. Kim et al. (1971) suggest that a bursting event consists of three different stages:

1. Lifting of the near wall low-velocity streaks from the innermost layer to form unstable inflectional instantaneous velocity profiles.

2. Growth of an oscillatory motion in the region beyond the inflectional zone.

3. Break up of the oscillatory motion into more turbulent and chaotic motions, accompanied by a return to the wall motion of the low-speed streak with a more quiescent flow.

Kim et al. (1971) also postulate that the energetic near-wall ejections (or bursts) move to the outer region and give rise to larger scale motions such as *'bulges'*. Interestingly however, Kim et al. (1971) do not mention any sweep type event which was reported by Corino and Brodkey (1969).

Wallace et al. (1972) extended the work of Corino and Brodkey (1969) with hot-film measurements and found positive Reynolds stress contributions between ejection and sweep events and a negative contribution from their interactions at $z^+ = 15$ ($+70\%$ from ejections and sweeps, -40% from the interaction between ejections and sweeps). A year later Nychas et al. (1973) improved the PIV-type measurements of Corino and Brodkey (1969) by incorporating a high-speed camera that moved along with the flow. Through

this unique set up, Nychas et al. (1973) were able to capture and follow the development of flow for a longer time and allowed a more complete observation of the sequences of the events. Their observations showed a transverse vortex (which is a part of the sequence of accelerated and decelerated flows) that extended from near the wall to the outer region. The acceleration or deceleration flow events are not mentioned by Kline et al. (1967) or Kim et al. (1971), probably due to the limitations of their experimental technique. The accelerating and decelerating motions trigger the ejection/bursting and sweep events which were reported earlier by Corino and Brodkey (1969). Furthermore, it seems that Nychas et al. (1973) have touched the cause-and-effect relationship between the inner-region event and outer-region effect. They believe that the wall-region activities are caused by conditions in the outer region: *'The transverse vortex of the present work was not the result of growth of smaller scale fluid motions... More important, it was the outer accelerated fluid which caused it'*.

Three years after Kim et al. (1971), Kline and co-workers finally addressed the neglect of the sweep event from their previous work. Using two dye injectors, bubble wire and a moveable pitot-tube, Offen and Kline (1974) tried to improve the understanding between the low-velocity streaks near-wall burst and the outer flow field. The results reveal that the ejections/bursts lead to sweep and then back to ejection/burst and so forth. Offen and Kline (1974) postulate that: *'The interaction between bursts and the flow in the logarithmic region produces sweeps which, in turn, influence the generation of bursts further downstream'*. It was the first time that a study touched the *'regenerative'* cycle of turbulence production. One year later Offen and Kline (1975) revisited and summarised the work of Kline et al. (1967); Kim et al. (1971); Offen and Kline (1974) from the Stanford group and concluded that the three oscillatory stages reported by Kim et al. (1971) were actually only one type of flow structure, the stretched and lifted vortex from the original work of Kline et al. (1967). They reached this conclusion by incorporating a sweep event into the stretched and lifted vortex model. Furthermore, they also touched the possible interactions between near-wall structures and much larger structures and the connection between the lifted, stretched vortex model and the hairpin/horse shoe models (see section 2.1.2).

Offen and Kline (1975) did not specifically mention that their stretched and lifted vortex is the now famous hairpin/horse shoe vortex, however

they admit that their findings bear a striking resemblance to the horse shoe vortex of Theodorsen (1952). Finally, and perhaps the strongest statement by Kline and co-workers is that *The turbulence processes near the wall are due to nearby interactions; they are not driven directly by the large-scale motions which are observed as 'bulges' in the superlayer.* In other words, they believe that the small-scale near-wall/inner region activities are the driving force of large-scale motions in the outer region.

The different views between the Stanford group and Ohio state group cannot be clearer. Praturi and Brodkey (1978) summarised the Ohio state group's findings and gave the conceptual model that relates coherent motions in the outer region to near-wall turbulence production. They also re-emphasise that: *'the outer region transverse vortices induce near-wall ejections and streamwise vortices, as well as bulges in the outer turbulent/potential interface and entrainment of new free-stream fluid'* (Robinson, 1991). The debate over whether the near-wall small scales affect the larger scales motions away from the wall or whether the large scales influence the near-wall small scales is still an ongoing study.

Later in section 2.1.3 we will discuss the nature of large-scale structures/motions (including bulges) and how they affect the near-wall structures in more detail. Furthermore, the recently discovered very large scale motions and superstructures will be discussed.

2.1.2   Hairpin vortices

Within turbulent boundary layers there exist vortices that are believed to be the main element in the turbulence-production cycle and in the transport of momentum between the inner and outer layers (Robinson, 1991). The shape of these vortices are commonly identified to be in the shape of a hairpin/horse shoe. The idea of hairpin/horse shoe vortices as turbulent elements was first put forth by Theodorsen (1952) where he hypothesised the existence of vortices in the shape of a hairpin that arose from near the wall to transport fluid flow. Theodorsen considered these vortices to be the building blocks of turbulent flow (see figure 2.4).

At around the same time, independent of Theordosen's work, Townsend
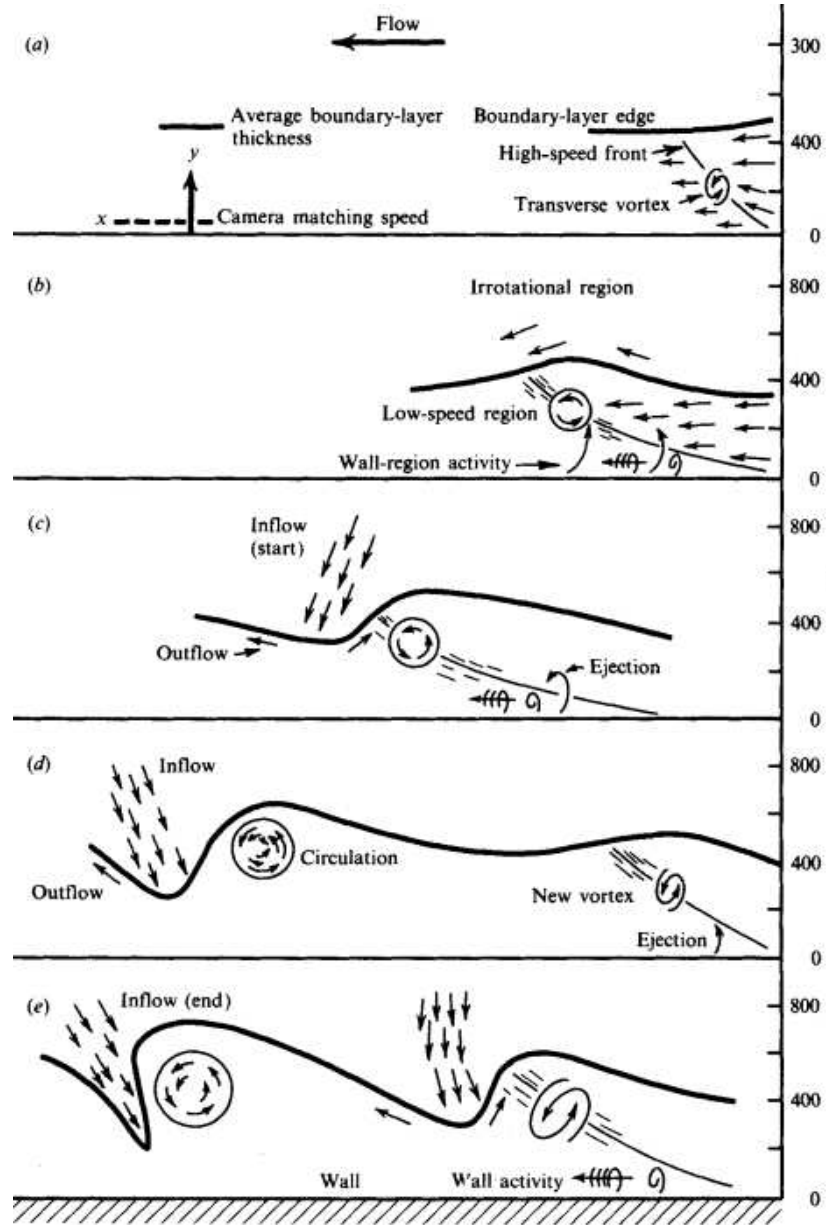
Figure 2.3: Mechanism of interactions between outer-flow motion with wall-region viewed in a downstream convecting frame (Praturi and Brodkey, 1978).

(1956, 1961, 1976) put forth the *attached eddy* hypotesis, proposing double cone vortices attached to the wall, and extending all the way to the logarithmic region (Panton, 2001b). His concept of an attached eddy is described in Townsend (1976) as '*a flow pattern which is of finite size, mechanically coherent and resistant to disintegration. If energy is supplied to or removed*
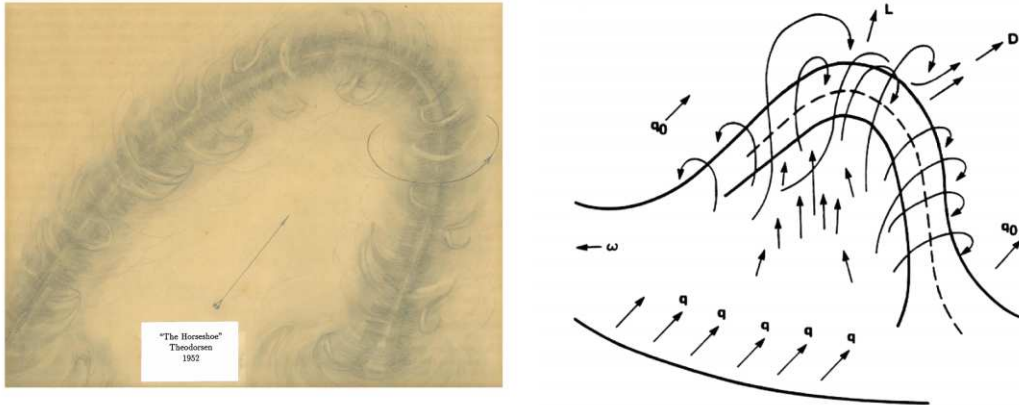
Figure 2.4: Hairpin/horse shoe vortex by Theodorsen (1952).
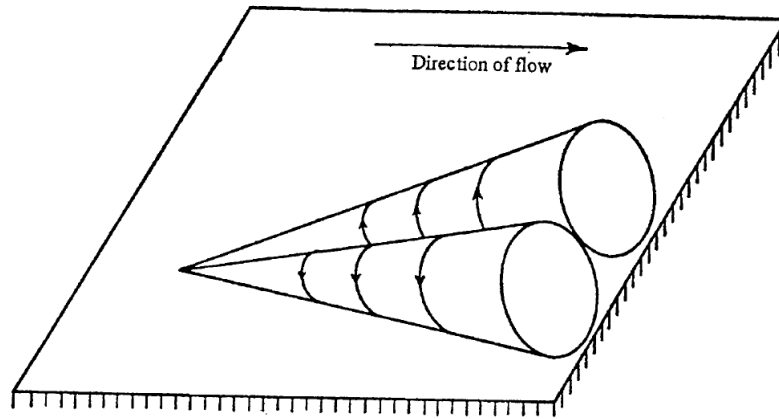
Figure 2.5: Townsend's attached vortices (Townsend, 1976).

in one part of the pattern, energy ows to or from that part to preserve the structure'. Based on suggestion by Peter Bradshaw, Panton (2001b) wrote the following explanation of Townsend's concept: *'The double-cone attached eddy Townsend deduced from correlation measurement is best described as a Headless horse shoe - in other words I think it is the same thing as the (symmetrical or asymmetrical) horse shoes everybody talks about today. Like all concentrations of vorticity it moves with (the motion of) the fluid. One can imagine the horse shoe arising from a small, local, upward perturbation of a spanwise vortex line in a shear flow: the head of the incipient horse shoe is dragged downstream, the legs are stretched and rotate faster, and the velocity induced by the legs is in a sense that pushes the head upward (into a higher velocity region). With an eye of faith one can regard the elongated legs as*

streaks - though in pairs rather than a continuous distribution. I think that Townsend used the word attached to distinguish between a large eddy that was influenced by the impermeability condition and the smaller eddies in a wall flow which are not'. Based on this explanation, it seems that the horse shoe/hairpin vortex and attached eddy are the same feature. Hence, both Theodorsen and Townsend describe the same flow feature. Figure 2.5 shows the attached vortices illustration from Townsend (1976).

The question of whether hairpin vortices exist or not has been debated for almost 60 years and goes to the very core of uncovering the mechanism of wall bounded turbulence (Marusic, 2009). The Stanford and Ohio State groups have touched on the idea of the existence of hairpin vortices, however they never directly mention it. This section will discuss several important aspects of hairpin vortices, such as the evidence of their existence. Furthermore, there are suggestions that these hairpin vortices organise themselves into a group and convect coherently forming a packet of hairpins (Zhou et al., 1999; Adrian et al., 2000; Christensen and Adrian, 2001; Ganapathisubramani et al., 2003, 2005; Hutchins et al., 2005).

Evidence of hairpin vortices

Although Theordosen proposed a hairpin vortex model in the early 1950's, it took almost two decades for researchers to detect their existence (see Offen and Kline (1975)). The quest to find the hairpin shaped vortices has proven to be an arduous one due to the complexity of turbulent flow and experimental equipment limitations. Various visualisation techniques such as the use of dye, particles, smoke, laser doppler velocimetry (LDV), and early types of particle image velocimetry (PIV) have been employed to hunt down hairpin vortices. Falco (1977) used simultaneous hot-wire and the fog oil flow visualisation technique to study the large-scale motions in the outer region of turbulent boundary layers. By recording the hot-wire data and film of the smoke marked layer simultaneously, Falco could perform conditional sampling of the hot-wire signals for a specific flow feature. Therefore, the ensemble averages of the fluctuating velocities associated with the smoke patterns could be obtained (see figure 2.6).

Bandyopadhyay (1980) and Head and Bandyopadhyay (1981) extended Falco (1977) experimental technique by using an inclined light sheet in order to

Figure 2.6: Visualised turbulent boundary layers by Falco (1977)

provide strong experimental evidence of hairpin-vortices. Head and Bandy-opadhyay (1981) performed flow visualisation over the momentum thickness Reynolds number (Re_θ) range of $500 < Re_\theta < 17500$. Their results show images of hairpin-shaped vortices densely populated inside the boundary layers. These hairpin vortices are found to be elongated at 45° and form 20° turbulence interface for high Reynolds number (see figure 2.7).
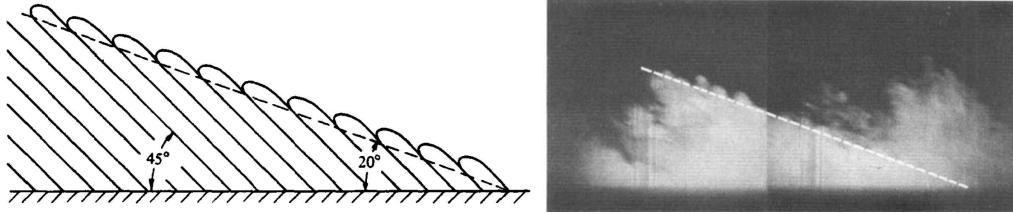
Figure 2.7: Schematic of inclined 45° hairpin vortices with 20° inclined interface relative to the surface (a) and flow visualisation taken at $Re_\theta = 17500$(Head and Bandyopadhyay, 1981).

Figure 2.8 shows the schematic diagram of the effects of Reynolds number to the vortex structure. At lower Reynolds number on the vortices are less elongated and the shape closely resembles a horse shoe. However, as Reynolds number increases, the horse shoe shaped vortex is stretched and become more elongated (and closely resembles a hairpin shape). The results also reveal that the hairpin-vortices extend from the wall to the edge of boundary layer. Furthermore they seem to grow and organise themselves into larger structures. Head and Bandyopadhyay (1981) are often credited as the first to have actually detected and identified what appears to be hairpin vortices.

At around the same time, Perry et al. (1981) also observed similar structures where horse shoe vortices were stretched and formed into hairpin vortices.
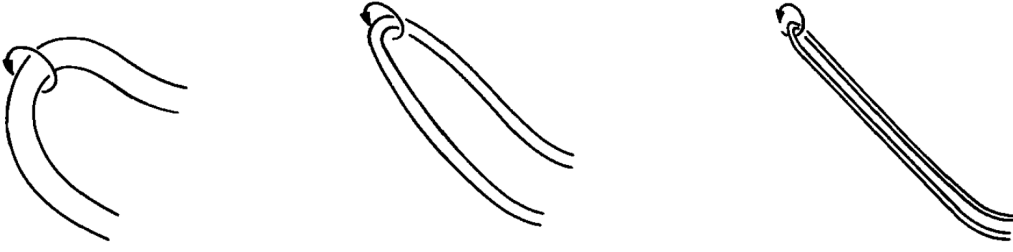
Figure 2.8: Effects of Reynolds number (Re) to the vortex structure. (a) low Re, (b) moderate Re, (c) high Re (Head and Bandyopadhyay, 1981)

Perry and co-workers called the hairpin-shaped structure Λ vortex filaments. The hairpin vortices resemblance between Perry et al. (1981) result and Head and Bandyopadhyay (1981) hairpin illustration can be seen in figure 2.9 and figure 2.8. The strong resemblance suggests that they are referring to the same structures.

Results from Bandyopadhyay (1980); Head and Bandyopadhyay (1981) and Perry et al. (1981) have renewed interest in hairpin vortices as important elements of turbulent boundary layers. In order to see the coherent structures in more detail, Moin and Kim (1982, 1985); Kim and Moin (1986) performed low Reynolds number Large-Eddy Simulation (LES) of turbulent channel flow. Their results show hairpin-shaped lines inclined at 45° inside the turbulent flow. Hence Moin and Kim have provided one of the earliest three-dimensional structures of hairpin vortices (figure 2.10). Since then, with the advent of computational power, the study of coherent motions using numerical techniques has become ever more important, particularly complementing experimental studies.

To understand the role of hairpin vortices in more detail, Acarlar and Smith artificially generated hairpin vortices through a hemispherical perturbation (Acarlar and Smith, 1987a) and fluid injection (Acarlar and Smith, 1987b). Although the experiments were performed in laminar flow condition, through various flow visualisation methods, they allowed clear observations of the hairpin vortices developments in detail. Acarlar and Smith (1987a) indicate there are two types of vortices, standing vortices (formed at the upstream stagnation point of the hemisphere) and hairpin-type vortices (periodically shed into the wake of the hemisphere). Figure 2.11 demonstrates the birth of both vortices.
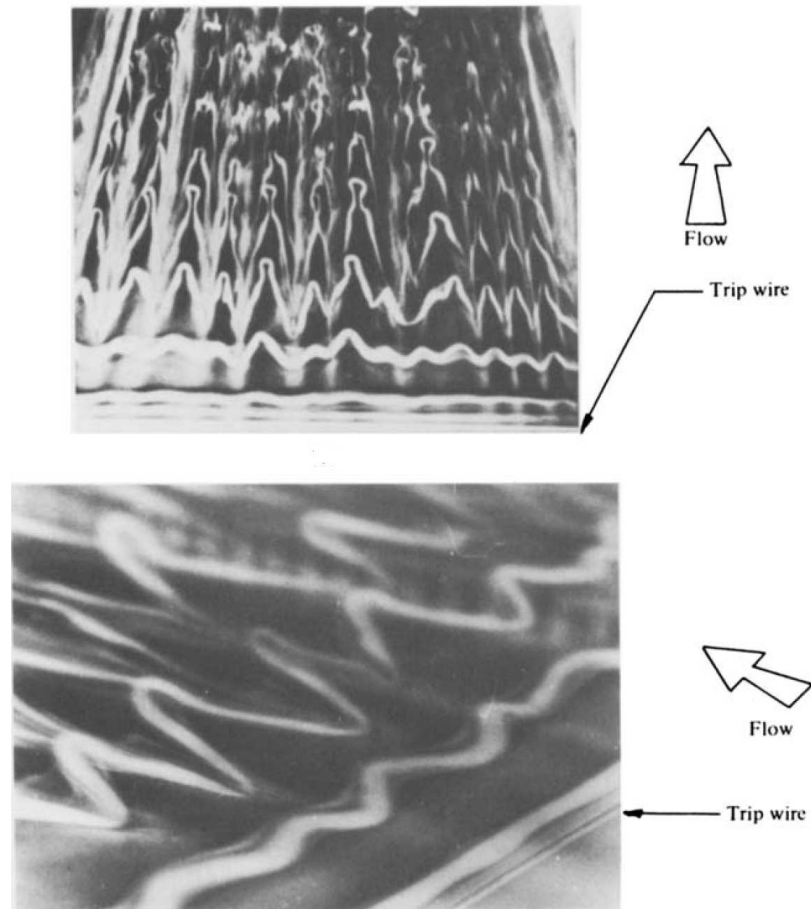
Figure 2.9: Λ shaped vortices from Perry et al. (1981)

The results from Acarlar and Smith (1987a) reveal a striking similarity be-
tween the near-wall flow patterns and the flow patterns generated by the
hairpin vortices. They suggest that hairpin vortices are the building block
and basic flow structure of turbulent boundary layers. However, the ori-
gin of the hairpin vortices within turbulent boundary layers is still unclear
from this type of experiment. In their second paper, using a different hair-
pin vortex generation technique, Acarlar and Smith (1987b) postulate that
the origin and generation of hairpin vortices in turbulent boundary layer
are from the roll-up of three dimensional shear layers. Further examination
also revealed that the older and larger hairpin vortices generate long and
persistent low-speed flow between their counter-rotating legs near the wall.
It seems that the hairpin vortices have an important role in the production
of the low speed-streaks that had previously been reported by Kline et al.
(1967). Acarlar and Smith (1987b) also show that secondary vortices are
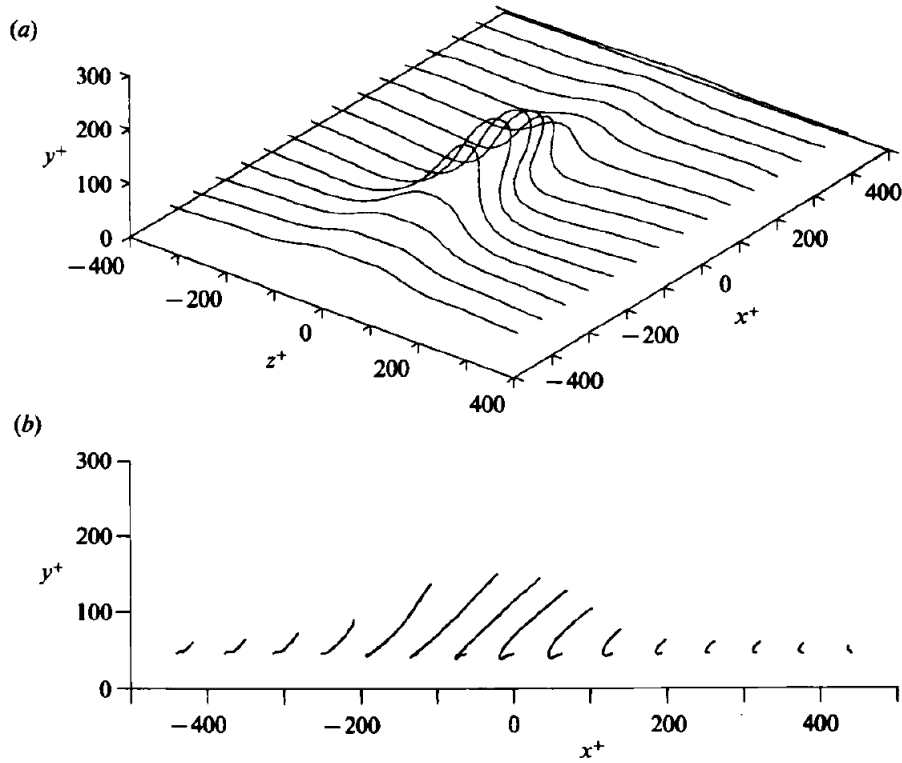
Figure 2.10: Hairpin vortices from LES of channel flow at low Reynolds number (Kim and Moin, 1986)

formed through the interaction between the lifted up/ejected low-speed fluid from the near-wall and the higher-speed flow of the outer region (see figure 2.12). The secondary vortices interact very strongly with the primary hairpin vortices and generate burst-type events. Based on those experiments, the fluid injection technique more closely resembles the natural formation of hairpin shaped structures than the hemispherical perturbation (Zhou et al., 1999).

Smith et al. (1991) refined their original work in Acarlar and Smith (1987a,b) and provided significant development in the theoretical analysis of the mechanism of hairpin vortex regeneration and the existence of groups of hairpins. They introduced an inviscid model to further explain the generation of secondary hairpin vortices from a single primary vortex. These successive or groups of secondary hairpins, are latter know as *hairpin packets*. Intrigued by the continuously generated train of hairpins, Haidari and Smith (1994) extended the work of Acarlar and Smith (1987a) to a more detailed study
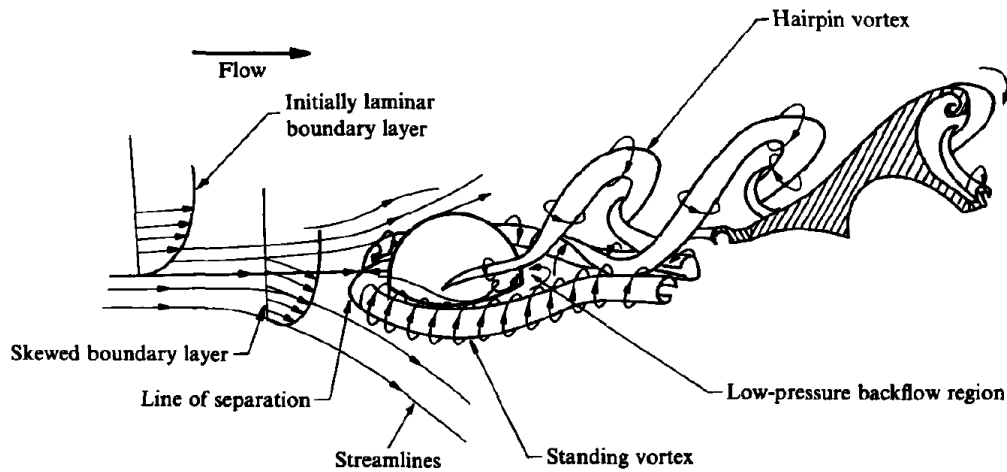
Figure 2.11: Schematic of near-wake structures in the hemisphere wake (Acarlar and Smith, 1987a)
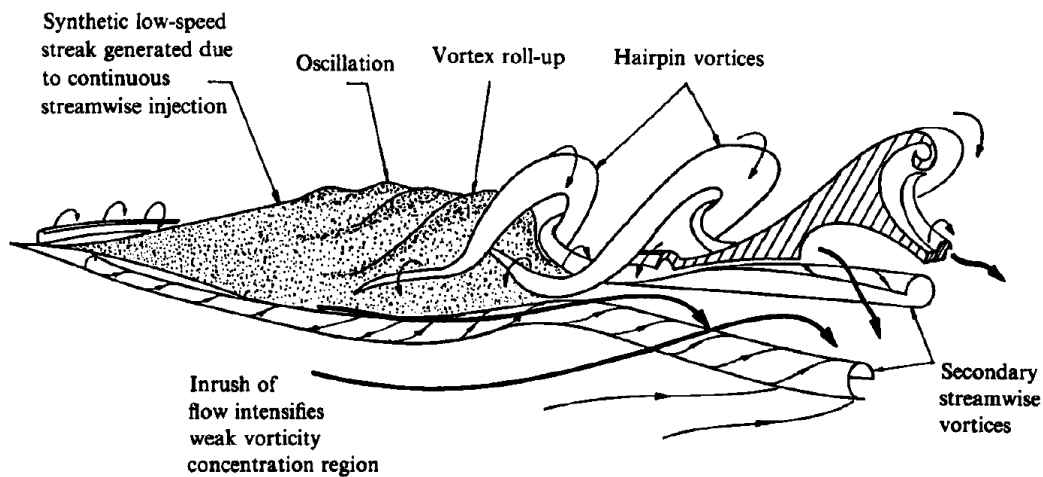
Figure 2.12: Schematic of break-up of a synthetic low-speed streak generating primary and secondary hairpin vortices (Acarlar and Smith, 1987b)

of individually generated hairpin vortices. Haidari and Smith (1994) questioned whether these vortices are regenerating or reproduce themselves, or whether they arise from the periodic shedding of the bump. They produced a single hairpin vortex by injecting dye through a slot on the wall. Using a linear actuator they could control the injection velocity and injection time duration. The results showed that the number of hairpin vortices are depended upon the injection velocity. A slow injection velocity does not produce hairpin vortices, however, a higher velocity can produce a single

hairpin vortex, and for even higher velocity it generates multiple hairpin vortices. From these results, Haidari and Smith (1994) suggest that *hairpin vortices are a generic flow structure that develop from a three-dimensional perturbation of an otherwise two-dimensional shear flow.* DNS of a flow similar to the experiments by Haidari and Smith (1994) was performed by Singer and Joslin (1994), the results revealed hairpin vortices which resemble the injection of dye. Over time the primary vortex develops multiple hairpin vortices beneath its elongated legs.

The late 1980's and early 1990's also mark a period where a new type of measurement technique called Particle Image Velocimetry (PIV) became an important part of fluid mechanics research (Adrian, 2005a). One such study using PIV was done by Liu et al. (1991), where they showed spanwise vorticity fields in channel flow that have similar patterns to the hairpin vortices (figure 2.13). The development of PIV proved to be an important addition, complementing the previously existing experimental technique (hotwire and flow visualisation) and computational studies (LES and DNS)
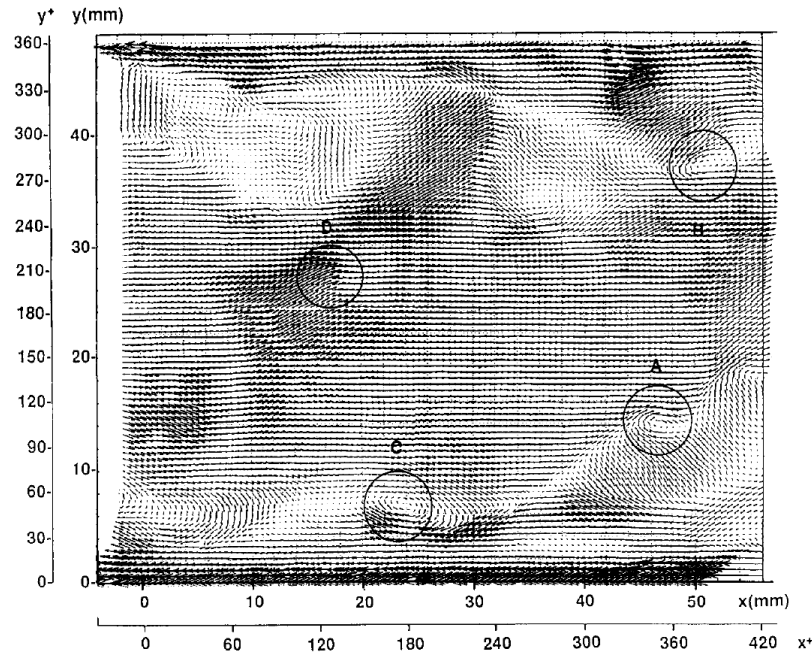
Figure 2.13: Hairpin vortices detection by PIV (Liu et al., 1991)

Robinson (1991) summarised various studies of hairpin-vortices and came up with an idealised schematic of vortical-structure populations at different wall normal locations (figure 2.14). In his model, quasi-streamwise

vortices populate the near wall/buffer region. Slightly higher in the loga-
rithmic/overlap region, the quasi-streamwise vortices co-exist with arch-like
vortices (when the hairpin is incomplete or one sided, it is often referred as
arch). Finally, in the wake region, the arch-like vortices dominate.
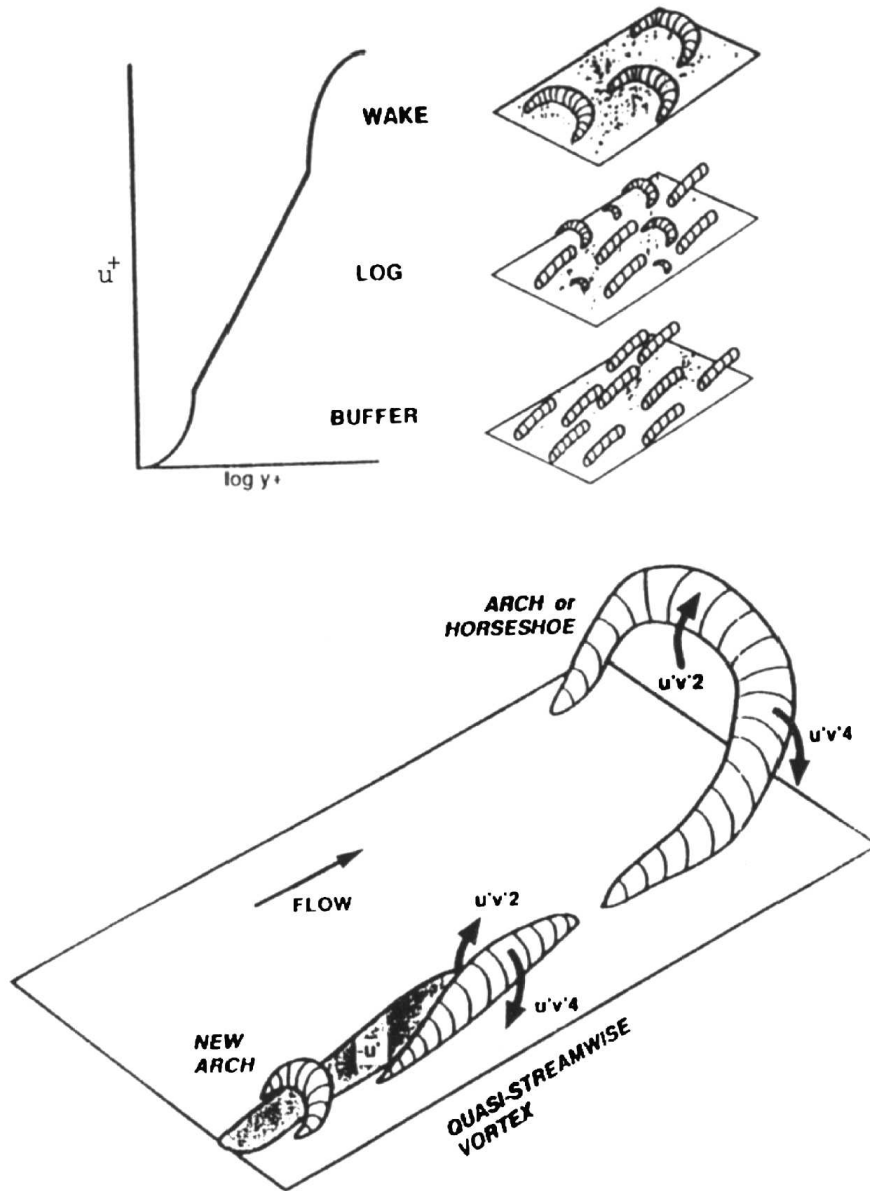
Figure 2.14: Hairpin vortices model for different wall normal distance
(Robinson, 1991)

2.1.3 Large and very-large structures

From three decades of various studies in coherent structures, Kline and Robinson (1989a,b) and Robinson (1991) have categorised the taxonomy of turbulent structures into eight different phenomena:

1. Low-speed streaks in the near-wall region.

2. Ejections and liftings of low-speed fluid from the wall

3. Sweeps of high-speed fluid toward the wall.

4. Vortical structures in form of hairpin/horse shoe.

5. Sloping of near-wall shear layers.

6. Near-wall pockets visible.

7. Large-scale motions and bulges in the outer layer observed.

8. Shear-layer of large-scale outer region motions.

These eight categories are now widely accepted as the basic building blocks of wall bounded turbulent flow. However a decade later Panton (2001b) added another category, called hairpin packets, which has been investigated extensively by Adrian and co-workers (Zhou et al., 1999; Adrian et al., 2000; Christensen and Adrian, 2001) and Marusic and co-workers (Ganapathisub-ramani et al., 2003, 2005; Hutchins et al., 2005). These hairpin packets are believed to concatenate and form the large-scale motions (LSMs).

Recently, a new element has been added to the list, *very large-scale motions* (VLSMs). These recently discovered very large-scale features have attracted plenty of attention, and have raised questions regarding their contribution to the small-scale near-wall structures and the Reynolds shear stress. The full picture of their origin and how they are formed is still uncertain and more investigations (especially at very high Reynolds numbers) are needed. This section will discuss the nature of LSMs and VLSMs, and their effect on the near-wall turbulence structure.

Evidence of large and very large-scale motions (LSMs and VLSMs)

Large-scale structures in turbulent flow were first recognised by Townsend
(1956) and Grant (1958) in the turbulent wake behind a circular cylin-
der (Kim and Adrian, 1999). Subsequent flow visualisation studies by
Kline et al. (1967); Kim et al. (1971); Offen and Kline (1974, 1975) in-
dicate low-speed streaks and burst-type events that have period scaled
with outer/large-scale and lead to the formation of bulges in the loga-
rithmic region (Kim et al., 1971; Narahari Rao et al., 1971; Laufer and
Badri Narayanan, 1971). Although some argued that the bursting period
is scaled with inner flow, it seems clear that the bulges observed are as-
sociated with the large-scale structures. Further investigations by Kovasz-
nay et al. (1970); Blackwelder and Kovasznay (1972); Brown and Thomas
(1977); Falco (1977, 1991); Robinson (1991); Kim and Adrian (1999), re-
vealed that these bulges are scaled with δ, which indicate large-scale mo-
tions.

PIV works of Adrian and Marusic and their co-workers (Zhou et al., 1999;
Adrian et al., 2000; Christensen and Adrian, 2001; Ganapathisubramani
et al., 2003, 2005; Hutchins et al., 2005) indicated that hairpin packets may
be associated with the formation of bulges due to their similar size and
scale. Furthermore, it is believed that several hairpin packets at various
stages of growth (older and younger packets) may exist inside one bulge
(Kim and Adrian, 1999; Adrian, 2007). From these conjectures, it seems
that LSMs are generated by a group of hairpin packets traveling at the same
streamwise velocity (Smits et al., 2011b; Balakumar and Adrian, 2007).

In addition to LSMs that scale with δ, there is evidence of the existence
of even larger features in the turbulent boundary layer. From pipe flow
experimental data, this very large feature is known to have a streamwise
length of 12 - 14 times the pipe radius or scales as large as $12 - 14\delta$, (Kim
and Adrian, 1999; Guala et al., 2006; Balakumar and Adrian, 2007). This
is much larger than the standard large-scale bulge length (which generally
scales in $1-3\delta$). Hence the term very large-scale motions (VLSMs) or *super-
δ scale* motions is coined (Kim and Adrian, 1999; Guala et al., 2006). Figure
2.15 illustrates the process that creates VLSMs. Here hairpin vortices align
coherently in groups to form long packets, and then groups of packets align
coherently to form VLSMs. Prior to Kim and Adrian (1999) discovery of
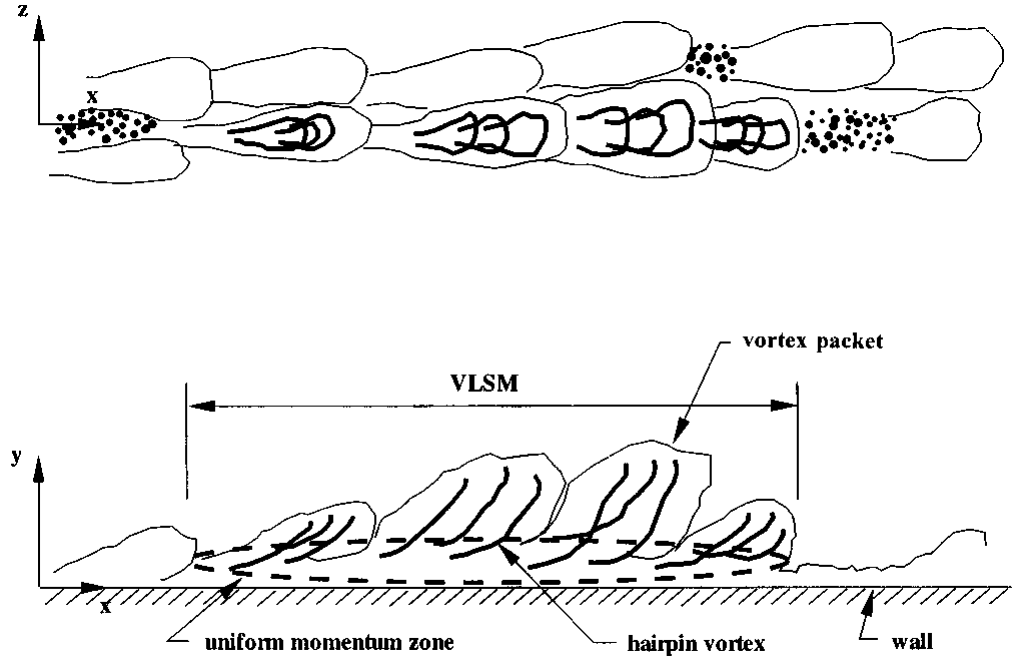
Figure 2.15: The conceptual model of the process that generates very large-scale motions. Here, y is wall normal direction (Kim and Adrian, 1999).

VLSMs, despite the existence of evidence of VLSMs, for almost two decades it was almost neglected. According to Guala et al. (2006) one source of this problem was that there was no consensus regarding the definition of LSMs and VLSMs, nor the turbulent bulges and its associated bursting. It was not until the beginning of 21st century that various experimental, theoretical, and numerical studies clarified the distinction/difference between these two important features (Guala et al., 2006).

Realising the limitation of PIV to examine the very long streamwise length of VLSMs, Hutchins and Marusic (2007a) performed an experiment that employed a spanwise rake of 10 hot-wires in a ZPG turbulent boundary layer. The aim of the experiment technique was to capture the fluctuating streamwise velocity u over a certain spanwise range. The signal is then projected in time, and through Taylor's hypothesis (frozen convection), a much larger streamwise domain than what is possible in PIV can be obtained. Details and limitations of Taylors hypothesis can be found in studies by Taylor (1938); Zaman and Hussain (1981); Dennis and Nickels (2008); Moin (2009) and del Álamo and Jiménez (2009). Through this technique, an extended view of the very long low- and high-speed streaks can be obtained.
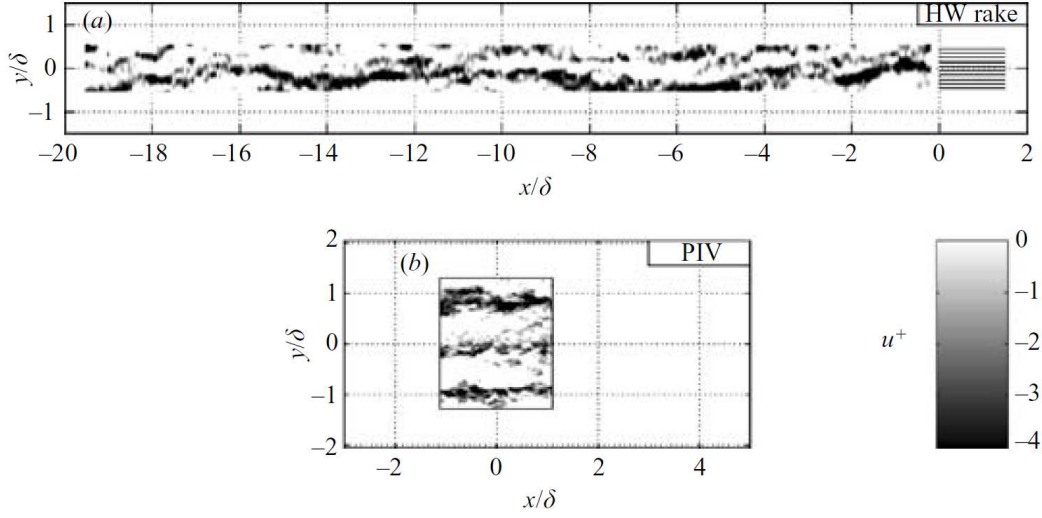
Figure 2.16: Very long meandering positive and negative streamwise velocity fluctuations extending over 20δ. Here y is spanwise direction, x is streamwise direction, and z is wall normal direction. (a) superstructures from hot-wire rake. (b) superstructures from PIV (Hutchins and Marusic, 2007a)

Figure 2.16 reveals that very long meandering positive and negative streamwise velocity fluctuations extending over 20δ reside in the logarithmic region of the turbulent boundary layer. The feature is termed *superstructures* and seem to be the same VLSMs that Kim and Adrian (1999); Guala et al. (2006) and Balakumar and Adrian (2007) observed in turbulent pipe flow and channel flow. Monty et al. (2007) performed similar hot-wire rake experiments in both pipe and channel flow to see whether the same meandering features also exist in all canonical wall bounded flows. For the pipe-flow experiment, Monty et al. (2007) used a semicircular rake with 15 hot-wire sensors, while for the channel flow experiment, a spanwise array of 10 hot-wire probes were used. The hot-wire rake data indicate that the same very-long meandering features also exist in both pipe and channel flow (Monty et al., 2007).

The discovery of VLSMs (typically used when referring to internal flow such as pipe and channel flow) and superstructures (generally used when referring to external flows such as a ZPG turbulent boundary layer) have raised further questions regarding their origin and influence on the Reynolds shear stress and overall turbulent production. However, it seems clear that this newly discovered feature holds the key to understanding turbulent boundary

layers further.

Further observations in pre-multiplied energy spectra across the boundary layer indicate that the superstructures contribute to the streamwise turbulence intensities (hence contributing to turbulent production and Reynolds shear stress). The contribution seems to be increasingly significant with the increase of Reynolds number. As Reynolds number increases, there is a significant increase/spike in the pre-multiplied energy spectra located at the midpoint of logarithmic region $z/\delta = 0.06$, which again suggests the existence of VLSMs or superstructures (Hutchins and Marusic, 2007a). This location is later corrected to be $z^+ \approx \sqrt{15Re_\tau}$ by Mathis et al. (2009a). Furthermore, when it is compared with the near-wall small-scale structures, the scale of superstructure is larger by approximately a factor of at least $6Re_\tau/1000$.

Apart from the laboratory experiments, superstructures have been shown to exist in the atmospheric surface layer at very high Reynolds number. Hutchins and Marusic (2007a) analysed data from experiments conducted in the salt flats of the Great Salt Lake Dessert using sonic anemometers. The sonic anemometers were arranged in both wall normal (nine sensors logarithmically spaced) and spanwise (ten sensors linearly spaced). Figure 2.17 shows a superstructure with a physical length of approximately half a kilometre with $Re_\tau = 660,000$. According to Hutchins and Marusic (2007a), the physical size of near-wall structures in an atmospheric surface layer is around 90 mm. With such high physical scale separation, it seems unlikely that near-wall structures can influence or generate the much larger superstructures.

Effect of large-scale structures on the near-wall small-scale structures

The debate whether near-wall structures influence large-scale structures or vice versa has been ongoing since the flow visualisation era of 1960 - 1971(see section 2.1.1). With the recent discovery of VLSMs, it seems that the conjecture that large-scale structures influence or affect the near-wall small-scale structures is becoming more acceptable. A thorough investigation by Hutchins and Marusic (2007a,b) has revealed that VLSMs/superstructures tend to actively modulate the amplitude of the small-scale structures and leave a skin friction foot print at the wall. Furthermore, as Reynolds num-
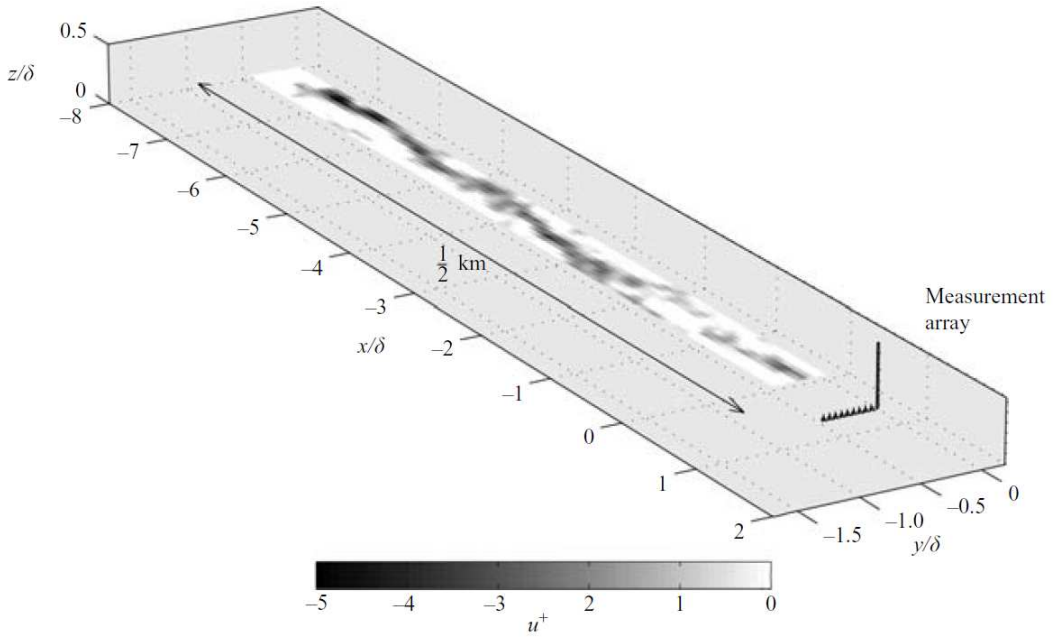
Figure 2.17: Superstructures in atmosphere (Hutchins and Marusic, 2007a)

ber increases, the superstructures seem to become more dominant when compared to the highly energetic near-wall structures.

Mathis et al. (2009a) extended the work of Hutchins and Marusic (2007b) to examine the impact of superstructures on amplitude modulation of the near-wall small-scale structures in more detail. They used spectral filter to separate the streamwise velocity into two components (small- and large-scale) and then used a Hilbert transform to obtain the envelope of the small-scale component. The filtered envelope of the small-scale fluctuations is then correlated with the large-scale fluctuations. The result shows that near the wall, the large-scale component acts as a modulating signal and the small-scale behave as a modulated signal.

The existence of VLSMs and superstructures in ZPG turbulent boundary layers, channel flow, and pipe flow have led Monty et al. (2009) to compare the three canonical wall bounded flows at a nominally equal Reynolds number of $Re_\tau \approx 3000$. The unique aspect of Monty's experiment is the constant non-dimensional hot-wire length (with viscous scaled hot-wire length $l^+ = 30$ for all three wall-bounded flows) which provides an accurate comparison of velocity fluctuation statistics. The results indicate an excellent agreement between the structure of turbulent channel and pipe flow. How-

ever, when they are compared with the turbulent boundary layers there are modal differences in the largest scales (observed in pre-multiplied energy spectra). Using data from Monty et al. (2009), Mathis et al. (2009b) investigated the differences in amplitude modulation for the three canonical wall-bounded flows. The data show that the VLSMs or superstructures induce the same amplitude modulation effect for all three cases with minor differences in energetic distribution between small and large-scales.

The amplitude modulation effect also exists in the atmospheric surface layer at very high Reynolds number ($Re_\tau \approx 500,000$). Guala et al. (2011) analysed atmospheric surface layer data from thermally neutral conditions in the salt flats of the Great Salt Lake Dessert over a two week period. Their analyses showed that the large-scale features amplitude modulate the small-scale features, with the strongest modulation occurring at wall normal distance $^+z < 1000$. More recently, Ganapathisubramani et al. (2012) show that both the amplitude and frequency of the near-wall small-scales increase with increasing values of the large-scale structures and decrease with decreasing values of the large-scale structures. Finally, Talluru et al. (2014a) have extended the amplitude modulation study by looking at all three velocity components and found that the small-scale spanwise and wall-normal fluctuations are also modulated.

Possible flow control strategy

Up to this point, this section has shown the importance of VLSMs and superstructures in turbulent boundary layers. Although it is still an ongoing investigation, it seems clear that these structures have an important part in affecting the turbulent fluctuations near the wall. Closer inspection of VLSMs and superstructures reveal that they have accompanying roll-modes between the high and low streamwise velocity fluctuations (Balakumar and Adrian, 2007; Marusic et al., 2010b; Chung and McKeon, 2010b). The diameter of these roll-mode is in the order of the width and height of hairpin packets ($1 - 3\delta$), they also exist in the atmospheric surface layer (Hutchins et al., 2012). The existence of the large scale roll-modes that accompany the superstructures raises the question whether it is possible to disturb and eventually control the roll-modes. By controlling the large scale roll-modes it may also control the superstructures, and arrive at an effective drag

reduction technique. One such control method is through generating large-scale counter rotating roll-modes through highly aligned surface roughness (see section 2.2.6)

2.2   Riblets

Nature provides many examples of ways to reduce skin-friction drag in fluid flow. From the moving feathers on the wing tip of eagles that reduce wing tip vortices, to the effortless movement of fast swimming fishes, dolphins and sharks under water (Bechert et al., 2000b; Dean and Bhushan, 2010). The mucus on the skin of fast swimming fish such as barracuda operates as a drag reduction agent. Its artificial derivatives can be seen in the polymer additive to reduce drag in oil pipe industry (i.e. Alaska oil line). Various studies have shown that the skin of dolphins and sharks play an important role in allowing them to swim at such high speeds. In the case of dolphins, it is believed that they have a compliant skin which responds to pressure fluctuations and suppresses the development of Tollmien-Schlichting (TS) waves. The suppression of Tollmien-Schlichting (TS) waves causes the delay of flow transition from laminar to turbulent, resulting in a net reduction in drag. Details and summaries of studies in drag reduction through compliant surfaces are provided in Lucey and Carpenter (1995); Choi et al. (1997).

For fast swimming sharks, their skin is covered with dermal denticles which have similar shape to small riblets or a corrugated wall, and are aligned in the direction of fluid low (Reif, 1985; Dean and Bhushan, 2010). People have realised the unique pattern of fast swimming shark skin for more than a century (see figure 2.18). However, it is only recently that scientists have realised the connection between shark skin and fluid flow. Studies by Burdak (1969) and Chernyshov and Zayets (1970) are the first (to the best of our knowledge) that hypothesise the significance of shark skins on the fluid flow around them. Unfortunately, due to their microscopic size and fine structure, and the limitation of fluid mechanics understanding at that period, there were no further studies involving sharks skin for a decade. One general perception at that time was; it is considered futile to have a lower skin-friction drag than that generated by a smooth surface (Bechert and Bartenwerfer, 1989). Furthermore, the idea that such a small pattern can affect the flow around a very large shark ($\mathcal{O}100 - \mathcal{O}1000$, relative to

the dermal denticles) was difficult to accept.
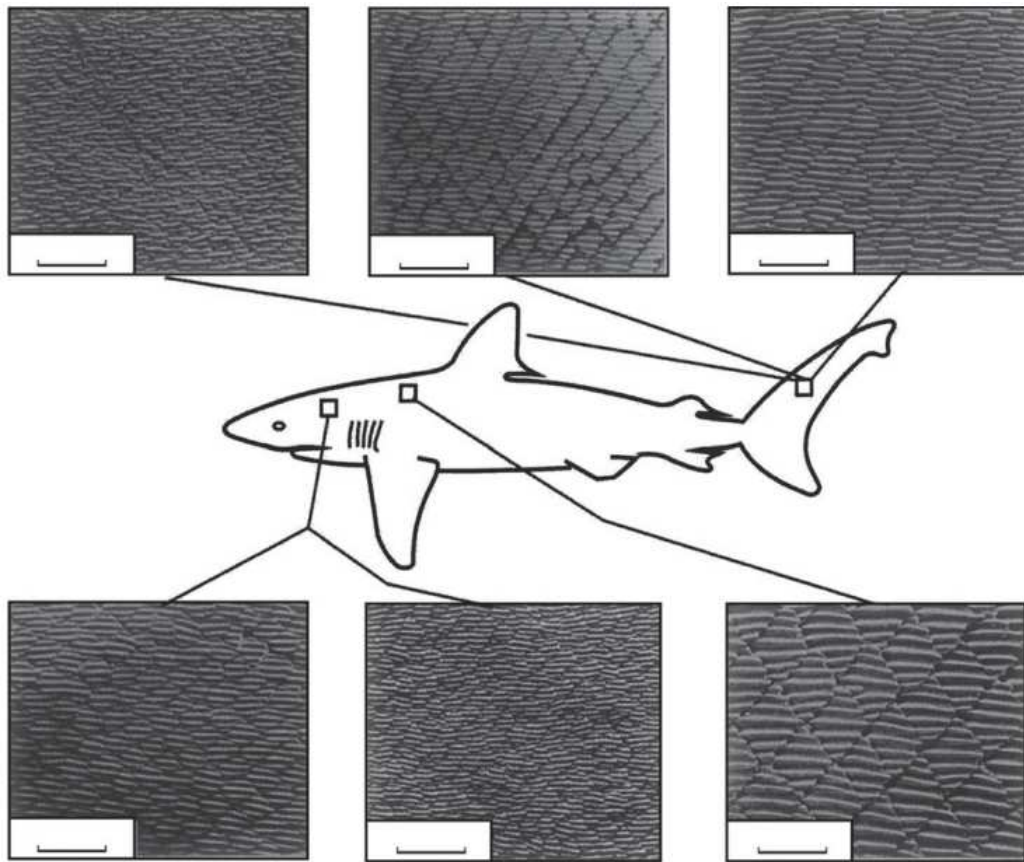
Figure 2.18: Scale pattern of a fast-swimming shark (from Reif (1985) and Dean and Bhushan (2010), scale bar is 5 mm).

2.2.1 Early riblet studies

It was not until the end of 1970's when researchers started to look into riblets in more detail. The study of flow over riblets was caused by the 1970's world oil crisis, which resulted in soaring fuel prices and burdened many aerospace and naval industries. Faced with this situation, efforts were made to find ways to reduce fuel consumption. According to a report by Walsh (1990), the initial idea of implementing riblets as a drag reduction mechanism came from the seminal work of the Stanford group (Kline et al., 1967; Kim et al., 1971; Offen and Kline, 1974, 1975), where they reported a low-and-high speed region of fluid near the wall of a turbulent boundary

layer. Flow visualisations indicate that the near-wall low speed regions move in a streawise, oscillating, bursting, and lifting away from the surface. It is believed that these processes have a dominant role in the production of turbulence (see section 2.1.1). Based on the findings of Kline et al. (1967); Kim et al. (1971); Offen and Kline (1974, 1975), the NASA Langley research group proposed the idea of controling and modifying the near-wall structure of a turbulent boundary layer by applying 'small fences' on a smooth-wall to reduce skin-friction drag. The "small fence", which is now known as riblets, has rectangular/blade, trapezoidal, triangular, or scalloped cross section. These types of riblets are classified as two-dimensional riblets and they are the most common type investigated. In this report, unless otherwise mentioned, we will refer 'riblets' as two-dimensional riblets.

Initial studies of the effect of riblets on turbulent boundary layers revealed that they can reduce skin-friction drag, albeit rather small (Walsh and Weinstein, 1978). In the early stages of the NASA Langley group research, it was found that the Stanford group (Liu et al., 1966) had carried out preliminary studies on small rectangular riblets, which were similar to Walsh and Weinstein (1978). The results from these two studies show a reduction in burst frequency and a small reduction in net drag Walsh (1990). Initial works by Liu et al. (1966) and Walsh and Weinstein (1978) are considered instrumental, because it showed conclusively for the first time that riblets are able to reduce drag, and provided direction for further investigations.

At around the same period of the riblets investigation by the NASA Langley group, on the other side of the Atlantic, the search for drag reduction techniques were also gaining momentum. The European Research Community on Flow, Turbulence and Combustion (ERCOFTAC) initiated continent-wide cooperation to find the best method to reduce drag through their Drag Reduction Special Interest Group (Choi, 2000). Since 1986, the group has held many specialised drag reduction meetings, resulting in many important developments (i.e. riblets, polymer additives, compliant coating, and wall oscillation). Riblets in particular, have received more attention than the other methods. The extra attention can be seen in the large number of research groups involved: The University of Southampton (UK), DLR/German Aerospace Berlin (Germany), The University of Milan (Italy), Institute of Theoretical and Applied Mechanics (Russia), and TU Delft (Netherlands) (Choi, 2000).

2.2.2 Drag reduction mechanism of riblets

Interest in the ability of shark skin to reduce drag and control flow was renewed in the middle of 1980's, as details about its microscopic properties became much more clear (Reif, 1982; Reif and Dinkelacker, 1982; Reif, 1985). The first study in drag reduction that specifically mentioned the effectiveness of shark skin inspired riblets are from the DLR Berlin group (Bechert et al., 1985). Their results are remarkably similar to the NASA Langley group findings (see Walsh (1982, 1983); Walsh and Lindemann (1984)), where the effect of riblets on the skin-friction drag reduction is dependent on Karman number Re_τ, and can be expressed in the wall units of the riblet's dimensions i.e. viscous riblets spacing $s^+ = sU_\tau/\nu$ and viscous riblet height $h^+ = hU_\tau/\nu$, where s is riblet spacing, h is riblet height. According to Walsh (1983), drag reduction occurs under the geometric condition of $s^+ < 30$ and height $h^+ < 25$, for V-groove riblets. Furthermore, the reduction can be as high as 8% (which is very significant for drag reduction through surface modification) for two riblet configurations: a symmetric V-groove riblet with $h^+ = s^+ = 12$, and sharp peaked riblets with large valley curvature with $h^+ = 8$ and $s^+ = 16$ (Walsh, 1982, 1983).
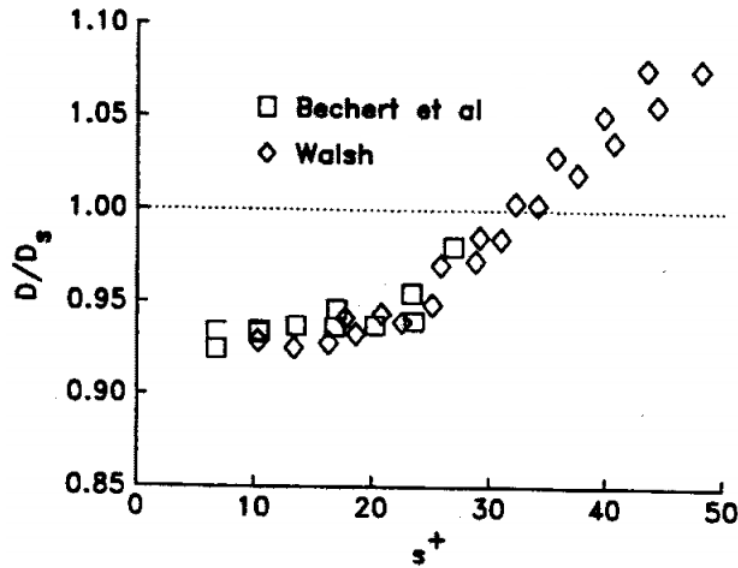
Figure 2.19: Drag reduction performance from Walsh (1983) and Bechert et al. (1985). The vertical axis is drag over riblets normalised by drag over smooth surface, the horizontal axis is viscous scaled spacing s^+.

Encouraged by the works of NASA Langley and the DLR Berlin group, in-

vestigations that involved riblet-type surface roughness on turbulent boundary layer flow and targeting the drag reduction mechanism were intensified. In the last three decades various studies involving different types of riblets, both experimentally and numerically, have given better insight into the mechanism of drag reduction. Most of the experimental studies are utilising sensitive drag balance/shear stress balance to measure the shear stress directly. By taking the shear stress differences between the riblet-covered surface and reference surface (i.e. smooth-wall) at similar flow conditions, it is possible to determine whether the drag is increased or decreased. Other methods include obtaining the velocity profile through hot-wire anemometry, Preston tube, or PIV, and utilize the Clauser method to obtain the skin-friction velocity U_τ (Clauser, 1954, 1956).

The most comprehensive and thorough results of riblet experiments are from Walsh (1982); Walsh and Lindemann (1984); Bechert et al. (1997, 2000a,b); and Dean and Bhushan (2010) where it has been shown that the maximum drag reduction can reach up to 10% for riblets with spacing of $s^+ = 15$. Figure 2.19 shows the dependence of riblets drag reduction ability in terms of its spacing. From the figure, it is clear that in the region with very small riblets spacing which is commonly called "viscous regime" ($s^+ \approx 15 - 20$), the drag reduction is comparable or proportional to the riblet viscous geometry. As the riblets' viscous geometry increases, their effect decreases until it reaches a minimum, or no drag reduction $\Delta\tau/\tau_0 \approx 0$ at $s^+ \approx 30$ (figure 2.20), here τ is frictional wall shear stress, $\Delta\tau$ is change in wall shear stress, and τ_0 is reference wall shear stress. For $s^+ > 30$, the riblets behave as a standard rough surface and drag starts to increase.

As mentioned previously, the core idea of using riblets in a wall bounded turbulent flow is to damp/hamper and modify crossflow or the near-wall cycle of streaks and quasi streamwise vortices (Kline et al., 1967) and reduce the near wall velocity gradient at the wall (i.e. reduce drag). According to Bechert and Bartenwerfer (1989) the geometry that has crucial role for hampering the crossflow is called *protrusion height*, the virtual length or distance between the apparent origin of the velocity profile and the riblet's tip. The origin of this velocity profile is located below the riblet's tip and above the bottom valley between riblet tips. The left hand side of figure 2.21 shows the protrusion height of the longitudinal/streamwise flow h_{pl}, and the right of figure 2.21 shows the protrusion height of the crossflow h_{pc} (Bechert et al., 1997). Initially, Bechert and Bartenwerfer (1989) suggested that h_{pl}
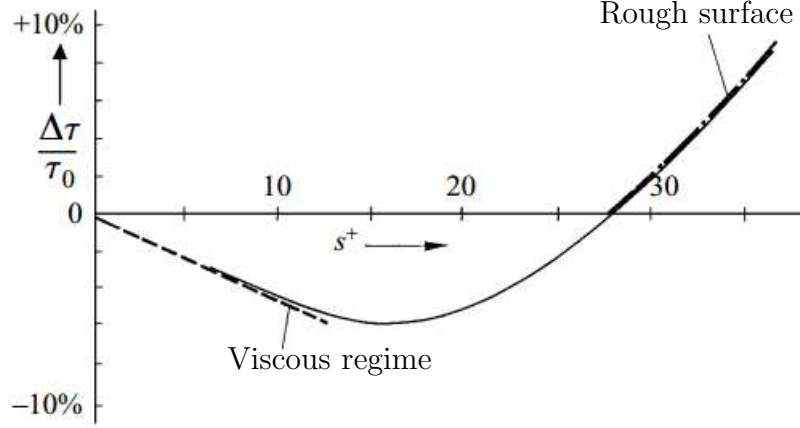
Figure 2.20: General structure of a drag reduction curve (Bechert et al., 1997), where $\Delta\tau/\tau_0$ is change of wall shear stress normalised by reference wall shear stress and s^+ is riblets spacing.

was the cause of the drag reduction, by impeding the cross flow. However, Luchini et al. (1991) extended this view and contend that the important parameter is $\Delta h = h_{pl} - h_{pc}$. It is clear from both figures that the origin of the longitudinal flow is different from the crossflow. If the crossflow protrusion height lies above the longitudinal protrusion height (i.e. $h_{pc} < h_{pl}$), secondary cross-flow will experience a higher viscous dissipation than the main longitudinal flow, resulting in lower near-wall turbulence. The notion of protrusion height has been verified through DNS and the results suggest that h_{pl}, h_{pc} and Δh are all comparable and proportional to the riblet size (Jiménez, 1994; García-Mayoral and Jiménez, 2011b). In effect, *Δh gives a quantitative characterization of whether and how much the corrugated wall impedes the cross-flow more than it does the longitudinal flow, and is the only parameter on which the behavior of the turbulent boundary layer may depend* (Luchini et al., 1991).

Evidence of lower turbulence fluctuations both inside the riblet valley and above the riblet tip are put forth by Vukoslavcevic et al. (1992); Pulles et al. (1989); Park and Wallace (1994). Using both standard and miniature hot-wires, the higher order statistics from these studies (turbulence intensity, skewness, flatness) reveal that turbulence fluctuations rarely penetrate inside the groove. The hot-wire results also reveal that the shear stress inside the riblets is lower than the corresponding smooth-wall case.
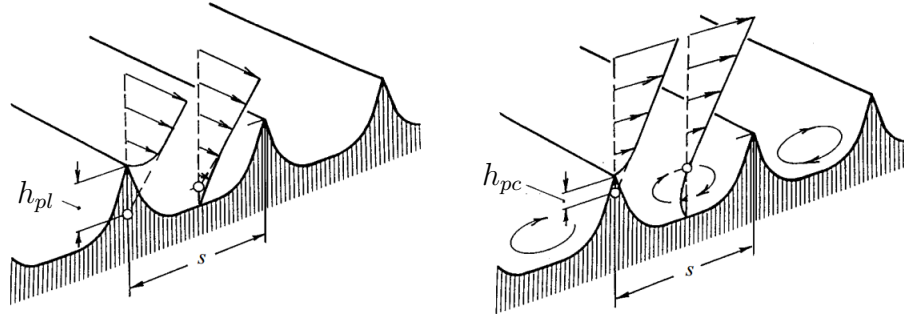
Figure 2.21: Protrusion height for viscous longitudinal h_{pl} and crossflow h_{pc} on riblets surface. $\Delta h = h_{pl} - h_{pc}$ (Bechert et al., 1997).

In order to see the turbulent structure near the riblets surface in much more detail, various flow visualisation and imaging studies have been performed in the last three decades (see Bacher and Smith (1986); Suzuki and Kasagi (1994); Lee and Lee (2001)). Figure 2.22(a) from Lee and Lee (2001) shows a flow visualisation of the drag reduction mechanism by riblets. The figure reveals that a large-scale streamwise vortex resides above the riblets, and the size of the vortex is larger than the riblet's dimension. As the vortex forms above the riblets, it remains there and interacts with the riblet tips. Since the vortex only interacts with the relatively small area on the tips, only these minute regions experience high-shear stress. The riblet tips also act as a barrier to impede the spanwise movement of the streamwise vortices/crossflow and prevent it from moving as freely as the vortices on the corresponding smooth-wall. Sometimes the large-scale streamwise vortices generate a small secondary vortex when they interact with the riblet tips, however due to their small size and weak vorticity, there is hardly any increase in skin-friction drag. Furthermore, because the vortex stays above the riblet peak/tips, the crossflow fluctuations within the riblets are relatively small. Figure 2.22(b) shows that at higher velocity the vortex penetrate the valley of the riblets and increase the velocity fluctuation. This situation results in the increase of skin-friction drag. It seems that as free-stream velocity increases the viscous dimension of the riblets become larger, allowing the vortex to move inside between the riblets wall.

Numerical studies demonstrate good agreement with the experimental data, and support the hypothesis that the riblets are affecting the near wall turbulent structure by damping the crossflow/spanwise velocity fluctuations, and hence reduce the skin-friction drag (Chu and Karniadakis, 1993; Choi

Drag decreasing ($U_\infty = 3$ m/s) Drag increasing ($U_\infty = 5$ m/s)

Flat plate ($U_\infty = 3$ m/s) Flat plate ($U_\infty = 5$ m/s)
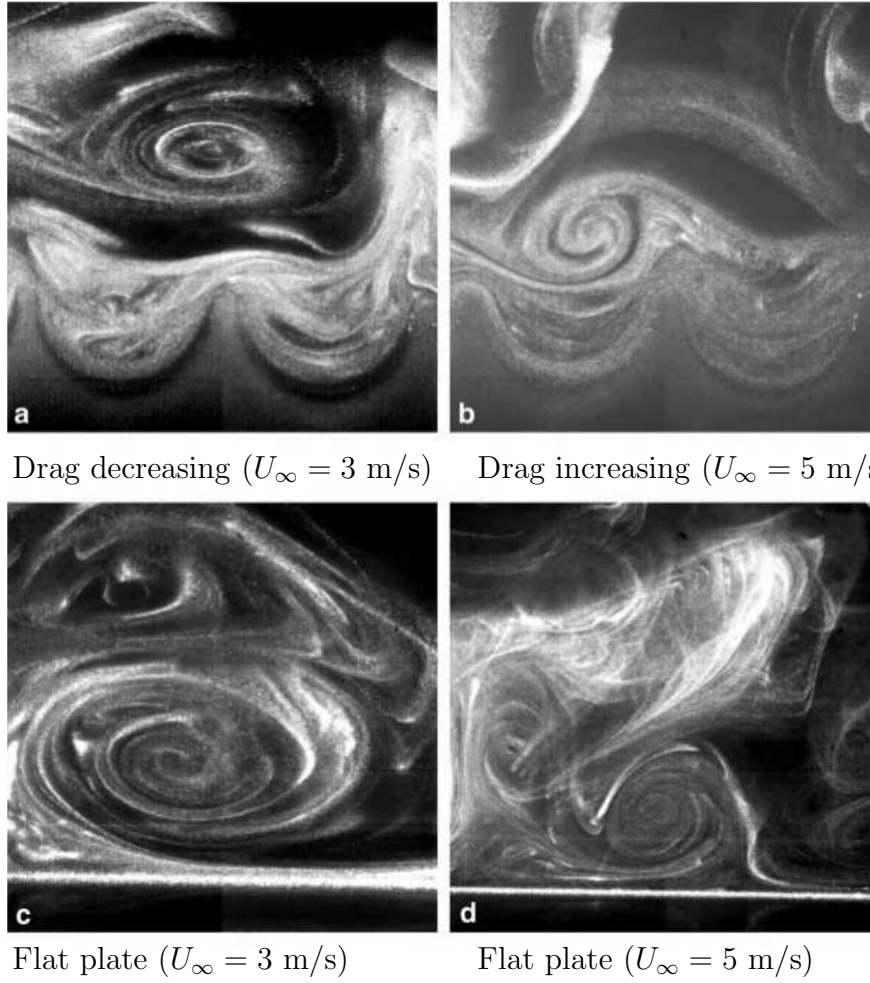
Figure 2.22: Flow visualisation images of streamwise vortices for drag decreasing and increasing (Lee and Lee, 2001).

et al., 1993; Goldstein et al., 1995; El-Samni et al., 2007; García-Mayoral and Jiménez, 2011a,b). Figure 2.23 shows DNS flow-visualisation of triangular riblet with $s^+ = 18$ (top figure) and $s^+ = 12$ (bottom figure) channel flow from Goldstein et al. (1995). For $s^+ = 18$ the vortices are able to penetrate the riblet valley and reduce the drag reduction effectiveness. For $s^+ = 12$, the vortices reside above the riblets peak unable to move inside the valley.

El-Samni et al. (2007) report similar channel flow DNS results for thin rectangular riblets with $s^+ = 18$ (drag reduction case) and $s^+ = 41$ (drag increase case). Figure 2.24 (top figure) shows the Reynolds shear stress
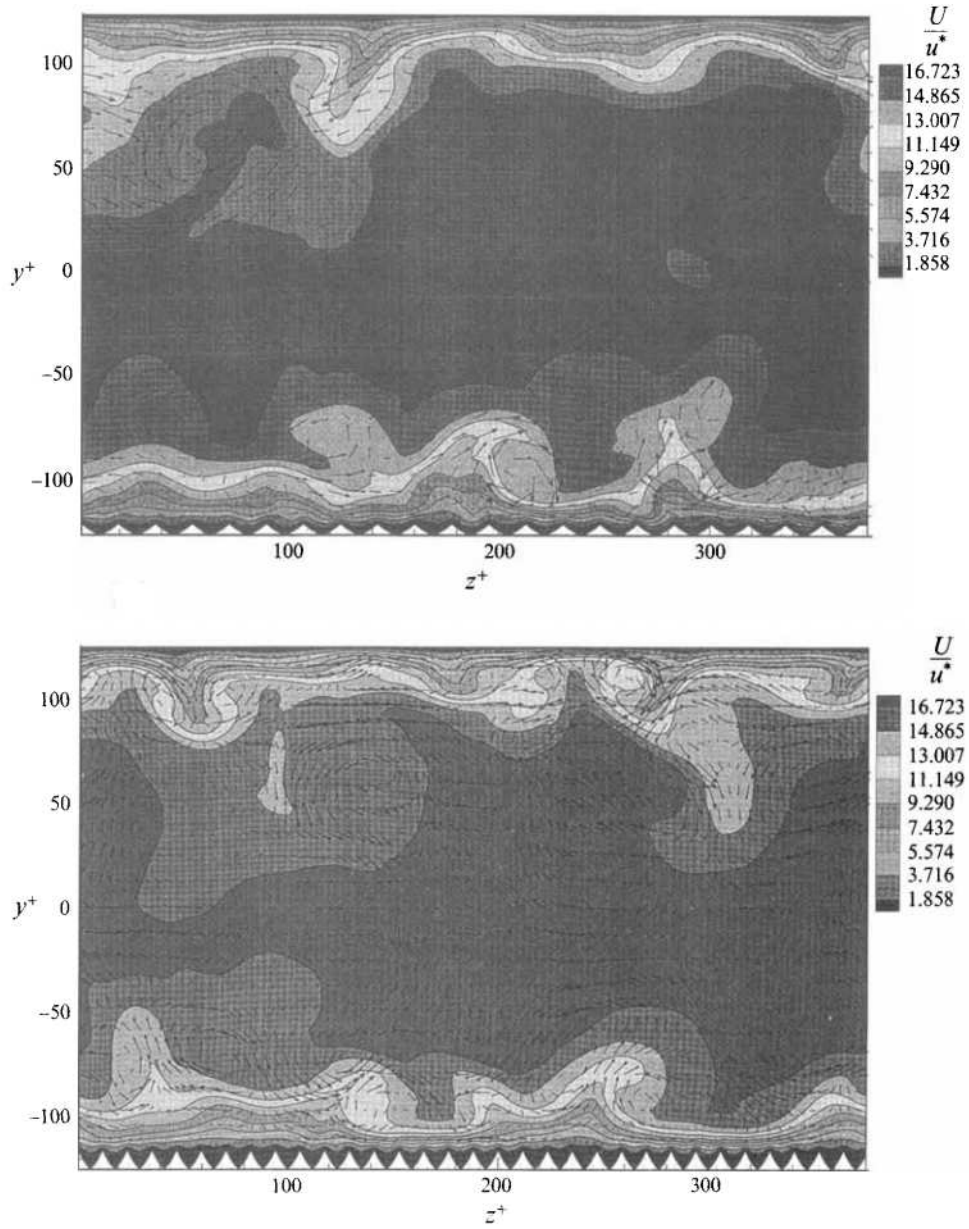
Figure 2.23: DNS of streamwise vortex above triangular riblets with $s^+ = 18$ (top figure) and $s^+ = 12$ (bottom figure) inside channel flow(Goldstein et al., 1995). The vertical axis is viscous scaled wall-normal distance and the horizontal axis is viscous scaled spanwise distance.

for the drag reduction case. Several regions of Reynolds shear stresses are observed hovering above the riblets and they are not penetrating inside the riblets. This results in low turbulent fluctuations inside the riblet valley.
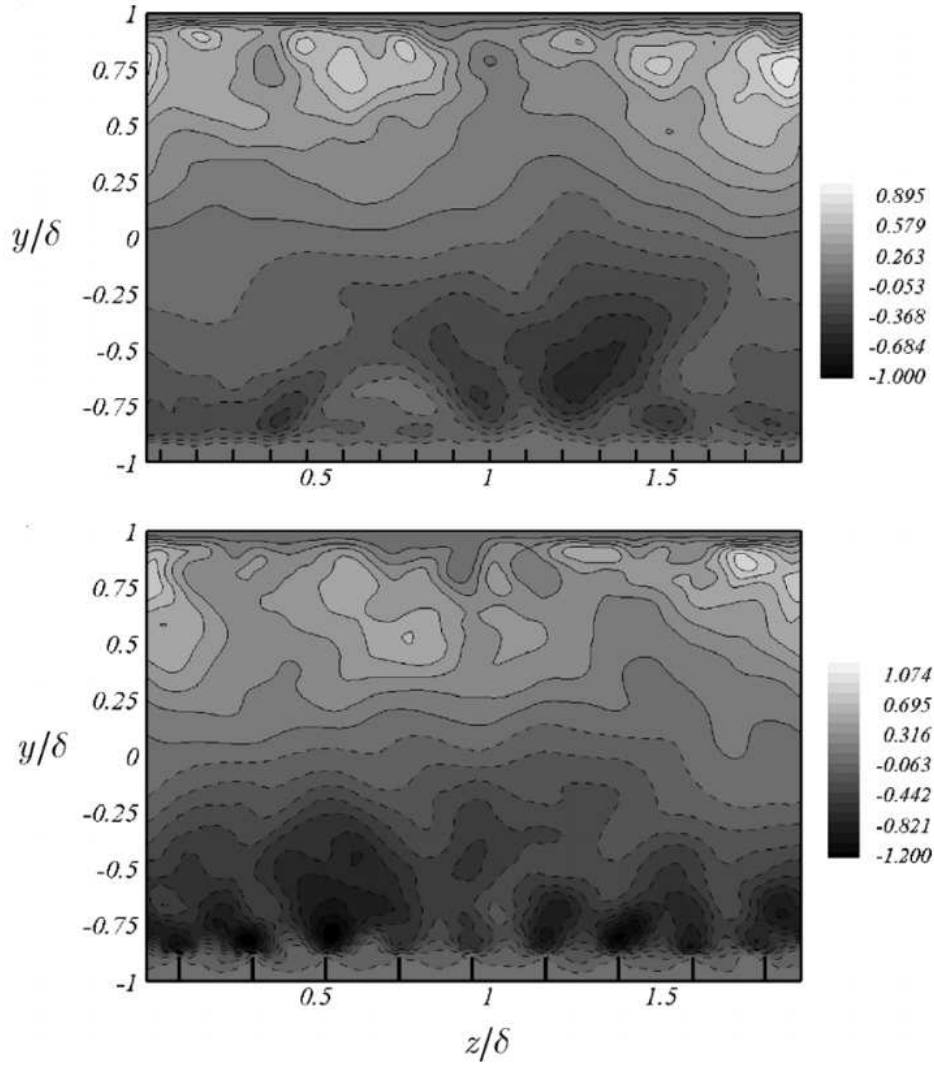
Figure 2.24: DNS of Reynolds shear stress above thin rectangular riblets with $s^+ = 18$ (top figure) and $s^+ = 41$ (bottom figure) inside channel flow (El-Samni et al., 2007). The vertical axis is wall-normal distance normalised by boundary layer thickness and the horizontal axis is spanwise distance normalised by boundary layer thickness.

Conversesely, for the drag increasing case, the wide riblet spacing allows the shear stress to move into the riblet valley and increase turbulent fluctuations. Figure 2.25 show the effect of increased Reynolds shear stress above the riblets towards the crossflow inside the riblets. The figure clearly reveals that rotating vortices reside inside the riblet valley, which stir and increase the turbulent fluctuations.
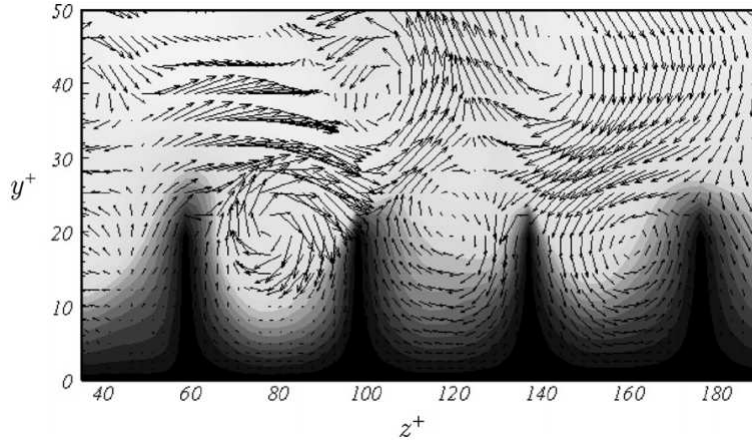
Figure 2.25: DNS of cross-flow inside thin rectangular riblets with $s^+ = 41$ inside channel flow (El-Samni et al., 2007)

.

Recent reports have shown that conventional straight riblets are also able to influence Tollmien-Schlichting (TS) wave in laminar flow and constrain or limit the growth of turbulent spots (Strand and Goldstein, 2011). This mechanism delays transition from laminar to turbulent flow, which results in lower skin-friction drag (Joslin, 1998). It seems that riblets are able to reduce skin-friction drag through laminar flow control and influencing the near-wall structure.

From various studies it is known that the drag reduction ability of riblets is dependent on their geometry, such as s^+ and h^+ (see figure 2.20). As s^+ increases further away from the viscous regime ($s^+ > 20$), the riblets' ability to reduce drag starts to decline, and for $s^+ > 30$ it behaves as a standard rough-wall. The drag reduction mechanism inside the viscous region/regime is fairly well understood and has been the subject of many investigations. However, beyond $s^+ > 20$, where the viscous regime starts to break down and drag increases, the mechanism is still poorly understood.

According to García-Mayoral and Jiménez (2011a,b) there are two groups of theories proposed in the literature. The first group hypothesises that the losses of cross-flow effectiveness beyond the viscous regime is the dominant mechanism (Goldstein and Tuan, 1998). They suggest that as the riblets spacing increases, the riblets wall ability to damp the cross-flow fluctuations decrease and the cross-flow fluctuations inside the riblet valley increase. The relatively strong crossflow generates a secondary streamwise vorticity over

the riblets and causes vertical mixing that leads to increased drag

The second group hypothesises that the penetration of vortices into the riblet valley is the cause of the breakdown in the riblets drag reduction ability (Choi et al., 1993; Suzuki and Kasagi, 1994; Lee and Lee, 2001). Their reports indicate that as s^+ increases well beyond the viscous regime ($s^+ = 30$ to $s^+ = 40$), vortices which were previously unable to penetrate the riblets, become able to enter the riblet valley. Inside the riblet valley, the vortices actively interact with the surface and increase the skin-friction velocity (see figure 2.22).

García-Mayoral and Jiménez (2011a,b) argue that the hypothesis put forth by both groups are based on observations in which the spacing s^+ is already well beyond the viscous regime. Therefore, the theories are still unable to explain the physical process just prior to the break down of the viscous regime, which they believe is more critical. As a result, it is difficult to determine whether their observations are the cause or a consequence of the breakdown. García-Mayoral and Jiménez (2011a,b) propose a different hypothesis for the breakdown of the viscous region based on the observations from DNS data. They argue that the breakdown is due to the emergence of long spanwise vortices below wall-normal height, $z^+ \approx 30$, with streamwise wavelength $\lambda_x^+ \approx 150$. The quasi-two-dimensional spanwise vortices seem to develop from instabilities which are similar to the Kelvin-Helmhotz instabilities in streamwise flow.

2.2.3   Optimization of riblets

Studies of riblets optimisation are typically performed by changing the viscous geometry sizes, h^+ or s^+, through different fluid flow velocity. Comprehensive studies of standard two-dimensional riblets (triangular, scalloped, and rectangular/blade) optimisation were performed by Walsh (1983); Walsh and Lindemann (1984); Bechert et al. (1997); Dean and Bhushan (2010). Based on these results, it is found that rectangular/blade geometry can generate a maximum 10% drag reduction for $h/s \approx 0.5$, scalloped geometry can reduce drag by up to 6.5% for $h/s \approx 0.7$, and triangular geometry can have optimum 5% reduction (with $\beta = 60°$) for $h/s \approx 1$ (Dean and Bhushan, 2010). Although the triangular geometry has the lowest drag re-

duction ability, it is the most durable shape and can withstand high speed
fluid flow (Dean and Bhushan, 2010).

In addition to the standard two-dimensional riblets, three-dimensional ri-
blet designs that mimic shark skin, such as staggered and continuous blade
riblets, have also been investigated (see Bechert et al. (1997, 2000a); Dean
and Bhushan (2010)). To the best of our knowledge this type of riblet is
rarely investigated due to its complex shape, and is difficult to manufacture.
Detailed experiments have shown that the performance of three-dimensional
staggered blade riblets are inferior when compared to continuous blade ri-
blets. The highest drag reduction performance recorded for staggered blade
riblets is $\approx 6\%$ with $h/s \approx 0.5$.

2.2.4   Effect of yaw angle

Early studies that investigated the effect of yaw angle α (riblets angle rel-
ative to the mean flow) on the drag reduction performance of riblets were
conducted by Walsh (1982) and Walsh and Lindemann (1984). Their re-
sults demonstrate that the optimum drag reduction ability is unchanged
up to yaw angle $\alpha = 15°$. However, at $\alpha = 25°$ to $30°$ and above, there
is a significant decrease in the drag reduction performance. A more re-
cent investigation by Hage et al. (2000) shows the losses in drag reduction
ability for various types of riblet geometry at different angles. In figure
2.26, trapezoidal with tip angle $\beta = 45°$ is the least sensitive geometry for
misalignment. For trapezoidal geometry with smaller tip angle ($\gamma = 30°$),
the drag reduction performance is more susceptible to misalignment and s^+
than the $\beta = 45°$. The triangular and scalloped riblets geometry have the
weakest resistance on misalignment and the losses also highly depend on
the selected s^+. Higher s^+ resulting in lower drag reduction performance.

2.2.5   Alternative riblets scaling method

In the previous discussions the majority of riblet studies discuss drag re-
duction as a function of the riblet viscous scaled size, i.e. s^+ or h^+. This
method proves to be very reliable for comparing drag reduction values for
different s^+ with similar riblet shape. However, this method is difficult to
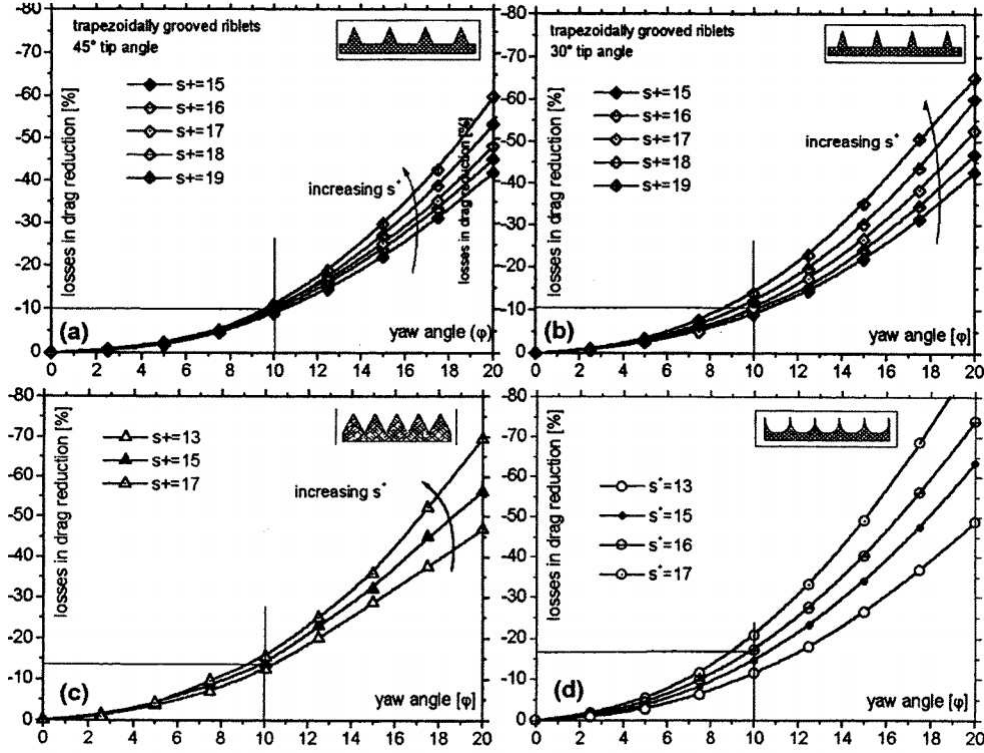
Figure 2.26: Riblets sensitivity towards yaw angle (Hage et al., 2000). Figure (a) shows trapezoidal grooved riblets with 45° tip angle, Figure (b) is trapezoidal grooved riblets with 30° tip angle, Figure (c) is triangular grooved riblets, and figure (d) is scalloped grooved riblets. For all figures the vertical axis is percentage loss in drag reduction and the horizontal axis is riblets yaw angle.

use when we try to compare drag reduction and s^+ ranges for different riblet shapes (such as triangular, trapezoidal, scalloped or rectangular).

García-Mayoral and Jiménez (2011a,b, 2012) offer a new geometric parameter that describes experimental results better and captures the effect of both riblet spacing and geometry. They use the ratio of the groove cross section to the square of the spacing (aspect ratio) A_g/s^2 from several standard riblet geometries and plot it against optimum spacing s_{opt}^+. This method offers an alternative to riblet spacing as a method to characterise the breakdown of drag reduction proportion to the riblet size. García-Mayoral and Jiménez (2011a,b, 2012) also propose an alternative scaling $l_g^+ = (A_g^+)^{1/2}$. The results are shown in figure 2.28, it demonstrate that there is a good collapse on the data, with maximum drag reduction at $l_g^+ \approx 11$. However, care must
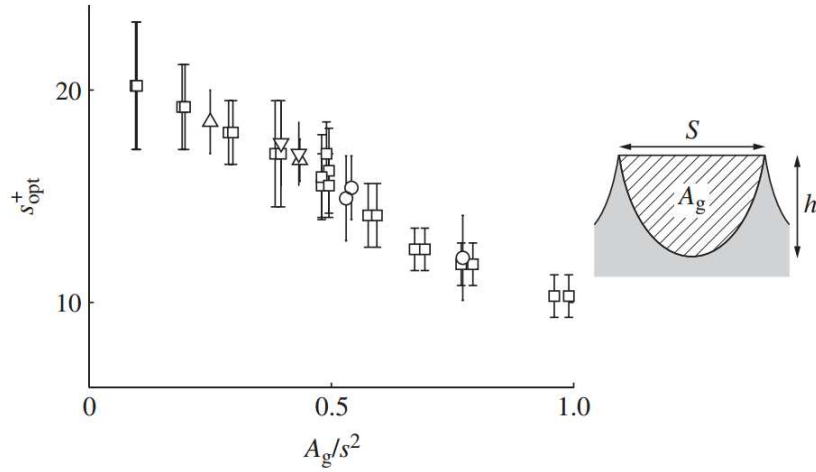
Figure 2.27: Riblet spacing for maximum drag reduction, as a function of groove cross section to the square of spacing (García-Mayoral and Jiménez, 2011a)
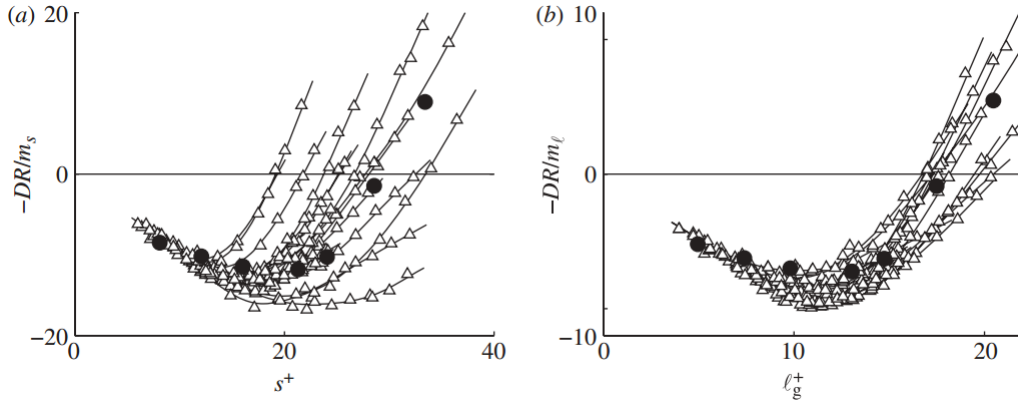
Figure 2.28: Drag reduction plot for various type of riblets as a function of spacing s^+ (a) and as a function of the square root of the riblet cross section (b) (García-Mayoral and Jiménez, 2011a)

be taken when using this method, as it will not work with unconventional riblets and should only be used as an empirical curve fit (García-Mayoral and Jiménez, 2011a)

2.2.6 Converging-diverging riblets pattern

A new class of riblet-type surface roughness with converging-diverging (herringbone) pattern has been reported by Koeltzsch et al. (2002). The unique riblets pattern is inspired by the converging pattern observed on the skin upstream of the sensory receptors (nose and ears) of fast swimming sharks and the diverging texture on the skin upstream of the lateral-line organ of the same animal. In Koeltzsch et al. (2002) experiment, a herringbone riblet pattern is applied inside a turbulent pipe flow. Figure 2.29 shows the experiment set-up, where one half of the inner surface of the pipe is covered with riblets yawed at $-45°$ to the axial direction, and the other half is yawed at $+45°$.
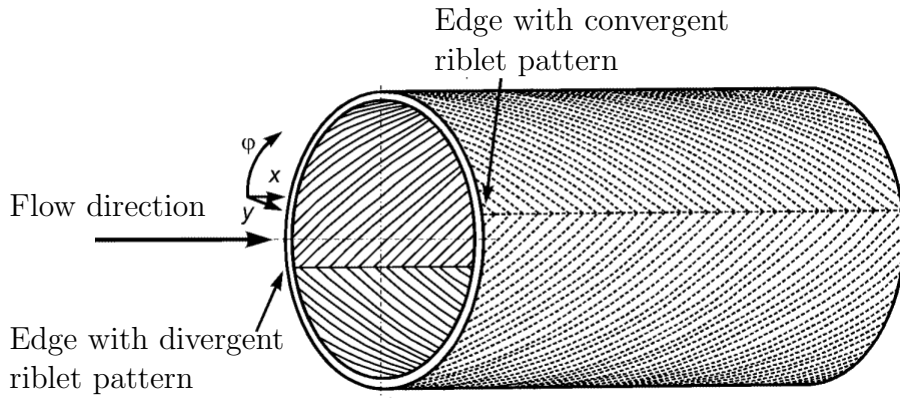
Figure 2.29: Divergent and convergent riblet patterns inside the pipe-flow (Koeltzsch et al., 2002)

The result of Koeltzsch et al. (2002) experiments show that the herringbone pattern is able to impose large-scale roll-modes onto to the boundary layer, causing an azimuthal variation on the streamwise velocity U and turbulence intensity $\overline{u^2}$. Above the converging region the mean streamwise velocity is decreased and the turbulence intensity is increased. Conversely, above the diverging region, the mean streamwise velocity is increased and the turbulence intensity is decreased. These results can be interpreted as: the converging region forces the near wall fluid (which is slow and highly turbulent) to converge together and move away from the wall. For the diverging region, the flow is moving away from each other, and by continuity, this causes the flow from higher locations (with high velocity and low turbulent fluctuations) to move towards the wall. It seems that the converging

and diverging riblet pattern has generated large-scale roll-modes inside the turbulent boundary layer with the converging region forming the common-flow-up part of the vortex and the diverging region forming the common-flow-down region of the vortex. Unfortunately, the lack of cross-wire data prevents them from reaching this conclusion.

Recently, during the preparation of this thesis Chen et al. (2013, 2014) showed that converging-diverging riblet paper can generate drag reduction up to 16%. Although this value is yet to be confirmed with other independent measurements such as drag balance, according to Schoppa and Hussain (1998), such a high drag reduction is indeed possible. DNS studies from Schoppa and Hussain (1998) have demonstrated that large-scale counter-rotating streamwise vortices inside turbulent channel flow can reduce skin-friction drag by up to 20%. Furthermore, the herringbone surface pattern may also delay transition from laminar to turbulence. Recent findings from Fransson and Talamelli (2012) have shown that counter-rotating vortices can delay transition. It seems that this type of riblet configuration may have far reaching engineering applications, for example, as a low profile vortex generator and flow control mechanism. Beyond such attempt of using the herringbone riblet pattern as a flow control purposes, this type of roughness could be applied as a means to generate a very large-scale modes which can affect the recently discovered very-large structures or 'superstructures' (Kim and Adrian, 1999; Hutchins and Marusic, 2007a). Looking at the potential of this surface roughness type, it is surprising that findings of Koeltzsch et al. (2002) (to the best of our knowledge) are yet to be repeated and studied in more detail. Therefore, we believe that investigating the converging-diverging riblet pattern in more detail is important.

2.3 Summary

In summary, from various studies across different fields it is clear that some of the most pressing issue that the current generation face are global warming and ongoing energy crisis. This situation may force many governments to impose laws that aim to reduce carbon emissions, hence reducing energy consumption. One of the primary energy usage in high performance engineering applications is to overcome skin-friction drag that is caused by turbulent boundary layer. There have been many attempts to effectively

control turbulent boundary layer with the hope of reducing skin friction drag, however it proves to be very challenging.

One of the main challenges in controlling turbulent boundary layers is due to the complexity of turbulent flow itself, especially for high Reynolds numbers. As Reynolds number increases, skin friction velocity (which directly translate to skin friction drag) also increases. Furthermore, recent studies have shown the existence of very large-scale features that consist of high and low velocity fluctuations that reside in the logarithmic region. These features are known to leave a footprint in the near-wall structures, modulate both the amplitude and frequency of the small-scale structures, and contribute a large percentage of Reynolds shear stress.

By employing a new class of highly directional riblet type surface roughness, arranged in a herringbone pattern, it is possible to generate large-scale counter rotating roll-modes and control turbulent boundary layers without introducing additional form drag. This novel technique has the potential to capture and disturb the newly discovered very large-scale features. Our attempt here is to understand the capability of the herringbone shaped riblets and identify the important parameters that may affect their effectiveness.

Chapter 3

Experimental apparatus

3.1 Wind tunnel facility

All experiments are carried out in an open-return blower wind tunnel located in the Walter Basset Aerodynamics Laboratory at the University of Melbourne. The wind tunnel has been used extensively to study various pressure gradient turbulent boundary layers by Marusic and Perry (1995); Jones et al. (2001); Monty et al. (2011b), and Harun et al. (2013) among others. For the current study, the wind tunnel has been refurbished to improve its flexibility and capability. The wind tunnel shown in figure 3.1 consists of a settling chamber with honeycomb and several mesh screens followed by a contraction with an area ratio of 8.9:1, resulting in a low free-stream turbulence level of 0.2%. It has a working section with 6.7 m length and a cross-sectional area of 0.94×0.375 m. The air flow is delivered by a centrifugal fan belt driven by a 19 kW DC motor. Throughout this report x, y, and z are streamwise, spanwise, and wall-normal direction respectively.
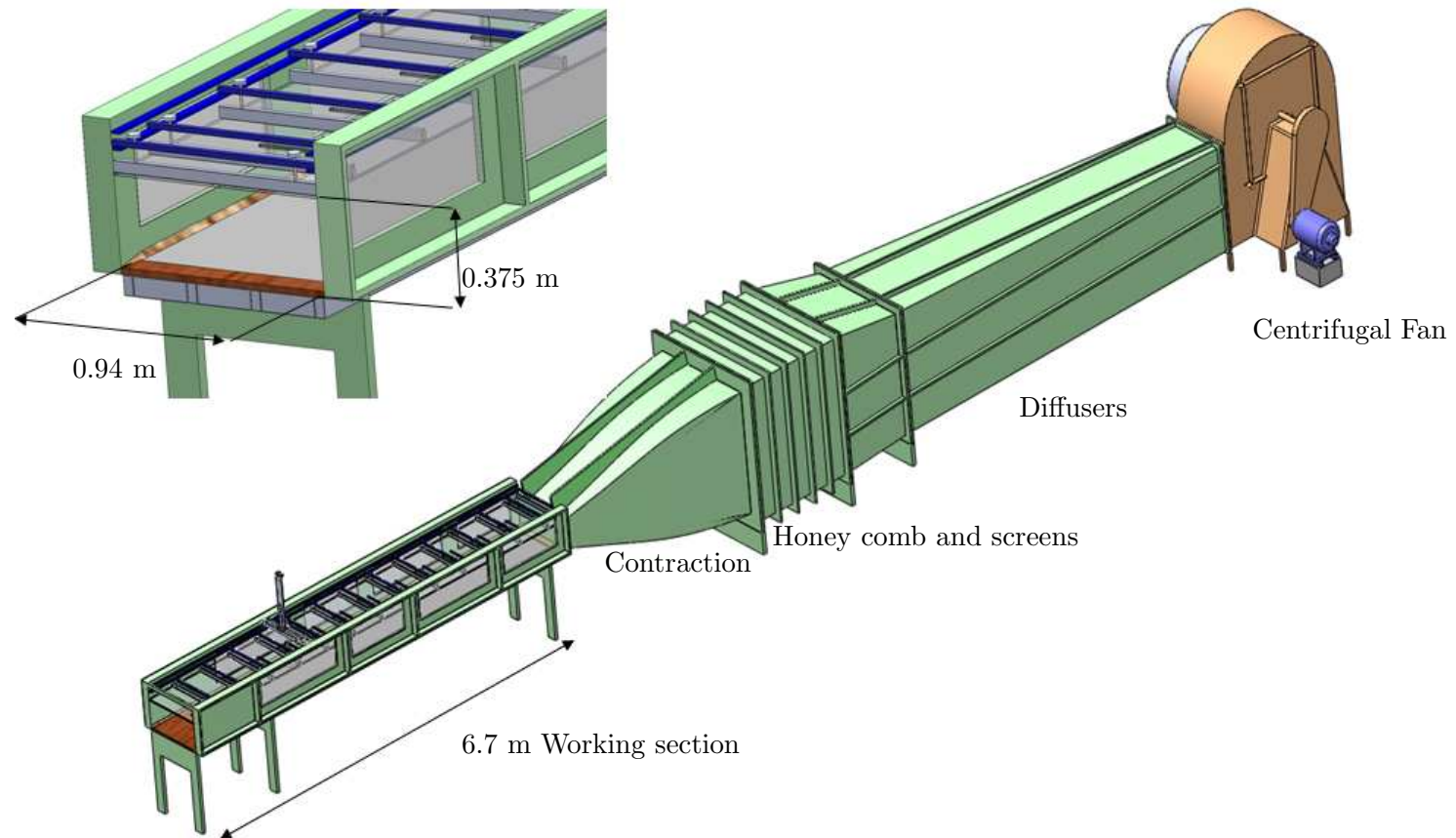
Figure 3.1: Isometric view of wind tunnel

The wind tunnel has a fully adjustable roof hung by threaded rods attached to knobs that go through horizontal steel beams. There are 22 horizontal beams holding the roof and each beam has two knobs at either end. The knobs allow the adjustment of the roof's height. In this study, all experiments are performed at Zero Pressure Gradient (ZPG). The roof has sealed slots for the traverse system access that holds the measurement sensors (see figure 3.2). In total there are 10 sealed slots separated by 0.5 m starting from the inlet. Each slot has a cross sectional area of 15 × 250 mm. The slots enable the sting to perform both wall-normal and spanwise direction movements at 10 different streamwise locations along the working section.
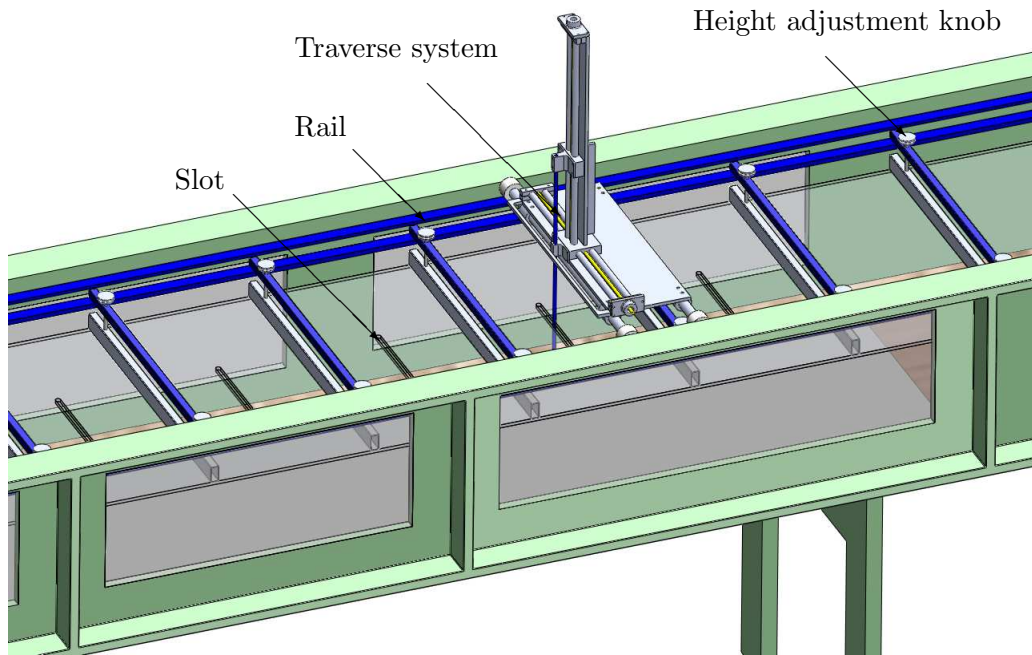
Figure 3.2: Adjustable roof and traverse system

The floor of the working section can be lowered and detached using two hydraulic lifts located beneath the wind tunnel floor. It allows the floor to be interchanged seamlessly between smooth-wall and any type of rough surface. A thin steel sheet is laid permanently on the floor frame, enabling different magnet-embedded rough surfaces to be firmly attached.

To stabilize the transition from laminar to turbulent flow and reduce the length needed for the boundary layer to grow, a trip is installed at the inlet of the working section. For this experiment we chose a very coarse P40 sand

paper as the trip. This type of sand paper gives a smooth-wall development consistent with the study by Erm (1988) and Kulandaivelu (2012).

3.2   Traversing system
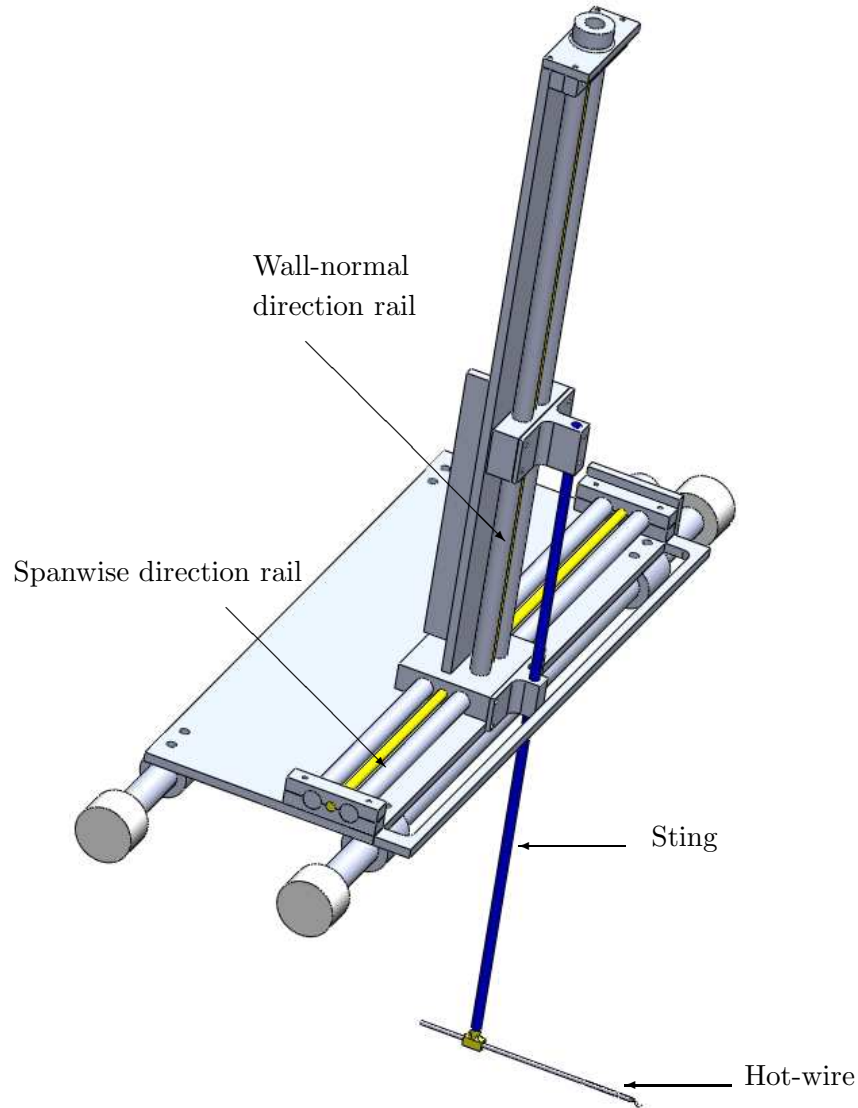
Figure 3.3: Two-dimensional traverse

The traversing system for the experiment is a custom built computer controlled two-dimensional traverse mounted on the top of the tunnel. It is

able to accurately position the hot-wire both in the wall-normal and span-wise direction via a long cylindrical section sting that goes into the tunnel from one of the ten different slots located on the tunnel's roof (figure 3.3). The traverse is mounted on four wheels rolling on a track which enables the user to move upstream or downstream. The traverse system is powered by two Vexta PKK266M-03A stepper-motors (one for wall-normal direction and one for spanwise direction) connected to a high precision Velmex VXM-2 controller which interfaces with the computer for fully automated movement. To ensure accurate height measurement, the wall-normal traverse is equipped with a Renishaw RGH24 linear optical laser encoder with an accuracy of ± 0.5 μm.

3.3 Flow condition

3.3.1 Zero pressure gradient

A zero pressure gradient condition inside the wind tunnel is achieved by adjusting the height of the roof. To measure the pressure differences, pressure taps are inserted on the roof centerline covering the entire length of the working section. The coefficient of pressure is given by

$$C_p = \frac{p - p_0}{p_t - p_0} = 1 - \left(\frac{U_{\infty(x)}}{U_{\infty(0)}}\right)^2 \tag{3.1}$$

Here p is the local static pressure, p_0 is the static pressure reference, p_t is the free-stream total pressure reference, $U_{\infty(x)}$ is the local free-stream velocity, and $U_{\infty(x=0)}$ is reference free-stream velocity. To switch between locations, the pressure taps are connected to a scanivalve. A Pitot static tube is also placed in the inlet ($x = 0$) to measure p_0 reference pressure. To ensure statistically converging data, the measurement time for each pressure tap location is set to 30 s.

Figure 3.4 shows pressure coefficient distribution (C_p) over the working section of the smooth-wall case for free-stream velocity 20, 15, 10, and 5 m/s respectively. For all velocity cases, the pressure gradient is $C_p = 0\pm0.01$
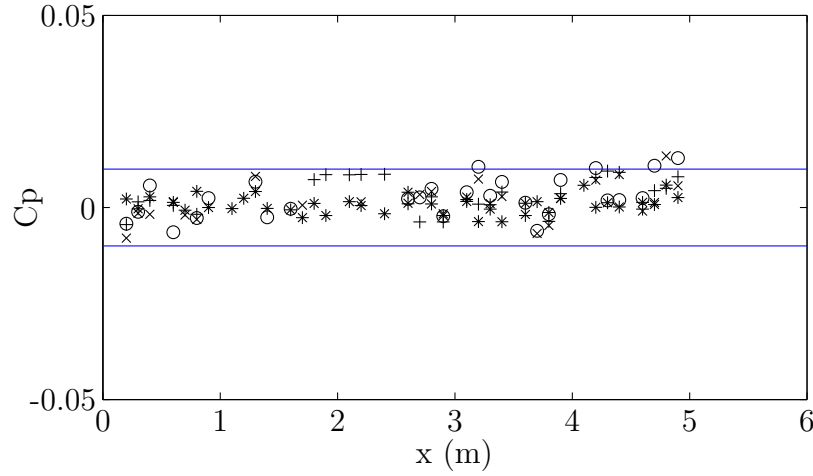
Figure 3.4: The coefficient of pressure (C_p) distribution along the centerline of the wind tunnel over streamwise distance x from the inlet over the smooth surface at various speed. (○) for 20 m/s, (+) for 15 m/s, (×) for for 10m/s, (∗) for 5 m/s

(horizontal lines). There are several points that are outside the $C_p = 0\pm0.01$ limit at the rear of the tunnel, which we deemed acceptable.
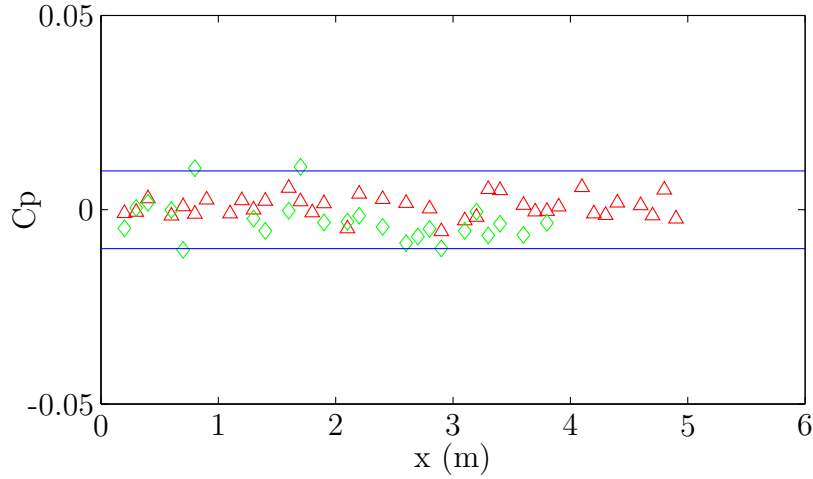
Figure 3.5:   The coefficient of pressure (C_p) distribution along the centerline of the wind tunnel over streamwise distance x from the inlet. The measurements are performed over the rough surface. △ = 10° riblets, ◇ = 20° riblets

Figure 3.5 shows the pressure gradient over the working section with the

riblets laid on the tunnel's floor. Here we analysed the pressure gradient for the $\alpha = 10°$ riblets and $\alpha = 20°$ riblets cases. The figure shows that the pressure gradient is zero and within the limit of ± 0.01

3.3.2 Spanwise variability

A large part of this study involves both wall-normal and spanwise measurements above the riblets. Therefore it is critical to have nominally two-dimensional flow for the smooth-wall case. However, spanwise variability may emerge due to the characteristics or imperfection of the wind tunnel that is being used (Erm and Joubert, 1991). Several possible causes are uneven roof or surface, leakage, or imperfection with the settling chamber screens.
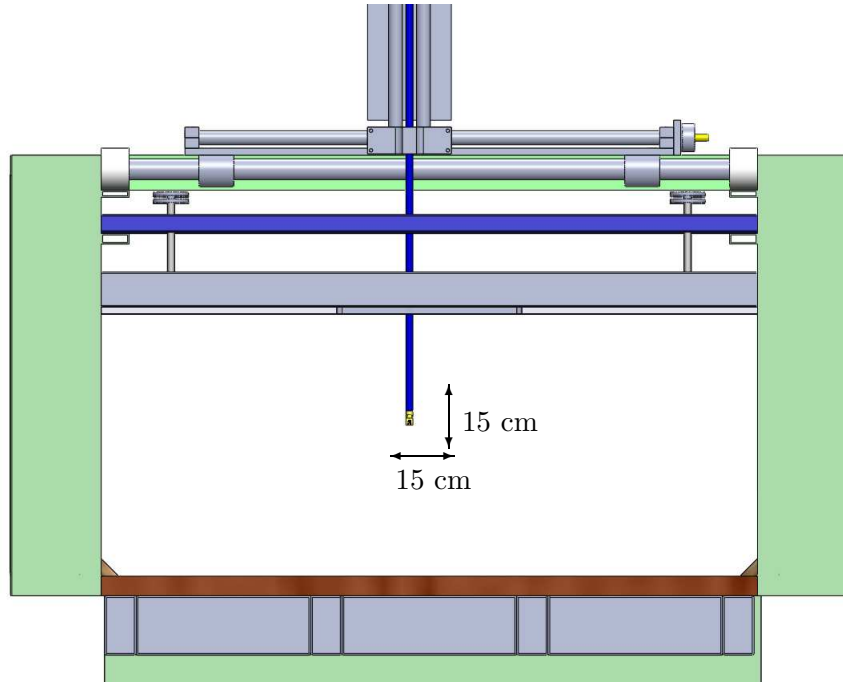
Figure 3.6: Spanwise and normal to wall free-stream measurement

The purpose of screens in any wind tunnel's settling chamber is to suppress turbulent fluctuations and adjust mean flow directions (Groth and Johansson, 1988; Laws and Livesey, 1978; Tan-Atichat et al., 1982). However, various studies have shown that an imperfection in settling chamber

screens causes spanwise variability in a nominally two-dimensional smooth-wall boundary layer (Bradshaw, 1965; Mehta and Hoffmann, 1987; Erm and Joubert, 1991). This variability tends to exist within the boundary layer, not in the free-stream. According to Watmuff (1998), the imperfection of meshes generates weak streamwise vortices which interact with the boundary layer and result in background noise/unsteadiness (thus causing spanwise variability). This disturbance was first observed by Klebanoff and Tidstrom (1959), hence the phenomenon is called Klebanoff modes. Further studies by Klebanoff (1971); Kendall (1998, 1991); and Leib et al. (1999) confirmed the role of Klebanoff modes in causing a spanwise variation in boundary layer studies.
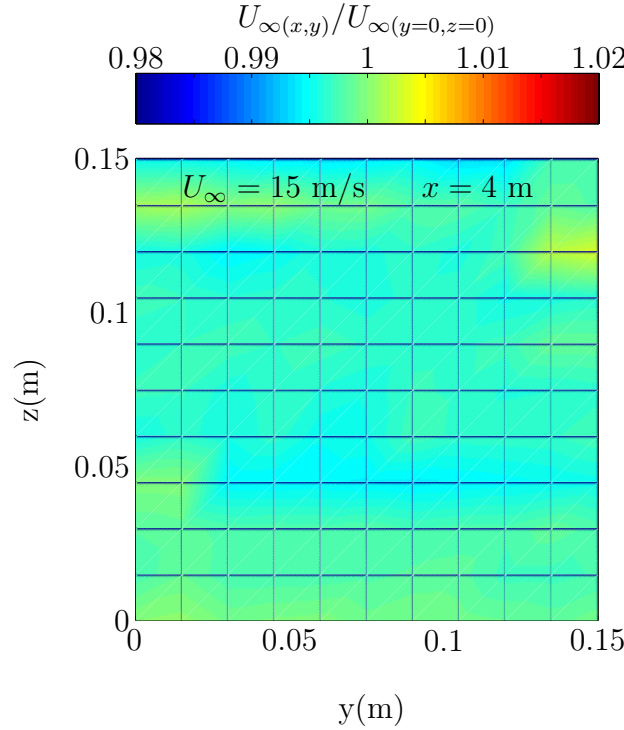
Figure 3.7: The relative spawise variation of the free-stream $U_\infty = 15$ m/s at $x = 4$ m downstream.

In order to see if our tunnel suffers from screens' imperfection we have performed two type of tests. The first test involve a two-dimensional measurement in both wall-normal and spanwise direction at the free-stream location. The aim of this test is to to ensure minimum free-stream spanwise and wall-normal variation. The measurement is performed over the smooth-wall at free-stream velocity $U_\infty = 15$ m/s using a Pitot static tube attached to the two-dimensional traversing system (figure 3.6). The two-dimensional

measurement covers a cross-sectional area of 0.15×0.15 m of the wind tunnel centerline at downstream location of $x = 4$ m. Velocity measured at each location are normalised with the initial measurement located at $y = 0$ and $z = 0$ of the free-stream. Figure 3.7 shows that the velocity variation is varies between -0.31% to 0.66%, which asserts the minimum undesirable spanwise variation in the free-stream.
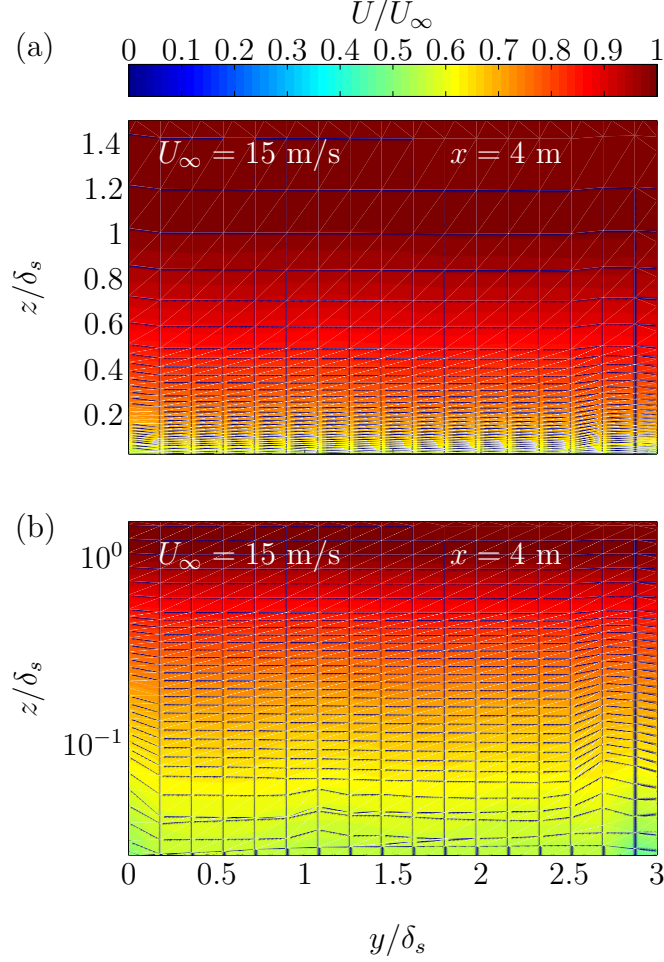
Figure 3.8: Spanwise and wall-normal measurement of mean velocity profile over smooth-wall at $U_\infty = 15$ m/s located at $x = 4$ m downstream. Comparison for wall normal direction plotted in (a) linear scale and (b) logarithmic scale.

The second test involve hot-wire measurement in both wall-normal and spanwise directions closer to the surface. Here, the wall normal direction covers the entire boundary layer and the spanwise direction covers $3\delta_s$ (δ_s is boundary layer thickness over the corresponding smooth-wall). The mea-

surements are performed with free-stream velocity $U_\infty = 15$ m/s at $x = 4$ m downstream. This type of two-dimensional measurements are also performed for the parametric study of the converging-diverging surface roughness in the next chapter. Therefore, this measurement over the smooth-wall can be treated as reference case.
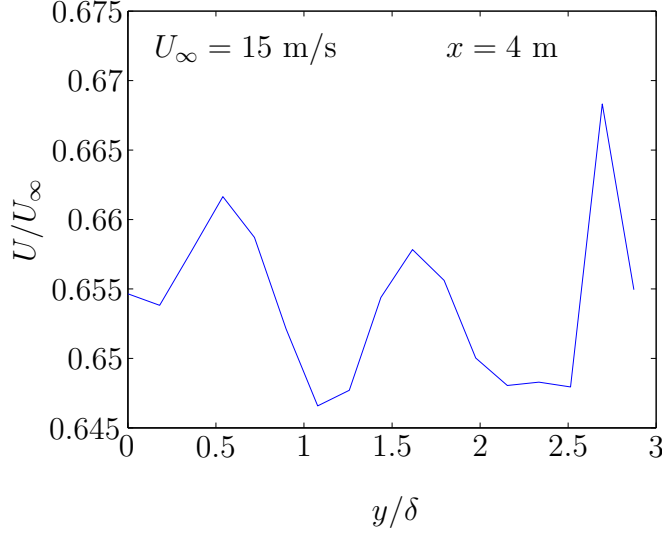
Figure 3.9:   Mean velocity variability over spanwise length of $3\delta_s$ at $z/\delta_s \approx$ 0.1 for $U_\infty = 15$ m/s located at $x = 4$ m downstream.

Figure 3.8 shows the color-contour spanwise and wall-normal measurement of mean velocity over a smooth surface. Here the vertical axis is the wall normal position and the horizontal axis is the spanwise position. The top figure (figure 3.8(a)) shows the wall-normal direction in linear scale and the bottom figure (figure 3.8(b)) shows the wall-normal region in logarithmic scale. Figure 3.8(a) reveals that at the logarithmic and wake region, the flow is relatively two-dimensional. However, figure 3.8(b) shows that very close to the wall there is a slight three-dimensionality at $y/\delta_s = 0$ and $y/\delta_s = 3$ caused by the imperfection of the screens on the settling chamber. Figure 3.9 shows a much closer inspection near the wall (at $z/\delta_s \approx 0.1$). The figure shows that over spanwise distance of $3\delta_s$ there is mean velocity variability of approximately 1.5%. This variability is deemed acceptable due to its relatively small value.

3.4 Data acquisition and automation

For all measurements, the data are acquired using a Data Translation DT9836 data acquisition (DAQ) board connected via USB to a computer. The DAQ board has 16-bit digital resolution covering -10 V to 10 V with 12 single-ended analog input channels and a maximum sampling rate of 800 kHz. Unless stated, the sampling frequency f_s for all measurements are set at 50 kHz. The signal is filtered at 25 kHz using a low-pass analogue filter to prevent aliasing when calculating discrete Fourier transform. The sampling frequency is set at $f_s = 50000$ Hz to obtain a sample interval $\Delta t^+ = \Delta t U_\tau^2 / \nu < 1.0$, here $\Delta t = 1/f_s$ is time between samples, U_τ is skin-friction velocity, and ν is the kinematic viscosity.

The experiments are fully automated through a combination of computer and DAQ board analog output, which is connected to the traverse system and wind tunnel controller. The only exception is the pressure gradient measurement, where the scanivalve fluid switches need to be operated manually.

3.5 Mean flow and pressure measurement

Pressure measurement is obtained using a 10 Torr MKS Baratron pressure transducer together with an MKS type 670 signal conditioner. For pressure gradient measurements, as mentioned in section 3.3.1, a Pitot tube is attached at the ceiling of the inlet at $x = 0$ to measure the free-stream reference pressure. For the mean flow measurements and calibration, a Pitot tube from NPL (National Physical Laboratory) is attached on the side wall of the wind tunnel to record the free-stream velocity. The Pitot tube is located at $x = 5.5$ m from the tunnel and adjusted to be $\approx 5\delta$ from the floor and $\approx 4\delta$ from the side wall. The relatively long Pitot tube distance from the tunnel's floor and side wall ensure minimum interference from the boundary layer.

3.6 Hot-wire measurement

3.6.1 Anemometer and probe details

In this study, the flow is measured using a hot-wire (single-wire and cross-wire) and a Constant Temperature Anemometer. There are two types of anemometer used in this study: AA Lab systems AN-1003 and Melbourne University Constant Temperature Anemometer (MUCTA). Details of anemometer theories and design are given in Comte-Bellot (1976); Perry (1982); Perry and Morrison (1971) and Bruun (1995). The hot-wire probes used in this study are single-normal hot-wire and cross-wire probe. The single-normal wire probe is a *Dantec 55P05* connected to a 4 mm diameter probe supports (*Dantec 55H21*). The cross-wire probe is *Dantec 55P51* connected to a 6 mm diameter dual-sensor probe support (*Dantec 55H25*). The single-normal hot-wire probe support is mounted to a 4 mm diameter tubing and attached to the wind tunnel traverse sting. The cross-wire probe support is mounted to a 6 mm diameter tubing. The tubing and traverse attachment allow the hot-wire probe to be adjusted for the correct yaw angle, rotation angle, and angle of attack with respect to the streamwise direction.

The sensing element of the hot-wire is a 5μm diameter Platinum Wollaston wire. To prepare a single-normal hot-wire, firstly a 3 mm length of Wollaston wire is soldered onto the prong tips. The wire is then etched for 1 mm length using acid to expose the Platinum central core. The length-to-diameter (l/d) ratio of the etched hot-wire sensors equals or exceeds 200 to minimise attenuation due to end conduction (Ligrani and Bradshaw, 1987). The viscous-scaled wire length l^+ will vary from $l^+ \approx 14$ to $l^+ \approx 47$ for the free-stream velocities investigated. These values mean that some measurements will suffer from some attenuation because of insufficient spatial resolution (Hutchins et al., 2009). However, since the measurements are made for comparative purposes, such attenuation is deemed acceptable. The wire is then heated for 24 hours using the anemometer with an overheat ratio of 1.8. For the cross-wire, the preparation and etching technique are similar with the single-normal hot-wire. For all experiments, the frequency response is set between 25 - 30 kHz at 1/3 of the free-stream velocity U_∞. Both the AN-1003 and MUCTA are able to work with commercially
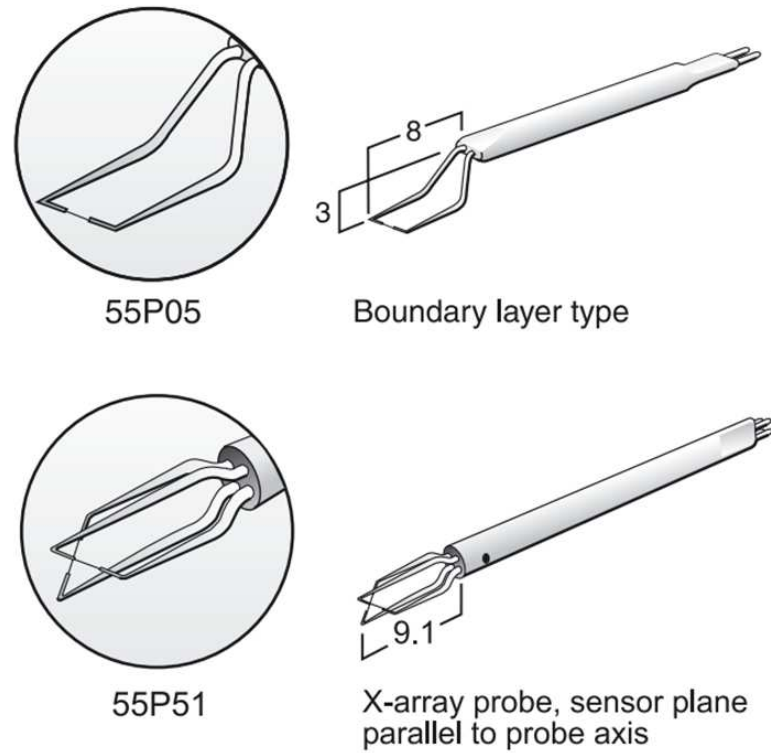
Figure 3.10: Hot-wire sensors from Dantec (lengths are in mm)

available 5 and 2.5μm Wollaston wire.

3.6.2 Calibration procedure

The hot-wire is calibrated statically inside the wind tunnel using a calibrated NPL Pitot tube. The calibration is performed twice for each measurement, prior and after each traverse, from here onwards this will be referred to as pre-calibration and post-calibration respectively. Each calibration is carried out by positioning the hot-wire at the free-stream location and recording several different velocities incrementally from zero to slightly above free-stream velocity ($\approx 110\%$ of U_∞). A third-order polynomial is then fitted between the hot-wire voltage and Pitot tube velocity. Figure 3.11 shows an example of calibration data where the pre-calibration and post-calibration collapse on top of each other. The cross-wire is calibrated in the same manner as single wire, assuming a 45° angled wire. We did not use articulating
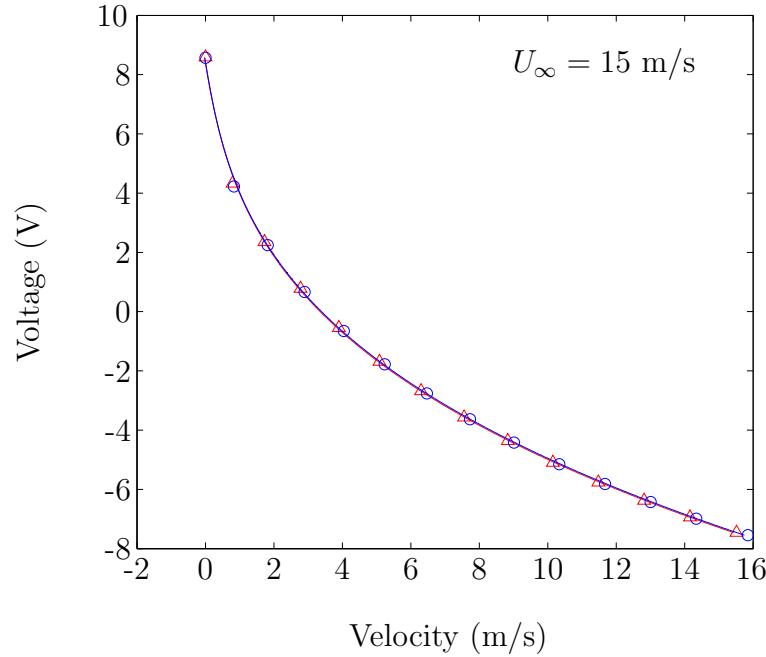
Figure 3.11: Hot-wire calibration curve for $U_\infty = 15$ m/s; where $\triangle$ is pre-calibration and $\circ$ is post-calibration

jet calibration technique which is commonly used. However, because this investigation is for comparative purposes, it is deemed acceptable.

3.6.3 Hot-wire drifting and correction technique

One of the main challenges in using the hot-wire measurement technique is calibration drift. Figure 3.12 shows severe hot-wire drift where the pre-calibration and post-calibration do not collapse on top of each other. According to Perry (1982), hot-wire drift is caused by several factors, such as: ambient temperature changes, atmospheric changes, changes in hot-wire geometry, and contaminants on the sensing element. Each of these factors needs to be considered and minimised to avoid drifting.

Temperature drift is a common source of error in hot-wire measurement and for lengthy measurements it is difficult to avoid without a temperature controlled facility. Two common causes of temperature drift are changes in atmospheric temperature and friction in the wind tunnel facility (Cim-
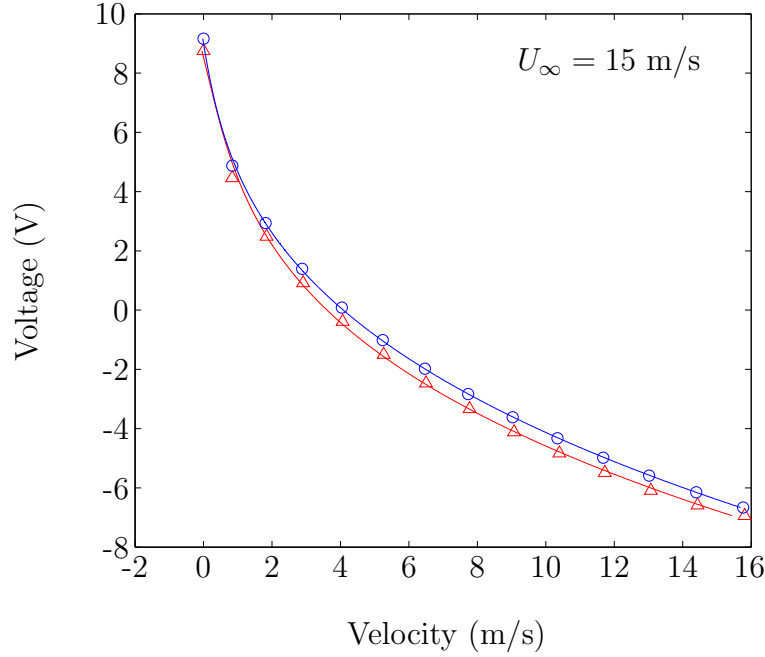
Figure 3.12: Severe drifting of hot-wire calibration curve for $U_\infty = 15$ m/s; where $\triangle$ is pre-calibration and $\circ$ is post-calibration

bala and Park, 1990). The ambient temperature T_a is observed using an Omega DP25-TH Precision Thermistor-meter with a stainless steel probe ON-403-PP located at $x = 5$ m from the inlet of the wind tunnel. Atmospheric pressure is also constantly monitored using a digital barometer (SensorTechnics 144SC0811-BARO).

The change in hot-wire geometry such as buckling and bowing due to thermal expansion is another issue that causes inaccurate measurements. According to Perry (1982), as the deformed hot-wire is exposed to an air flow, it fluctuates and can distort the hotwire frequency output. Hence it is imperative to make a straight wire and to periodically check the straightness. Preheating a new hot-wire for 24 hours prior to measurements is also desireable, this process is known as *'cooking'* or *'annealing'*. The 24 hour heating time does not prevent the hot-wire from deforming, however it will reduce the probability that the sensing element will deform further during measurement.

Contaminants from dusts and fumes that build up on the hot-wire surface will affect the hot-wire reading or even damage the wire. Due to its small

size, the hot-wire is prone to damage from high velocity impacts with dust carried by the flow inside the wind tunnel. To prevent this, the intake of the tunnel is covered with a filter. This filter must be replaced regularly. Fume contamination is more difficult to control. According to Jones (1999) one of the most persistent fume contaminants for hot-wires comes from the welding process. In order to minimise contamination, it is best not to perform any experiment during lab refurbishment and allow any welding fumes to dissipate for at least 12 hours prior to commencing on experiment.

Although care has been taken during experiments, for a long experiment, such as the two-dimensional measurements ($\approx$ 10 hours), hot-wire drifting may occur. To overcome this, a calibration correction scheme is needed. The most common correction scheme is temperature correction (see, Perry (1982); Cimbala and Park (1990); Bruun (1995), and Hultmark and Smits (2010)). Recently however, Kulandaivelu (2012) and Talluru et al. (2014b) have shown a more robust correction technique by periodically sampling the free-stream voltage. This method is incorporated for the two-dimensional measurements due to its long measurements time, which makes it prone to hot-wire drifting. The method is performed by obtaining single point recalibrations in the free-stream flow at certain intervals during the measurement. Using the multiple interval free-stream voltage, one can record the voltage drift, and correct it during post processing.

3.6.4   Determining initial distance between wall and hot-wire

To determine the initial distance between the hot-wire sensing element and the wall, a height measuring microscope is used. The microscope is a Titan Tool ZDM-1 with a digital measuring indicator DI-15MM. The microscope has $\pm$0.001 mm accuracy and is imaged via a Mightex MCE-C030-US CMOS digital camera. The microscope has high resolution with very shallow depth of field, allowing for an accurate height measurement. Due to the short distance between the lens and the measured object, co-axial illumination is needed. The illumination allows the microscope to focus on the wire or the wall (or in this case the peak of the riblet). By changing focus between the wire and the wall, the distance between them can be obtained with high accuracy (figure 3.13). This measurement must be performed

with the flow off.
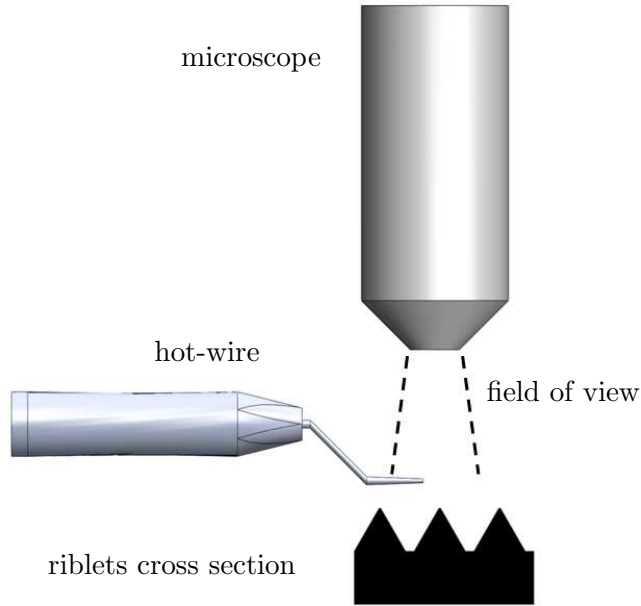
Figure 3.13: Method for determining hot-wire to wall distance (note that the figure is for illustration purposes only and is not drawn to scale)

When the flow is turned on, the probe can experience a slight shift in the wall position owing to aerodynamic loading on the sting. To account for this shift, the initial height position of the sensor relative to the wall with/without the flow is documented using a digital camera. The camera is a Nikon D800 with a long range macro lens (Tamron 180 mm) and extension tube (Kenko 36 mm). This process enables us to determine the shift of the sensor due to aerodynamic drag.

3.6.5 Boundary layer traverse details

Two types of hot-wires investigations are performed throughout this study. The first is a wall-normal direction measurement. Here the hot-wire moves in wall-normal direction at 50 logarithmically-spaced points between $0 < z \lesssim 2.5\delta$ and sampled at 50 kHz for 150 seconds to ensure it is statistically

converge. The sampling time results in boundary layer turn-over time of $\approx 15000\delta/U_\infty$ to $\approx 60000\delta/U_\infty$ (between the lowest and the highest free-stream velocity in this study). The second measurement type is a two-dimensional measurement. Here the hot-wire sensors are moved in both the wall-normal and spanwise direction. The hot-wire moves 30 or 40 points logarithmically in the wall normal direction over the range of $0 < z \lesssim 2.5\delta$, and 21 points in the spanwise direction covering $-\Lambda/2 < y < \Lambda/2$, here Λ is the repeating wavelength of converging-diverging-converging surface (see firgure 3.15). The two-dimensional measurements are sampled for shorter periods, 30 seconds at 50 kHz, giving a boundary layer turn-over time of $\approx 3000\delta/U_\infty$ to $\approx 12000\delta/U_\infty$. The short measurement time is to minimise the excessive changes in atmospheric condition and hot-wire drift during these experiments.

3.7   Hot-film sensors

In this study the near-wall flow is measured using two flush-mounted hot-film sensors affixed on the converging and diverging regions. The two hot-film sensors, hereafter referred as hf_c for converging and hf_d for diverging. The hot-film sensors are Dantec 55R47 glue-on-type sensors, operated using Melbourne University Constant Temperature Anemometer. The over-heat ratio for both hot-film sensors is set at 1.05. Each sensor has 0.1×0.9 mm nickel film deposited on a 0.05 mm thick insulating polyimid foil carrying a 0.5 μm quartz coating. Both hot-films are glued to the wall using Loctite 495. The hot-film sensors are calibrated in the same manner as hot-wire.

3.8   Surface roughness manufacturing

Figure 3.15 shows the key dimensions of the herringbone pattern surface roughness used in this study. The surface has four strips of yawed riblets of spanwise width $\Lambda/2$, with two strips yawed at $+\alpha$ and two strips yawed at $-\alpha$ forming the converging-diverging pattern. The individual riblets have a spacing $s = 0.675$ mm and height $h = 0.5$ mm, giving a height to spacing
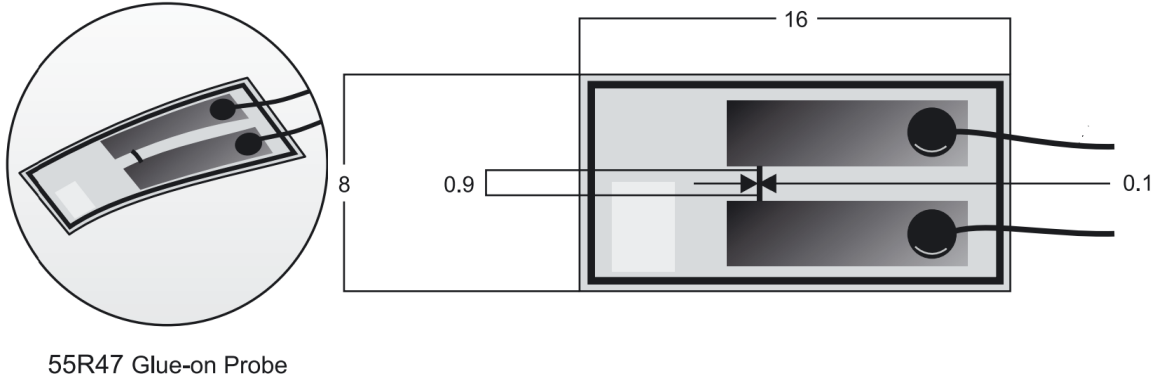
Figure 3.14: Hot-film sensors (lengths are in mm)

ratio h/s ratio of 0.74. The cutter used in making the surface roughness has a tip angle of $\beta = 60°$ and chamfered flat tip of 0.1 mm, resulting in a slightly flat trough. Therefore, the riblets do not represent the standard/classical triangular profile and are close to trapezoidal. It is also noted that the riblet geometries do not have the optimal trapezoidal dimension of $h/s = 0.5$ and $\beta = 30°$ that can reduce drag by as high as 8% at $s^+ \approx 18$ (see Bechert et al. (1997)). For triangular type riblets, the maximum drag reduction for tip angle $\beta = 60°$ is around 5% at $s^+ = 16$.

Figure 3.16 shows the possible scope of trapezoidal groove configuration (taken from Bechert et al. (1997)). The vertical axis is longitudinal protrusion height (see chapter 2 for explanation of protrusion height) and the horizontal axis is h/s ratio. From figure 3.16 the more the riblet deviate from the blade riblet set-up, the lower h_{pl}/s become. A lower h_{pl}/s translate to lower $\delta h/s$, which in turn results in a lower drag reduction ability. Here $\Delta h = h_{pl} - h_{pc}$, h_{pl} is longitudinal protrusion height and h_{pc} is crossflow protrusion height. From the figure, it is clear that our riblets (with $h/s = 0.74$ and tip angle 60°) is still within the curve and have medium range drag reduction capability. As a side, According to Bechert et al. (1997), the best riblet type is blade with $h/s = 0.5$ and $s^+ = 18$, which have optimum drag reduction of 10%.

Recently, García-Mayoral and Jiménez (2011a,b, 2012) offer a new geometric parameter that involves the ratio of the groove cross section to the square of the spacing (aspect ratio) A_g/s^2 from several standard riblet geometries and plots them against optimum spacing s^+_{opt} (shown in figure 3.17). This
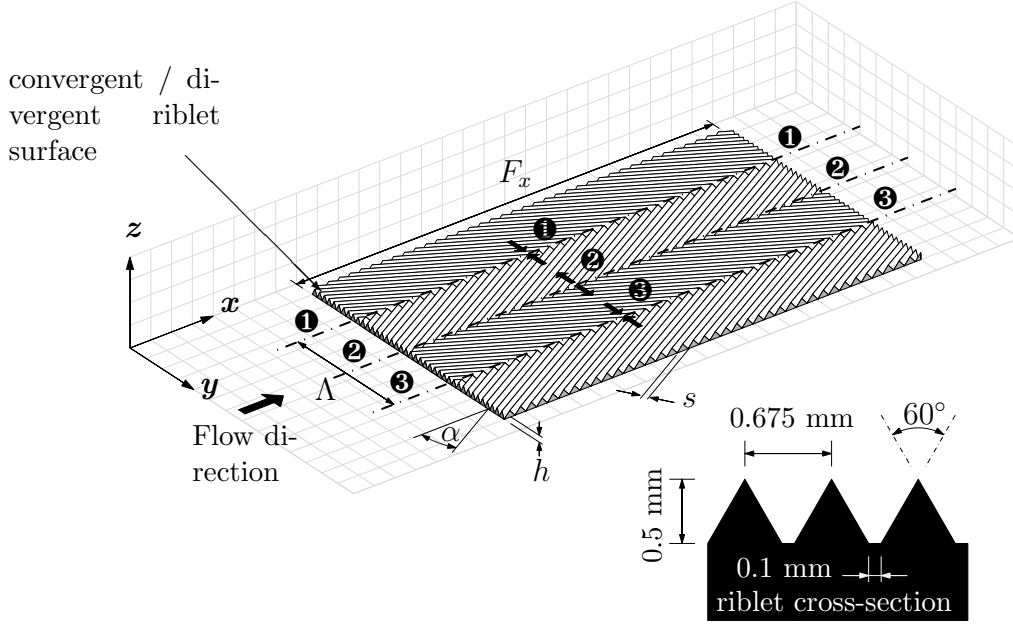
Figure 3.15: Schematic diagram of converging and diverging riblet pattern, showing expected regions of converging (regions ❶ and ❸) and diverging (region ❷) spanwise flow.

method was discussed in chapter 2, here we are interested in applying it for our riblets. From figures 3.15 and 3.17, the square of the spacing (aspect ratio) of our current riblet is $A_g/s^2 = 0.425$ which gives an optimum viscous spacing length $s^+ \approx 18$. García-Mayoral and Jiménez (2011a,b, 2012) went further by proposing an alternative scaling $l_g^+ = (A_g^+)^{1/2}$ instead of the standard s^+. From figure 3.18 (a and b), this new scaling technique has smaller scatters than the previous method (10% instead of 40%). Looking at the plot 3.18 (a and b), our optimum $s^+ \approx 18$ would translate to l_g^+ of ≈ 10. Nevertheless, the aim of this investigation is to study the ability of this type of surface to generate large-scale secondary flows. In this study, we have not attempted to optimize the geometries for drag reduction purpose.

For all cases studied, the width of each strip is 73.75 mm, resulting in a spanwise wavelength $\Lambda = 147.5$ mm. To study the effect of riblet yaw angle α, three different sets of yaw angle are manufactured, $\alpha = 10°$, $\alpha = 20°$, and $\alpha = 30°$. The riblet yaw angles are smaller than the 45° case investigated in Koeltzsch et al. (2002). The choice to use smaller riblet yaw angles is
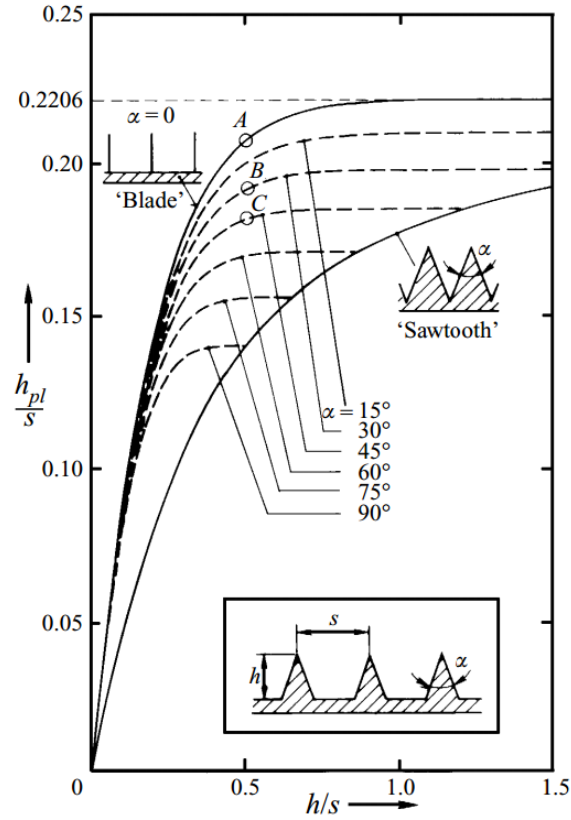
Figure 3.16: Longitudinal protrusion height for ribbed surfaces with trape-zoidal grooves (Bechert et al., 1997)

based on the investigations of Walsh and Lindemann (1984) and Hage et al. (2000), where they have shown that riblet yaw angle greater than $25° - 30°$ will reduce the riblet performance in the case of a conventional streamwise aligned riblet.

The riblets are manufactured in the form of cast tiles, where each tile has a dimension of 515×295 mm (figure 3.15). A total of 30 riblet tiles are manufactured and used to cover the wind tunnel working section, covering the tunnel's full width (6Λ) with a distance of 5 m starting from the inlet of the working section.
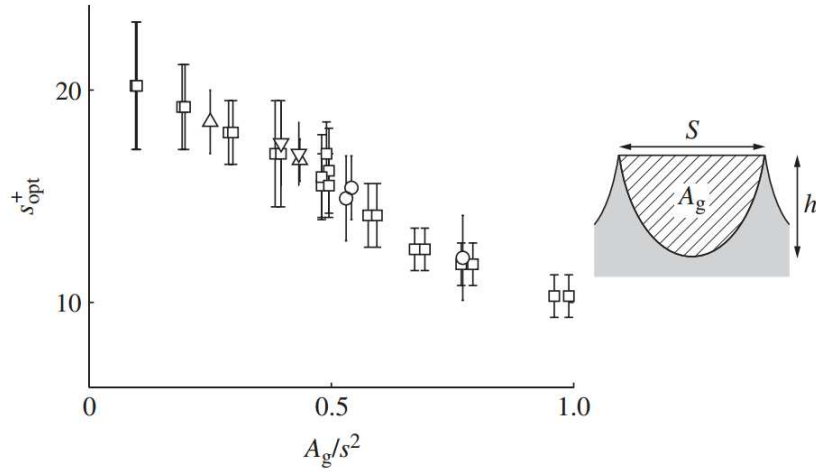
Figure 3.17: Riblet spacing for maximum drag reduction, as a function of groove cross section to the square of spacing (García-Mayoral and Jiménez, 2011a)
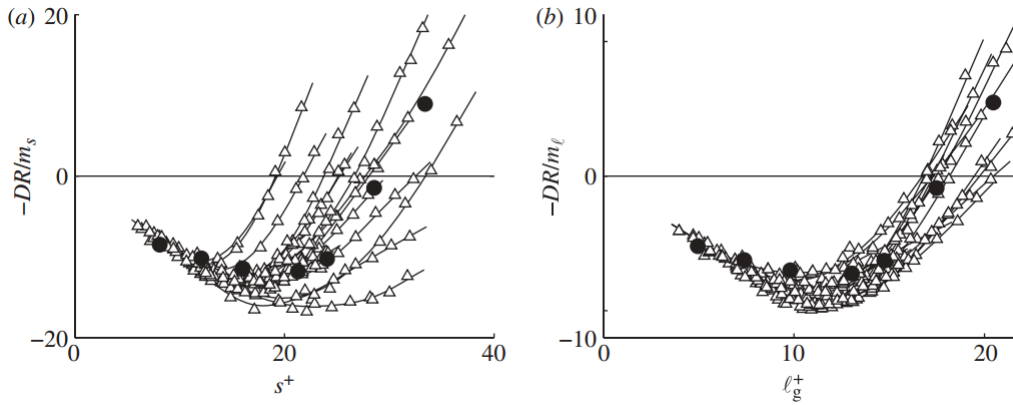
Figure 3.18: Drag reduction plot for various type of riblets as a function of spacing s^+ (a) and as a function of the square root of the riblet cross section (b) (García-Mayoral and Jiménez, 2011a)

3.8.1   Master tile cutting

The first phase in manufacturing the surface roughness is to create the master tile. Initially a two-dimensional model is drawn on the computer using SolidWorks CAD Software. Unlike traditional CAD where the actual model is drawn in a three dimensional environment, due to the small size of the riblets, a two dimensional drawing is chosen. Here the lines on figure 3.19 shows the path that the CNC machine cutter (a 60° V-shaped engraving

cutter) follows. The distance between each line (which represents the riblet spacing s) is set at 0.675 mm. We ensure that each end of the roughness plate tesselates to one another.
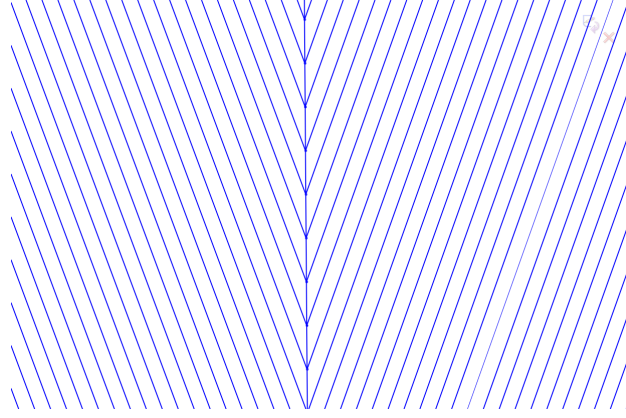
Figure 3.19: SolidWorks CAD lines with $\alpha = 20°$ and $s = 0.675$ mm.

The CAD design is then transferred to the CNC programming software Vectric-2D. The software translates the earlier CAD drawing to a cutting strategy (a set of vectors for the motor controller of the 3D traverse). During the vector assignment, several machining parameters such as depth of cut (that form the riblet height h) and cutter bit size are adjusted accordingly. The depth of cut is set at $h = 0.5$ mm. The output from this software is a code file that is compatible with the CNC machine.

The next step is to find the best material for the master tile. Various types of commercially available materials such as acrylic, acetal copolymer, and aluminum are considered and tested. Acetal copolymer is found to be the most reliable and produces the best cut quality without putting too much stress into the cutter bit and the CNC machine. The acetal copolymer normally comes in two different colours: black or white. For this experiment black colour is chosen as it is easier to detect any defect under the microscope than when using white. Prior to machining, the surface is carefully analyzed to reveal any uneven surface height or defect.

The master tile in figure 3.20 is cut using a three-axis CNC machine from CNC-Technik Heiz High-Z S-1000. The CNC machine has a working area of 1000×600 mm and maximum cutting depth of 110 mm. The maximum working speed of this particular CNC-machine is 25 mm/s with a cutting accuracy of 0.03 mm. The drill is a Kress 1050 FME capable of running
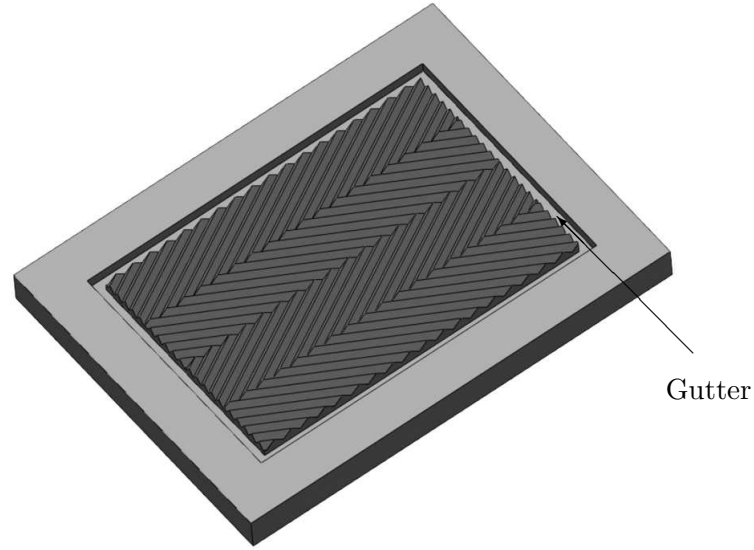
Figure 3.20: Master tile cut diagram (not to scale)

from 5000 - 25000 rpm.

Prior to riblet machining, the master tile perimeter is cut using a standard 6 mm end mill cutter to create a gutter with depth of 8 mm and a width of 10 mm. The gutter will house the aluminum frame for the later moulding process. The cutter bit for the riblet shape is from Harvey Tool, and is shown in figure 3.21, with a tip angle of 60° coated with amorphous diamond. It has a body diameter of 3.175 mm and a web thickness (the chamfered end of the tip) of ≈ 0.1 mm.

Figure 3.21: Cutter with amorphous diamond coating from Harvey Tool with dimension: $D_2 = 3.175$ mm, $L_1 = 38$ mm, $L_2 = 4.6$ mm, A = 60°, W = 0.1 mm

The CNC machine is set to a working speed of 10 mm/sec and the drill rotation speed is set at 20000 rpm. To prevent over heating, the Acetal Copolymer is doused with coolant (Houghton Hocut-807). The cutting

process takes around 12 hours to perform and during this process the coolant needs to be maintained at a constant amount. The machining process may leave a feathering on the tip of the riblet, which can be removed using a compressed jet. Finally, to ensure a clean riblet, a small quantity of mould material is poured on the surface. After the mould is hardened it will capture and clean any residual and feathers that may be left on the surface.

3.8.2 Master tile moulding
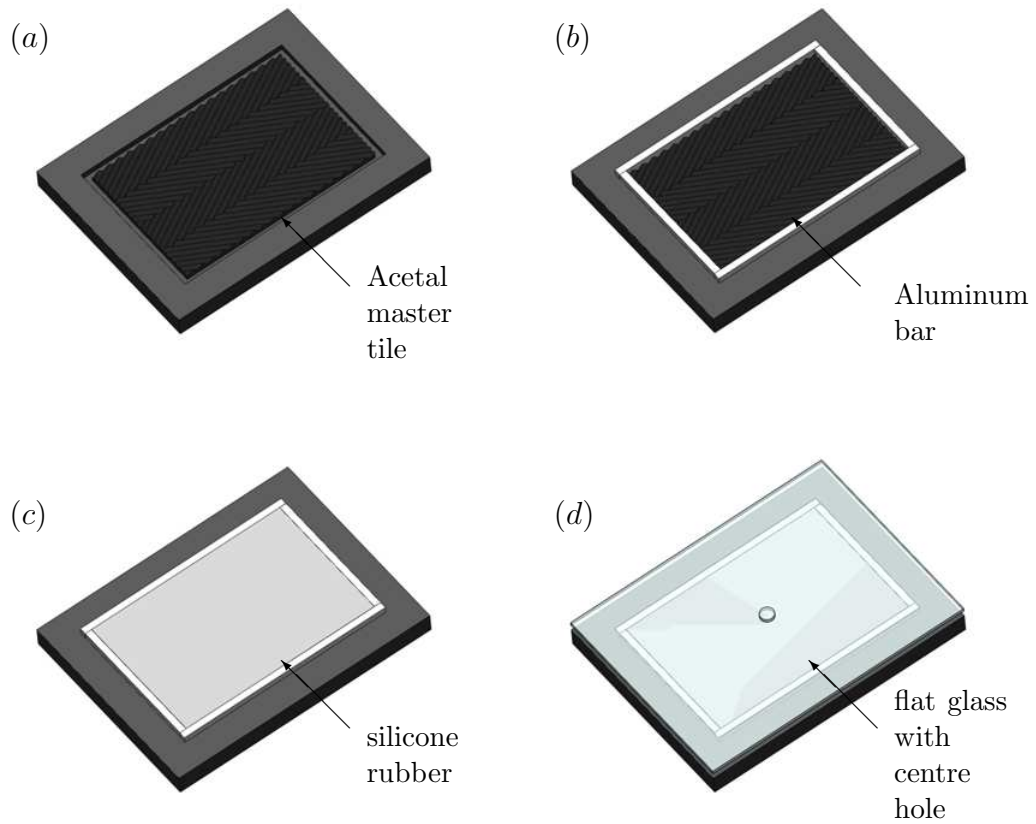
Figure 3.22: Moulding methods: (*a*) acetal master tile, (*b*) aluminum bar surrounding the master cut, (*c*) silicone rubber poured onto the master cut, (*d*) flat glass with centre hole pressing the master cut.

The moulding material which forms the negative side of the acetal master tile is made of platinum cured silicone rubber (Silastomer P35) with a hardness of Shore 35A. The silicone rubber is a two component solution in which both parts need to be mixed together to harden. The mixture has

a long pot life of 90 minutes that ensures enough time for the solution to cover the valley of the riblets thoroughly. Care needs to be taken when both solutions are mixed as an imperfect solution will cause non-uniform hardness. To make the master tile mould, aluminum bars with dimensions $10 \times 20 \times 535$ mm (two pairs) and $10 \times 20 \times 295$ mm (two pairs) are inserted inside the side gutters to form a frame (figure 3.22b). The side of the aluminum bar that faces the riblet cut is coated with 255A Mould Release lubricant solution to ease the mould release and prevent any damage. The master tile surface does not need to be sprayed by lubricant as the acetal copolymer does not bond with the silicone rubber.

The pouring of the silicone rubber mixture is done in two stages. The first silicone rubber mix is $\approx 25\%$ of the overall mould volume. Once the two components are mixed and stirred thoroughly, they need to be degassed for one minute in a pressure chamber. The degassing process removes trapped air and prevents the formation of large bubbles when the solution is poured onto the master tile. The pouring process may produce some small bubbles on the surface. To remove them, gentle brushing is helpful, and the brushing process also ensures the silicone rubber solution covers the entire master tile surface. After 24 hours, the second silicone rubber solution ($\approx 75\%$ of the overall mould volume) is poured on top of the first solution until it slightly over flows (figure 3.22(c)). The second silicone rubber mixture does not need to be degassed inside the pressure chamber.

To ensure a flat surface, a lubricant covered flat glass plate is laid on top of the solution and pressed (figure 3.22(d)). To allow the excess silicone rubber solution to escape, a hole with a diameter of 10 mm is cut at the center of the glass. The glass has to be covered with a release agent to prevent it from sticking to the silicone rubber mix. After 24 hours the silicone rubber is removed, resulting in a negative copy mould of the master tile.

3.8.3   Tile casting

For the casting process, firstly an aluminum frame with an identical size as the master cut is assembled (figure 3.23(a)) and the silicone rubber mould is laid inside the frame (figure 3.23(b)). The casting material is polyurethane plastic that consists of two parts with a solution ratio of 1:1 by volume

and a pot time of five minutes. To obtain a stronger mechanical strength, a fine aluminum powder (25% of the solution weight) is added into the polyurethane plastic solution solution.
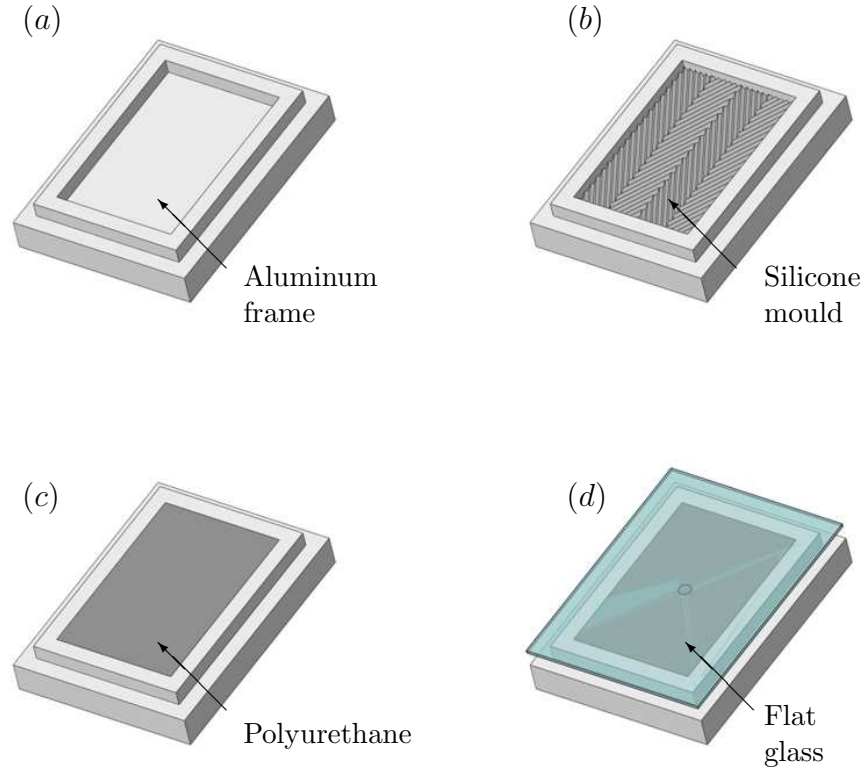
Figure 3.23: Casting methods: (*a*) aluminum frame, (*b*) silicone rubber mould applied inside aluminum frame, (*c*) polyurethane plastic is poured onto the mould, (*d*) flat glass pressing the casting mix and mould

The polyurethane plastic solution process is an exothermic proces. Therefore, to reduce the mould expansion, the casting process is performed in two stages. Firstly, $\approx 25\%$ of the total polyurethane plastic volume is mixed and degassed using a vacuum chamber for 30 seconds to remove trapped air. The degassed solution is poured onto the mould and brushed to remove any small bubbles that may have formed during the pouring process (figure 3.23(c)). Once the first $\approx 25\%$ polyurethane plastic solution is slightly hardened (≈ 1 hours), five magnet bars are laid on the four corners and center surface of the hardened surface. To prevent overflowing and to ensure a uniform and flat surface, a lubricant covered glass with a center hole is laid on top of the frame covering the first mixture. The remaining $\approx 75\%$

of the mixture is poured on top of the first solution through the glass center
hole (figure 3.23(d)). Note that the second solution does not need to be
degassed in the vacuum chamber as it will not affect the riblets quality. It
will take approximately three to four hours until the polyurethane plastic
cast is fully hardened and ready to be separated from the frame and mould.
This is a cost-efficient method allowing the manufacture of three tiles per
day.

3.9   Flow validation and smooth wall case

This section discusses statistical results from the reference smooth-wall case
by analysing the mean velocity, velocity defect, and turbulence intensity.
The discussions are divided into two sub-sections: the first is a comparison
between one smooth-wall case and Direct Numerical Simulation (DNS) data
to show and validate that flow inside the wind tunnel is in good quality, the
second sub-section is the analysis of the smooth-wall reference case from
table 3.1.

Table 3.1 shows the parameters and key flow properties for the smooth-
wall case. These data serve as a reference for rough-wall cases with similar
downstream location x and freestream velocity U_∞. The boundary layer
thickness δ, is based on the wall-normal location where the velocity recovers
98% of the freestream velocity U_∞ (i.e $U/U_\infty = 0.98$). Here, the subscript s
(i.e. δ_s or U_{τ_s}) refers to the smooth-wall case. The wall skin-friction velocity
U_τ is obtained using the Clauser method (refer to section 5.1.1 for details).
$U_\tau = \sqrt{\tau_w/\rho}$ where τ_w is the wall shear stress and ρ is the fluid density.
Kármán number Re_{τ_s} is defined as $Re_{\tau_s} = U_{\tau_s}\delta_s/\nu$, where ν is kinematic
viscosity. Here d and l^+ represent hot-wire diameter and viscous hot-wire
length respectively.

Exp code (symbol)	U_∞ (m/s)	x (m)	F_x (m)	α (°)	r_s (m)	h_s^+	s_s^+	U_{τ_s} (m/s)	δ_s (m)	Re_{τ_s}	wire	d μm	l^+
S1 (○)	20	4	-	-	-	-	-	0.707	0.0519	2311	single	5	47
S2 (+)	15	4	-	-	-	-	-	0.547	0.0522	1828	single	5/2.5	36/18
S3 (×)	10	4	-	-	-	-	-	0.387	0.0523	1299	single	5	26
S4 (∗)	5	4	-	-	-	-	-	0.212	0.0569	764	single	5	14
S5 (▷)	15	5	-	-	-	-	-	0.544	0.0629	2251	single	5	36
S6 (☆)	15	4.5	-	-	-	-	-	0.550	0.0587	2083	single	5	37
S7 (◇)	15	3.5	-	-	-	-	-	0.562	0.0459	1700	single	5	37
S8 (□)	15	3	-	-	-	-	-	0.562	0.0433	1577	single	5	37

Table 3.1: Experimental parameters for smooth surface.

3.9.1 Smooth-wall comparison with DNS
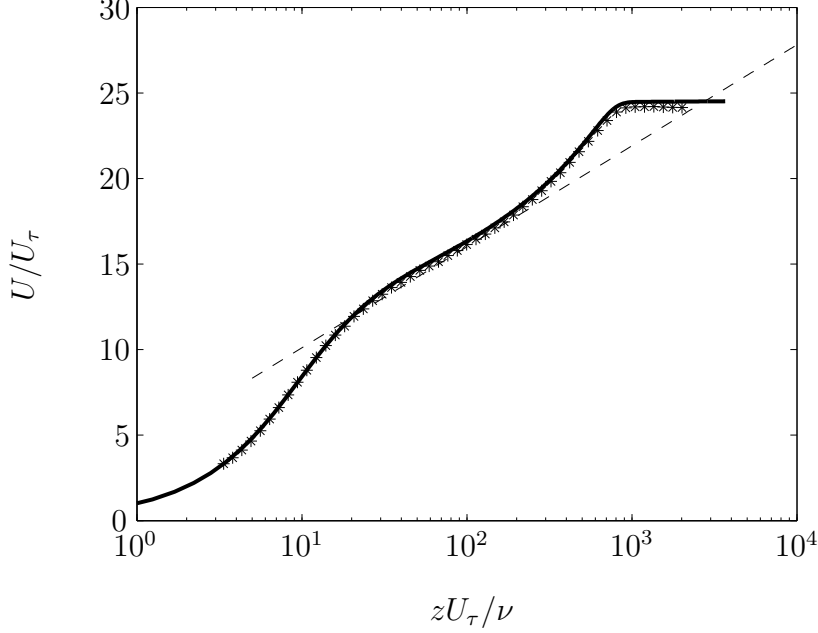
Figure 3.24: Comparison of mean velocity between DNS at $Re_\tau = 830$ (from Schlatter et al. (2009, 2010)) and the experiment from case S4 with $Re_{\tau_s} = 765$. Symbol ($*$) represents experiment and (-) represent DNS.

To check the wind tunnel flow, a wall normal measurement at moderate Reynolds number was performed and compared with Direct Numerical Simulation (DNS) data. The DNS data is taken from Schlatter et al. (2009, 2010) at $Re_\tau = 830$ and the experiment is from case S4 with $Re_{\tau_s} = 765$. Case S4 was chosen because it has the lowest hot-wire viscous length $l^+ = 14$. Note that because all figures in section 3.9.1 and 3.9.2 are from smooth-wall case, and we do not need to differentiate between rough and smooth surface, therefore we do not use the subscript s for the U_τ in the figures.

Figure 3.24 shows the mean velocity profile comparison between the experiment and DNS data. The velocity is normalised with skin-friction velocity U_τ and the wall-normal length is made non-dimensional by inner scaling of ν/U_τ, where ν is kinematic viscosity. It reveals that there is a good agreement between both sets of data on the near-wall and logarithmic regions. However, in the wake region they slightly deviate due to the experiment data being slightly lower in Reynolds number than the DNS data.
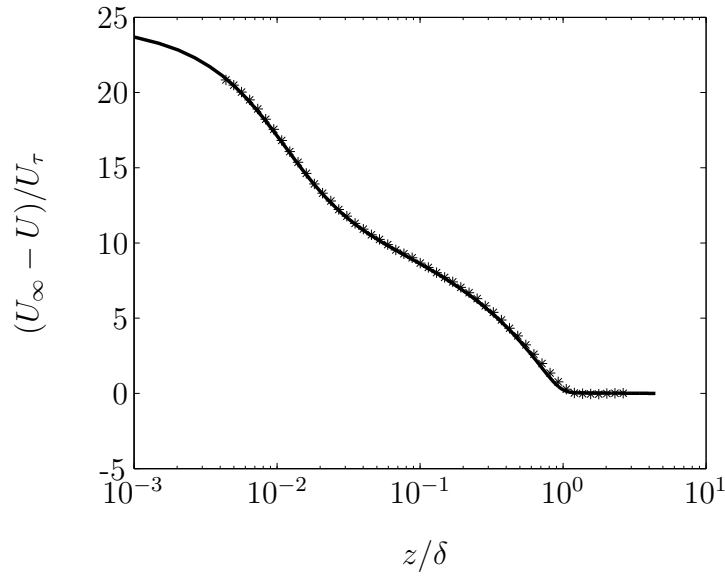
Figure 3.25: Comparison of the velocity defect between DNS at $Re_\tau = 830$ and experiment from case S4 with $Re_{\tau_s} = 765$. Symbol ($*$) represents experiment and (-) represents DNS.
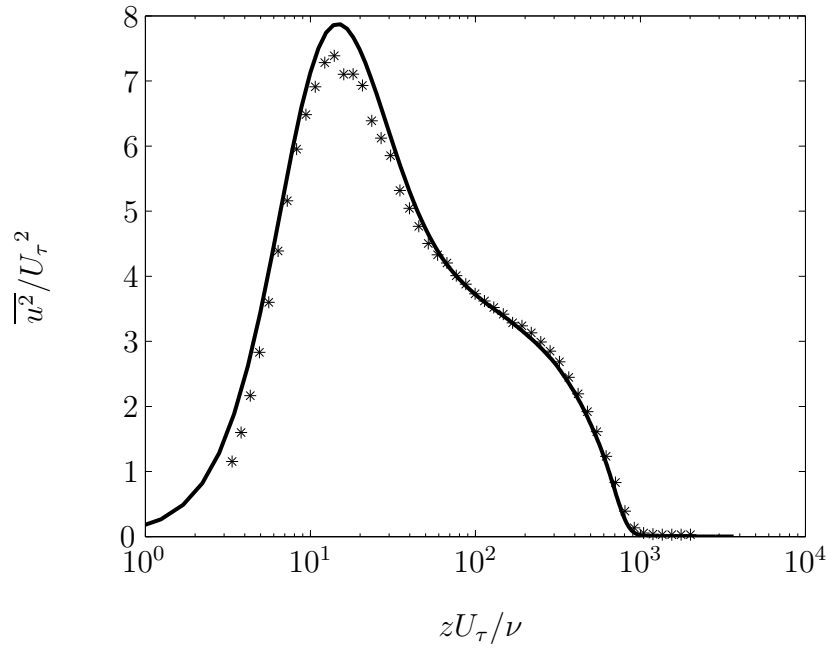
Figure 3.26: Comparison of turbulence intensity between DNS at $Re_\tau = 830$ (from Schlatter et al. (2009, 2010)) and experiment from case S4 with $Re_{\tau_s} = 765$. Symbol ($*$) represent experiment and (-) represent DNS.

Figure 3.25 shows the velocity defect comparison between the experimental

and DNS data. The experiment data collapse over the DNS data, showing an excellent agreement over the whole boundary layer. The velocity defect profile provides similar information with the mean velocity profile, except the former takes out the effect of Reynolds number.

Figure 3.26 shows comparison of the turbulence intensity for the same sets of data and reveal a good agreement across the layer. Both of the DNS and experiment data are peaked at $z^+ = 15$ where the turbulence production is at its maximum. The experimental data peak is slightly lower than the DNS data due to the spatial attenuation effect. From these three profiles it is clear that the experimental data are in good agreement with the DNS data, and they have shown that the flow quality over the smooth-wall case is acceptable.

3.9.2 Smooth-wall reference case
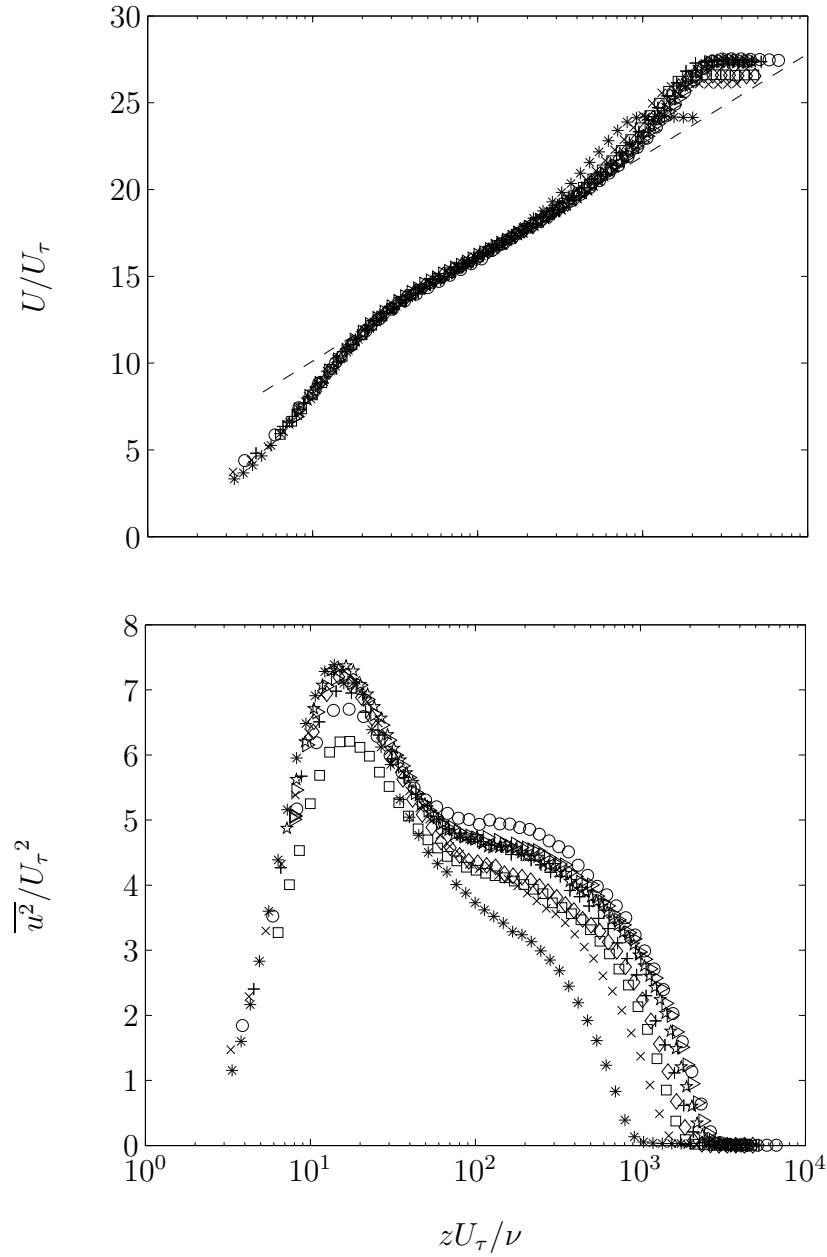
Figure 3.27: Mean velocity and turbulence intensity profile normalized with inner scale for smooth-wall case. Symbols represent the data : ($\circ$) for S1, ($+$) for S2, ($\times$) for S3, ($*$) for S4, ($\triangleright$) for S5, ($\star$) for S6, ($\diamond$) for S7, ($\square$) for S8

The smooth-wall measurements were made to show the comparison with the corresponding rough-wall cases. There are eight different smooth-wall
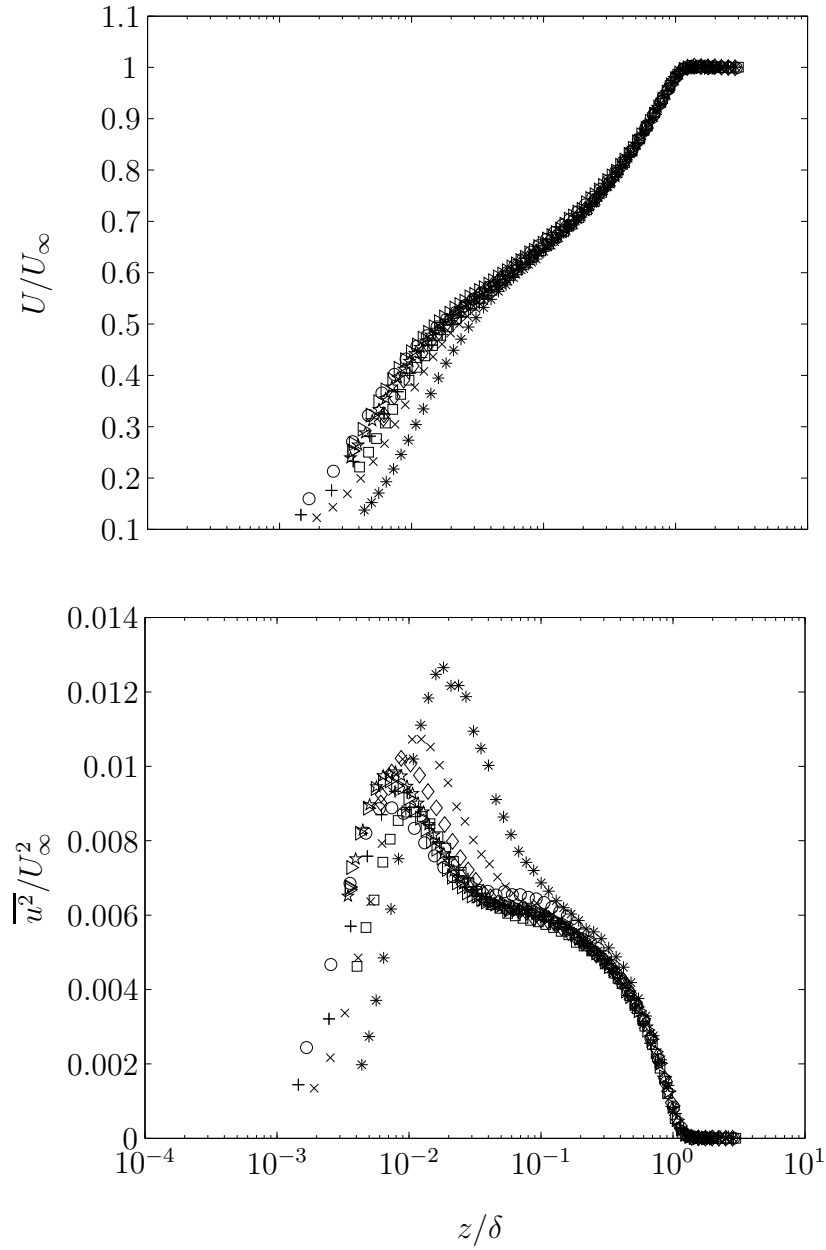
Figure 3.28: Mean velocity and turbulence intensity profile normalized with oiter scale for smooth-wall case. Symbols represent the data : (○) for S1, (+) for S2, (×) for S3, (∗) for S4, (▷) for S5, (☆) for S6, (◇) for S7, (□) for S8

cases, four measurements were performed at different freestream velocities at the same location (S1 - S4) and another four with similar freestream velocities measured at different locations downstream from the trip (S5 -

S8). Here the statistics are analysed using mean velocity profile, turbulence intensity profile, and the velocity defect profile.
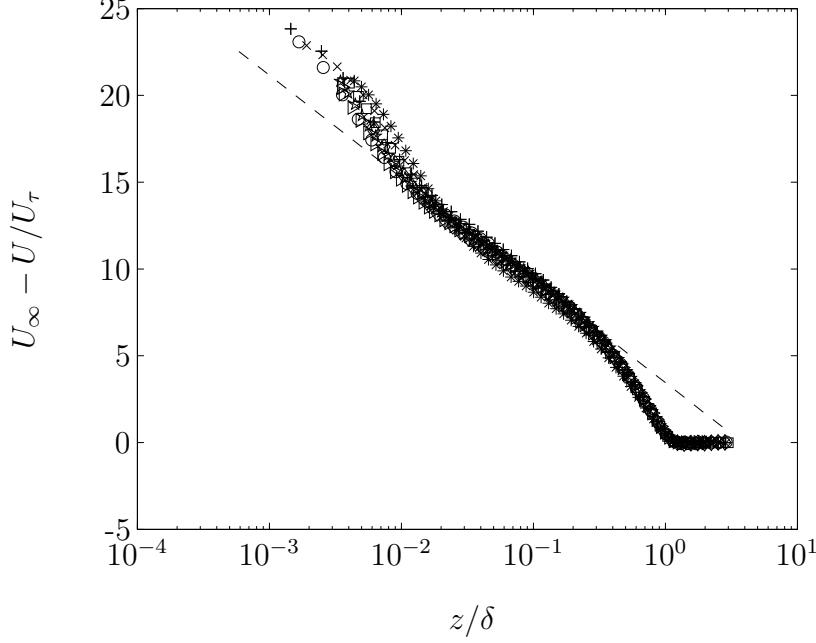
Figure 3.29: Velocity defect profile for the smooth-wall case normalised with the outer-scale. Symbols represent the data : ($\circ$) for S1, ($+$) for S2, ($\times$) for S3, ($*$) for S4, ($\triangleright$) for S5, ($\star$) for S6, ($\diamond$) for S7, ($\square$) for S8

Figure 3.27 shows the mean velocity profile (top) and turbulence intensity profile (bottom) for the smooth-wall case (S1 - S8). Both plots are normalised with the inner scale, and the mean velocity and turbulence intensity are made non-dimensional with U_τ, while the wall normal direction is non-dimensionalised with ν/U_τ. The mean velocity profile shows that the data are collapse well in the logarithmic region between the assumed range of $100 < z^+ < 0.15Re_\tau$. The turbulence intensity profile reveals a peak at $z^+ = 15$ for all cases, indicating the location where turbulent production is most active. According to various studies, as the Reynolds number increases, the near-wall peak also increases (DeGraaff and Eaton, 2000; Metzger and Klewicki, 2001; Hoyas and Jiménez, 2006; Hutchins and Marusic, 2007a,b). However, due to the spatial attenuation issue, there are some cases (particularly at high Reynolds number) that are unable to capture the trend. On the logarithmic and outer regions, the turbulence intensity magnitude clearly increases steadily with Reynolds number.

For completeness, figure 3.28 shows the mean velocity profile (top) and

turbulence intensity profile (bottom) normalised with the outer scale. The velocity and turbulence intensity are non-dimensionalised by U_∞, while the wall normal direction is normalised by δ (or in this case is δ_s, the boundary layer over smooth-wall). The mean velocity plot shows that all the data collapse from the edge of the logarithmic region ($z/\delta_s \approx 0.15$) up to the wake region. For the turbulence intensity, the data starts to collapse at $z/\delta \approx 0.2$. Later in section 5.1, these outer-scaled plots will be used to compare the smooth-wall with the rough-wall for both converging and diverging regions at equal freestream velocity and streamwise location. This outer scaling method allows one to compare and judge the non-dimensional effect of the converging-diverging riblet-type surface roughness on the boundary layer thickness and spanwise velocity variation.

Figure 3.29 shows the velocity defect profile for the smooth-wall measurements (case S1 - S8). The profile reveals good collapse of all eight data from the logarithmic to the wake region, indicating a reasonably good agreement with Townsend (1956, 1976) outer layer similarity hypothesis.

Chapter 4

Experimental results

This chapter presents the measurement results (mean flow and turbulence intensity) for the rough-wall case study. Tables 4.1, 4.2, and 4.3 show the parameters and key flow properties for the rough-wall case with a converging-diverging angle $\alpha = 10°$, $20°$, and $30°$ respectively. The tables contain skin-friction velocity $(U_{\tau_{sa}})$, friction Kármán number $(Re_{\tau_{sa}})$, boundary layer thickness δ_{sa}, and the roughness with viscous-scaled units h_{sa}^+ and s_{sa}^+. Subscript sa denotes spanwise averaged value over one whole wavelength Λ of the rough-wall case. See section 5.1.1 for finding spanwise averaged skin-friction velocity. There are four parametric cases investigated for the rough surface: converging - diverging riblet yaw angle α, viscous-scaled riblet height h^+, streamwise fetch F_x, and relaxation distance r_s. Note that unless mentioned, the viscous scaled height h^+ in this chapter are obtained by normalising the riblets physical height with the spanwise averaged friction velocity $U_{\tau_{sa}}$ (h^+ and h_{sa}^+ are used interchangeably in this chapter).

Exp code	U_∞ (m/s)	x (m)	F_x (m)	α (°)	r_s (m)	h_{sa}^+	s_{sa}^+	$U_{\tau_{sa}}$ (m/s)	δ_{sa} (m)	$Re_{\tau_{sa}}$	wire	d (μm)	l^+
A1	20	4	4	10	-	28	38	0.843	0.0663	3626	single	5	56
A2	15	4	4	10	-	20	27	0.600	0.0585	2247	single/cross	5	40
A3	10	4	4	10	-	14	19	0.410	0.0546	1485	single	5	27
A4	5	4	4	10	-	7	10	0.219	0.0597	872	single	5	15
A5	15	4	3	10	-	20	27	0.607	0.0565	2300	single	5	40
A6	15	4	2	10	-	20	27	0.589	0.0541	2079	single	5	39
A7	15	4	1	10	-	20	27	0.591	0.0544	2145	single	5	39

Table 4.1: Experimental parameters for rough surface with $\alpha = 10°$.

Exp code	U_∞ (m/s)	x (m)	F_x (m)	α (°)	r_s (m)	h_{sa}^+	s_{sa}^+	$U_{\tau_{sa}}$ (m/s)	δ_{sa} (m)	$Re_{\tau_{sa}}$	wire	d (μm)	l^+
B1	20	4	4	20	-	n/a	n/a	n/a	0.0790	n/a	cross	5	n/a
B2	15	4	4	20	-	20	27	0.589	0.0736	2950	single/cross	5	39
B3	15	4	2	20	-	n/a	n/a	n/a	0.0541	n/a	cross	5	n/a
B4	15	3	3	20	-	20	27	0.605	0.0577	2251	single/cross	5	40
B5	15	3.5	3	20	0.5	-	-	0.609	0.0625	2471	single/cross	5	41
B6	15	4	3	20	1	-	-	0.638	0.0715	3074	single/cross	5	43
B7	15	4.5	3	20	1.5	-	-	0.583	0.0784	3019	single	5	39
B8	15	5	3	20	2	-	-	0.601	0.0838	3321	single/cross	5	40

Table 4.2: Experimental parameters for rough surface with $\alpha = 20°$.

Exp code	U_∞ (m/s)	x (m)	F_x (m)	α (°)	r_s (m)	h_{sa}^+	s_{sa}^+	$U_{\tau_{sa}}$ (m/s)	δ_{sa} (m)	$Re_{\tau_{sa}}$	wire	d (μm)	l^+
C1	15	3	3	30	-	21	28	0.623	0.0715	2867	single	5	42
C2	15	3	1	30	-	22	30	0.668	0.0476	936	single	5	45

Table 4.3: Experimental parameters for rough surface with $\alpha = 30°$.

4.1   Parametric study of riblet surfaces

This section discusses statistical results from the converging-diverging riblet type surface roughness. Here four different key parameters are analysed and discussed, namely: converging - diverging riblet yaw angle α, viscous-scaled riblet height h^+, streamwise fetch F_x, and relaxation distance r_s. The measurements were performed by single hot-wire and cross-wire in the wall-normal and spanwise direction, covering one whole wavelength Λ of the converging-diverging region. Details of the experiment parameters and the spanwise averaged values are given in tables 4.1, 4.2, and 4.3. The specific method to obtain the spanwise averaged properties for the converging-diverging riblet (such as $U_{\tau_{sa}}$ and δ_{sa}) using the modified Clauser method is discussed in section 5.1.

Caution is necessary when interpreting the values in tables 4.1, 4.2, and 4.3. Many factors add uncertainty to the values of U_τ determined over rough surfaces. These include uncertainty over the log law constant A and κ, the precise limit in z for the log region, Reynolds number effects, and uncertainty locating the virtual origin (see section 5.1). In light of these uncertainties, it is estimated that the accuracy of the estimation is around $\pm 10\%$, with greater errors for the strongest case (i.e. $\alpha = 30°$ and $h^+ = 28$). In spite of these errors, the results are good indicators of the spanwise variation caused by the converging-diverging riblet on the turbulent boundary layers.

Figures 4.1 (a) and (b) show the variation in the mean velocity and turbulence intensity over one whole wavelength of the surface from case B2. The mean velocity and turbulence intensity are made non-dimensional by the freestream velocity U_∞. The wall-normal distance is normalised with the corresponding smooth-wall δ_s from case S2 at the same streamwise location x and freestream velocity U_∞ to show the spanwise modification by the surface roughness. The solid line shows the boundary layer thickness over the smooth surface δ_s. The dot-dashed line represents the spanwise variation in boundary layer thickness over the rough surface δ_r. The dashed line represents δ_{sa}, the spanwise averaged boundary layer thickness over one complete wavelength Λ. The circled numbers point out the converging region (❶ & ❸ at $y/\Lambda = \pm 0.5$) and diverging region (❷ at $y/\Lambda = 0$). The resolution of the spanwise movement is 21 points. The turbulence intensity is calculated as
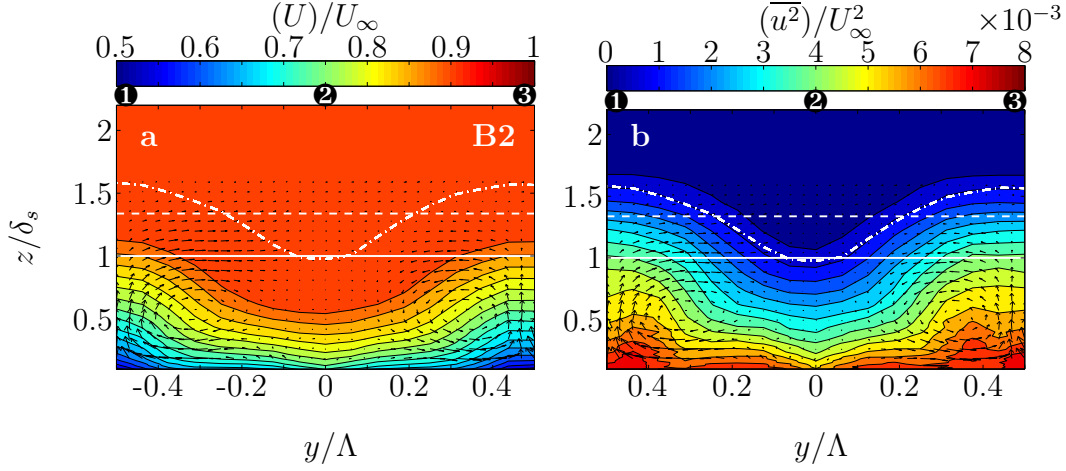
Figure 4.1: Spanwise variation of the streamwise mean velocity (a) and turbulence intensity (b) for the rough-wall case B2, where $\alpha = 20°$, $h^+ = 20$, $F_x = 4$ m and $x = 4$ m. The mean velocity and turbulence intensity are normalised by the freestream U_∞. Wall normal distance is normalised by δ_s, the boundary layer thickness over the smooth-wall, shown here by straight horizontal line. The dot-dashed line represents the spanwise variation in boundary layer thickness over the rough surface δ_r. The dashed line represents δ_{sa}, the spanwise averaged boundary layer thickness over one complete wavelength Λ. The overlaid vectors show the counter rotating vortex pair.

the variation of the total/instantaneous velocity $\breve{u}$ about the local mean at that particular location U (which is a function of y and z with the surface roughness installed).

$$\overline{u^2} = \overline{[\breve{u}(y,z,t) - U(y,z)]^2} \tag{4.1}$$

Thus the turbulence intensity contours of figure 4.1(b) shows the variation of turbulent fluctuations about the modified mean velocity shown in figure 4.1(a). The counter-rotating vortex pair/roll-modes are visualised via the overlaid vectors of spanwise V and wall-normal W mean velocity components. Both V and W velocity components are non-dimensionalised by the freestream velocity U_∞. The results confirm the hypothesis of Koeltzsch et al. (2002) that the converging-diverging/herringbone surface roughness pattern generates large-scale counter-rotating roll-modes. Note that V and W velocity components are measured separately (by rotating cross-wire 90°) and their U components are similar with single-wire. Figures 4.1 (a) and (b) clearly show the spanwise variation in the streamwise mean velocity and
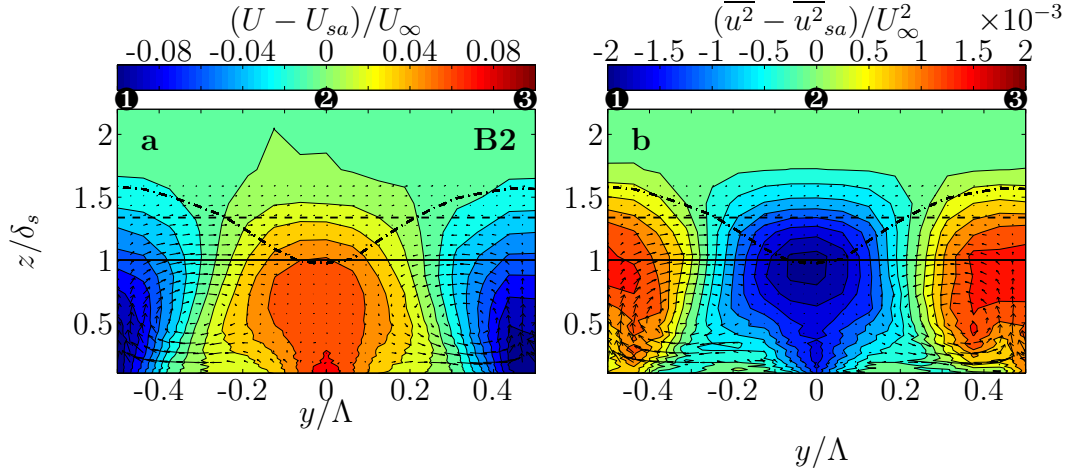
Figure 4.2: Spanwise variation of the streamwise mean velocity (a) and turbulence intensity (b) about the spanwise averaged value for rough-wall case B2. The streamwise mean velocity and turbulence intensity are subtracted with their respective spanwise averaged value and normalised by the freestream U_∞. Wall normal distance is normalised by δ_s, the boundary layer thickness over the smooth-wall, shown here by straight horizontal line. The dot-dashed line represents the spanwise variation in boundary layer thickness over the rough surface δ_r. The dashed line represents δ_{sa}, the spanwise averaged boundary layer thickness over one complete wavelength Λ. The overlaid vectors show the counter rotating vortex pair.

turbulence intensity due to the converging-diverging pattern of the riblet-type surface roughness. The boundary layer thickness over the rough-wall δ_r shows a clear variation across the spanwise wavelength. For this particular case, the boundary layer thickness varies from $z/\delta_s \approx 1$ at the converging region to around $z/\delta_s \approx 1.6$ at the diverging region. The strength of the counter-rotating vortices for this particular case (B2) is relatively small, with the maximum spanwise mean velocity V and wall-normal velocity W components are around 1.12% and 1.76% of the freestream velocity respectively. To ease the discussion, in this chapter we use the magnitude of maximum V and W, and define it as $O = \sqrt{V^2\|_{max} + W^2\|_{max}}$. Hence the maximum magnitude for V and W in case B2 is $\approx 2.09\%$. Section 4.2 contains the summary of individual $\frac{V}{U_\infty}\|_{max}$ and $\frac{W}{U_\infty}\|_{max}$ for all parametric study cases. All overlaid vectors of V and wall-normal W mean velocity components have an equal range scale.

To illustrate more clearly the effects of the converging - diverging roughness on the turbulent boundary layer, figures 4.2 (a) and (b) show the spanwise

variation for the streamwise mean velocity and turbulence intensity about the respective spanwise averaged value at each wall-normal position. These plots highlights the large-scale spanwise variation and reveal the position where the flow is locally accelerated or decelerated. It is very unusual and surprising that such a small perturbation, where the roughness height $h \approx 0.01\delta$, can generate such strong and pronounced spanwise variation. The secondary flows produced by the rough surfaces seem to penetrate the entire turbulent boundary layer.
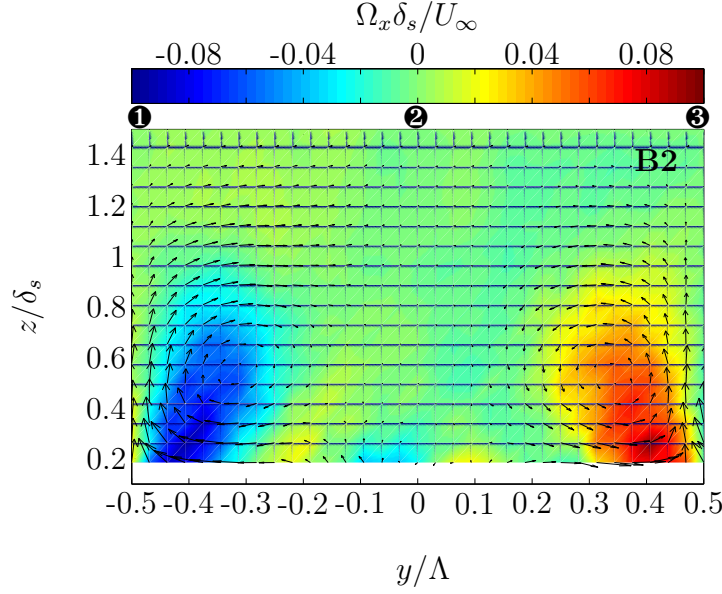
Figure 4.3: Streamwise vorticity for rough-wall case B2 over one whole wavelength Λ normalised by the boundary layer thickness of the corresponding smooth-wall δ_s and freestream velocity U_∞. Wall normal distance is normalised by δ_s, the boundary layer thickness over the smooth-wall.

Figures 4.1 and 4.2 clearly reveal that over the converging region, the flow near the wall is being forced to coincide and converge together, and then move away from the wall, forming a *common-flow-up*. This vertically upwards movement carries low velocity fluid from close to the surface to the outer region, resulting in a low local mean velocity over the converging region (hence causing a thicker local boundary layer). The common-flow-up also carries the near-wall turbulent fluctuations (which are relatively high) to the outer region resulting in higher local turbulence intensities. Over the diverging region, the opposite situation occurs. The fluid flow near the wall is forced to diverge away from each other in the spanwise direction, hence (from continuity) a *common-flow-down* occurs with high speed fluid that

resides further from the wall moving downwards towards the surface. This vertically downwards transport results in higher local mean velocity and a thinner turbulent boundary layer. Furthermore, the high speed fluid from the higher wall-normal location has a relatively low turbulence intensity, hence, it causes a lower local turbulent intensity over the diverging region. The results are consistent with vortex generator studies which reported an increase in turbulent intensities in common-flow-up regions of the vortical flow field and a decrease in turbulent intensities within the common-flow-down region (Mehta and Hoffmann, 1987).

In order to observe the strength of the counter-rotating vortices more clearly, figure 4.3 shows the vorticity contour over one whole wavelength Λ of the converging-diverging roughness. Here the vorticity is normalised with boundary layer thickness of the corresponding smooth-wall δ_s and freestream velocity U_∞, while the wall normal location is also made non-dimensional by the boundary layer thickness of the smooth-wall δ_s. From figure 4.3 there is a clear indication that the counter-rotating vortices are very large in size, reaching the edge of the boundary layer. Furthermore, the figure shows that between location $0 < y/\Lambda < 0.5$ (0 for diverging and 0.5 for converging) the vorticity is counter-clockwise (positive), while between location $0.5 < y/\Lambda < 0$ the vorticity is clockwise (negative).

The relatively weak strength of the counter-rotating vortices observed for this particular case (B2) raises some questions regarding the difference with conventional vortex generators. According to Fransson et al. (2004); Lögdberg et al. (2009); Fransson and Talamelli (2012) typical vortex generators can generate vortices with a V and W component of anywhere between $\approx 2 - 30\%$ of U_∞. Hence our converging - diverging riblet type surface roughness generate secondary flows in the lower range of standard vortex generators. However, these generators have physical height of 2.5 - 18 mm, or more (Lögdberg et al., 2009; Fransson and Talamelli, 2012), which are signficantly higher than our surface pattern. Further information and a summary of various vortex generator experiments can be found in a report by Lögdberg et al. (2009).

Although it is relatively weak compared to conventional vortex generators, one main advantage of the converging-diverging surface roughness is its small dimension. Having such a small size could enable the roughness to minimise or avoid the form-drag penalty that exists for conventional vortex

generators.

The possibility of applying a low profile secondary-flow or vortex generator could be important in a situation where it is necessary to introduce vortices into turbulent boundary layer flow with a minimum form-drag penalty. Schoppa and Hussain (1998) have shown (through DNS of turbulent channel flow) that large-scale counter-rotating streamwise vortices are able to reduce skin-friction drag by up to 20%. A more recent study by Chen et al. (2013, 2014) reveal that herringbone shaped surface roughness in a fully developed pipe flow is able to reduce skin-friction drag by up to 16%. These numbers are significantly higher than standard straight riblets which have maximum drag reduction of $\approx 10\%$ (see Bechert et al. (1997)).

Another potential application of the converging-diverging surface roughness pattern is to act as a flow-control device to delay transition from laminar flow to turbulent flow by introducing streaks to stabilize Tollmien-Schlichting (TS) waves. According to Herbert (1988), if TS waves in laminar flow exceed the critical amplitude of 1% of freestream velocity, it will generate a secondary instability that leads to fast flow transition to turbulence. Therefore, by introducing certain amplitude streaks, TS waves can be stabilised and transition delay may occur (Cossu and Brandt, 2002; Fransson et al., 2004, 2005, 2006; Fransson and Talamelli, 2012). Some of the streaks generators used by Fransson and co-workers are miniature vortex generators that produce counter-rotating vortices and spanwise patterns of high and low speed large-scale streaks similar to those generated by the converging-diverging surface roughness in this study. Their results suggest a prospect of applying the converging-diverging surface roughness to generate streaks to influence flow transition.

4.1.1   Influence of yaw angle α

The first parametric study is undertaken to demonstrate the effect of the converging-diverging angle α on the strength of the secondary flows and spanwise variation introduced by the converging/diverging surfaces. Other parameters such as free-stream velocity U_∞, fetch distance F_x, and measurement location x are kept constant. For this study, two pairs of comparable cases are selected, the first cases are C1 and B4 (single-wire measurements) while the second pair are cases B2 and A2 (cross-wire measurements).

Single-wire

Figure 4.4: Spanwise variation for mean velocity (left-hand-side) and turbulence intensity (right-hand-side) about the spanwise averaged value for rough-wall case C1, $\alpha = 30°$ and B4, $\alpha = 20°$.

Figure 4.4 compares the single wire data from case C1 with $\alpha = 30°$ (a and b) and case B4 with $\alpha = 20°$ (c and d). Both cases have the same free-stream velocity $U_\infty = 15$ m/s, streamwise fetch $F_x = 3$ m, and measurement loca-

tion $x = 3$ m. The viscous scaled height for case C1 and B4 are relatively close ($h^+ = 21$ and 20 respectively), hence a direct comparison is possible. From figure 4.4, it is clear that lower yaw angle α results in lower spanwise variation magnitude in mean velocity and turbulence intensity. The maximum spanwise variation in mean velocity ($(U - U_{sa})/U_\infty\|_{max}$) for cases C1 and B4 are 0.164 and 0.103 respectively, while for turbulence intensities ($(\bar{u}^2 - \bar{u}_{sa}^2)/U_\infty^2\|_{max}$) are 3.4×10^{-3} and 1.7×10^{-3} respectively.

The boundary layer thickness variation for $\alpha = 30°$ is $\approx 51.39\%$, while for $\alpha = 20°$ is $\approx 43.88\%$, indicating that larger yaw angle α results in larger spanwise variation in boundary layer thickness. In line with the reductions in spanwise variation magnitude, the size of the area/regions of spanwise variation in both mean velocity and turbulence intensity also diminish slightly as yaw angle α decreases.

Cross-wire

To investigate the relationship between α and the strength of the roll-modes, we compare cases B2 and A2 for which we have measured all three velocity components (using cross wires). The first row of figure 4.5 (a and b) shows the cross wire data from case B2 with $\alpha = 20°$ and the second row (c and d) are data from case A2 with $\alpha = 10°$. Other parameters are kept constant with $U_\infty = 15$ m/s, $F_x = 4$ m, and $x = 4$ m, resulting in $h^+ = 20$ for both case B2 and case A2. The super-imposed cross-wire data show that the counter-rotating vortices for case B2 are stronger than that of case A2. The maximum magnitude for V and W induced for case B2 are $\approx 2.09\%$ of U_∞ while for case A2 they are $\approx 1.65\%$ of U_∞.

In order to see the effect of different α more clearly, figure 4.6 shows the vorticity contour from cases B2 and A2. The plot reveals that the vorticity magnitude in case B2 (with $\alpha = 20°$) is stronger than in case A2 (with $\alpha = 10°$). Furthermore the vorticity size/area in case B2 are larger than in case A2.

Hence a lower yaw angle α will generate a weaker counter-rotating vortices strength, smaller area/regions of spanwise variation, and a smaller vorticity area, which results in a weaker spanwise variation in mean velocity and turbulence intensity. In turn this will cause a smaller change in the boundary

Figure 4.5: Spanwise variation and periodicity for mean velocity (left-hand-side) and turbulence intensity (right-hand-side) about the spanwise averaged value for rough-wall case B2, $\alpha = 20°$ and A2, $\alpha = 10°$.

layer thickness variation δ_r.
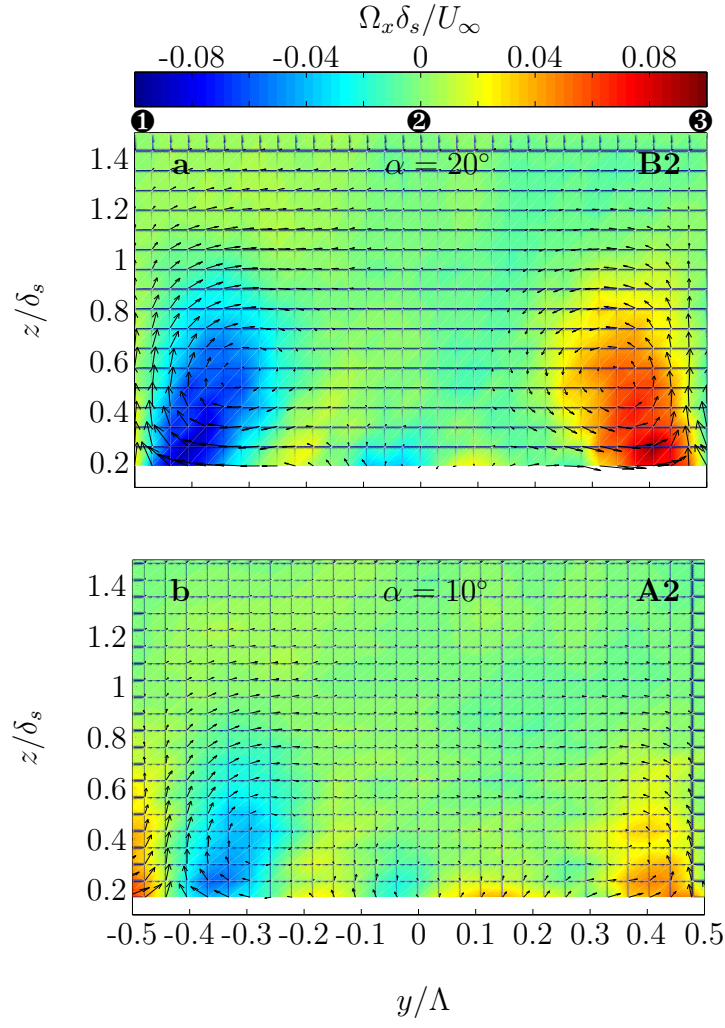
Figure 4.6: Streamwise vorticity for rough-wall case B2, $\alpha = 20°$ and A2, $\alpha = 10°$

4.1.2   Influence of viscous-scaled height h^+

The second parametric study is to investigate the effect of viscous scaled riblet height h^+ by varying the freestream velocity U_∞. Unless mentioned, the viscous-scaled height in this section is obtained by normalising it with the spanwise averaged skin-friction $U_{\tau_{sa}}$. Here the other parameters such as α, F_x, and x are unchanged. For the single-wire experiment, cases A1 - A4 are chosen. For the cross-wire data set, we discuss cases B1 and B2. It should be noted that h^+ is varied by altering U_∞, hence each h^+ case will have a different Reynolds number.

Single-wire

Figure 4.7 shows the results from cases A1 - A4. From the top rows (a and b) to the bottom rows (g and h), the corresponding h^+ are 28, 20, 14, and 7 respectively. The other parameters are kept constant with $\alpha = 10°$, $F_x = 4$ m, and $x = 4$ m. The different h^+ values are obtained by varying the freestream velocity U_∞ from 20 m/s to 5 m/s, in 5 m/s decrements. The right-hand column in figure 4.7 shows the spanwise variation for turbulence intensity and the left-hand column for mean velocity.

From figure 4.7 it is clear that as h^+ decreases, the strength of the three-dimensionality imposed by the converging-diverging surface on the mean velocity (left-hand column) and turbulence intensity (right-hand column) decreases. For the weakest case A4 ($h^+ = 7$), the viscous scaled height approaches the hydrodynamically smooth-wall, hence the converging-diverging riblets are unable to generate the large-scale three-dimensionality. Therefore for case A4, there is a less pronounced spanwise variation in the boundary layer thickness over the converging-diverging roughness.

Figure 4.8(a and b) shows the maximum spanwise variation for mean velocity and turbulence intensity as a function of viscous-scaled riblet height h^+ for case A1 - A4. The figures clearly indicate that an increase in h^+ results in higher maximum spanwise variation for the mean velocity and turbulence intensity. In this set of experiment, the maximum spanwise variation for mean velocity is ≈ 0.073 and turbulence intensity is $\approx 15 \times 10^{-3}$ for $h^+ = 28$.

Figure 4.7: Spanwise variation for mean velocity (left-hand-side) and turbulence intensity (right-hand-side) about the spanwise averaged value for rough-wall cases A1 - A4. (a and b) case A1, $h^+ = 28$; (c and d) case A2, $h^+ = 20$; (e and f) case A3, $h^+ = 14$; (g and h) case A4, $h^+ = 7$.
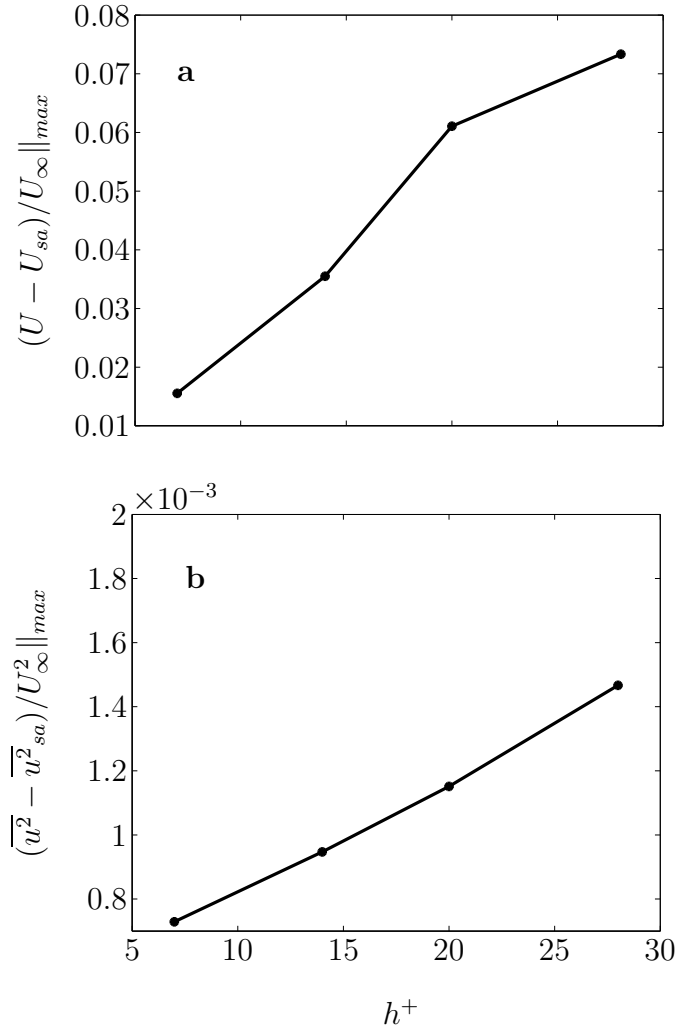
Figure 4.8: Maximum spanwise variation about the spanwise averaged value for (a) mean velocity and (b) turbulence intensity as a function of viscous-scaled riblet height h^+ for cases A1 - A4

Cross-wire

The influence of different h^+ on the strength of counter-rotating vortices is shown in figure 4.9. The first row shows the mean velocity (a) and turbulence intensity (b) from case B1 with $U_\infty = 20$ m/s, while the second row shows results from case B2 with $U_\infty = 15$ m/s. Note that for case B1, the measurements were performed with cross-wire only, which has a large hot-wire holder size compared with the smaller single-wire holder. The physical

Figure 4.9: Spanwise variation and periodicity for mean velocity (left-hand-side) and turbulence intensity (right-hand-side) about the spanwise averaged value for rough-wall cases B1, $U_\infty = 20$ m/s and B2, $U_\infty = 15$ m/s.

limitation of the cross-wire prevented us from measuring the flow closer to the wall, hence we lost measurement points on the logarithmic region. With less logarithmic measurement points, it is very difficult to obtain the skin-friction wall $U_{\tau sa}$. Therefore we are unable to provide the viscous scaled height for this particular case. However, looking at the freestream velocity it is somewhat apparent that the viscous scaled height from case B1 is higher than B2. We predict that the viscous height for case B1 is $h^+ \approx 28$. Finally, for case B1 the counter-rotating vortices have a maximum spanwise and wall-normal induced component magnitude of 2.69% of U_∞, while case B2 is 2.09% of U_∞.

Figure 4.10 shows the vorticity contour plot for cases B1 and B2, with $U_\infty = 20$ m/s and $U_\infty = 15$ m/s respectively. The figure shows that case B1 with higher U_∞ (hence larger h^+) has a significantly higher vorticity magnitude and area than case B2. Hence smaller h^+ results in weaker counter-rotating vortices.

In summary, based on the single-wire and cross-wire experiments, smaller h^+ values translate to weaker counter-rotating vortices, which as in case A4 (see figure 4.7), result in a less pronounced spanwise variation area for both the mean velocity and turbulence intensity. Furthermore, at the lowest h^+ (cases A3 and A4), the boundary layer thickness over the spanwise wavelength of the converging and diverging region does not vary significantly.
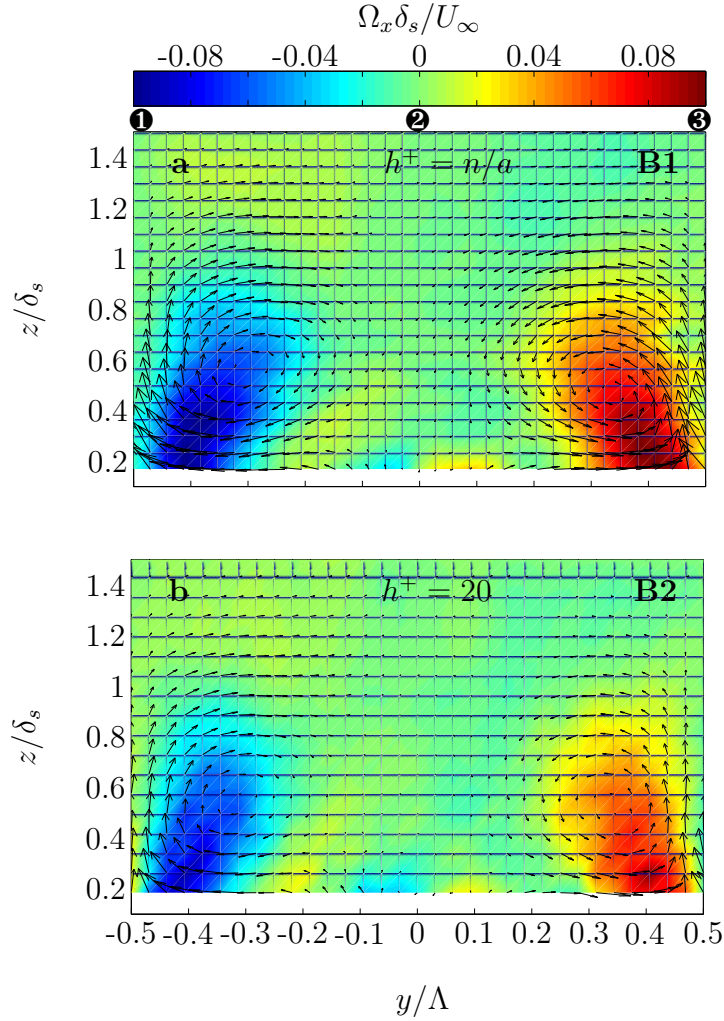
Figure 4.10: Streamwise vorticity for rough-wall case B1, $U_\infty = 20$ m/s and B2, $U_\infty = 10$ m/s

4.1.3 Influence of fetch F_x

The third parametric case is the streamwise fetch F_x, which is defined as the length of the rough surface over which the flow has developed. For this study, cases A2, A5 - A7 and cases C1 - C2 are compared for the single-wire experiments. For the cross-wire experiments we compare cases B1 and B3. For each case group the parameters α, x, and h^+ are kept nominally constant.

Single-wire

Figure 4.11 documents the effect of different streamwise fetch lengths for the converging-diverging riblet surface roughness. All results are at nominally equal $h^+ = 20$, with converging-diverging yaw angle $\alpha = 10°$, and measured at a downstream location $x = 4$ m. The fetch length F_x was decreased from 4 m to 1 m with a decrement of 1 m (cases A2, A5 - A7). Here the 1 m decrement is approximately equal to $20\delta_s$ (see table 3.1).

The left hand side column of figure 4.11 shows the mean velocity, while the right hand side shows turbulence intensity. The top row in figure 4.11 (a and b) show the longest fetch $F_x = 4$ m, and the subsequent figures below show a progressively shorter F_x. The shorter fetch cases are obtained by replacing the upstream rough surface with a smooth surface. For example, in the case of $F_x = 1$ m (case A7), the measurement is performed at downstream location $x = 4$ m for a flow that has developed initially over 3 m of smooth surface, and followed by 1 m of rough surface.

Comparison between $F_x = 4$ m to $F_x = 1$ m reveals the effect of F_x on the spanwise variation magnitude and area for both mean velocity and turbulence intensity. As the streamwise fetch decreases, the size of the region/area of spanwise variation in mean velocity and turbulence intensity shrinks/diminishes and is constrained closer to the surface. The weaker spanwise variation in mean velocity results in a less pronounced or weaker spanwise variation in boundary layer thickness. Cases A6 and A7 in figure 4.11 show that for the smallest fetch cases, there is almost no variation in boundary layer thickness (δ_r and δ_{sa} are almost equivalent)
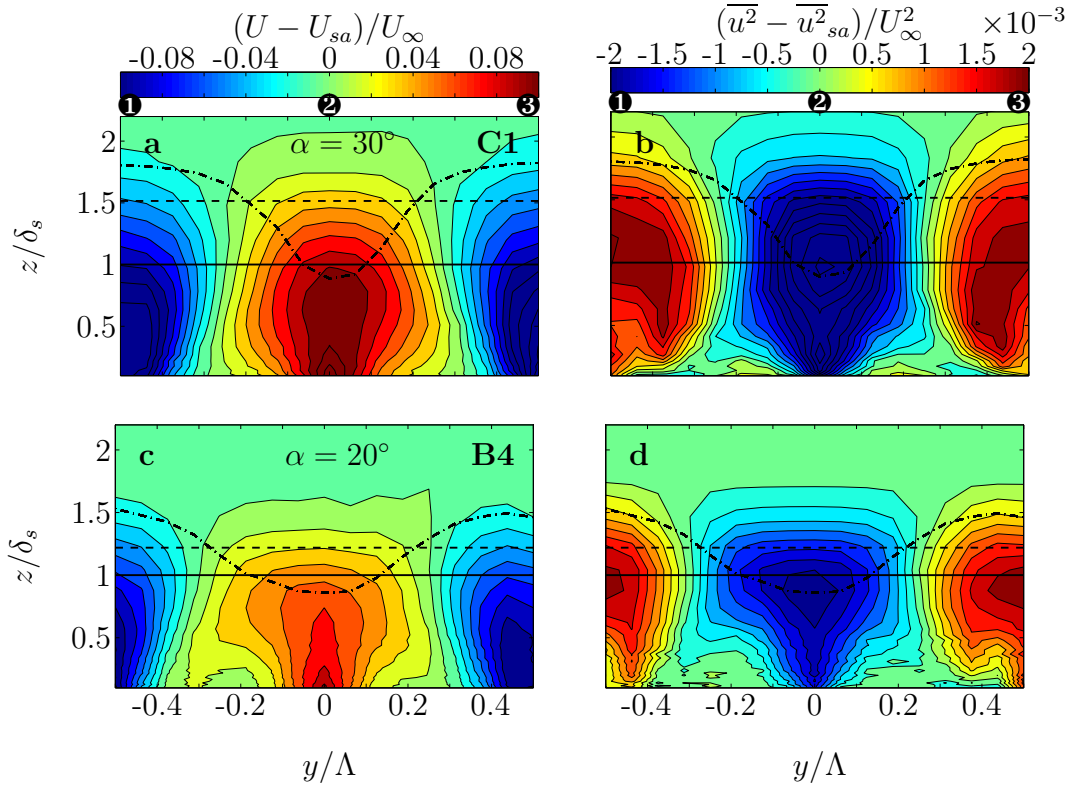
Figure 4.11: Spanwise variation for mean velocity (left-hand-side) and turbulence intensity (right-hand-side) about the spanwise averaged value for rough-wall case A2, A5 - A7. (a and b) case A2, $F_x = 4$ m; (c and d) case A5, $F_x = 3$ m; (e and f) case A6, $F_x = 2$ m; (g and h) case A7, $F_x = 1$ m.

Figure 4.12: Maximum spanwise variation about the spanwise averaged value for (a) mean velocity and (b) turbulence intensity as a function of F_x/δ_{sa} for cases A2, A5 - A7

It is interesting however, that even at the shortest fetch length in ($F_x = 1$ m) the surface roughness is still capable to generate an observable/noticeable three-dimensionality onto the flow. A much closer examination of the mean velocity and turbulence intensity near the wall reveal that the maximum magnitude for these quantities is unchanged and almost equivalent in all of the fetch cases. Figure 4.12 shows the optimum variation for both the mean velocity and turbulence intensity for $18 < F_x/\delta_{sa} < 70$. From the plots, it is clear that the change of F_x does not significantly alter the spanwise variation magnitude in both the mean velocity and turbulence intensity. Furthermore, from table 4.1 the skin-friction velocity $U_{\tau sa}$ from cases A2,
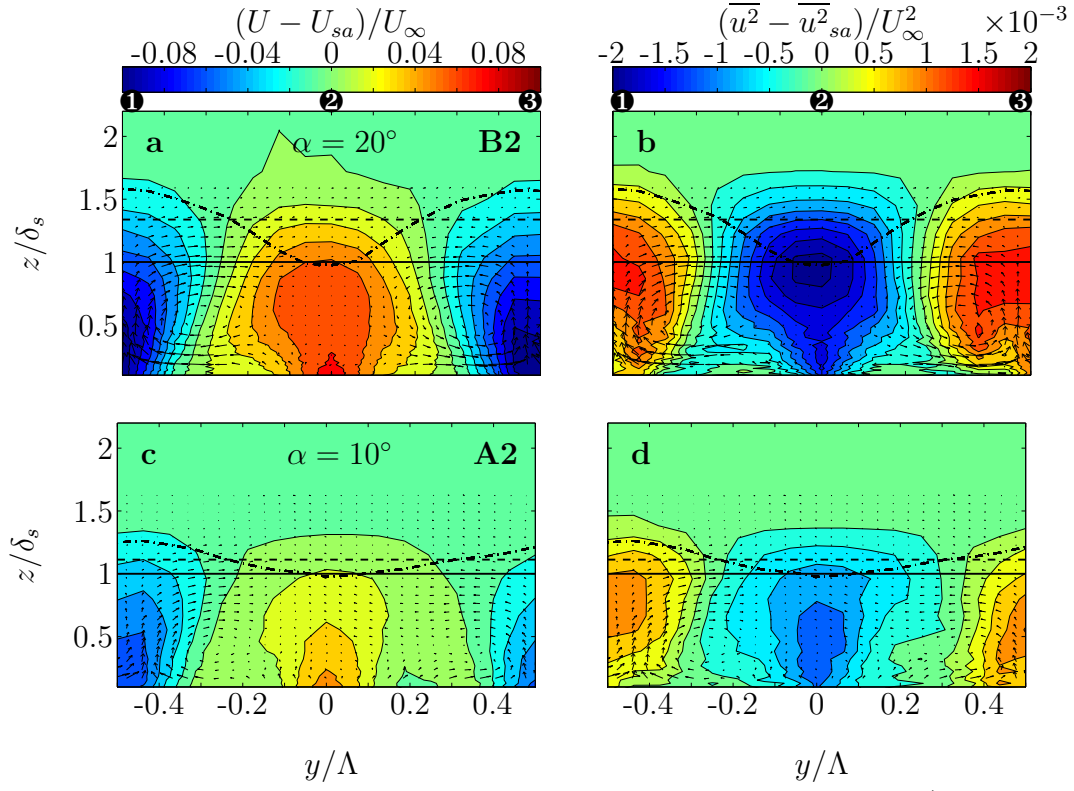
Figure 4.13: Spanwise variation for mean velocity (left-hand-side) and turbulence intensity (right-hand-side) about the spanwise averaged value for rough-wall cases C1 - C2. (a and b) case C1, $F_x = 3$ m; (c and d) case C2, $F_x = 1$ m

A5 - A7 are very close, signalling that for this particular case there is almost no change in skin-friction drag as F_x decreases.

Figure 4.13 compares the effect of fetch for a much stronger yaw angle $\alpha = 30°$ (cases C1 and C2) instead of the more acute $\alpha = 10°$ (cases A2, A5 - A7) analysed figure 4.11. Case C1 has $F_x = 3$ m and case C2 has $F_x = 1$ m, and both cases have similar $U_\infty = 15$ m/s and measured at location $x = 3$ m downstream of the tunnel's inlet. The plots show similar trends with fetch as observed in figure 4.11 for the more acute $\alpha = 10°$. Figure 4.13 reveals that a shorter fetch results in a smaller spanwise variation area in mean velocity and turbulence intensity (spanwise variation is constrained closer to the surface as F_x is reduced). However, the change in the maximum spanwise variation magnitudes for mean velocity and turbulence intensity are relatively minor. The maximum spanwise variations in mean velocity for $F_x = 3$ m and $F_x = 1$ m are approximately 0.164 and 0.151 respectively.

For turbulence intensity, the maximum spanwise variation for $F_x = 3$ m and $F_x = 1$ m are 3.4×10^{-3} and 3.1×10^{-3} respectively. Thus as flows develop for increasing fetch lengths over the converging-diverging surface, the secondary flows seem to develop in the wall normal direction, growing further from the wall as F_x increases, until eventually they exceed the boundary layer height.

Interestingly however, for $\alpha = 30°$, when the spanwise averaged friction velocity $U_{\tau_{sa}}$ is calculated, the shorter fetch (case C2) has $U_{\tau_{sa}} = 0.668$ m/s while the longer fetch (case C1) has $U_{\tau_{sa}} = 0.623$ m/s. This variation in $U_{\tau_{sa}}$ is very similar to that recorded with similar changes in F_x for the $\alpha = 10°$ cases (see table 4.1 and table 4.3). Furthermore, there is a much stronger boundary thickness variation for the $\alpha = 30°$ at $F_x = 1$m (case C2) compared to the less pronounced $\alpha = 10°$ at similar fetch (case A7). It seems that the strength of flow is more sensitive to the changes in yaw angle α than fetch length F_x.

Cross-wire

Figure 4.14 demonstrates the effect of fetch F_x on the strength of the involved vortices over the rough surface. Here we analyse case B2 with $F_x = 4$ m (first row) and case B3 with $F_x = 2$ m (second row). For both cases the other parameters are kept constant with $U_\infty = 15$ m/s, yaw angle $\alpha = 20°$, and measured at a downstream location $x = 4$ m. The resulting magnitude of maximum spanwise and wall-normal induced component value for case B2 is $\approx 2.09\%$ of U_∞ while for case B3 it is $\approx 1.44\%$ of U_∞.

In order to analyse the change of the secondary flow strength due to different fetch length more clearly, figure 4.15 shows the vorticity contour of cases B2, $F_x = 4$ m and B3, $F_x = 2$ m. Here the plot shows that case B2, which has a longer fetch length, generates stronger vorticity than that of case B3, which has a shorter fetch length. Furthermore, the shorter fetch results in smaller vorticity size and confined closer to the wall. From this result it suggests that as F_x decreases the strength of the counter-rotating vortices are also decreased owing to the shorter development length.

Based on the single-wire and cross-wire results it is clear that lower F_x results in weaker counter-rotating vortices which are constrained closer to the surface, leading to more compact regions of spanwise variation in mean
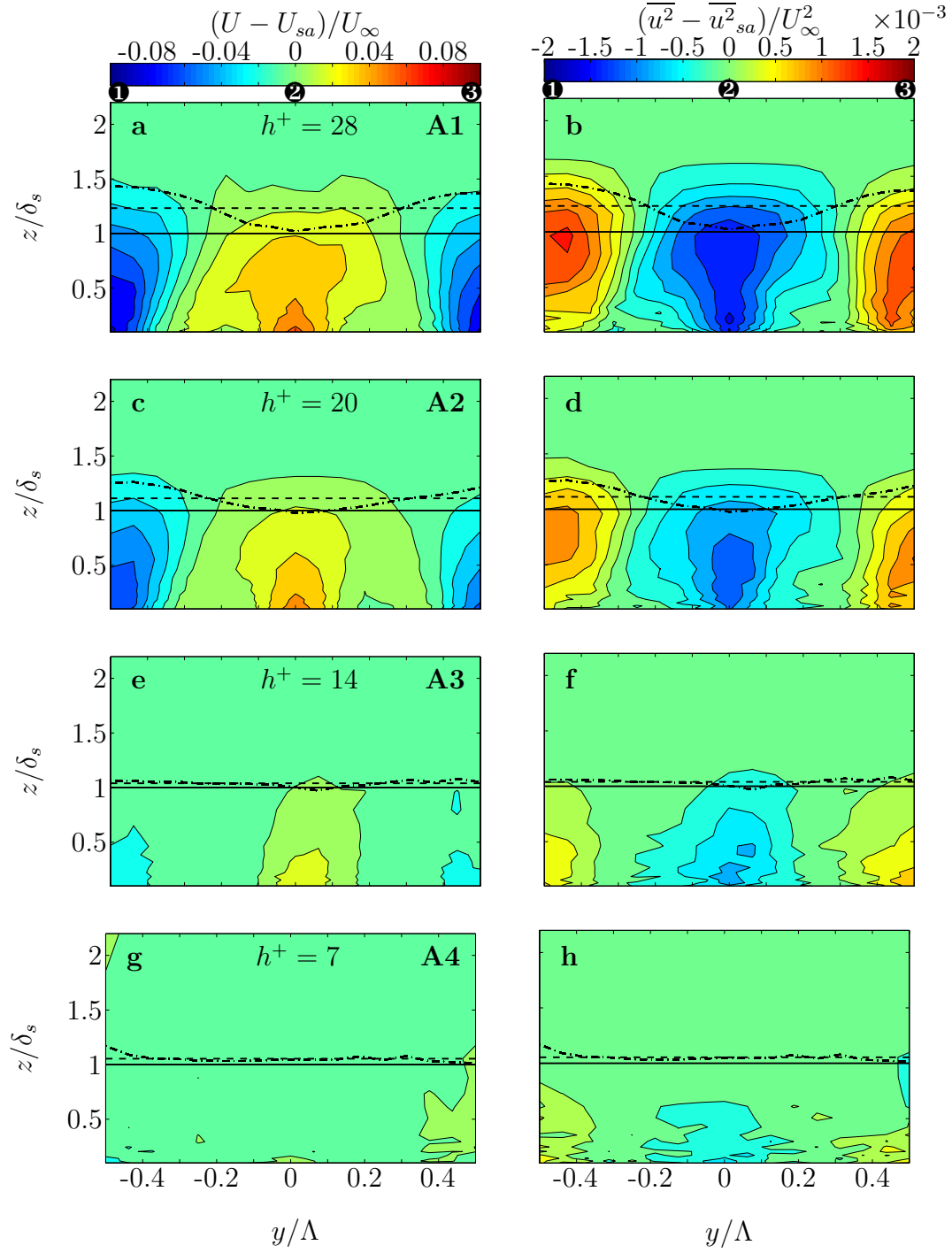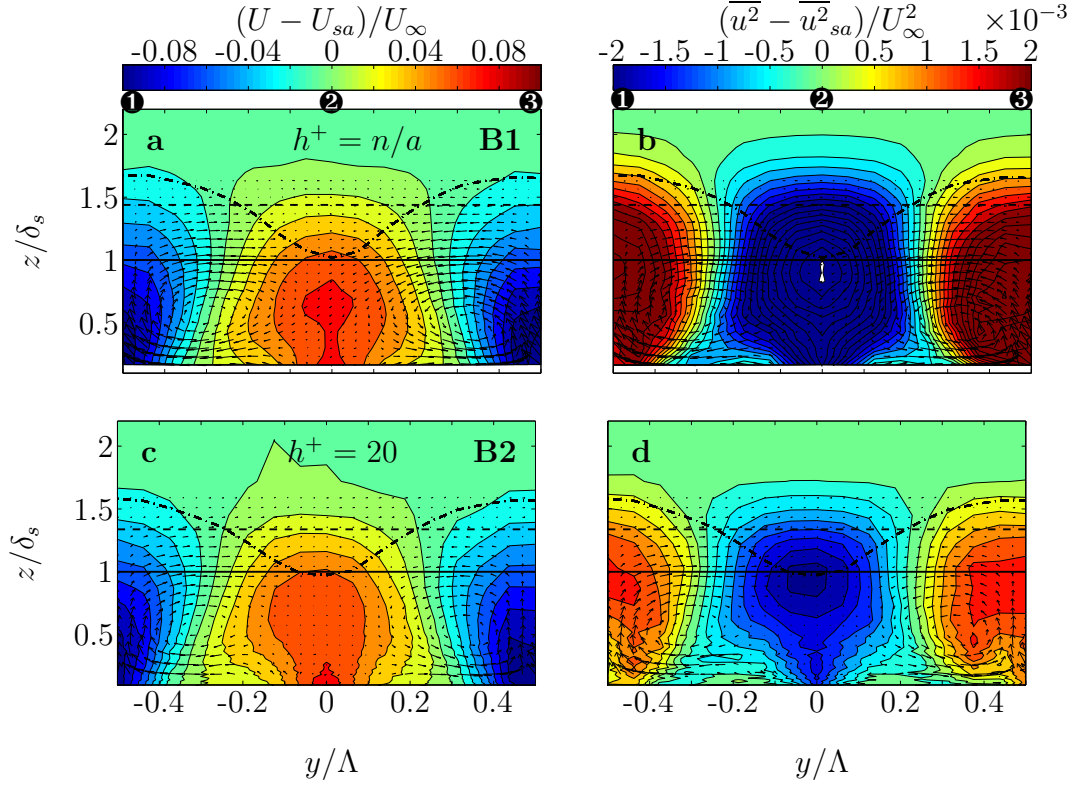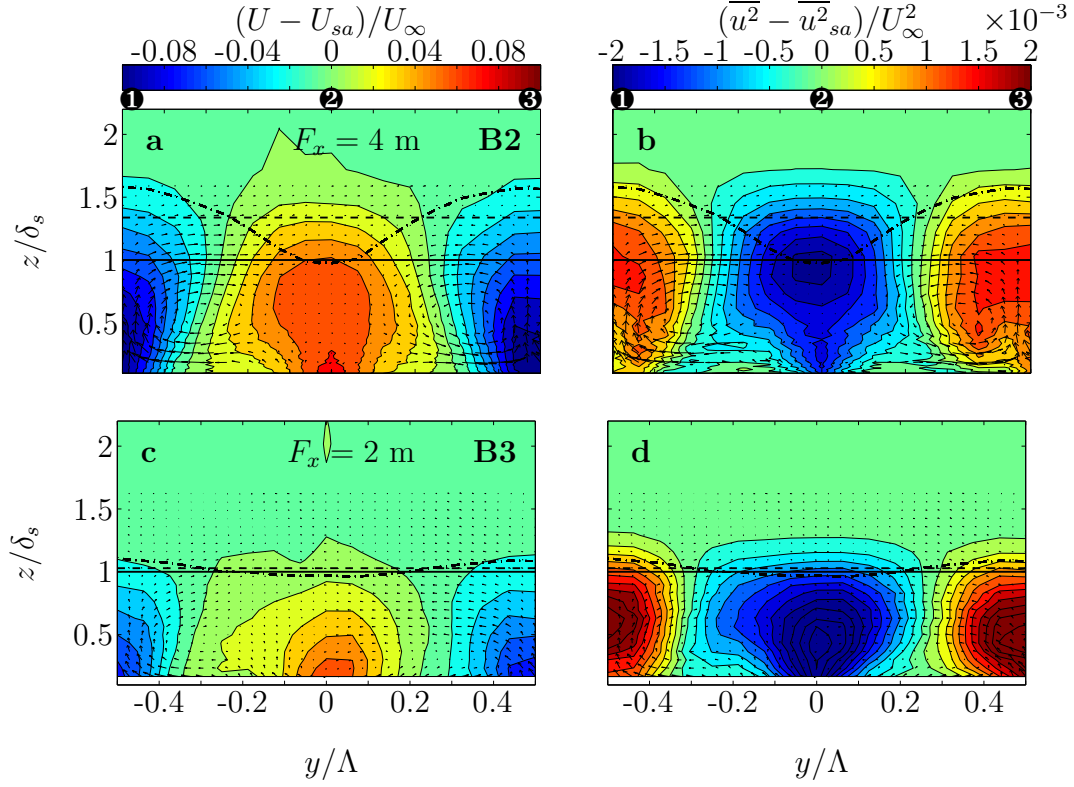
Figure 4.14: Spanwise variation and periodicity for mean velocity (left-hand-side) and turbulence intensity (right-hand-side) about the spanwise averaged value for rough-wall cases B2 and B3. (a and b) case B2, $F_x = 4$ m; (c and d) case B3, $F_x = 2$ m

velocity and turbulence intensity. However even for the shortest fetch case ($F_x = 1$), for both $\alpha = 10°$ and $\alpha = 30°$, the roughness is still able to generate roll modes that produce a near-wall spanwise variation strength that has nominally equal magnitude to that of longer F_x. Finally, yaw angle α has a very dominant effect in the spanwise variation strength and area. For a similar change in fetch length F_x, a wider yaw angle α produces stronger spanwise variation magnitude and a variation that is less confined to the near-wall.

In some respects, this experiment is similar to the already well documented studies on the response of turbulent boundary layers to sudden change in surface roughness, specifically an abrupt change from smooth to rough ($S \to R$) (see Antonia and Luxton (1971); Wood (1982); Smits and Wood (1985)). Step changes from a smooth to rough surface generate an internal turbulent boundary layer which propagates outward from the wall. Accord-
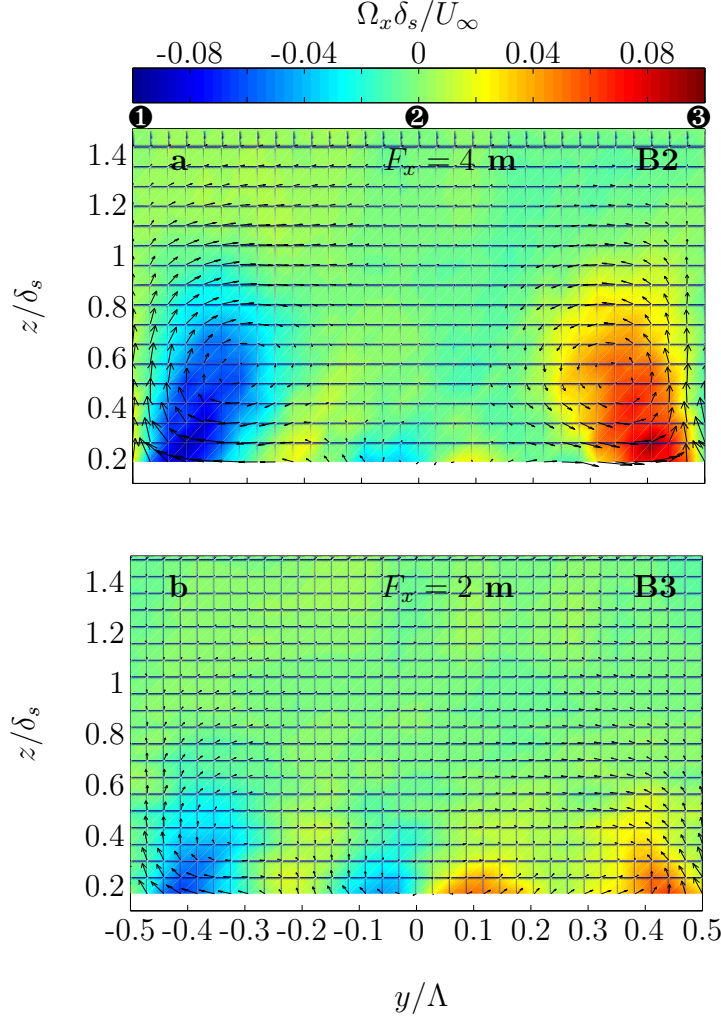
Figure 4.15: Streamwise vorticity for rough-wall cases B2, $F_x = 4$ m and B3, $F_x = 2$ m

ing to Antonia and Luxton (1971) and Smits and Wood (1985), the flow returns to a self-preserving state by $\approx 20\delta$ downstream of the step change in roughness. This means that in this location, the skin-friction, integral parameters, and velocity profiles attain a form that is consistent with the rough-wall in the absence of any step change. Hence, from this classical standpoint (based on a standard random isotropic roughness with no directional preferences and introducing no large-scale spanwise periodicity) all but perhaps the smallest fetch experiment listed here should be self preserving or fully developed. However, the results in figure 4.11 demonstrate that this is not the case for these particular converging-diverging surfaces, where the spanwise periodicity introduced by the roughness continues to

grow with fetch (at least up to the limits of these experiments at $F_x = 4$ m, or $F_x/\delta_{sa} \approx 70$).

4.1.4   Influence of a reversion from rough to smooth surface r_s

The final part of the parametric study investigated is the effect of a reversion from rough to smooth surface. We define the distance r_s as the distance downstream of a step change in surface from rough to smooth. Here we are interested to see whether the counter-rotating roll modes/vortices still persist over the smooth-wall downstream of the change in surface from rough to smooth.

For this type of experiment, the rough-wall (with yaw angle $\alpha = 20°$) covered the first 3 m of the test section while the remaining 2 m is formed by the smooth-wall. The measurements were performed above the smooth-wall at various r_s. To a certain extent, this experiment is the inverse of the fetch study. The choice of 3 m as the rough surface fetch is a compromise between the need to develop a flow with well established strong counter-rotating roll-modes, while also maintaining a long enough smooth section to investigate the relaxation from rough to smooth. The maximum available wind tunnel working section length is 5 m.

For the single-wire case, measurements were made at $x = 3.5$, 4, 4.5, and 5 m, which give $r_s = 0.5$, 1, 1.5, and 2 m respectively (case B5 - B8). The measurements were all performed at $U_\infty = 15$ m/s, however the change in measurements location x and reversion from rough to smooth will result in different $U_{\tau_{sa}}$ values. Because the aim of this experiment is to observe how far the large-scale periodicity persists downstream of the change from rough to smooth, the change in $U_{\tau_{sa}}$ is considered acceptable. For the cross-wire measurement, the experiments were performed at $r_s = 0.5$, 1, and 2 m respectively (cases B5, B6 and B8)

Single-wire

The reversion from rough to smooth surface is shown in figure 4.16. The first row (a and b) illustrates the strongest case where the r_s distance is the shortest with $r_s = 0.5$ m (case B5). The subsequent rows below reveal a progressively longer r_s distance with 0.5 m increments.

Figure 4.16 shows that as r_s increases, the strength of the spanwise variation in mean velocity (left column) and turbulence intensity (right column) diminishes. However, the overall extent of the region of the spanwise variation seems to be relatively constant. Furthermore, the boundary layer thickness variation over the converging-diverging regions δ_r for all r_s cases only changes slightly when compared to the other parametric studies.

Figure 4.17 shows the change in the maximum spanwise variation for mean velocity and turbulence intensity as a function of r_s. The figure shows that the perturbation strength of the converging-diverging riblet type surface roughness diminishes with the increase of r_s. Interestingly however, even at $r_s = 2$ m, which corresponds to $\delta_{sa} \approx 24$ or $\delta_s \approx 30$ (see table 3.1), the roughness is still able to generate considerable spanwise variation in both mean velocity and turbulence intensity.

Cross-wire

Figure 4.18 (a and b) shows cross-wire results with $r_s = 0.5$ m (Case B5), (c and d) for $r_s = 1.5$ m (Case B7), and (e and f) with $r_s = 2$ m (Case B8). The measurements were performed at $U_\infty = 15$ m/s, while other important parameters such as yaw angle and fetch distance are kept constant with $\alpha = 20°$ and $F_x = 3$ m respectively. The maximum counter-rotating vortex strength (magnitude of maximum spanwise and wall-normal induced component value) for cases B5, B7 and B8 are found to be $\approx 1.9\%, 1.6\%$ and 1.4% of U_∞ respectively. From these values it is clear that as r_s increases, the strength of the large-scale counter-rotating vortices are diminishes, albeit at a relatively slow rate. Closer inspection of the vector plot shows that the rotation radius of each of the counter-rotating vortices barely changes as r_s increases. This seems to be the reason for the relatively unchanged extent of the spanwise variation area even though the magnitude decreases.
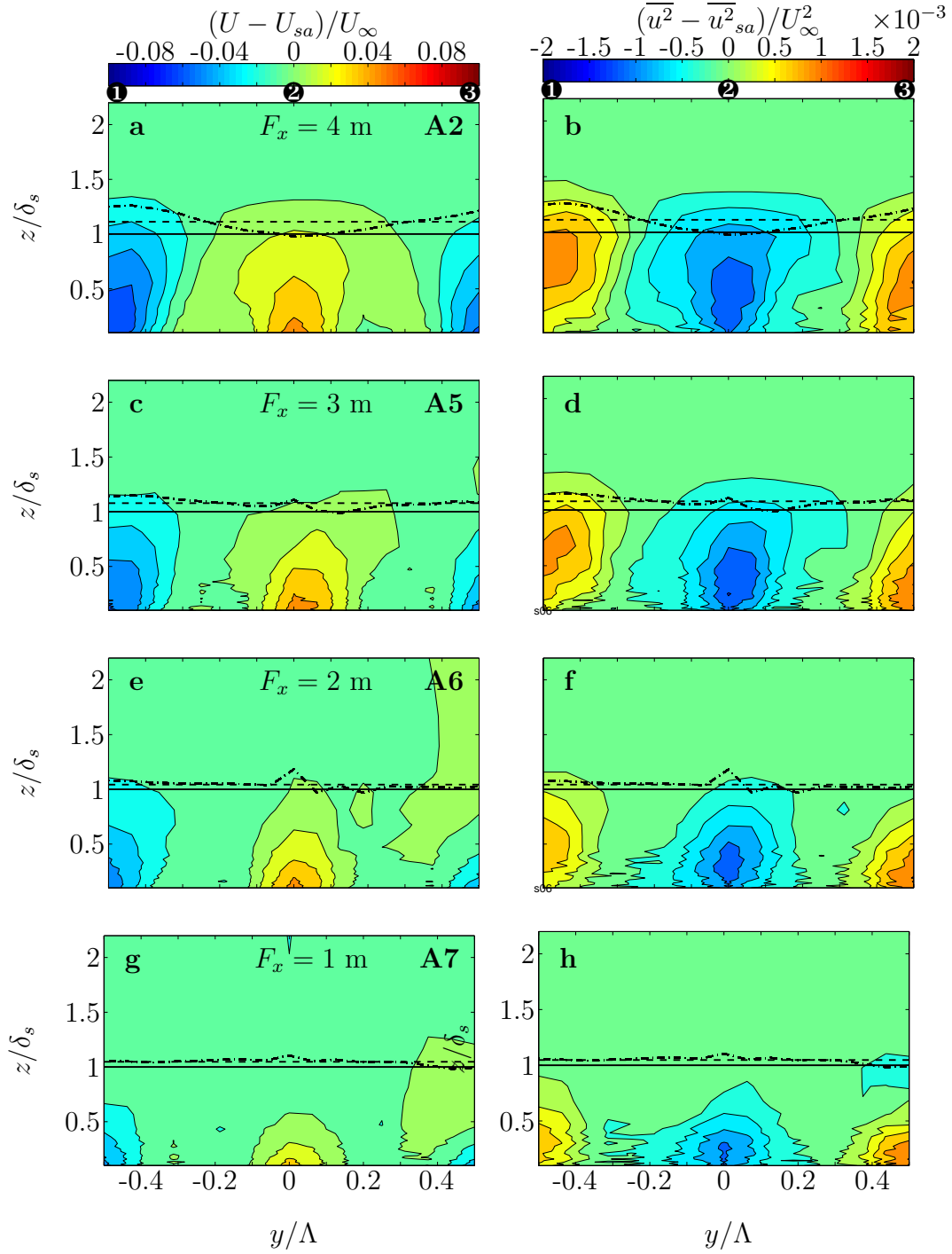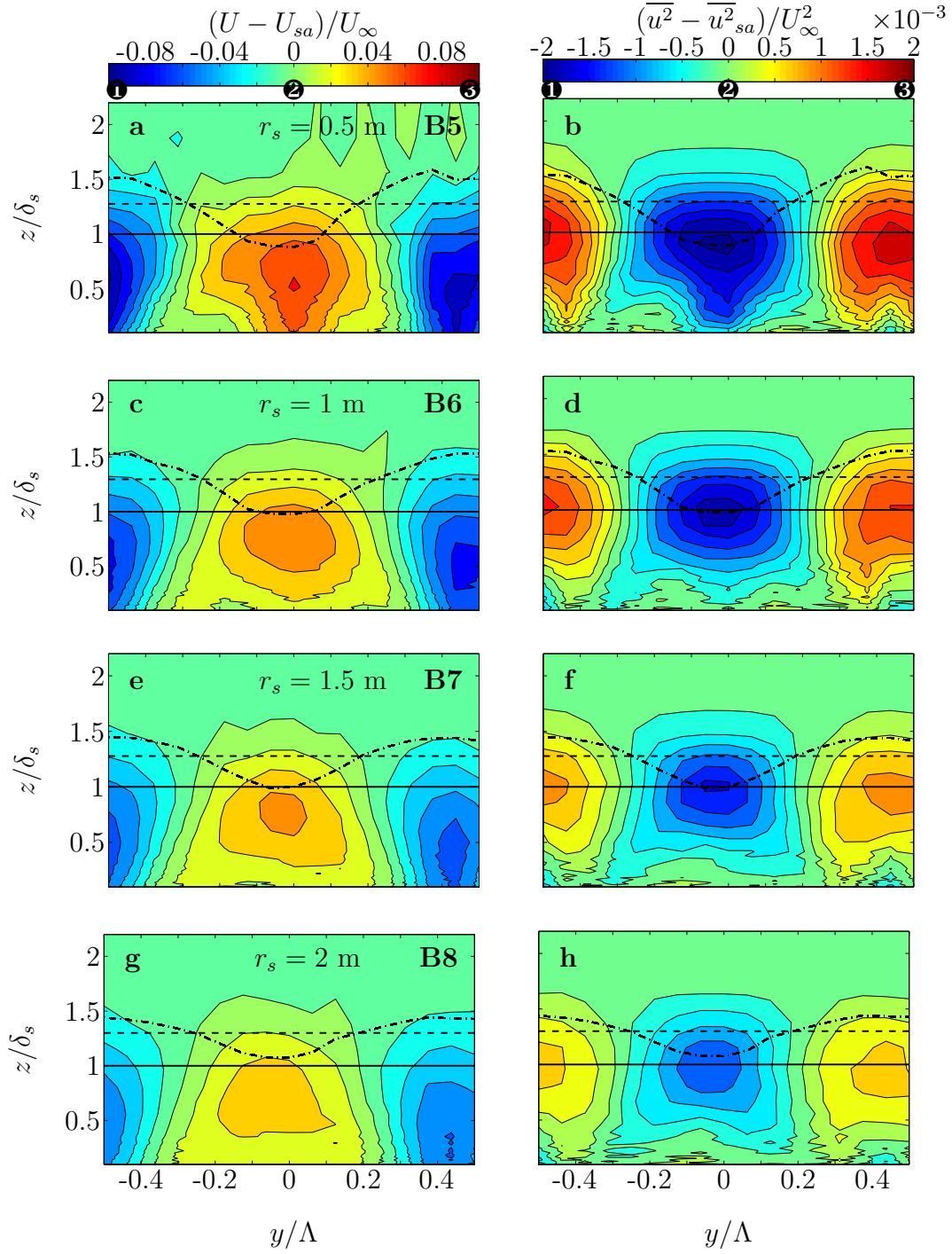
Figure 4.16: Spanwise variation for mean velocity (left-hand-side) and turbulence intensity (right-hand-side) about the spanwise averaged value for rough-wall cases B5-B8. (a and b) case B5, $r_s = 0.5$ m; (c and d) case B6, $r_s = 1$ m; (e and f) case B7, $r_s = 1.5$ m; (g and h) case B8, $r_s = 2$ m.
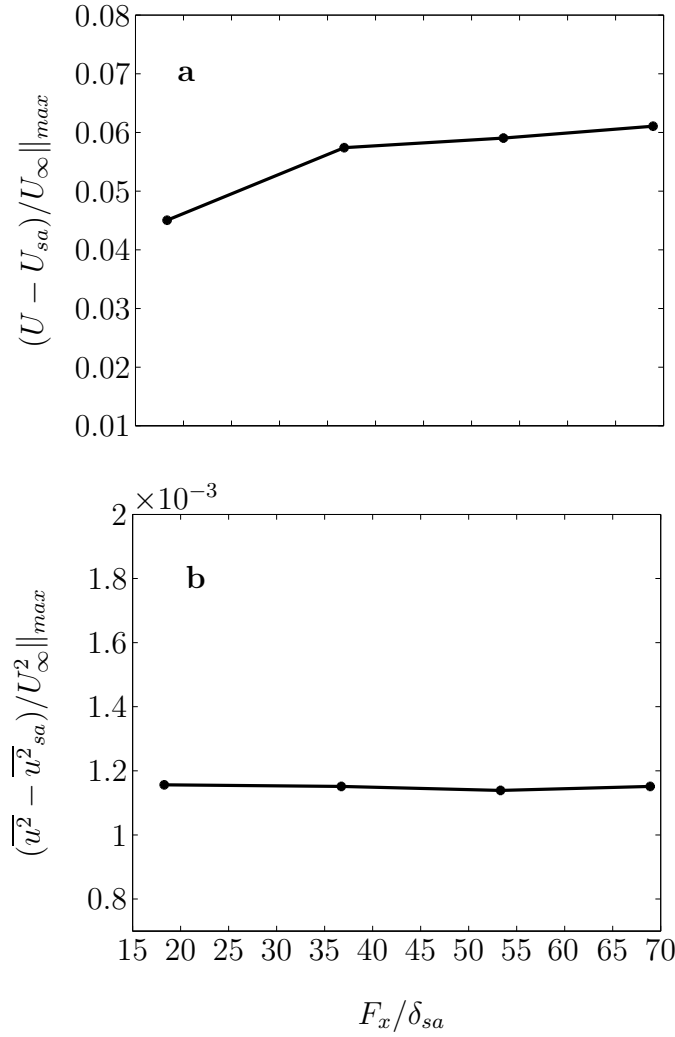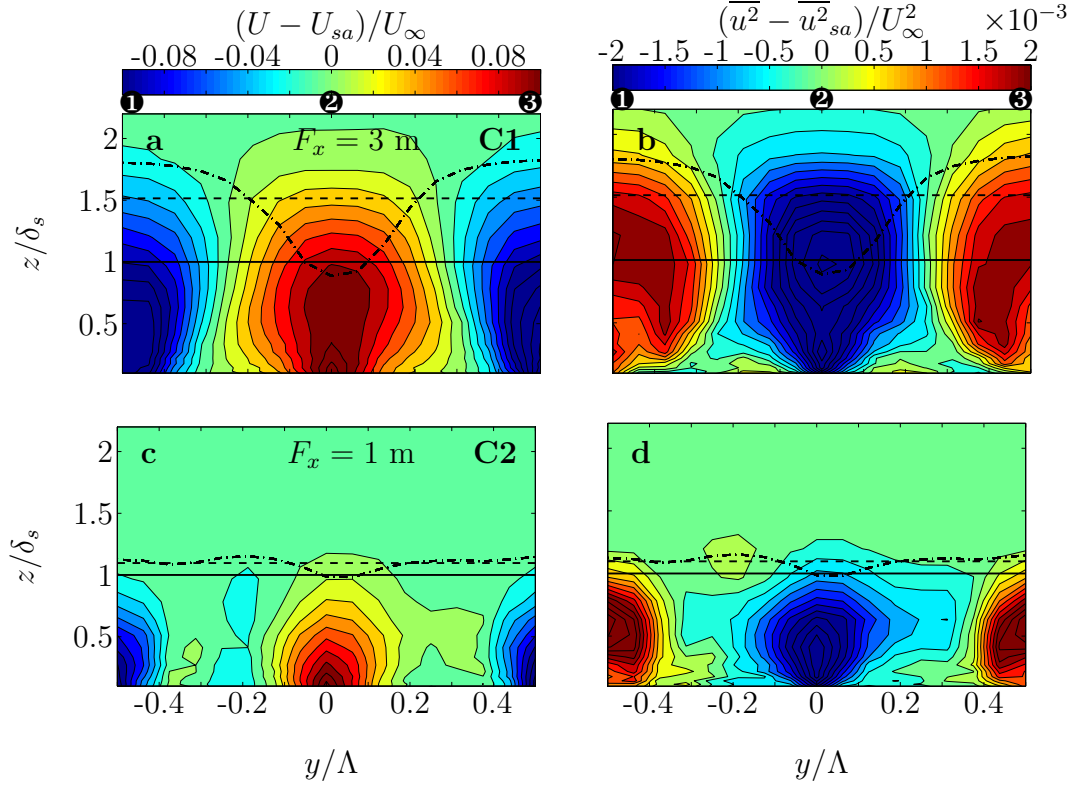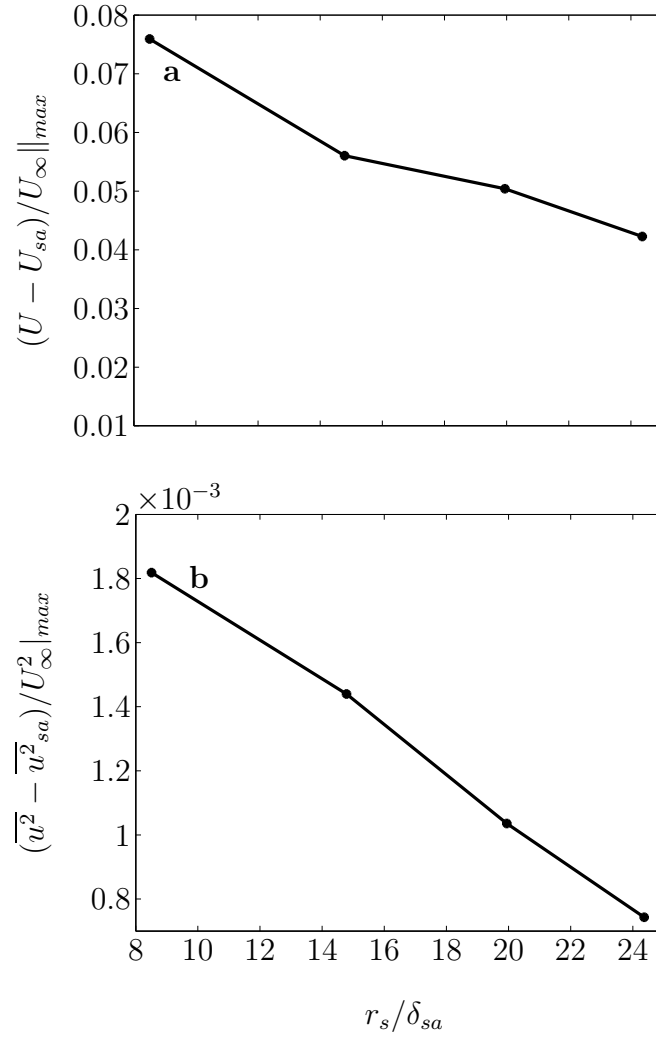
Figure 4.17: Maximum spanwise variation about the spanwise averaged value for (a) mean velocity and (b) turbulence intensity as a function of r_s/δ_{sa} for cases B5 - B8.

In order to see the change of the counter-rotating strength and size with r_s more clearly, figure 4.19 shows the vortices plot from case B5, B6 and B7. The plots reveal that as r_s increases the vorticity strength diminishes, however its size does not change significantly.

In summary, as r_s distance increases the strength of the counter-rotating vortices diminishes and the effect from smooth-wall starts to take over and dominate. The diminishing counter-rotating vortices strength causes the magnitude of the spanwise variation in the mean velocity and turbulence intensity to reduce. However, although the counter-rotating vortex strength

diminishes, its area size/dimension does not change much.
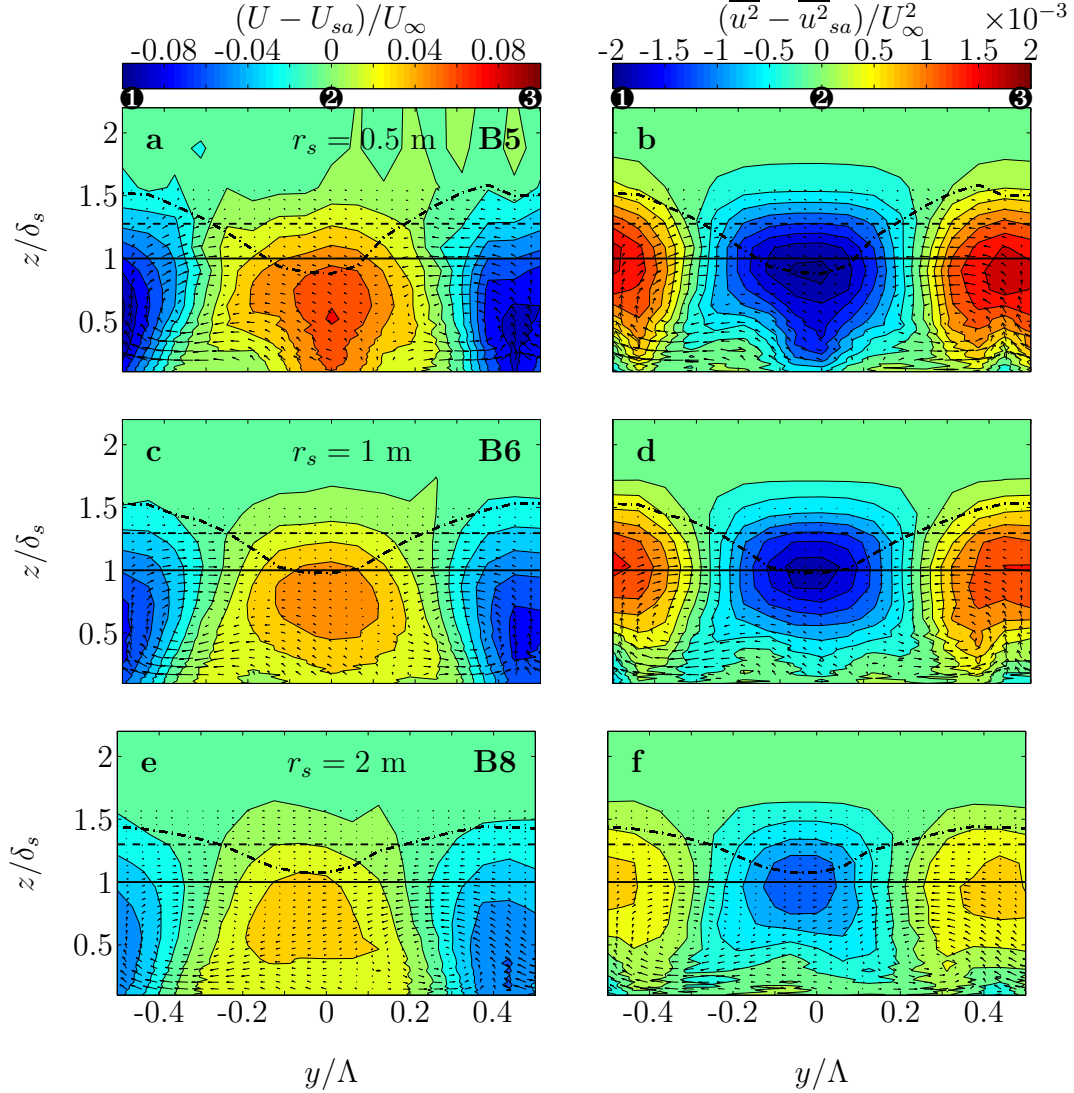
Figure 4.18: Spanwise variation and periodicity for mean velocity (left-hand-side) and turbulence intensity (right-hand-side) about the spanwise averaged value for rough-wall cases B5, B6 and B8. (a and b) case B5, $r_s = 0.5$ m; (c and d) case B6, $r_s = 1$ m; (e and f) case B8, $r_s = 2$ m.

The parametric study of the reversion from rough to smooth surface r_s in some respects is similar to the investigation by Antonia and Luxton (1972), where they explored the response of a turbulent boundary layer to a step change from rough to smooth surface $(R \rightarrow S)$. Similar to the flow over smooth to rough surface $(S \rightarrow R)$, the rough to smooth case also generates an internal layer with a certain thickness δ_i which grows over the streamwise distance x. Antonia and Luxton (1971) report that the internal layer for

the $R \to S$ case has a growth rate of $\delta_i \approx x^{0.43}$, while the $S \to R$ case has a slower growth rate of $\delta_i \approx x^{0.8}$. For this study however, we do not investigate the growth of internal layer over the converging and diverging riblet type surface roughness.
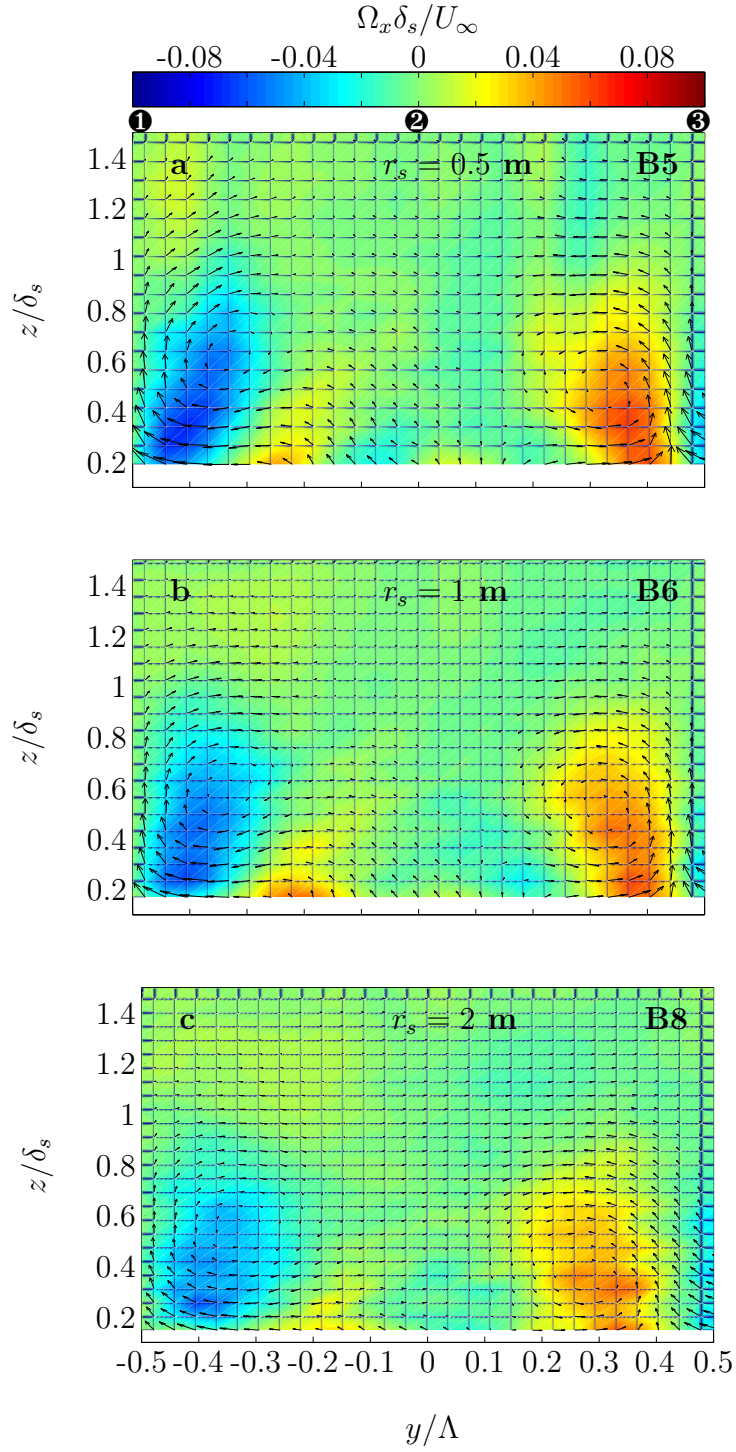
Figure 4.19: Streamwise vorticity for rough-wall cases B5, $r_s = 0.5$ m; B6, $r_s = 1$ m; and B8, $r_s = 2$ m

Furthermore, Antonia and Luxton (1972) have reported that even at a rel-

atively long distance $\approx 16\delta$ downstream of the step change from $R \to S$, the flow has not attained self-preservation (unlike the $S \to R$ case that reaches self preservation after $\approx 20\delta$). Antonia and Luxton (1972) hypothesised that the reason for the relatively long 'memory' in the rough surface boundary layer is that the majority of the turbulent energy resides in the large-scale turbulence in the outer layer region instead of the small-scale turbulence closer to the wall. Our experimental results show that even at $30\delta_s$ downstream of the rough surface (the limit of our working section), the flows are still unable to reach self preservation and the large-scale counter-rotating vortices are still exist. We believe the flow will eventually become self preserving, however it may take a relatively long time.

The relatively long decay time over the smooth-wall for the counter-rotating vortices could be an attractive engineering application for practising engineers (such as for vortex generator in an aircraft). For economic reasons the counter-rotating vortices can be applied on the appropriate region without covering the entire surface of interest. For example, on the certain locations of the upper surface of an aircraft to influence separation, or the forward section of the hull of a ship.

4.2 Summary

This section summarises the parametric study from four different parameters, namely : converging - diverging riblet yaw angle α, viscous-scaled riblet height h^+, streamwise fetch F_x, and relaxation distance r_s.

Exp code	U_∞ (m/s)	x (m)	F_x (m)	α (°)	r_s (m)	h_{sa}^+	$\frac{(U-U_{sa})}{U_\infty}\|_{max}$	$\frac{(\bar{u}^2-\bar{u}_{sa}^2)}{U_\infty^2}\|_{max}$	$\Delta\delta_r\|_{max}$ (%)	$\frac{V}{U_\infty}\|_{max}$ (%)	$\frac{W}{U_\infty}\|_{max}$ (%)	O (%)	wire
C1	15	3	3	30	-	21	0.164	3.4×10^{-3}	51.39	-	-	-	single
B4	15	3	3	20	-	22	0.103	1.7×10^{-3}	43.88	-	-	-	single
B2	15	4	4	20	-	20	0.088	1.4×10^{-3}	38.26	1.12	1.76	2.09	cross
A2	15	4	4	10	-	20	0.061	1.2×10^{-3}	22.57	1.10	1.23	1.65	cross

Table 4.4: Summary for various yaw angle α

Exp code	U_∞ (m/s)	x (m)	F_x (m)	α (°)	r_s (m)	h_{sa}^+	$\frac{(U-U_{sa})}{U_\infty}\|_{max}$	$\frac{(\bar{u}^2-\bar{u}_{sa}^2)}{U_\infty^2}\|_{max}$	$\Delta\delta_r\|_{max}$ (%)	$\frac{V}{U_\infty}\|_{max}$ (%)	$\frac{W}{U_\infty}\|_{max}$ (%)	O (%)	wire
A1	20	4	4	10	-	28	0.073	1.5×10^{-3}	28.79	-	-	-	single
A2	15	4	4	10	-	20	0.061	1.2×10^{-3}	22.57	-	-	-	single
A3	10	4	4	10	-	14	0.036	9.5×10^{-4}	10	-	-	-	single
A4	5	4	4	10	-	7	0.016	7.3×10^{-4}	3.79	-	-	-	single
B1	20	4	4	20	-	n/a	0.076	3.4×10^{-3}	39.06	1.61	2.15	2.69	cross
B2	15	4	4	20	-	20	0.088	1.4×10^{-3}	38.26	1.12	1.76	2.09	cross

Table 4.5: Summary for various viscous scaled height h^+

Exp code	U_∞ (m/s)	x (m)	F_x (m)	α (°)	r_s (m)	h_{sa}^+	$\frac{(U-U_{sa})}{U_\infty}\|_{max}$	$\frac{(\bar{u}^2-\bar{u}_{sa}^2)}{U_\infty^2}\|_{max}$	$\Delta\delta_r\|_{max}$ (%)	$\frac{V}{U_\infty}\|_{max}$ (%)	$\frac{W}{U_\infty}\|_{max}$ (%)	O (%)	wire
A2	15	4	4	10	-	20	0.061	1.2×10^{-3}	22.57	-	-	-	single
A5	15	4	3	10	-	20	0.059	1.1×10^{-3}	14.20	-	-	-	single
A6	15	4	2	10	-	20	0.057	1.2×10^{-3}	18.04	-	-	-	single
A7	15	4	1	10	-	20	0.045	1.2×10^{-3}	11.07	-	-	-	single
C1	15	3	3	30	-	21	0.164	3.4×10^{-3}	51.39	-	-	-	single
C2	15	3	1	30	-	22	0.151	3.1×10^{-3}	14.80	-	-	-	single
B2	15	4	4	20	-	20	0.088	1.4×10^{-3}	38.26	1.12	1.76	2.09	cross
B3	15	4	2	20	-	n/a	0.032	2.4×10^{-3}	13.35	0.58	1.32	1.44	cross

Table 4.6: Summary for various fetch F_x

Exp code	U_∞ (m/s)	x (m)	F_x (m)	α (°)	r_s (m)	h_{sa}^+	$\frac{(U-U_{sa})}{U_\infty}\|_{max}$	$\frac{(\bar{u}^2-\bar{u}_{sa}^2)}{U_\infty^2}\|_{max}$	$\Delta\delta_{r_s}\|_{max}$ (%)	$\frac{V}{U_\infty}\|_{max}$ (%)	$\frac{W}{U_\infty}\|_{max}$ (%)	O (%)	wire
B5	15	3.5	3	20	0.5	-	0.076	1.8×10^{-3}	57.70	-	-	-	single
B6	15	4	3	20	1	-	0.056	1.4×10^{-3}	36.23	-	-	-	single
B7	15	4.5	3	20	1.5	-	0.050	1.0×10^{-3}	31.84	-	-	-	single
B8	15	5	3	20	2	-	0.042	7.4×10^{-4}	25.48	-	-	-	single
B5	15	3.5	3	20	0.5	-	0.076	1.8×10^{-3}	57.70	1.11	1.58	1.9	cross
B6	15	4	3	20	1	-	0.056	1.4×10^{-3}	36.23	0.94	1.27	1.6	cross
B8	15	5	3	20	2	-	0.042	7.4×10^{-4}	25.48	0.94	1.01	1.4	cross

Table 4.7: Summary for various reversion from rough to smooth surface r_s

Chapter 5

Scaling and energy spectra

In the last decade, there has been considerable efforts dedicated to understand high Reynolds number scaling behaviour in turbulent flow (Marusic, 2009; Marusic et al., 2010a,c; Smits et al., 2011a; Smits and Marusic, 2013). According to Smits et al. (2011a), A high Reynolds number turbulent flow is defined by sufficient separation of scales. In wall bounded turbulent flow, there are three main length scales, namely the Kolmogorov scale η, viscous length scale ν/U_τ, and the boundary layer thickness δ. One area of particular interest is the scaling behaviour of the streamwise turbulence intensities $\bar{u}^2$. Many reports have shown that $\bar{u}^2$ depends on Reynolds number and exhibits an increase in the turbulence intensity peak at $z^+ = 15$ with increasing Re (Metzger and Klewicki, 2001; Hutchins and Marusic, 2007a,b; Marusic et al., 2010a). This peak is commonly termed the *inner-peak* and the location can be identified in the energy spectra as the *inner-site* (see figure 5.1).

The spectral analysis of high Reynolds number data have further revealed the existence of a secondary peak at the logarithmic region, $z/\delta = 0.06$(Hutchins and Marusic, 2007a). Mathis et al. (2009a) later refined this location to be the midpoint of the logarithmic location $z^+ \approx \sqrt{15Re_\tau}$. This secondary peak is termed the *outer-peak* and the location can be referred to as the *outer-site*. Figure 5.1 shows the existence of outer pick at high Reynolds number.
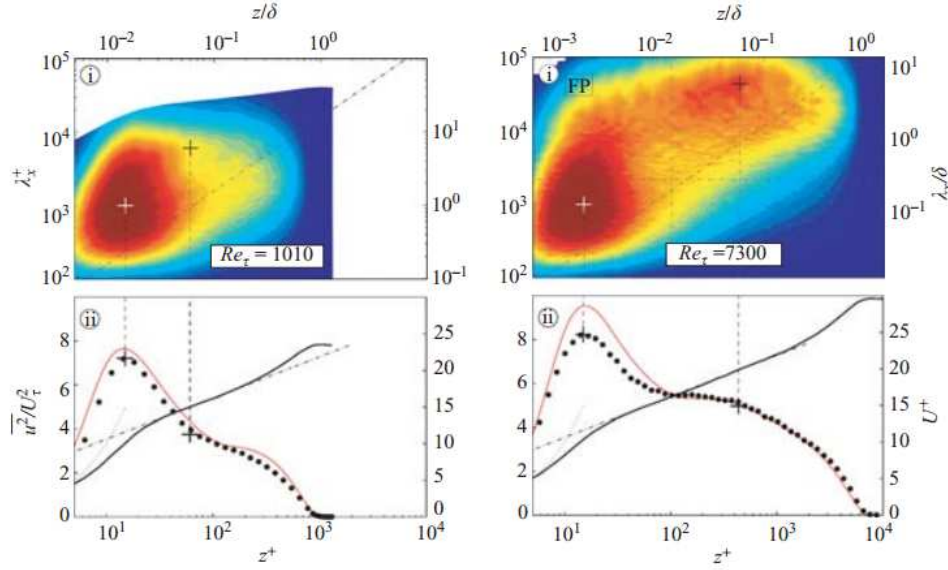
Figure 5.1: Contour maps showing variation of one-dimensional pre-multiplied energy spectra with wall-normal distance for two different Reynolds numbers. The inner peak location is marked by white + sign and the outer peak by black + sign (Hutchins and Marusic, 2007a)

.

		U_∞ (m/s)			δ_s (m)	U_{τ_s} (m/s)	Re_{τ_s}
smooth (S2)		15	-	-	0.052	0.547	1828
		U_∞ (m/s)	h_r^+	s_r^+	δ_r (m)	U_{τ_r} (m/s)	Re_{τ_r}
div(B2)	❷	15	16	22	0.051	0.479	1631
con(B2)	❶❸	15	23	31	0.082	0.680	3698

Table 5.1: Experimental parameters for smooth, diverging, and converging surface for cases B2 and S2. The boundary layer thickness listed here for the rough surfaces is the local thickness at that particular spanwise location δ_r. The h^+ and Re_τ shown here for the rough-wall are based on the local values of friction velocity and boundary layer thickness (based on U_{τ_r} and δ_r).

In this chapter we discuss and compare the scaling results and energy spectra between the smooth-wall and the converging - diverging surface, with the aim of identifying potential large- and very large-scale events above the rough surface. To analyse the effect of the surface roughness on large- and very-large-scale structures, we look at the diverging and converging region

for case B2 and the corresponding smooth-wall case S2 (see table 5.1). Note that the subscript r (i.e U_{τ_r}, δ_r, and Re_{τ_r}) is used to indicate a local value over the riblets at a particular spanwise location (i.e wall-normal measurement over the converging or over the diverging position), while the subscript s (i.e. δ_s, U_{τ_s}, and Re_{τ_s}) refers to the smooth-wall case

5.1   Finding skin-friction velocity U_τ

This section discusses methods of estimating skin-friction velocity U_τ by analysing data from a single-normal hot-wire over the converging and diverging regions and their corresponding smooth-wall. Before explaining these methods, it is important to understand the importance of finding U_τ, particularly for scaling in turbulent boundary layer.

In the study of turbulent boundary layers, it is desirable to present data (such as length and velocity) in a non-dimensionalised manner. This method also serves as a scaling technique, which has been a subject of intense study since the time of Ludwig Prandtl. There are two common scales used to describe the turbulent boundary layer, namely inner-scaling and outer-scaling. Inner scaling is used to explain flow close to the wall (inner layer) where viscosity dominates. Here the proper scaling is skin-friction velocity U_τ to normalise velocity, and the viscous length scale ν/U_τ to non-dimensionalise length. Away from the wall (outer layer) inertia dominates, and an outer-scaling is used, based on boundary layer thickness δ to non-dimensionalise length, and freestream velocity U_∞ to normalise velocity. The boundary layer thickness δ is obtained based on the wall-normal location where the velocity recovers 98% of the freestream velocity U_∞ (i.e $U/U_\delta = 0.98$).

One of the most important principle of boundary layer study is the idea that, for any turbulence statistics measured at different facilities and Reynolds number, they will collapse to a single universal profile when non-dimensionalised with the correct length and velocity scales (Buschmann and Gad-el Hak, 2003). This universal profile is also known as the mean velocity profile, plotted in the semi-logarithmic manner. The universal logarithmic (log) profiles allow fluid dynamicists to describe the overlap region between the inner and outer layers of the streamwise mean velocity.

Obtaining skin-friction velocity for inner-scaling is difficult, particularly in the developing turbulent boundary layer. According to Smits et al. (2011a), for pipe and channel flows, the skin-friction velocity can be obtained with relatively good accuracy from the pressure drop (around $< 1\%$ of U_τ), however in turbulent boundary layer it is more challenging. In the experimental investigation of the turbulent boundary layer, there are two general methods to determine U_τ value. The first is through obtaining wall-shear stress τ_w with direct measurements such as drag balance (Bechert et al., 1992; Hall and Joseph, 2000), micro-pillar (Großbe and Schröder, 2008; Gnanamanickam et al., 2013) and Oil Film Interferometer (OFI) (Fernholz et al., 1996; Chauhan et al., 2010). The second is an indirect method through fitting mean velocity profiles from hot-wires (Perry and Morrison, 1971; Perry, 1982; Comte-Bellot, 1976; Bruun, 1995), Pitot tubes(Barker, 1922), Preston tube (Head and Rechenberg, 1962), Particle Image Velocimetry (PIV) (Liu et al., 1991; Adrian, 2005a) or Laser Doppler Velocimetry (LDV) (Adrian and Yao, 1987). Typically, the profile is fitted to a log law or power law to obtain an estimate of U_τ. For summaries and reviews of skin-friction measurements see Winter (1977); Perry (1982); Goldstein (1983); Gad-el Hak (1989); Bruun (1995); Fernholz et al. (1996); Raffel et al. (1998); Naughton and Sheplak (2002); Adrian (2005b, 2010). Discrepancies between direct and indirect methods may occur due to the uncertainties and inherited error from different measurement techniques. Onsrud et al. (1987) shows that two measurement techniques in the same facility can produce a different value of U_τ

Due to the nature of the current study, where the velocity profile is measured with a hot-wire above a rough surface, an indirect measurement technique is used to estimate U_τ. There have been considerable debates concerning the use of classical log-law and the alternative power-law to describe the mean velocity profile and U_τ.The debate between these two techniques is already well documented by Buschmann and Gad-el Hak (2003), and will not be discussed in this report. Further reading regarding the universality of the log-law of the wall and its associated theory (Townsend's attached eddy hypothesis) can be seen in the seminal work of Townsend (1961); Perry and Chong (1982); Marusic et al. (2013); McKeon (2013).

To illustrate the method for obtaining skin-friction velocity over a rough and smooth-wall using the log-law, here we use data from the rough case B2 and the hydrodynamically smooth case S2. The data are from single-

normal hot-wire probe traversed normal to the wall with 50 logarithmically spaced measurement points between $0 < z \lesssim 2.5\delta$. The fluctuating hot-wire signals are sampled at 50 kHz for 150 seconds to ensure converged statistics ($\approx 43000\delta/U_\infty$). Details of the three individual measurements are given in table 5.1

5.1.1 Streamwise mean velocity profile

Equation 5.1 is the classical log-law for the smooth-wall while equation 5.2 is the velocity defect equation, where κ is the Kármán constant and A is the wall intercept. The Kármán constant and the wall intercept are universal constants, and their average values are obtained from experiments. The existence of universal constants have been discussed heavily in the literature since the beginning of the 20th century. A recent report by Marusic et al. (2013) illustrates the lack of consensus among scientists regarding the value of the constants. The κ value varies between 0.38 - 0.421 while A varies between 4.1 - 6.5 (see Coles (1956); Zagarola and Smits (1998); Österlund et al. (2003); George (2007); Nagib and Chauhan (2008)). We believe this is not the end of the discussion, and the work is continuing.

$$\frac{U}{U_\tau} = \frac{1}{\kappa}ln\left(\frac{zU_\tau}{\nu}\right) + A \tag{5.1}$$

$$\frac{U_\infty - U}{U_\tau} = -\frac{1}{\kappa}ln\left(\frac{z}{\delta}\right) + B \tag{5.2}$$

For this study, the smooth-wall skin-friction velocity is obtained using the Clauser technique (Clauser, 1954, 1956). The mean velocity profile is fitted to the logarithmic law with a constant $\kappa = 0.39$ and an intercept $A = 4.2$ (from Perry and Li (1990)). The resulting smooth-wall skin-friction velocity is then compared with the Coles-Fernholz relation (see Fernholz and Finley (1996); Monkewitz et al. (2007); Nagib et al. (2007)). Comparison between the two methods shows good agreement, with the estimated U_τ values agreeing to within $\approx 1\%$.

Determining skin-friction velocity over a rough-wall environment is more challenging and uncertain. According to Clauser (1956) the velocity profile

needs to corelatable in U/U_τ, zU_τ/ν, and eU_τ/ν, where e is the *'roughness offset'*. In such a scenario, the effect of the roughness is to shift the intercept A as a function of eU_τ/ν. A downward shift in the mean velocity profile represents an increase in turbulent skin-friction, while an upward shift shows a decrease in turbulent skin-friction. The vertical shift of the logarithmic curve that is caused by the roughness can be defined as *'roughness function'* $\Delta U/U_\tau$. The addition of e and $\Delta U/U_\tau$ in the log-law (equation 5.1) results in a modified log-law :

$$\frac{U}{U_\tau} = \frac{1}{\kappa} \log \frac{(z+e)U_\tau}{\nu} + A - \frac{\Delta U}{U_\tau}. \qquad (5.3)$$

By fitting the measured mean velocity profile between the assumed range $100 < (z+e)U_\tau/\nu < 0.15Re_\tau$) to a modified log-law (equation 5.3), one could estimate the skin-friction velocity over a rough-wall (U_{τ_r}). This method is commonly termed as a modified Clauser technique.
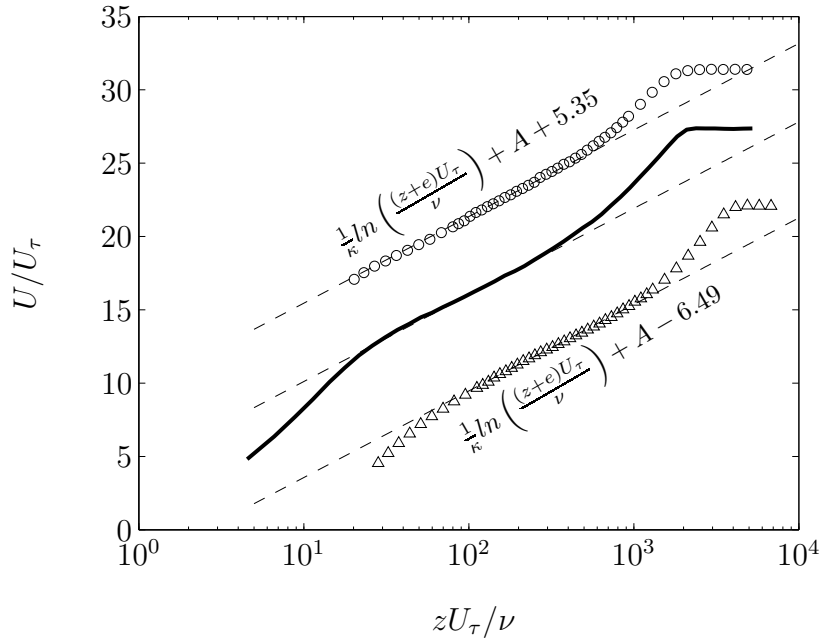
Figure 5.2: Mean velocity profile normalised with an inner-scale for cases B2 and S2. Symbols represent the rough surface data ($\circ$) for the diverging region and (Δ) for the converging region. The solid line shows the smooth-wall case at similar freestream velocity and downstream location.

The challenge in using this method to determine U_{τ_r} is that we have to deal with two extra free parameters (e and ΔU). Studies by Bechert et al. (1985); Choi (1989) show that the roughness offset e can be assumed based on the shape of the riblet geometry, i.e. $0.25h$ for triangular and $0.37h$ for scalloped riblets. Throughout this analysis $e = 0.25h$ is used because the riblet cross section closely resembles the triangular shape.

Figure 5.2 illustrates the application of the modified Clauser methods to obtain skin-friction velocity over the converging-diverging surface. It shows a pronounced upward shift over the diverging region (negative $\Delta U/U_\tau$), indicating a decrease in skin-friction drag. Over the converging region however, the downward shift (positive $\Delta U/U_\tau$) suggests an increase in wall-drag. Such a high negative roughness function is surprising. Previous observations show values over conventional riblets give a much smaller value ($\Delta U/U_\tau \approx -1$) (see Choi (1989)).
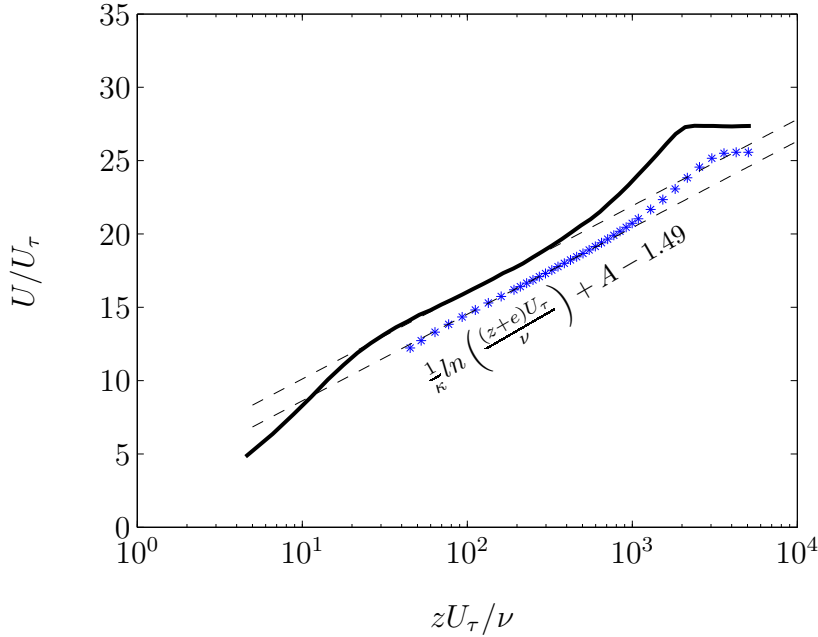
Figure 5.3: Spanwise averaged mean velocity profile normalized with inner-scale for case B2 and S2. Symbols represent the rough surface data ($*$). Solid line shows the smooth-wall case at similar conditions.

For the current study It is also desirable to obtain an average value of U_τ across the full spanwise wavelength Λ (see figure 5.3). It allows us to determine the net effect of the surface. This value is obtained by averaging the entire 21 mean velocity profile across the span (from the two dimen-

sional measurements), and then fitting the single averaged profile using the modified Clauser Method. The resulting spanwise averaged skin-friction velocity is denoted by $U_{\tau_{sa}}$. Spanwise averaged skin-friction velocity can also be calculated by obtaining U_τ for each of the 21 profiles across one whole spanwise length and then integrating these values. For all of the rough-wall cases in the parametric study section, unless otherwise stated, the U_τ value is obtained by spanwise averaged and termed $U_{\tau_{sa}}$.

5.2 Mean velocity
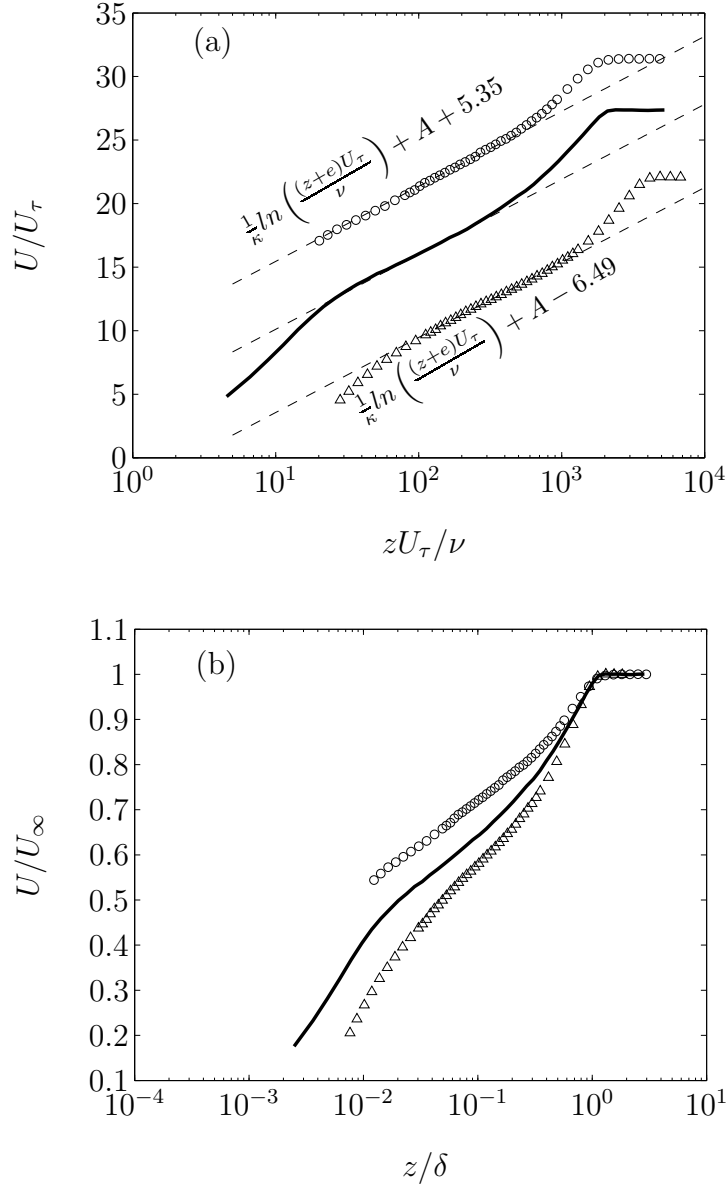
Figure 5.4: Mean velocity profiless for case B2 and S2 normalized with inner-scale (a) and with outer scale (b). Symbols represent the rough surface data (∘) for the diverging region and (Δ) for the converging region. Solid line shows the smooth-wall case at similar free-stream velocity and downstream location.

Firstly, let us return to the classical log-law where it is assumed that there is an overlap region between an inner and outer scale. This assumption

leads to a wide range of possibilities on where the log region starts and ends
(see for example, Smits et al. (2011a)). For this analysis, we have elected
to use the relatively classic limits of $100 < (z + e)U_\tau/\nu < 0.15Re_\tau)$ as the
approximate location of the logarithmic region. We use modified Clauser
chart to determine the skin-friction velocity U_τ. The ramification of using
Clauser chart has been discussed in the previous chapter. Figure 5.4(a)
shows the mean inner-scaled velocity profile. Above the diverging region
there is a clear vertical upward shift, indicating a decrease in skin-friction
drag. Over the diverging region, the vertical downward shift suggests an
increase in wall-drag.

Figure 5.4(b) shows the mean velocity profile normalised with the outer
scale. The local velocities are normalised with free-stream velocity U_∞ and
the wall-normal distance is non-dimensionalised with the local boundary
layer thickness. The plot reveals that the local mean velocity above the
diverging region is higher everywhere than the smooth-wall case, while the
local mean velocity above the converging region is lower. Since U_∞ is the
same for all three sets of data, it enables us to observe the differences in
local mean velocity directly. Although the log-law form of the mean velocity
profile reveals changes in wall-drag, it is not possible to infer variations in
the turbulence and coherent structures from such plots, hence a higher order
statistical analysis is necessary.

5.3   Turbulence intensity

It was mentioned earlier that the effect of higher Reynolds number is an
increase in the streamwise turbulence intensity magnitude in both the inner
and outer-site. In our case, for the three surface types, smooth, converging,
and diverging surface, we attain three different Re_τ values (despite being
measured at similar free-stream velocity and downstream location). The
differences in Re_τ are due to the large-scale periodicities that are induced by
the converging-diverging surface roughness (which induce variations in local
δ and U_τ). Hence, direct comparison in streamwise turbulence intensities is
difficult.

Figure 5.5(a) shows the inner-scaled streamwise turbulence intensity profile
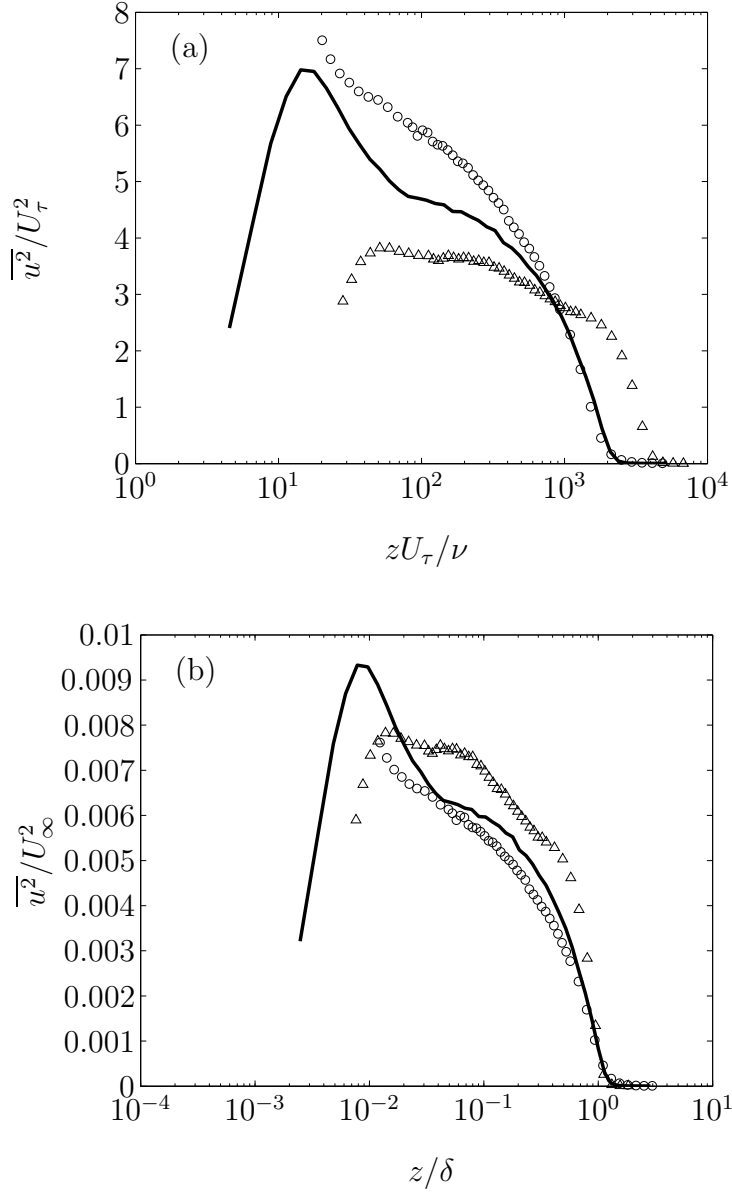
Figure 5.5: Turbulence intensity profiles for case B2 and S2 normalized with inner-scale (a) and outer-scale (b). Symbols represent the rough surface data (∘) for the diverging region and (Δ) for the converging region. Solid line shows the smooth-wall case at similar free-stream velocity and downstream location.

of the smooth-wall, and the converging and diverging region about the rough surface. The turbulence intensity $\overline{u^2}$ is normalised with skin-friction velocity U_τ and the wall normal distance z is made non-dimensional with ν/U_τ. For the smooth-wall case there is a clear peak in the inner site at $z^+ = 15$, sig-

nalling the highly energetic near-wall cycle of streaks and quasi streamwise vortices (Kline et al., 1967). The viscous scaled turbulence intensity over the diverging region is higher than the smooth-wall case between the sublayer region up to $z^+ \approx 825$, where the profile collapses onto the smooth-wall profile. The measurement over the diverging region were performed slightly further from the surface than the corresponding smooth-wall case to prevent the hot-wire from hitting the riblet's peak. Unfortunately, this resulted in an unresolved inner-peak. However, if such peak does exist, the figure indicates that it has been shifted closer to the surface over the converging region, we encounter the opposite, the turbulence intensity is lower than the smooth-wall case between the sublayer region up to $z^+ \approx 825$. Beyond the wall normal distance of $z^+ \approx 825$, the turbulence intensity over the converging region is higher than the smooth-wall and diverging case (which collapses onto the smooth-wall case at the wake region). The peak in the inner-site for the converging region seems to shift further from the wall. It is clear that the behaviour of the turbulence intensity for the converging and diverging riblet surface is very different than canonical turbulent boundary layer flow.

Figure 5.5(b) shows the outer-scaled streamwise turbulence intensity profiles for the three surface cases. The turbulence intensity $\overline{u^2}$ is normalised with free-stream velocity U_∞ and the wall-normal distance is normalised with boundary layer thickness δ. The outer-scaled turbulence intensities show that over the diverging region, the turbulence intensity is lower everywhere compared to the smooth-wall case. On the other hand, over the converging region, the turbulence intensity is higher than the smooth-wall case for the majority of the boundary layer,.

From figure 5.5 (a and b) one would realise that different scaling results in a quite different interpretation of turbulent intensity profiles, particularly for the converging and diverging surface. If we look at the turbulence intensity profile for the diverging region (○) and scaled it with inner-scaling (figure 5.5 (a)), it has higher magnitude for the majority of the layer than the smooth-wall reference case. However when it is scaled with the outer layer (figure 5.5 (b)), it has lower magnitude for the majority of the layer than the smooth-wall reference case. Similar changes in magnitude also occur with the turbulence intensity over the converging region when it is scaled with the inner and outer scale. Clearly this is because U_τ also changes across the spanwise location of the converging and diverging surface.

If we return to the cross wire results on previous chapter, one can see that over the converging region, the flow near the wall is being forced to converge and move vertically away from the wall. This vertically upward motion/common-flow-up transports the relatively slow and highly turbulent near-wall fluid towards the outer region. Over the diverging region the near-wall flow is being forced to move away from each other and thus, by continuity allowing the flow from the outer region to move towards the wall. The vertically downward motion/common-flow-down transport the relatively fast and low turbulent outer flow to move towards the wall. Between both figures 5.5 (a and b), we can see that figure 5.5 (b) more clearly illustrates this hypothesis, hence it appears that the scaling of turbulence intensity with the outer layer is the more logical option.

Based on the results from figures 5.4(a and b) and 5.5(a and b) it seems that the converging and diverging surface has not only changed the friction velocity, but also significantly altered the turbulence structure within the boundary layer.

5.4 Outer layer similarity

So far, from the mean velocity and turbulence intensity profiles, we have observed that the converging and diverging surface generates large-scale counter rotating vortices that radically alter the skin-friction velocity and turbulent boundary layer structure of wall-bounded turbulence. However, the inner- and outer-scaled mean velocity and turbulence intensity profiles have neither provided us with sufficient evidence of proper scaling, nor predictions of the large- and very large-scale motions. Before moving further, it is in our interest to see whether the positive and negative roughness characteristics exhibited by the converging and diverging regions affect the outer layer similarity hypothesis of Townsend (1956, 1976) .

The main argument of Townsend's hypothesis is that *'whatever the wall conditions, provided that their influence on the central flow is limited to a transfer of stress from the wall, the relative motion in the fully turbulent region depends only on the wall stresses and on the (layer) width'*. In the context of converging and diverging surface, the proviso from Townsend
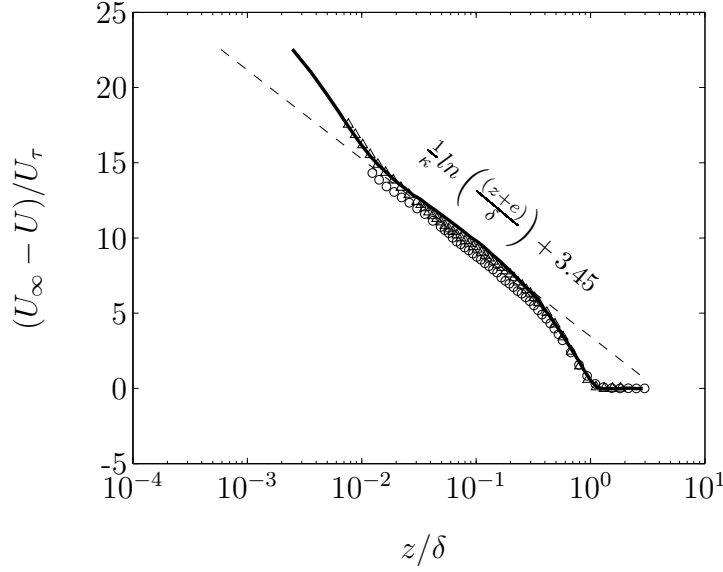
Figure 5.6: Streamwise velocity defect profiles for cases B2 and S2 where the variance is normalised with friction velocity and the wall normal distance is non-dimensionalised with boundary layer thickness. Symbols represent the rough surface data ($\circ$) for the diverging region and (Δ) for the converging region. Solid line shows the smooth-wall case at similar free-stream velocity and downstream location.

does not hold. The converging and diverging surface produce large-scale secondary flow that penetrate the entire layer. Their influence on the central flow is not limited to transfer of stress from the wall, and therefore violate the central proviso of Townsend's outer layer similarity hypothesis. The aim of the following analysis is to see how far does the converging and diverging surface causes the flow to depart from Townsend's outer layer similarity hypothesis.

Townsend's outer layer similarity hypothesis can be observed through velocity-defect plots which can be described by equation 5.2. To account for the height uncertainty in the rough-wall case, the equation becomes:

$$\frac{U_\infty - U}{U_\tau} = -\frac{1}{\kappa} ln \left(\frac{z + e}{\delta} \right) + B \qquad (5.4)$$

where κ is the Kárman constant, B is the velocity defect constant, and e is the riblet height offset. Figure 5.6 shows the velocity defect profile for rough

case B2 (converging and diverging) and smooth-wall case S2. From the profile, we observe a remarkably good collapse. However, the rough surface data deviates slightly from the reference smooth-wall data, signalling some departure from the similarity hypothesis for this converging-diverging riblet-type roughness. However, in general when one considers the uncertainty in estimating U_τ it is difficult to draw concrete conclusions. Note that, here we do not wish to challenge Townsend's outer layer hypothesis, we just wish to investigate how this hypothesis stands-up with this very unusual surface, which we suspect can directlyy influence the outer flow, via large-scale secondary flow.
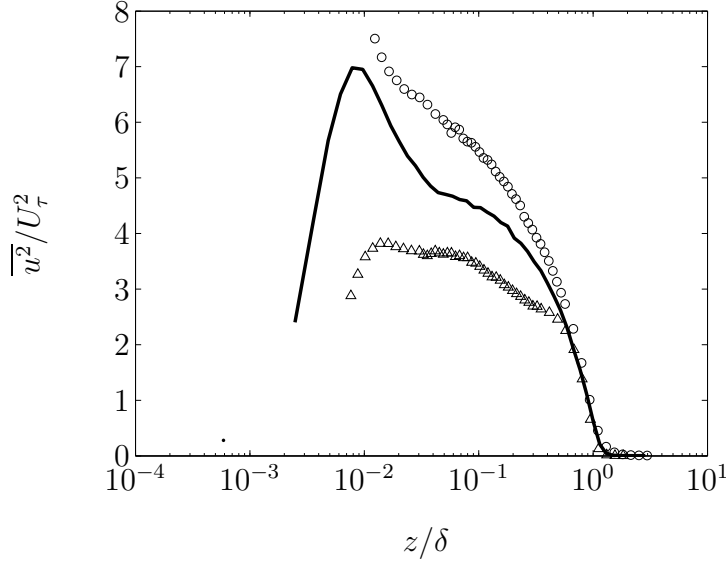
Figure 5.7: Turbulence intensity profile for cases B2 and S2 where the variance is normalised with friction velocity and the wall normal distance is non-dimensionalised with boundary layer thickness. Symbols represent the rough surface data (○) for the diverging region and (Δ) for the converging region. Solid line shows the smooth-wall case at similar free-stream velocity and downstream location.

Figure 5.7 shows the turbulence intensity for the smooth-wall, converging region and diverging region, all non-dimensionalised with friction velocity, whereas the wall-normal distance is normalised with boundary layer thickness of their corresponding surfaces. This type of scaling is also commonly used to investigate Townsend (1956, 1976) outer layer similarity hypothesis of rough surface (see for example Monty et al. (2011a)). From the figure, we can see that the three profiles collapse at $z/\delta > 0.7$, which is relatively far

from the logarithmic region. For comparison, Flack et al. (2005); Schultz and Flack (2005); Monty et al. (2011a) have reported an outer layer similarity from much lower wall-normal location (i.e. $z/\delta \approx 0.1$). Hence this higher order statistics also further strengthens the notion that the outer layer hypothesis does not hold over the converging-diverging surface roughness.

The failure in satisfying Townsend's proviso indicates that the surface roughness effect is clearly reaching the outer-layer. This could also suggest that the large-scale features (which scale with the outer scales δ) may play a dominant role within the modified turbulent boundary layer over the converging and diverging roughness.

5.5   Higher-order statistics

The mean velocity analysis have shown that the local mean velocity between the smooth-wall, converging region, and the diverging region are different. Here we are interested to analyse it further through the higher-order statistics by looking at the third and fourth order moments of the probability density function (PDF). The third order moment shows the skewness (asymmetry), while the fourth order moment describes the kurtosis (flatness) of the velocity signal. The skewness (S_u) is defined as,

$$S_u = \frac{\overline{u^3}}{\overline{u^2}^{3/2}} \tag{5.5}$$

where $u = \breve{u} - U$, u is fluctuation velocity, $\breve{u}$ is instantaneous velocity and U is mean velocity. Positive skewness/right-skewed shows that the right tail in PDF is longer and the velocity distribution is concentrated on the left. Negative skewness/left skewed is the opposite, where the left tail in PDF is longer and the velocity distribution is concentrated on the right (see Tennekes and Lumley (1972) for further examples). The flatness (F_u) is defined as,

$$F_u = \frac{\overline{u^4}}{\overline{u^2}^2} \tag{5.6}$$

it is a measure or representation of deviation from Gaussian distribution. A large kurtosis happens if the PDF has large tails value/sharp peaks while small kurtosis occurs if the PDF has small tails value/ shallow peaks (Tennekes and Lumley, 1972).

For illustration regarding skewness and kurtosis, figure 5.8 shows PDF of u/U_∞ for smooth-wall, converging region, and diverging region at $z/\delta = 0.1$. For the smooth-wall case, the PDF shows Gaussian characteristic, with the peak located at $u/U_\infty \approx 0$. The diverging region is slightly negatively skewed and has sharper shape, which translate to slightly larger kurtosis than that of the smooth-wall. The converging region is positive skewed and it is slightly less sharp than the smooth-wall case.
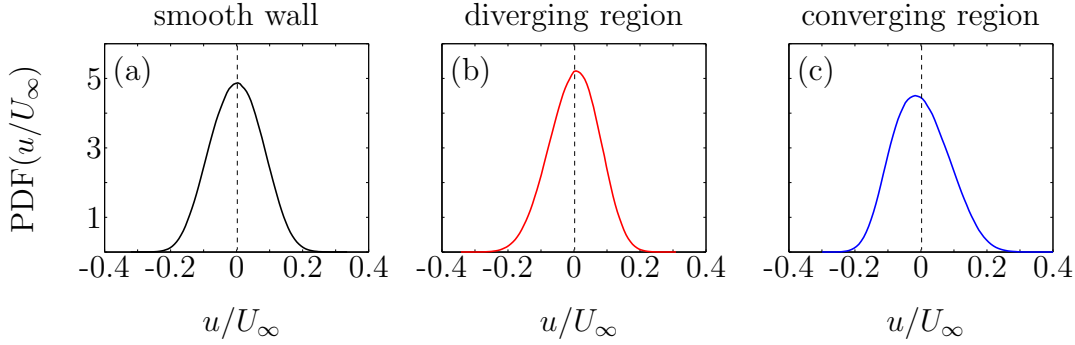
Figure 5.8: PDF of u/U_∞ for smooth-wall, converging region, and diverging region at $z/\delta = 0.1$

Figure 5.9(a) shows the skewness factors of the streamwise velocity component over the entire fluid flow layer for the smooth-wall (straight line), converging region (Δ), and diverging region ($\circ$). The wall normal distance is normalised with their respective boundary layer thickness δ. For all three cases, they exhibit a non Gaussian distribution, particularly in the near-wall and wake region. All three surface types exhibit a similar pattern at the edge of the boundary layer, the skewness plot shows that they have sharp negative skew and then change suddenly to positive. However, for the smooth-wall the skewness is $S_u \approx 0$ at the logarithmic region, which indicates a Gaussian characteristics. Over the converging region, the plot reveals that at the logarithmic region it is skewed positively. The positive
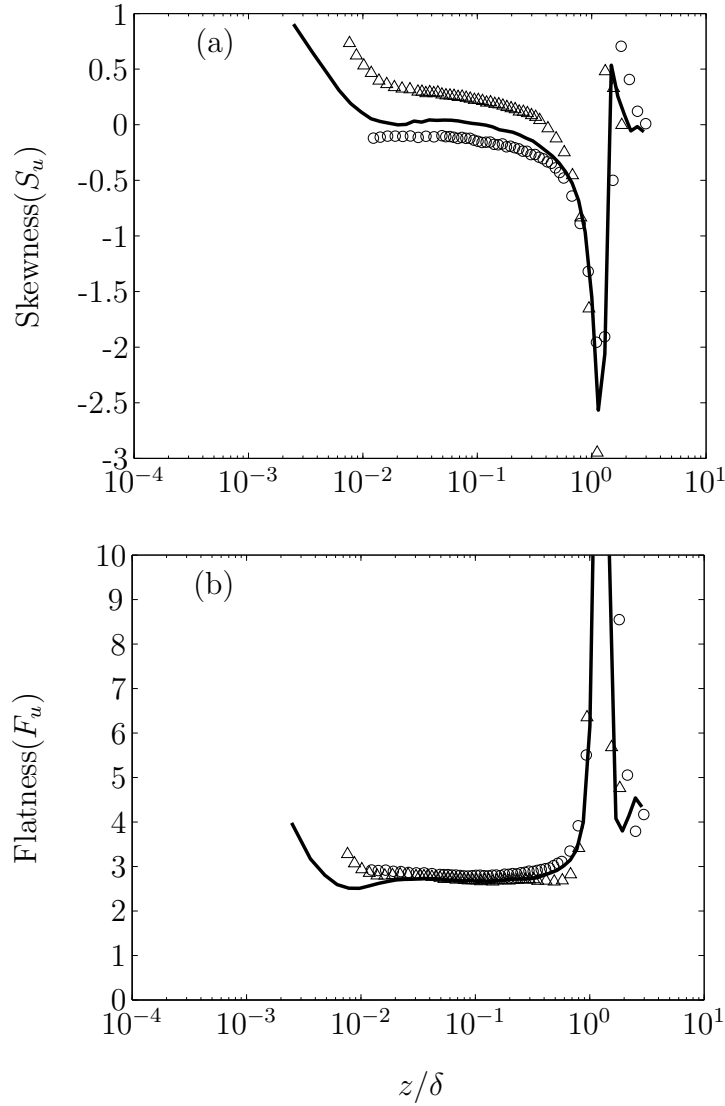
Figure 5.9: (a) Wall normal skewness (S_u) and (b) kurtosis K_u for cases B2 and S2. Symbols represent the rough surface data ($\circ$) for the diverging region and (Δ) for the converging region. Solid line shows the smooth-wall case at similar free-stream velocity and downstream location.

skew shows that the velocity distribution is concentrated on the left of PDF distribution, meaning that majority of the velocity fluctuations are low. The opposite behaviour is observed for the diverging region, it is skewed negatively. The negative skew reveals that majority of the velocity fluctuations are high.

Figure 5.9(b) shows the kurtosis factors streamwise velocity component for

all three cases. Similar with skewness, the plot shows a departure from the Gaussian characteristics in the near-wall and wake region. However, in the logarithmic region they are fairly constant at $F_u \approx 3$, which correspond to Gaussian behaviour. The kurtosis figure shows that at the edge of the boundary layer they have very sharp peak. The sharp changes at this particular location is associated with the intermittency of the turbulent and non turbulent interface.

5.6 Energy spectra

To study the importance of different scales of motion in the turbulent boundary layer, it is desirable to investigate their pre-multiplied streamwise energy spectra $k_x\phi_{uu}$, where k_x is the streamwise wave number and ϕ_{uu} is the spectral density of the streamwise velocity fluctuations. Here $k_x = 2\pi f/U$, where f is the frequency and U is local streamwise mean velocity. The velocity spectra are pre-multiplied so that the area under the curve of $k_x\phi_{uu}$ on the semilogarithmic plot is $\bar{u}^2$.

This section is divided into three subsections, the first subsection looks at the individual pre-multiplied energy spectra for the smooth-wall, converging region, and the diverging region located at the logarithmic region ($z^+ \approx$ 100). The second subsection analyses the pre-multiplied energy spectra at the outer region ($z/\delta \approx 0.1$ and 0.5). The third section discusses the energy spectragram for the entire boundary layer thickness for all three surfaces.

5.6.1 Logarithmic region

Figure 5.10 shows the pre-multiplied energy spectral plot at the log-region $z^+ \approx 100$ for the smooth-wall, converging region, and diverging region cases. Here the data is presented in terms of the streamwise length-scale λ_x, where $\lambda_x = 2\pi/k_x$. The left hand side (a) shows the energy spectra and wavelength scaled by inner scaling and the right hand side (b) is normalised with outer scaling. Here we show two types of scaling due to the uncertainty in turbulence intensity profile (see figure 5.5). We believe that normalisation with outer scale is the proper method in comparing the pre-multiplied energy

spectra (similar with turbulence intensity). However, for completion we plot both method to show how much they differ and to show the importance of proper scaling for flow over the converging and diverging riblets.

In figure 5.10(a) the energy is normalised with the local U_τ and the wavelength is normalised with ν/U_τ. At $z^+ \approx 100$ there is no particular collapse in the smaller scales ($\lambda_x^+ < 1000$), which shows the effect of the surface roughness. The energy for all three surfaces peak at $\lambda_x^+ \approx 1000-10000$, with the diverging region exhibits the most energetic, followed by the smooth-wall case, and finally the converging region. These peaks indicate that the most energetic u fluctuations are of this length scale. Beyond $\lambda^+ \approx 2 \times 10^4$ the energy spectra of smooth-wall and diverging region collapse on top of each other indicating that the diverging roughness does not influence the very large-scale structures at this wall-normal position. However, it is notable that at $z^+ \approx 100$, there is a reduced large-scale energy over the converging region.

Figure 5.10: Pre-multiplied energy spectra normalised with inner (a) and outer scales (b) for the smooth surface (black line), diverging region (red line), and converging region (blue line) in the log-region of $z^+ \approx 100$ from cases B2 and S2.

In figure 5.10(b) the energy is normalised with U_∞ and the wavelength is made non dimensional with their local boundary layer thickness δ. Note that when the wall normal distance $z^+ \approx 100$ is translated to outer scale, it is equal to $z/\delta \approx 0.051$ for smooth surface, $z/\delta \approx 0.061$ for diverging region, and $z/\delta \approx 0.030$ for converging region. Here the plot shows that over the smooth-wall and the diverging region the energy spectra magnitude is almost identical across the entire wavelength, which suggest that at this particular wall normal location ($z^+ \approx 100$) the diverging riblet does not

influence the flow. Over the converging region however, we can see that the magnitude is higher than the smooth-wall case and diverging region at $0.01 < \lambda_x/\delta < 3$ and peaked at $\lambda_x/\delta \approx 0.3 - 2$. At $\lambda_x/\delta > 3$, the energy spectra over the converging region is lower than the spectra over the smooth-wall and diverging region respectively.

5.6.2   Outer region

Figure 5.11(a and b) shows the pre-multiplied energy spectra at the wall normal location $z/\delta \approx 0.1$ for the smooth-wall, diverging case and converging case. Figure 5.11(a) shows the energy spectra normalised with the inner scaling. The spectra behave almost similar with the $z^+ \approx 100$ case, where there is no collapse for all three cases at the lower end of the wavelength ($\lambda_x^+ < 1000$), which translates to the effect of their respective surface. The converging region has weaker magnitude than the smooth-wall and the diverging region respectively for the entire wavelength. The diverging region has the highest magnitude and it is peaked at $\lambda_x \approx 10^4$. The energy spectra for the smooth-wall and diverging region collapse at $\lambda^+ > 2 \times 10000$.

Figure 5.11(b) indicates the energy spectra at $z/\delta \approx 0.1$ normalised with the outer scaling. The energy spectra trend at this location is almost similar with the case at $z^+ \approx 100$ (figure 5.10(b)). Here the smooth-wall and the diverging region case energy spectra behaves similarly for the entire wavelength. The converging region however, has higher magnitude between $0.01 < \lambda_x/\delta < 5$, and has a sharp peak at $\lambda_x/\delta \approx 1.5$. Beyond $\lambda_x/\delta = 5$, the converging region has lower magnitude than the smooth-wall and the diverging region.

Figure 5.12(a and b) shows the inner and outer scaling of pre-multiplied energy spectra for the smooth wall, converging region and diverging region at $z/\delta \approx 0.5$. For the inner scaling (figure 5.12(a)), at the lower end of the wavelength ($\lambda_x^+ < 1000$) there is no collapse for all three cases, and the diverging region has the highest magnitude peaked at $\lambda_x^+ \approx 5000$ (albeit weaker than at $z/\delta \approx 0.1$). Interestingly however, at $\lambda_x^+ > 20000$ the energy spectra for all three cases are collapse well, indicating that the roughness does not have considerable influence at this wall normal location.
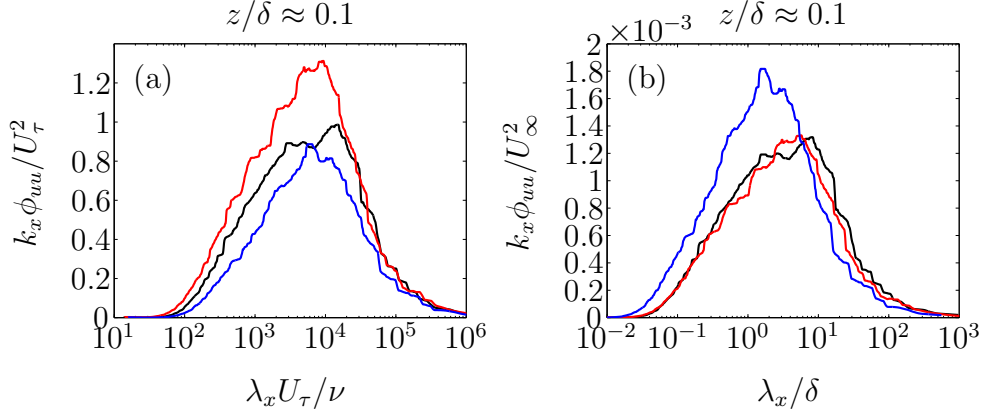
Figure 5.11: Pre-multiplied energy spectra normalised with inner (a) and outer scales (b) for the smooth surface (black line), diverging region (red line), and converging region (blue line) in the outer region of $z/\delta \approx 0.1$, from cases B2 and S2.

Figure 5.12(b) reveals the outer scaling for all there surface cases at $z/\delta \approx 0.5$. The plot shows that the energy spectra behave almost identical as the $z/\delta \approx 0.1$ case, with the converging region dominate the energy spectra magnitude at $0.01 < \lambda_x/\delta < 15$ and peaked at $\lambda_x/\delta \approx 3$.

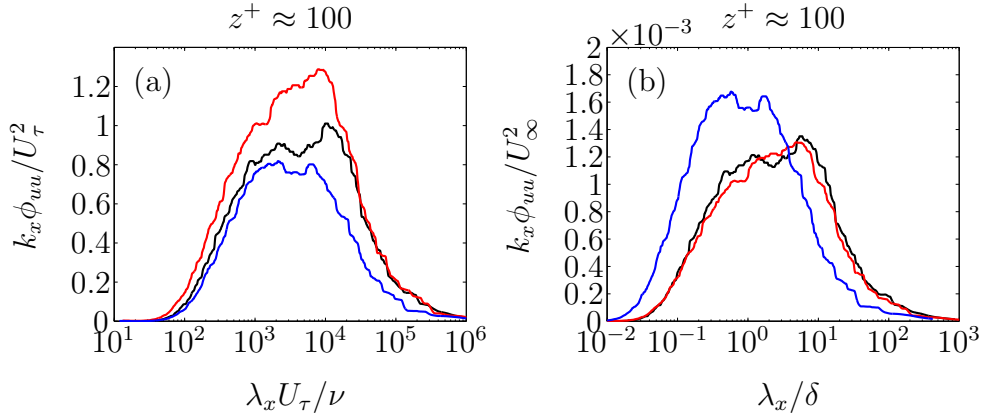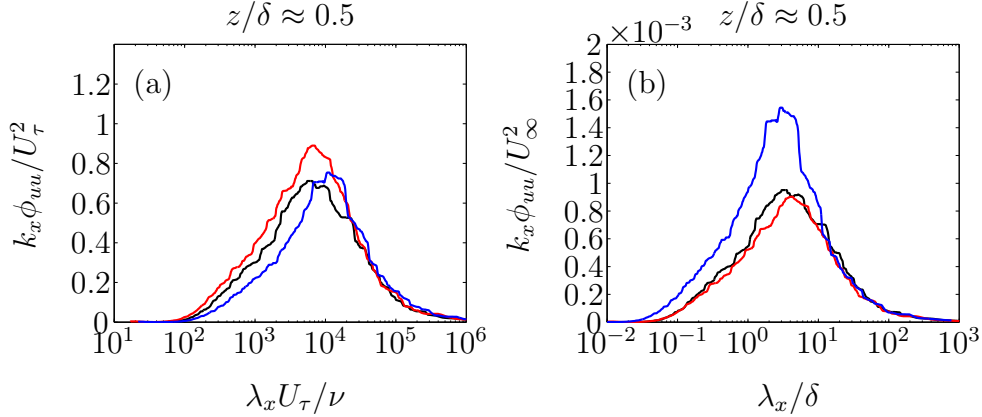Figure 5.12: Pre-multiplied energy spectra normalised with inner (a) and outer scales (b) for the smooth surface (black line), diverging region (red line), and converging region (blue line) in the outer region of $z/\delta \approx 0.5$, from cases B2 and S2.

5.6.3   Spectra map

In order to see the effect of large-scale motions in more detail, we present the pre-multiplied energy spectra contours over the smooth-wall, converg-

ing region and diverging region from the entire wall normal height of the turbulent boundary layer. Details regarding the construction of this plot can be found in Hutchins and Marusic (2007a,b).

From the turbulence intensity profile plot of figure 5.5(a and b) and pre-multiplied energy spectra plots 5.10, 5.11, and 5.12 one can see that different scaling results in different turbulence intensity profile and pre-multiplied energy spectra plot respectively. Due to the difficulty in using inner-scale, here we are interested to see the pre-multiplied energy spectra when it is scaled with outer-scale (i.e. $k_x\phi_{uu}/U_\infty^2$). Figure 5.13 shows the outer-scaled pre-multiplied energy spectra contours $k_x\phi_{uu}/U_\infty^2$ over the smooth-wall, converging region and diverging region covering the full wall-normal height of the turbulent boundary layer. The right hand column shows the wall-normal distance and wavelength normalised with boundary layer thickness δ of their respective surfaces. The left hand column, shows the wall-normal distance and wavelength normalised with boundary layer thickness of the smooth-wall case (δ_s).

Figure 5.13 reveals that above the diverging region the pre-multiplied energy is everywhere lower than the converging region. The energy plot reflects the outer-scaled turbulence intensity profile in figure 5.5(b), where the turbulence intensity over the diverging region is lower than the converging region across the entire boundary layer. Scaling the pre-multiplied energy spectra with U_∞ for all three surfaces seems to be more favourable because the free-stream velocities U_∞ for all three surfaces are identical, hence it provide us with a similar normalisation constant for all three cases. Apart from the pre-multiplied energy spectra, it is also desirable to scale the wavelength and wall normal distance for all three surfaces with similar normalisation constant, here we choose the boundary layer thickness from the smooth-wall δ_s.

The left-hand column of figure 5.13 (a, c and e) shows similar pre-multiplied energy spectra scaling (scaled with U_∞), while the wall normal distance and wavelength are scaled with boundary layer thickness of the smooth-wall (δ_s). Since U_∞ and δ_s have the same value for the three sets of data, it allows one to judge and determine the real (dimensional) effect of the roughness on the boundary layer. Figure 5.13(a) shows the smooth-wall case where there is an inner-peak at $z/\delta_s = 0.08$ and $\lambda_x/\delta_s = 0.6$ (marked by ✚) and an outer-peak at $z/\delta_s = 0.06$ and $\lambda_x/\delta_s = 6$ (marked by ✖).
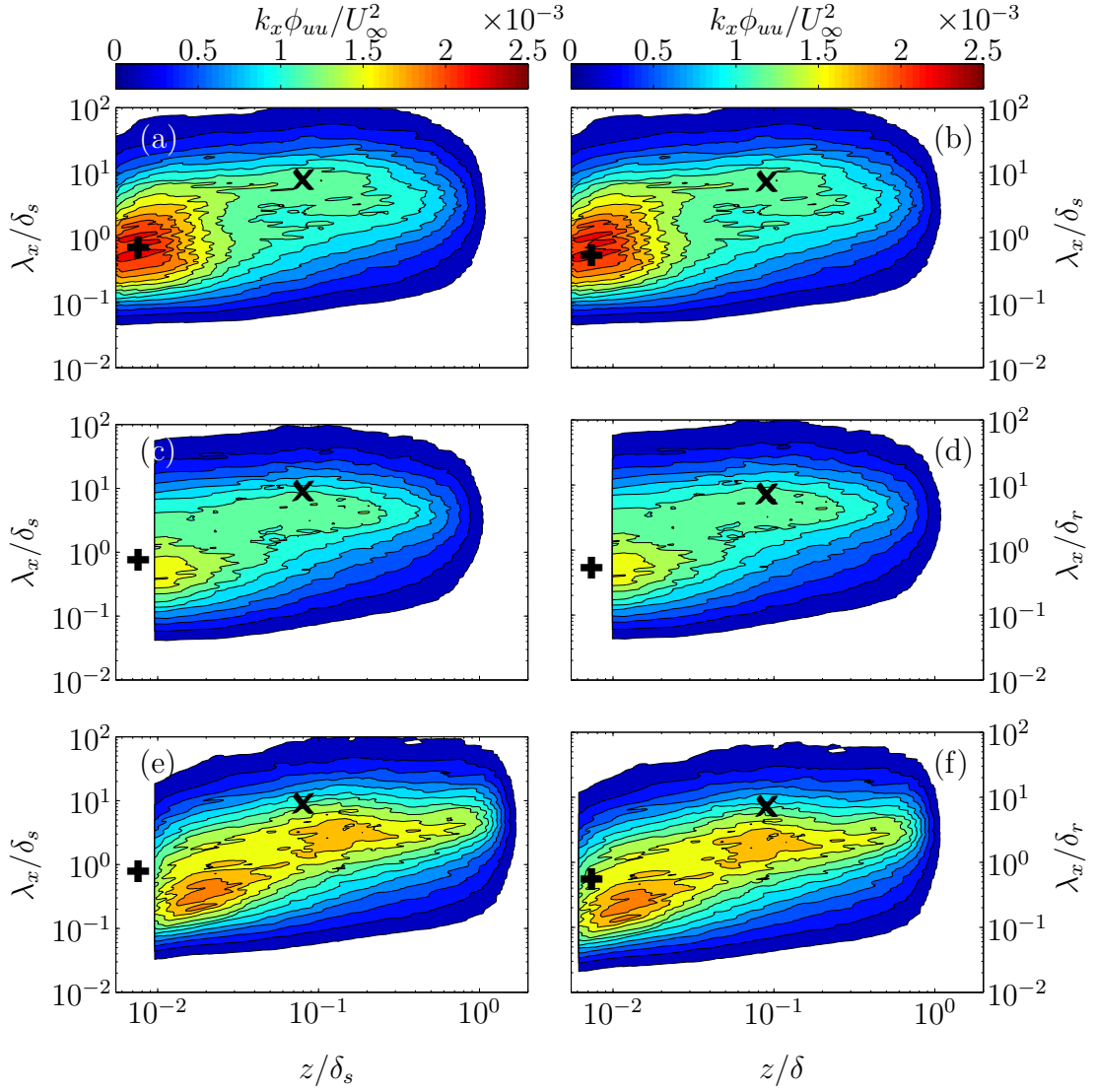
Figure 5.13: A surface plot of outer-scaled pre-multiplied energy spectra of streamwise velocity fluctuations $k_x\phi_{uu}/U_\infty^2$ covering the entire boundary layer from cases S2 and B2. The wave-length and wall-normal in the left hand column are scaled with the boundary layer of smooth-wall δ_s while the right hand column is scaled with their respective boundary layer thickness δ. Subscript r is signalling that the boundary layer thickness of the rough surface, while subscript s is for the smooth-wall. The top rows (a and b) show the smooth-wall case, the middle row (c and d) show the diverging case, and the bottom row (e and f) show the converging case. (✚) and (✖) represents the inner- and outer-peak location of the smooth-wall.

Figure 5.13(c) shows the pre-multiplied energy spectra over the diverging region. The figure reveals that the magnitude of the energy spectra for the

diverging region is lower than that of the smooth wall, particularly between the near-wall position and the end of the logarithmic region. The relatively lower energy spectra magnitude is due to the low turbulence fluctuations that are carried by the common-flow-down from the outer layer. The figure also shows that the inner-peak location is slightly shifted. It seems the downward flow confines the turbulent fluctuations closer to the wall and shifts the wall normal location of the inner peak closer to the surface (unfortunately the expected inner peak is below our first measurement location). Lastly, the damping of the near-wall fluctuations by the riblets seems to further contribute towards the lower energy spectra at the inner peak (see Choi (1989); Karniadakis and Choi (2003)). Closer inspection on the outer-peak location of the diverging region shows that it has been shifted to a lower wavelength although it does not seems to alter its wall normal location (which located at the log region). It seems that the large-scale secondary flow over the diverging region has altered the naturally occurred large-scale features and slightly modify its dimension.

Figure 5.13(e) shows the pre-multiplied energy spectra over the converging region. The plot shows that the energy spectra magnitude over the entire layer is higher than the diverging region. When it is compared to the smooth wall case, the energy spectra magnitude over the converging region at wall normal location $z/\delta_s < 0.02$ is lower, while beyond this position the energy spectra is higher. Two peaks are clearly visible at the inner and outer regions, and they are shifted further up from the wall when compared to the corresponding smooth-wall peaks. The shift is probably due to the common-flow-up which forces the near-wall flow to move away from the wall and transfers the small-scale near-wall structures to a higher location within the boundary layer. The relatively lower inner-peak magnitude of the converging region (when compared with the smooth-wall case) is also consistent with the scenario of the damping of the near-wall velocity fluctuations u by riblets.

The pronounced outer-peak in the converging region is contrasting with the weak/lack of the outer-peak over the smooth wall case and the diverging region. One could tentatively interpret it as though the large-scale events, which are generally randomly generated and distributed (both spatially and temporally) in the smooth-wall case, have been arranged and locked over the converging region. Therefore, the large-scale events occur more frequently or with larger magnitude over this particular region.

So far we have analysed the pre-multiplied energy spectra for all three surface cases by scaling it with the U_τ and U_∞ (see sections 5.6.1 and 5.6.2), the results (especially between the converging and diverging region) on the energy magnitude seem to contradict one and another. Judging from the outer-scaled energy spectra plot and the cross-wire evidence of common-flow-up and common-flow-down experienced by the flow over the converging and diverging region respectively, it seems that the scaling of the pre-multiplied energy spectra of streamwise velocity fluctuations $k_x\phi_{uu}$ with U_∞ is more appropriate and consistent with the available hypothesis. Furthermore, scaling the wall-normal distance z and wavelength λ_x of the converging and diverging region with boundary layer thickness of the corresponding smoothwall case δ_s provides a consistent scaling for all three surface cases.
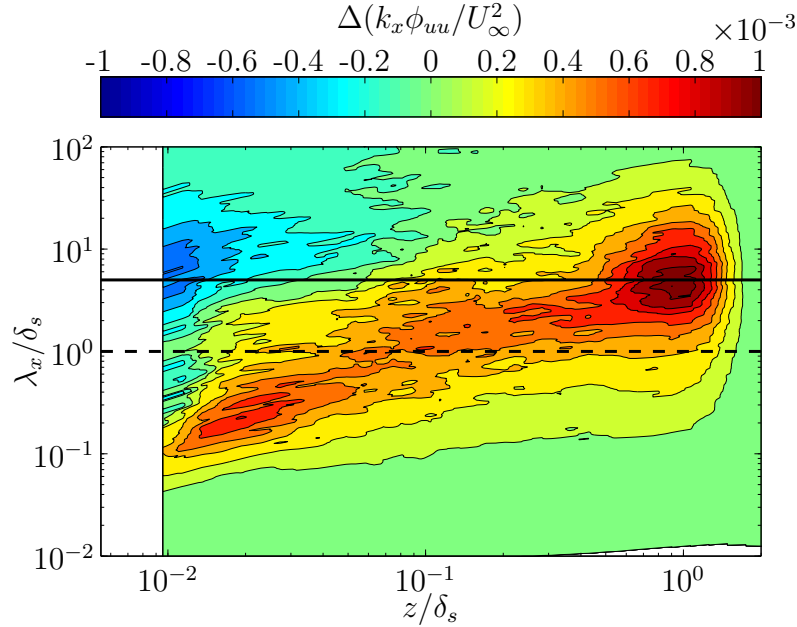
Figure 5.14: Contours of $|k_x\phi_{uu}/U_\infty^2(z,\lambda_x)|_{con}$ - $|k_x\phi_{uu}/U_\infty^2(z,\lambda_x)|_{div}$. The difference between the pre-multiplied energy spectra of the converging region and diverging region as a function of z and λ_x.

Since we are interested in the differences between the flow over the converging and diverging region, we need to subtract the pre-multiplied energy spectra of the converging (figure 5.13(e)) with the diverging region (figure 5.13(c)). Here we choose the outer-scaled pre-multiplied energy spectra (normalised with U_∞), with wavelength λ_x and wall-normal distance z normalised with boundary layer thickness of smooth-wall δ_s. Figure 5.14 shows

the spectral map difference between the converging region and the diverging region. Here the red shading show higher energy for the converging region and blue region correspond to the higher energy in the diverging region. We divide the wavelength into three categories, long wavelength ($\lambda_x/\delta_s > 5$ marked by horizontal line) , medium wavelength ($1 \leq \lambda_x/\delta_s \leq 5$), and short wavelength ($\lambda_x/\delta_s < 1$ marked by dashed line).

From figure 5.14, there are several clear distinctions observed. First, for the long wavelengths, there is more energy for the diverging region from near the wall ($z/\delta_s \approx 0.01$) up to the logarithmic region ($z/\delta_s \approx 0.1$). Beyond $z/\delta_s \approx 0.1$, the converging region has a more energetic long wavelength. Second, for the medium wavelength, the diverging region has more energy at $0.01 < z/\delta_s < 0.03$. Beyond the wall-normal location of $z/\delta_s = 0.03$, the pre-multiplied energy spectra for medium wavelength over the converging region is stronger. Finally, for the short wavelength, very close to the wall (at $z/\delta_s < 0.02$) the energy spectra magnitude for the converging and diverging region seems to co-exist. However, we suspect that for the diverging case there would be higher energy spectra magnitude below our first measurement location. At $z/\delta_s \geq 0.02$ the converging region has higher short wavelength magnitude.

In summary, from the spectral analysis, it seems that over the converging region, the large-scale is more dominant at the logarithmic region and beyond. Over the diverging region, the large-scale structures seems to be more dominant at the location much closer to the wall.

Chapter 6

Three dimensional conditional structure

In the last several decades various techniques have been employed to study the large- and very-large-scale features/structures of turbulent boundary layers. These include : hot-film measurements (Kim and Adrian, 1999), Particle Image Velocimetry (PIV) (Tomkins and Adrian, 2003), and spanwise rake of hot-wire probes (Hutchins and Marusic, 2007a). These studies have provided a lot of new information regarding the existence and behaviour of the large- and very-large-scale structures. However, most of these techniques only provide planar views (two-dimensional views) of the features. Recent studies by Hutchins et al. (2011) and Talluru et al. (2014a) have extended the view of the large- and very-large-scale features by looking at the three-dimensional structures.

Hutchins et al. (2011) utilised traversing hot-wire probes with an array of flush-mounted skin-friction sensors (hot-films) to identify the conditional structure of large-scale features in a high-Reynolds-number turbulent boundary layer. They used a spanwise array of 10 hot-films to detect a low-skin-friction footprint at the wall and then used this information to calculate conditional averages of the streamwise velocity signal from the hotwire. Their results show that the conditioning technique is able to detect the long meandering streamwise features or superstructures (as reported in Hutchins

and Marusic (2007a); Monty et al. (2007)).   Talluru et al. (2014a) have
extended the findings of Hutchins et al. (2011) by using subminiature cross-
wire probes capable of detecting all three velocity components. Their results
reveal the conditional existence of roll-modes that accompany the large-scale
structures. In this chapter, we are interested in using the same technique
as Hutchins et al. (2011) to detect the large-scale structures over the con-
verging and diverging surface roughness.

6.1   Detection and conditional technique

In order to perform the measurement, we utilise two hot-films and a two-
dimensional traversing hot-wire (wall-normal and spanwise direction). Fig-
ure 6.1 shows the schematic set-up of the hot-films and hot-wire. Note that
Hutchins et al. (2011) used ten hot-film arrays and a wall-normal traversing
hot-wire.   For this conditional structure experiment, the hot-wire is only
traversed over one half of the wavelength, or 0.5Λ, of the surface (i.e from
the converging to the diverging region), instead of one whole wavelength
Λ (converging to diverging and to converging region).   However, based on
previous results (chapter 4) we can assume symmetry about this point. Al-
though the hot-wire only covers 0.5Λ, the measurement time for each point
is 70 seconds at 50kHz (the previous two-dimensional hot-wire measure-
ments for the parametric studies were 30 seconds at 50KHz), which results
in more converged statistics. The hot-wire is traversed over a spanwise and
wall-normal plane with 35 points in the wall-normal (z) direction logarith-
mically (covering at least $3\delta_s$) and 18 points in the spanwise (y) direction
linearly (covering $0.5\ \Lambda$).

The two hot-films are glued on the converging and diverging roughness sur-
faces, and referred to as $\mathrm{hf_c}$ (for converging region) and $\mathrm{hf_d}$ (for diverging re-
gion). It should be noted that since this is a rough surface, the hot-films are
not measuring skin-friction. They are only measuring the local streamwise
velocity very close to the riblet surface. We are using the signal to detect the
passage of large-scale events, which are commonly identified as the footprint
of the large-scale structures (Mathis et al., 2009a,b). The footprint can be
detected by isolating the large-scale signature of the streamwise flow from
one of the two hot-films.   One such method is by filtering the streamwise
velocity fluctuating signal, u, using a Gaussian filter of length 1δ. For this

study, we use the boundary layer thickness of the smooth-wall δ_s, as the filter length. From hereafter the filtered hot-film signal is referred to as u_{hf}. The filtered signal gives a measure of the large-scale velocity fluctuations. Note that in their reports, Hutchins et al. (2011) and Talluru et al. (2014a) refer to the filtered hot-film signal as skin-friction fluctuation (i.e u_τ).
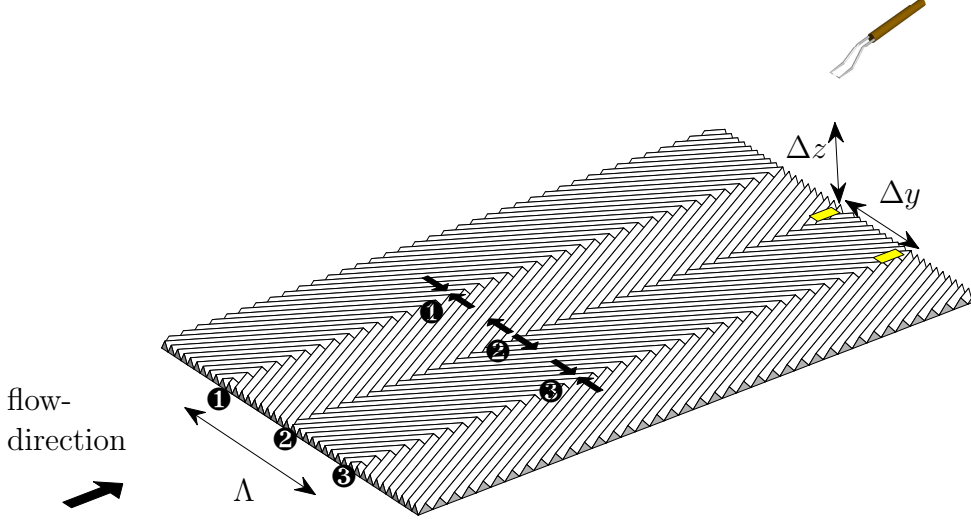
Figure 6.1: Diagram of hot-films and hot-wire setup

In this study we are interested in detecting the large-scale low-speed events associated with the large-scale structures as investigated for a canoical turbulent boundary layer by Hutchins et al. (2011). Therefore, when the fluctuating component from the filtered hot-film u_{hf} is less than zero, the hot-wire is conditionally sampled to generate an ensemble-averaged streamwise velocity signal. The hot-wire signal is conditionally sampled at every location over the entire wall-normal and spanwise measurement plane which enables reconstruction of a three-dimensional view of the conditionally averaged feature over the converging to diverging region (0.5 Λ). Here, the conditionally averaged streamwise velocity fluctuation is denoted with a tilde (i.e $\tilde{u}$) and defined as

$$\tilde{u}|_l(\Delta t, \Delta y, z) = \langle\, u(t, y, z) \;\mid\; u_{hf}(t - \Delta t, y - \Delta y < 0) \,\rangle \qquad (6.1)$$

where it is a function of temporal separation from the detected event (Δt), wall-normal position (z), and spanwise separation position (Δy). The hot-

film signals are converted from time-series to the spatial domain (to obtain length-scale) using Taylor's hypothesis with $x = -U_c t$ (for a review of Taylor's hypothesis see (Taylor (1938); Zaman and Hussain (1981); Dennis and Nickels (2008); Moin (2009); del Álamo and Jiménez (2009)). U_c is the convection velocity for the lage-scale features. Hutchins et al. (2011) obtained U_c from cross-correlations between two streamwise-separated hot-films. Unfortunately, in this experiment we do not have additional hot-films located upstream of our measurement locations. Furthermore, we have shown that the local mean velocity above the diverging and converging region are sensitive with streamwise fetch F_x and the flow dynamics behave differently when compared to a turbulent boundary layer over a smooth-wall. Therefore, it is difficult to obtain precise values of U_c over the converging or the diverging region. Previously Mathis et al. (2009a) have shown that the outer peak in the energy spectra due to the very-large-scale structures or superstructures occurs at a wall-normal location of $z^+ \approx \sqrt{15Re_\tau}$. This location is the midpoint of the logarithmic region, with the assumptioned range of $100 < z^+ < 0.15\delta^+$. Based on those findings, Hutchins et al. (2011) estimate the convection velocity as

$$U_c^+ \equiv U^+ = \frac{1}{\kappa} ln \sqrt{15Re_\tau} + A. \qquad (6.2)$$

In order to be consistent with Hutchins et al. (2011), the convection velocities for the the large-scale events over the converging and diverging riblet are estimated based on the modified log law :

$$U_c^+ \equiv U^+ = \frac{1}{\kappa} ln \sqrt{15Re_{\tau_r}} + A - \Delta U^+. \qquad (6.3)$$

Note that the friction Reynolds number is based on the local skin friction velocity of the riblets (i.e. U_{τ_r} over the diverging and over the diverging region respectively). At $U_\infty = 15$ m/s, the convection velocity over the diverging region is ≈ 10.8 m/s, while over the converging region is ≈ 7.9 m/s. The conversion of the conditionally averaged time-series to the spatial domain results in

$$\tilde{u}|_l(\Delta x, \Delta y, z) = \langle\ u(x, y, z)\ \ |\ \ u_{hf}(x - \Delta x, y - \Delta y < 0)\ \rangle \qquad (6.4)$$

		U_∞ (m/s)	h_r^+	s_r^+	δ_r (m)	U_{τ_r} m/s	Re_{τ_r}
div(B2)	❷	15	16	22	0.051	0.479	1631
con(B2)	❶❸	15	23	31	0.082	0.680	3698

Table 6.1: Experimental parameters for diverging and converging surface for case B2. The boundary layer thickness listed here for the rough surfaces is the local thickness at that particular spanwise location δ_r. The h^+ and Re_τ shown here for the rough-wall are based on the local values of friction velocity and boundary layer thickness (based on U_{τ_r} and δ_r).

for the low speed / shear-stress event. Note that we have two hot-films (one over the converging and one over the diverging), hence the equation above can be written as

$$\tilde{u}|_{lc}(\Delta x, \Delta y, z) = \langle \, u_c(x, y, z) \mid u_{hf_c}(x - \Delta x, y - \Delta y < 0) \, \rangle \qquad (6.5)$$

for the low speed event of the hot-films above the converging region and

$$\tilde{u}|_{ld}(\Delta x, \Delta y, z) = \langle \, u_d(x, y, z) \mid u_{hf_d}(x - \Delta x, y - \Delta y < 0) \, \rangle \qquad (6.6)$$

for the low speed event of the hot-films above the diverging region.

To investigate the effect of the surface roughness on the three dimensional conditional structure, we choose the diverging and converging region from case B2 as the study case (see table 6.1). This particular case is chosen in order to be consistent with the discussions from the previous chapters (spectra and intermittency). Throughout this chapter we only show ensemble averaged events conditioned on the detection of negative filtered fluctuations from the hot-films.
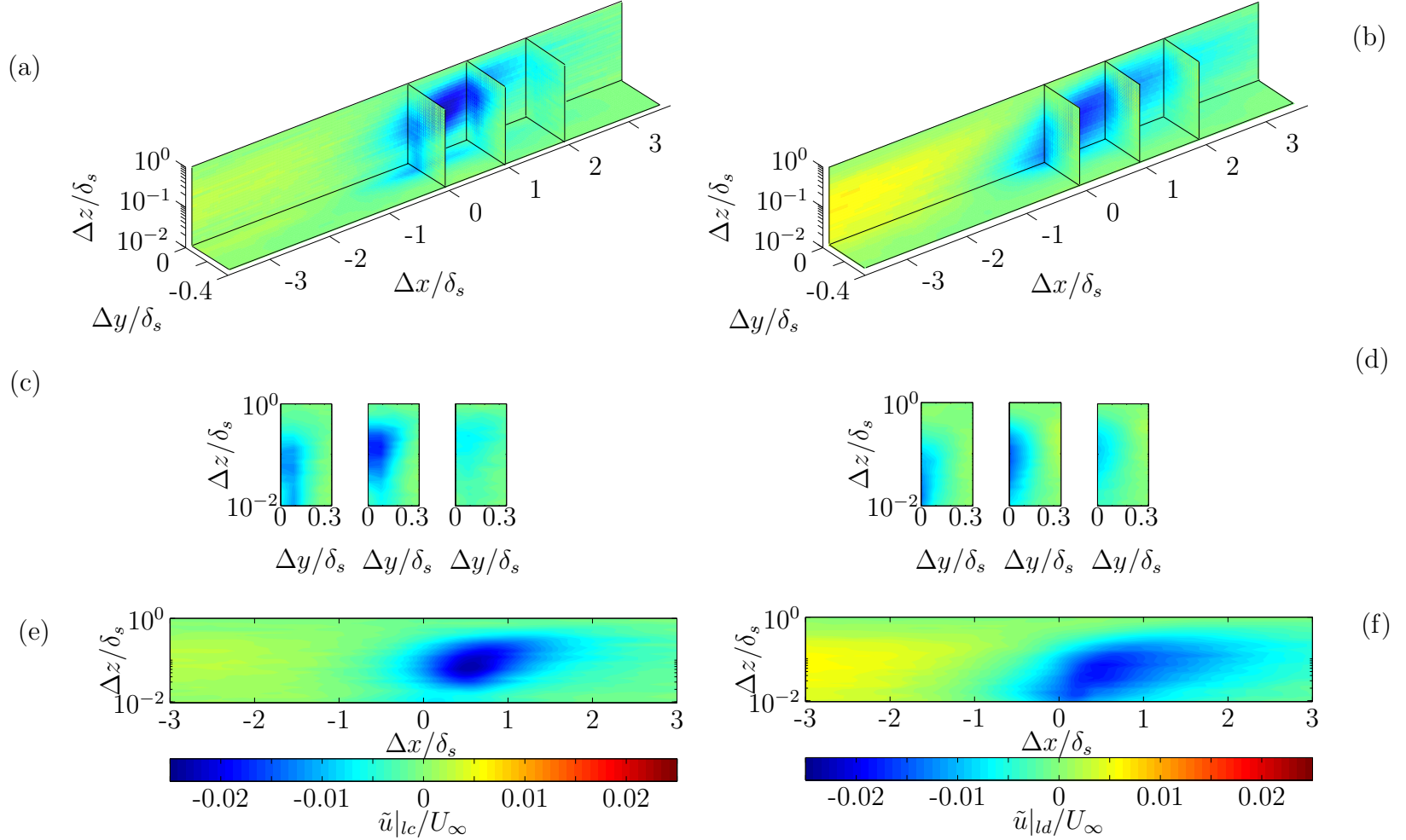
Figure 6.2: Iso-contours of the three dimensional conditional structure associated with large-scale negative velocity fluctuation over the converging (left hand side column) and the diverging (right hand side column) region. (a & b) Three-dimensional view of the $x - y$ plane at $z/\delta_s \approx 0.01$, $x - z$ plane at $\Delta y/\delta_s = 0$, and three $y - z$ planes at location of $\Delta x/\delta_s = 0, 1, 2$. (c & d) Two-dimensional view of $y - z$ planes shown at $\Delta x/\delta_s = 0, 1, 2$. (e & f) Two-dimensional view of $x - z$ plane $\Delta y/\delta_s = 0$ covering $\Delta x/\delta_s = -3$ to 3.

6.2 Three-dimensional view

Figure 6.2 shows iso-contours of a conditional structure associated with negative streamwise velocity fluctuation over the converging region (left hand side) and diverging region (right hand side) normalised by the free-stream velocity $\tilde{u}|_{lc}/U_\infty$ in various $x - y$, $y - z$, and $x - z$ planes. All three planes are normalised with boundary layer thickness over the smooth-wall δ_s, in order to provide similar scale comparison directly. The plots are centered at $\Delta x/\delta_s = \Delta y/\delta_s = \Delta z/\delta_s = 0$ with the $x - y$ plane at $z/\delta_s \approx 0.01$, $x - z$ plane at $\Delta y/\delta_s = 0$, and three $y - z$ planes at $\Delta x/\delta_s = 0$, 1, 2. The $z-$axis is plotted logarithmically while the x and y axes are linear to highlight the near-wall features of the large-scale structure.

6.2.1 Converging region

Figure 6.2 (a and e) shows the isometric view and $x - z$ plane over the converging region. It shows an elongated, forward leaning, large-scale low-speed feature extending a streamwise distance beyond $3\delta_s$. This result is comparable with the recent findings of Hutchins et al. (2011) and Talluru et al. (2014a) for the smooth-wall case. The streamwise development of the low-speed core is also in agreement with their findings. Where it is almost non-existent at $\Delta x/\delta = -1\delta_s$, it suddenly becomes stronger at $x/\delta = 0-1\delta_s$, and then weaker at $\Delta x/\delta = 2\delta_s$. This implies that the feature is inclined and predominantly located downstream of the detection point ($\Delta x/\delta_s = 0$)

Figure 6.2(c) shows the $y-z$ plane over the converging region. The spanwise width of the low-speed region at the centre location (at $\Delta x/\delta_s = 0$) appears to be approximately $0.5\delta_s$ (assuming mirror image at $\Delta y/\delta_s = 0$). At $\Delta x/\delta_s = 1$ the plot shows that the strength and dimension of the structure increases, and the width of the structure increases to approximately $0.6\delta_s$. Hutchins et al. (2011) and Talluru et al. (2014a) have reported that between $x/\delta = 0$ and 1, the spanwise width of the low-speed region does not increase and it stays consistent at approximately $0.5\delta_s$. However, this does not seem to be the case for the large-scale feature over the converging region. At $\Delta x/\delta_s = 2$, the structure seems lifted from the wall and its strength starts to diminish.

In the previous chapter, the pre-multiplied energy spectra above the converging region reveals the existence of a very pronounced outer-peak at the logarithmic region (signalling the presence of large or very large-scale structures). When the pre-multiplied energy spectra of the converging region is compared to the smooth-wall case, at similar U_∞ and streamwise location x, the smooth-wall case does not have such a pronounced outer-peak. The outer-peak observed over the converging region is consistent with the interpretation that the secondary flows induced by the converging section may preferentially arrange and lock the large and very large-scale features over this particular section. There is a possibility that several large- or very large-scale features that are generally separated by certain spanwise and wall-normal distances are being forced to merge and form an even larger feature. The merging and locking of the large- and very large-scale structures may explain the relatively wider slow-speed feature observed in the $y - z$ plane than that of the smooth-wall case of Hutchins et al. (2011) and Talluru et al. (2014a) (even when they have higher Re_τ).

Another possibility that may explain the relatively wide conditional structure over the converging region involves the meandering behaviour of the very large-scale features. Hutchins and Marusic (2007a) and Monty et al. (2007) have reported that as the very large-scale features of wall-bounded turbulence travel downstream, they have a tendency to meander in the spanwise direction. It is possible that the large-scale secondary flows may have altered the meandering. An increased width for the conditional average might suggest an increased meandering amplitude. Unfortunately, the lack of hot-film sensors prevent us from proving this. They can only be proven if we have at least two extra hot-films that are located on the positive and negative spanwise side of the $\mathrm{hf_c}$ (hot-films over converging region).

The most notable difference between the structure over the converging region of the riblets and the structures shown by Hutchins et al. (2011) and Talluru et al. (2014a) is in the near-wall low-speed feature (see figure 6.2(e)). In our case, it is clear that the near-wall low-speed feature seems to detach from the surface. In the previous chapter we showed that over the converging region the near-wall flow is being forced to move away from the surface due to the common-flow-up tendency of the counter-rotating vortices, resulting in a lower local mean velocity and higher local turbulence intensity than that of the smooth-wall case. Furthermore, the pre-multiplied energy spectra analysis over the converging region has shown that the near-wall

inner-peak is shifted further from the surface (both in inner and outer scaling). It seems that the phenomenon is reflected in the conditional structure where the large-scale feature does not extend to the surface due to the common-flow-up. Note that the conditional structure is constructed based on the detection of the foot print of the large-scale feature via hot-films. It appears that although the footprint is weak, the hot-films are still able to detect the passing of the large-scale structure.

6.2.2 Diverging region

The same conditionally averaged structure associated with a negative streamwise fluctuation detected by hf_d over the diverging region is shown in the right hand column of figure 6.2. The figure has a similar arrangement to the previous converging section, where it is centered at $\Delta x = \Delta y = z = 0$, $x - y$ plane at $z/\delta_s \approx 0.01$, and $\Delta y/\delta_s = 0$. There are three $y - z$ planes located at $\Delta x/\delta_s = 0, 1, 2$ to provide a much clearer overall three-dimensional view. Here the z axis is plotted logarithmically while the x and y axes are linear. The diverging region plot of figure 6.2 (b, d, and f) show similar trends to the converging region, where the large-scale low-speed feature is elongated and forward leaning extending a streamwise distance beyond $4\delta_s$. Over the diverging region it seems that the core extends slightly longer than that of the converging region. The longer extent may be caused by the higher convection velocity. Hutchins et al. (2011) suggest that convection velocity U_c is the local mean at the mid point of the log region. In the previous chapters we have shown that the local mean velocity over the diverging region is higher than over the converging region. This translates to a higher convection velocity over the diverging region than that of the converging region ($U_{c_d} > U_{c_c}$).

The spanwise width of the large-scale low-speed feature over the diverging region at the centre location $\Delta x/\delta_s = 0$ is approximately $0.4\delta_s$ (assuming mirror image at $\Delta y/\delta_s = 0$). The strength and dimension of the structure both increase slightly at $\Delta x/\delta_s = 1$, although this is not as large as the structure over the converging region. The structure finally starts to decay at $\Delta x/\delta_s = 2$, nevertheless the general shape and strength of the structure is still clearly observed. In general, the width of the low-speed feature over the diverging region is narrower than the converging region. Furthermore,

the magnitude of the low-speed feature core over the diverging region is slightly less in magnitude than the converging region. This situation is consistent with the scenario that the very large-scale features may have been suppressed and dispersed by the common-flow-down generated by the roughness. A second possible scenario is that the spanwise meandering amplitude of the very large-scale structures over the diverging region is smaller than that of the converging region. These two possible hypotheses may explain the relatively narrower large-scale low-speed structure width over the diverging region and the lack of an outer peak in the energy spectra. At this stage however, these hypotheses are highly speculative, and further study using multiple spanwise hot-films and PIV may shed more light on this phenomenon.

Figure 6.2(f) shows the $x - z$ plane of the large-scale low-speed structure over the diverging region. The figure reveals that the structure extends from the surface to the edge of the boundary layer. The result is the opposite of the converging region case (figure 6.2(e)), where the structure is detached from the surface. It seems that the common-flow-down over the diverging region has pushed the flow closer towards the wall. Evidence of this situation can also be observed on the pre-multiplied energy spectra surface plot over the diverging region. The pre-multiplied energy spectra analysis indicated that over the diverging region, the inner peak is shifted much closer to the surface. Furthermore, when we subtract the pre-multiplied energy spectra map of the converging region with the diverging region, the large-scale structure over the diverging region is more dominant at the location closer to the wall.

6.3   Amplitude modulation of small-scale events

Recently, various studies in wall-bounded flow have shown that large-scale structures in turbulent boundary layers are able to modulate the amplitude (Hutchins and Marusic, 2007b; Mathis et al., 2009a,b; Marusic et al., 2010b; Chung and McKeon, 2010a) and frequency (Ganapathisubramani et al., 2012) of the small-scale energy, particularly very close to the wall. Hutchins (2014) shows that the low-speed large-scale structures produce a large-scale region of low shear at the wall which results in a reduced friction velocity region and an increased viscous length-scale. Because the strength

and size of the near-wall structure scales with viscous units that are proportional to the friction velocity, it is believed that near-wall small-scale structures are reduced in magnitude (both in amplitude and frequency). At location further from the wall however, the modulation behaviour is inverted. Mathis et al. (2009a,b) report that beyond $z^+ \approx \sqrt{15Re_\tau}$, the small-scale energy is predominantly increased in magnitude. The shift in small-scale energy behaviour is difficult to explain. Chung and McKeon (2010a) show that the shift is due to an increase in the relative phase difference near-wall structure between small-scales and large-scales further from the wall. Hutchins et al. (2011) suggest that the increased small-scale energy further from the wall is closely associated with the large-scale structures that generate local streamwise deceleration, while the decreased/attenuated small-scale energy is associated with the large-scale structures that generate local streamwise acceleration. The same author went further by explaining that the increase in small-scale energy is suspected to be connected with the *preferred arrangements* of hairpin packets, which are known to increase vortical activity located along the inclined back of the large-scale low-speed feature (Adrian, 2007; Hutchins, 2014).

Using a combination of hot-films and hot-wires, Hutchins et al. (2011); Hutchins (2014); Talluru et al. (2014a) were able to observe the amplitude modulation in three-dimensional view. Their results show the reduction in small-scale energy near the wall is due to the passing of large-scale superstructure event. Further from the wall the opposite situation occurs, the small-scale energy is increased. In this section, we are interested in capturing the amplitude modulation event over the converging and diverging regions by conditional averaging the small-scale component of the hot-wire signal based on the detection of a large-scale event at the wall with hot-films. Here we follow a similar technique used by Hutchins et al. (2011); Hutchins (2014); Talluru et al. (2014a). Firstly, the hot-wire signal is decomposed into a large-scale component u_l and small-scale component u_s via a sharp spectral cut-off filter at $\lambda_x^+ \approx 7000$, where λ_x is the streamwise wavelength. The choice of this cut-off wavelength is based on observations of Mathis et al. (2009a), where it is shown that this cut-off wavelength is ideal to separate small-scale energy from the large-scale events. For this study, the skin-friction velocity used to normalise λ_x^+ is the spanwise averaged skin-friction velocity $U_{\tau_{sa}}$. We also have investigated other cut-off filter values, such as using local skin friction velocity U_{τ_r} to obtain $\lambda_x^+ \approx 7000$, and different cut-off filter values (i.e shorter λ_x^+ for the converging region and longer λ_x^+ for

the diverging region). However, those attempts do not significantly change the conclusion when we compare the differences in amplitude modulation of small-scale events between the converging and diverging region.

The conditional technique is performed in a similar manner as in the previous section, however in this case it is the small-scale variance that we ensemble average:

$$\tilde{u_s^2}|_l(\Delta x, \Delta y, z) = \langle\ u_s^2(x,y,z)\ \mid\ u_{hf}(x - \Delta x, y - \Delta y < 0)\ \rangle - \overline{u_s^2} \quad (6.7)$$

Because we have two different hot-films, the above equation becomes:

$$\tilde{u_s^2}|_{lc}(\Delta x, \Delta y, z) = \langle\ u_{s_c}^2(x,y,z)\ \mid\ u_{hf_c}(x - \Delta x, y - \Delta y < 0)\ \rangle - \overline{u_{s_c}^2} \quad (6.8)$$

for the small-scale fluctuations during a large-scale low event over the converging region and

$$\tilde{u_s^2}|_{ld}(\Delta x, \Delta y, z) = \langle\ u_{s_d}^2(x,y,z)\ \mid\ u_{hf_d}(x - \Delta x, y - \Delta y < 0)\ \rangle - \overline{u_{s_d}^2} \quad (6.9)$$

for the small-scale fluctuations during a large-scale low-speed event over the diverging region. Note that in the equations above the tilde notation $\tilde{u_s^2}|_l$ represents the conditionally averaged small-scale variance, while $\overline{u_s^2}$ is time-averaged unconditional small-scale variance.
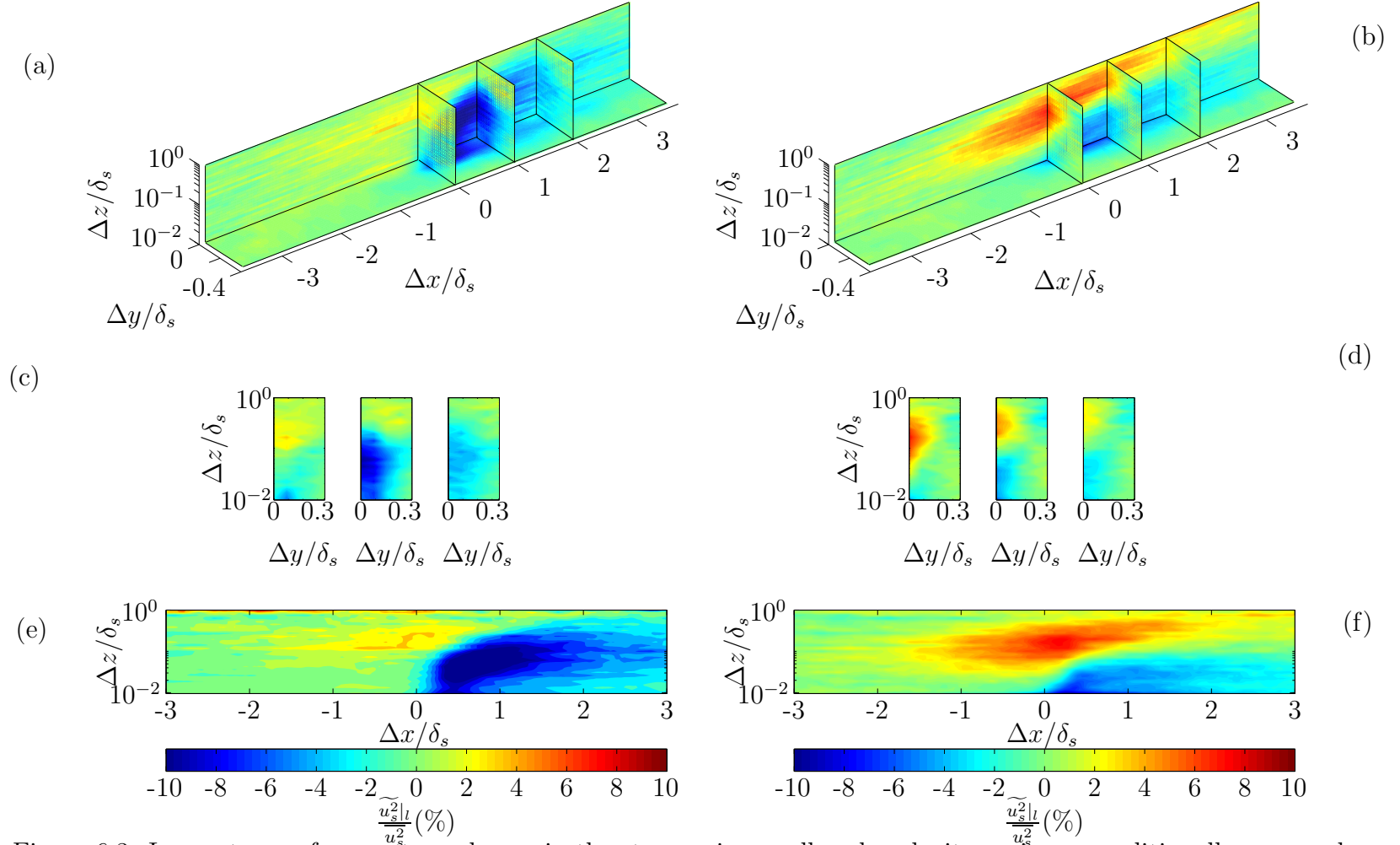
Figure 6.3: Iso-contours of percentage change in the streamwise small-scale velocity variance conditionally averaged on a low shear-stress event over the converging (left hand side column) and the diverging (right hand side column) region. (a & b) Three-dimensional view of the $x-y$ plane at $z/\delta_s \approx 0.01$, $x-z$ plane at $\Delta y/\delta_s = 0$, and three $y-z$ planes at location of $\Delta x/\delta_s = 0$, 1, 2. (c & d) two-dimensional view of $y-z$ planes shown at $\Delta x/\delta_s = 0$, 1, 2. (e & f) two-dimensional view of $x-z$ plane $\Delta y/\delta_s = 0$ covering $\Delta x/\delta_s = -3$ to 3.

Figure 6.3 shows the three-dimensional iso-contours of the conditioned small-scale variance normalised with the time-averaged unconditional small-scale variance. The colour contour shows the percentage variation which are the difference between conditional averaged small-scale variance and time-averaged unconditioned small-scale variance. The red shading represents increased small-scale variance/small-scale energy and the blue shading shows reduction. The plot shows the correlation between the large-scale skin-friction fluctuation near the wall and the amplitude of the small-scale fluctuations at certain wall-normal location. The left-hand column of figure 6.3 shows the result from the converging region and the right hand column shows the result from the diverging region. This figure has a similar structure to figure 6.2, plotted at $x - y$, $y - z$, and $x - z$ planes, and all three planes are normalised with boundary layer thickness over the smooth-wall δ_s.

6.3.1   Converging region

The left hand column of figure 6.3 (a, c, and e) shows the conditioned small-scale variance for the converging region. As mentioned previously, Mathis et al. (2009a) show that the large-scale structures attenuate the near-wall small-scale energy, however at the centre of the logarithmic position (i.e $z^+ \approx \sqrt{15Re_\tau}$) the behaviour switches. This switch can be observed at $\Delta x/\delta_s = 0$, with wall normal location $\Delta_z/\delta_s = 0.072$. The wall-normal position where the switch between the reduction and increase of small-scale energy takes place is higher than that of Hutchins et al. (2011). Their study showed similar switch in the conditioned small-scale variance at wall-normal location $z^+ \approx 450$ $(\Delta_z/\delta = 0.032)$ for a significantly higher Reynolds number. The increase/shift in the wall-normal location may happen due to the common-flow-up that exists over the converging region.

Closer inspection shows there is a significant reduction in the conditioned small-scale variance/small-scale energy at $\Delta x/\delta_s > 0$. The region of the attenuated small-scale energy is inclined to the wall, and extend beyond $\Delta x/\delta_s = 3$, eventually reaching the edge of the boundary layer. The increase in small-scale energy over the converging region is fairly weak and only extends $\approx 2.5\delta_s$. From the figure it is clear that the reduction in small-scale energy is much more pronounced than the increase. According to

Hutchins (2014), the low-speed region of the large-scale structure causes the near-wall cycle to have a reduced amplitude. Based on this conjecture, and from the data analysis that we have done so far, it seems that over the converging region the common-flow-up has captured and locked the very-large-scale structure/superstructure, and causes large-scale region of reduced small-scale near-wall cycle amplitude. The capture and locking mechanism causes the low-speed very-large-scale features to occur much more often over the converging region, which results in the reduced small-scale energy being detected more frequently. Furthermore, the common-flow-up transfers the low-speed structure further from the wall and causes the small-scale reduction to dominate across the entire wall-normal and streamwise domains.

The relatively weak region of small-scale energy increase over the converging region is more difficult to explain. Earlier we discussed that the increase and decrease of small-scale energy may be related to the large-scale structures. Hutchins et al. (2011) suggest that the increased small-scale energy is closely associated with local streamwise deceleration, while the decreased/attenuated small-scale energy is related with the streamwise acceleration of the large-scale structure. We suspect that over the converging region, the large-scale structure proportion that produces local streamwise deceleration is less active than the large-scale region that generates local streamwise acceleration (see figure 6.2(e) where the converging region has a weaker positive region than the diverging region). This would further explain the relatively strong reduced small-scale energy and the weak small-scale energy increase.

6.3.2   Diverging region

Figure 6.3 (b, d, and f) show the conditioned small-scale variance over the diverging region. The figure clearly reveals that the increase in small-scale energy is more pronounced than the reduction in small-scale energy. At $\Delta_x/\delta_s = 0$ the switch between the increase and reduction of small-scale energy occurs at $\Delta_z/\delta_s = 0.022$, this location is closer to the wall than the converging-region case. The lower shifting position seems to happen due to the common-flow-down that resides over the diverging region. Figure 6.3(f) shows that the increase in small-scale energy over the diverging region is

much larger in length than that of the converging region, it covers $\Delta_x/\delta_s > 5$ (this could be due to the convection velocity). Furthermore, the reduction in small-scale energy over the diverging region is weaker than the reduction over the converging region. The reduction in small-scale over the diverging region seems happen much closer to the surface.

The results over the diverging region show a similar pattern with the converging region, however over the diverging region the small-scale energy confined closer to the wall with weaker attenuation of small-scale energy close to the surface, and strong amplification of small-scale energy further away. The stronger amplification seems to match the stronger positive region observed for the conditional averaged low-speed event above the diverging surface in figure 6.2 (f).

Chapter 7

Turbulent and Non-Turbulent Interface (TNTI)

Certain locations in the flow can experience a mix (in time) of both turbulent and non turbulent regimes, experiencing periods of intense turbulence, interspersed with periods of quiescence. Such behaviour is identified as intermittency. The existence of intermittency was first detected by Corrsin (1943) from his study of an axisymetric jet. Corrsin (1943) observed a unique fluctuation pattern in the oscilloscope from a hot-wire located between the laminar and turbulent region of the jet, which had a striking resemblance to transition in a laminar boundary layer. In his report, Corrsin calls it an annular transition region. The phenomenon was later termed intermittency transition (or just intermittency) and commonly denoted by the symbol γ, where it is defined as the probability ratio/fraction of having turbulent flow at a certain location (Corrsin, 1943; Fiedler and Head, 1966).

The first intermittency fraction measurements were performed by Townsend (1948) by measuring the flatness factor (or kurtosis) of $\partial u/\partial t$ on the outer region of the wake. A year later, Townsend (1949) introduced another more direct technique to detect intermittency by counting the 'on-off' signal triggered by the detection of an intermittency signal (this is also known as an analog technique). Corrsin and Kistler (1955) extended and improved Townsend's analog technique to examine intermittency for round jet and

rough-walled turbulent boundary layers. From the seminal work of Corrsin and Kistler (1955), it is known that the non-turbulent region is a field of irrotational fluctuation and the front/interface separating the turbulent and non-turbulent flow is made up of a very thin fluid layer where viscous forces have an important role. The thin fluid layer is termed the *'laminar superlayer'* (or simply *superlayer*) by Corrsin and Kistler (1955). Laminar superlayers in intermittency are different to the more well-known laminar sublayer in canonical wall bounded flows of pipe, channel, and boundary layer. According to Corrsin and Kistler (1955), unlike a laminar sublayer, which is defined as a region near the wall where the mean flow momentum is transported by the viscous shear force, the laminar superlayer is a layer of fluid which moves randomly and transports small amounts of vorticity and mean momentum through viscous shear forces. In canonical wall bounded flow, the laminar sublayer is located near the wall, while the laminar superlayer is located at the outer interface of the boundary layer. As an aside, according to Chauhan et al. (2014) the term superlayer is interchangeable with the term *'interface'* more broadly found in the literature. For this discussion we follow Chauhan et al. (2014), where they define interface as a description of a region in which the fluid flow experiences a mix of both turbulent and non-turbulent flow.

The analog technique that was pioneered by Townsend (1949) and Corrsin and Kistler (1955) has been continuously extended to allow zonal and point averages of the variables to be calculated, hence it allows one to identify the turbulent and non-turbulent characteristics in the interface more clearly (Hedley and Keffer, 1974b). The improved analog technique has since been performed on various types of flows, such as: mixing layers (Wygnanski and Fiedler, 1970), circular jets (Townsend, 1970), and boundary layers (Fiedler and Head, 1966; Kovasznay et al., 1970; Hedley and Keffer, 1974b,a). In this discussion, we concentrate only on the intermittency of the turbulent boundary layer.

In the early 1970s, with the advancement of digital sampling and signal processing techniques, replacement of analog methods with digital methods become more affordable and desirable (Hedley and Keffer, 1974b). Since then, the study of turbulent flow has significantly evolved. Apart from hot-wires, PIV has become more important in assessing intermittency (see Semin et al. (2011); Westerweel et al. (2011); da silva et al. (2014); Chauhan et al. (2014)). The importance of this new measurement technique is re-

flected in the recently reported findings of a step change in velocity across the interface by Semin et al. (2011) with the aid of PIV. Corrsin and Kistler (1955) predicted the existence of a step change in velocity across the interface a few decades earlier, however, because of various factors such as limitation in instruments during that period, the detection of step change was difficult (Chauhan et al., 2014). Due to his work, Corrsin was credited with providing the theoretical foundation of intermittency.

Fiedler and Head (1966) utilised Corrsin & Kistler's analog method to investigate intermittency for adverse and favourable pressure gradient in turbulent boundary layers. They found that the characteristic parameters of the intermittency for the two pressure gradients are related to the form parameter H, where $H = \delta^*/\theta$, δ^* is the displacement thickness and θ is the momentum thickness. Fiedler and Head (1966) showed that with the adverse pressure gradients the turbulent and non-turbulent interface (TNTI) moves away from the wall while the width (where $0 < \gamma < 1$) becomes shorter as H increases. In a favourable pressure gradient however, the opposite behaviour occurs; the intermittency moves closer to the surface and the width of the intermittency zone becomes longer as H decreases. Further studies by Narahimsa et al. (1984) and Escuider et al. (1998) have strengthened the notion that intermittency is sensitive to a change in pressure gradient. The change in intermittency pattern due to different pressure gradients is expected and many studies have shown that a change in pressure gradient alters the mean velocity profile and the turbulence intensity (see for example Monty et al. (2011b); Harun et al. (2013)). The modifications in velocity profile, turbulence intensity, and boundary layer thickness are particularly evident in the wake region or the outer interface of the boundary layer in which intermittency resides. From the parametric studies of the converging and diverging riblets in the previous chapter, we can see that the spanwise mean velocity, turbulence intensity, and boundary layer thickness are also greatly modified. Furthermore, the modification covers the entire layer, from the near-wall region up to the boundary layer, which is akin to the modification caused by altering pressure gradients. Therefore the converging and diverging surface roughness may also alter the intermittency at the turbulent and non-turbulent interface in the same manner as differences in pressure gradients.

In the turbulent and non-turbulent interface (TNTI) there is another important dynamical process called *entrainment*, which is closely connected

to intermittency. According to Chauhan et al. (2014), entrainment can be defined as all mechanisms that are involved in the transfer of mass across the interface. The process of entrainment is believed to involve large-scale motions that transport non-turbulent flow into the turbulent interface which then modifies the previously non-turbulent flow into turbulent flow (Chauhan et al., 2014). This hypothesis can be applied to our current study. Previously, we have shown that the converging-diverging surface roughness induces large-scale counter rotating vortices. The vortices may transport non-turbulent flow (which was originally located above the interface) towards the interface and into the turbulent region.

Based on the previous studies mentioned, particularly in pressure gradient and entrainment, it is believed that the converging and diverging surface roughness can alter/modify the intermittency at the turbulent and non-turbulent interface (TNTI). We are interested to see the differences of the intermittency between the smooth surface and the converging and diverging surfaces. Furthermore, there are very few studies that investigate and compare intermittency over a rough and smooth surface. One such study is by Antonia (1972), where he analysed intermittency for rough and smooth surfaces at a nominally equal wall normal location of $z/\delta \approx 0.95$ (near the outer edge of a turbulent boundary layer). Therefore, in this chapter we discuss the effect of the converging and diverging surface roughness on intermittency and compare it with the smooth-wall case.

7.1 TNTI analysis

To analyse the intermittency transition, γ, we use the method devised by Chauhan et al. (2014). The intermittency is measured by applying a threshold limit of 0.05 on a detector function :

$$\Upsilon = 100 \times \left(1 - \frac{u}{U_\infty}\right)^2 \tag{7.1}$$

where u is streamwise velocity fluctuations and U_∞ is free-stream velocity. The regions in which the detector function has a value greater than 0.05 are

considered turbulent, while regions where the value of the detector function is lower or equal to 0.05 are considered non-turbulent.

7.2 TNTI over the smooth wall case and the rough surface

Figure 7.1 shows the intermittency for the smooth-wall region (case S2) and converging-diverging region with riblet yaw angle $\alpha = 20°$ (case B2). The horizontal axis represents the wall normal distance normalised by their respective boundary layer thickness z/δ, and the vertical axis represents the intermittency ratio γ. The three cases (smooth, converging, and diverging region) have the same free-stream velocity of $U_\infty = 15$ m/s and they are measured at the same downstream location of $x = 4$ m. Note that the intermittency location is sensitive to the threshold and definition of boundary layer thickness δ. Here the boundary layer thickness is based on the 98% of free-stream velocity. The intermittency plot shows that at $\gamma = 1$ the flow is turbulent while at $\gamma = 0$ the flow is non-turbulent. At $\gamma = 0.5$ the flow is intermittent between turbulent and non-turbulent flow with equal ratio. This is the position in which the term intermittency is generally referred to. The width where $0 < \gamma < 1$ is commonly identified as the turbulent and non-turbulent interface (TNTI) width. Figure 7.1 reveals that the smooth-wall intermittency ($\gamma = 0.5$) is located at $z/\delta \approx 0.94$. For the rough-wall case, the intermittency location of the converging and diverging regions are relatively identical at $z/\delta \approx 0.91$. These results suggest that the intermittency location of the smooth-wall is slightly higher than the rough-wall case (albeit small). Closer inspection at the entire width of the interface ($0 < \gamma < 1$) in figure 7.1 shows that the interface width over the converging region is shorter than the diverging region, $\approx 1.1\delta$ and $\approx 1.7\delta$ respectively. For the smooth-wall reference case, the width of the interface is $\approx 1.1\delta$.

The identical intermittency location ($\gamma = 0.5$) for the diverging and converging region for case B2, and its relatively close proximity with the smooth-wall case is intriguing and motivates a second analysis for different converging and diverging cases to be performed. Figure 7.2 shows the intermittency of the smooth-wall (case S2) and converging-diverging region with a riblet yaw angle $\alpha = 10°$ (case A2). For cases A2 and S2, the measurements are
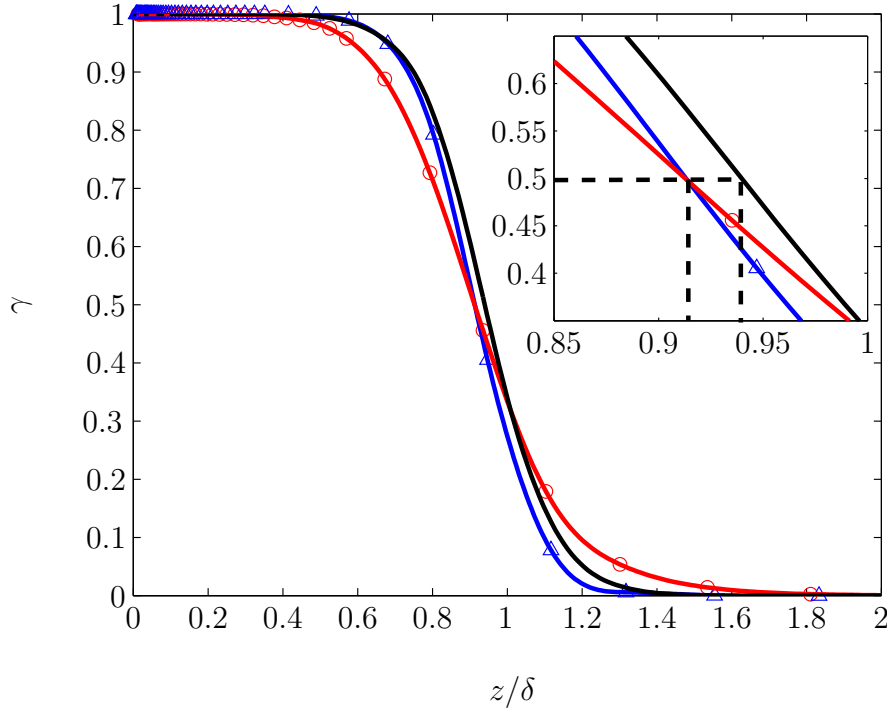
Figure 7.1: Turbulent and non-turbulent intermittency for a smooth surface (case S2) denoted by a black line, diverging region (case B2) denoted by a red line and ○ symbol, and converging region (case B2) denoted by a blue line and △ symbol. The free-stream velocities for all three cases are 15 m/s, and the riblet yaw angle for the converging and diverging regions is at $\alpha = 20°$. The wall normal distance is normalised with their respective local boundary layer thickness, δ.

performed at the same downstream location of $x = 4$ m and free-stream velocity $U_\infty = 15$ m. The plot shows that the intermittency location for the diverging and converging region are at $z/\delta \approx 0.932$ and $z/\delta \approx 0.929$ respectively, while the intermittency location for the smooth-wall case is at $z/\delta \approx 0.94$. The converging and diverging regions' intermittency locations are almost identical (rounded at $z/\delta \approx 0.93$), and they both are slightly lower than the smooth-wall intermittency position. These results show that the rough-wall with a yaw angle $\alpha = 10°$ (case A2) exhibits similar intermittency behaviour to the rough-wall with a yaw angle $\alpha = 20°$ (case B2). For case A2 (figure 7.2) the widths of the interface (where $0 < \gamma < 1$) over the converging and diverging region are $\approx 1.0\delta$ and $\approx 1.2\delta$ respectively.

The results from case A2 (figure 7.2) show a similar trend to case B2.
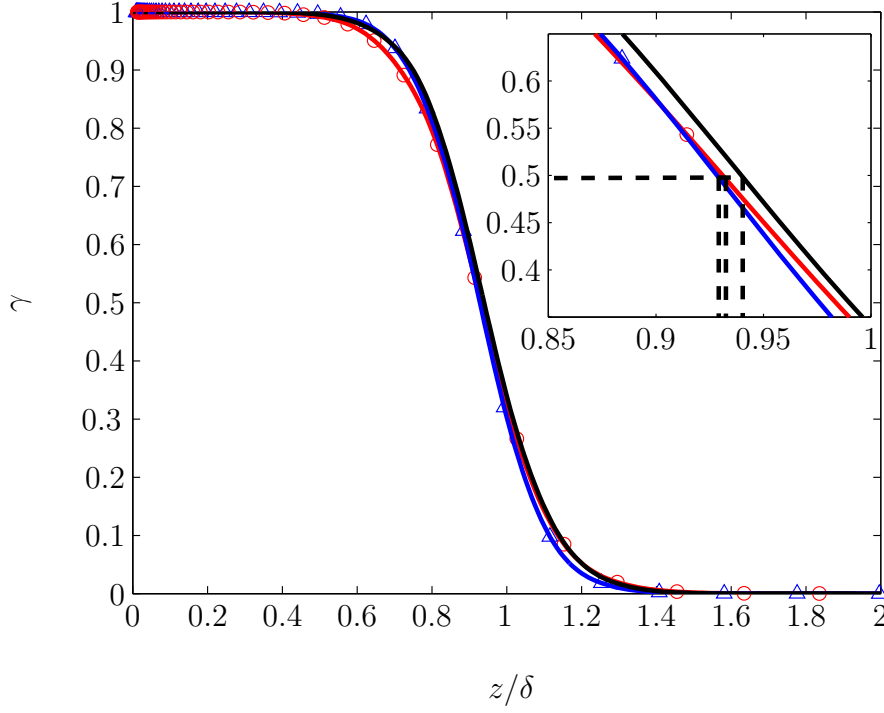
Figure 7.2: Turbulent and non-turbulent intermittency for a smooth surface
(case S2) denoted by a black line, diverging region (case A2) denoted by a
red line and ○ symbol, and converging region (case A2) denoted by a blue
line and △ symbol. The free-stream velocities for all three cases are 15
m/s, and the riblet yaw angle for the converging and diverging regions is at
$\alpha = 10°$. The wall normal distance is normalised with their respective local
boundary layer thickness, δ.

Here the intermittency position ($\gamma = 0.5$) of the converging and diverging
region are almost similar, and they are lower than the reference smooth-wall.
Antonia (1972) reports a similar trend when comparing the intermittency
of smooth and rough-wall. At the nominally similar wall normal location
of $z/\delta \approx 0.95$ (near the outer edge of a turbulent boundary layer), the
intermittency ratio γ of the rough surface is slightly lower than the smooth-
wall. In other words, their rough surface's z/δ location of $\gamma = 0.5$ is lower
than that of the smooth-wall.

The main difference between cases A2 and B2 is the width of the interface.
The TNTI width over the diverging region of case B2 is longer than case A2.
A similar trend is also observed for the converging region. The differences
in TNTI width between case A2 (figure 7.2) and case B2 (figure 7.1) may

case (code)		U_∞ (m/s)	α (°)	$\gamma = 0.5$ (z/δ_s)	$0 < \gamma < 1$ (z/δ_s)
smooth (S2)		15	-	0.94	1.1
		U_∞ (m/s)	(°)	$\gamma = 0.5$ (z/δ_r)	$0 < \gamma < 1$ (z/δ_r)
div(B2)	❷	15	20	0.91	1.7
con(B2)	❶❸	15	20	0.91	1.1
div(A2)	❷	15	10	0.93	1.2
con(A2)	❶❸	15	10	0.93	1.0

Table 7.1: Intermittency parameters for smooth, diverging, and converging surface for cases B2, A2 and S2 scaled with their local boundary layer thickness. The boundary layer thickness for the rough surfaces is the local thickness at their particular converging and diverging location δ_r. For the smooth surface the boundary layer thickness is denoted as δ_s

be caused by a different yaw angle α. A reduced yaw angle α leads to a reduced strength of secondary flows and less pronounced differences between converging and diverging region. A more acute yaw angle α such as in case A2 ($\alpha = 10°$) has less effect on the TNTI width than larger yaw angle in case B2 ($\alpha = 20°$). Table 7.1 summarises the intermittency properties for cases B2 and A2 scaled with their local boundary layer thickness, δ_r (for the rough-wall), and δ_s (for the smooth-wall). From the table, one could see that for the same yaw angle α, the TNTI location between a converging and diverging region are very similar to each other. For the TNTI width, the diverging region is slightly longer than the converging region. In general however, there are not many differences in TNTI properties between the smooth wall, converging, and diverging region.

To see the intermittency spanwise variation over one whole wavelength Λ in more detail, figure 7.3 shows the spanwise variation of the streamwise mean velocity from case B2. Here the wall normal direction is normalised with the boundary layer thickness of the smooth-wall case δ_s. The white horizontal line represents the boundary layer thickness of the smooth-wall, while the blue horizontal line shows the intermittency location from the
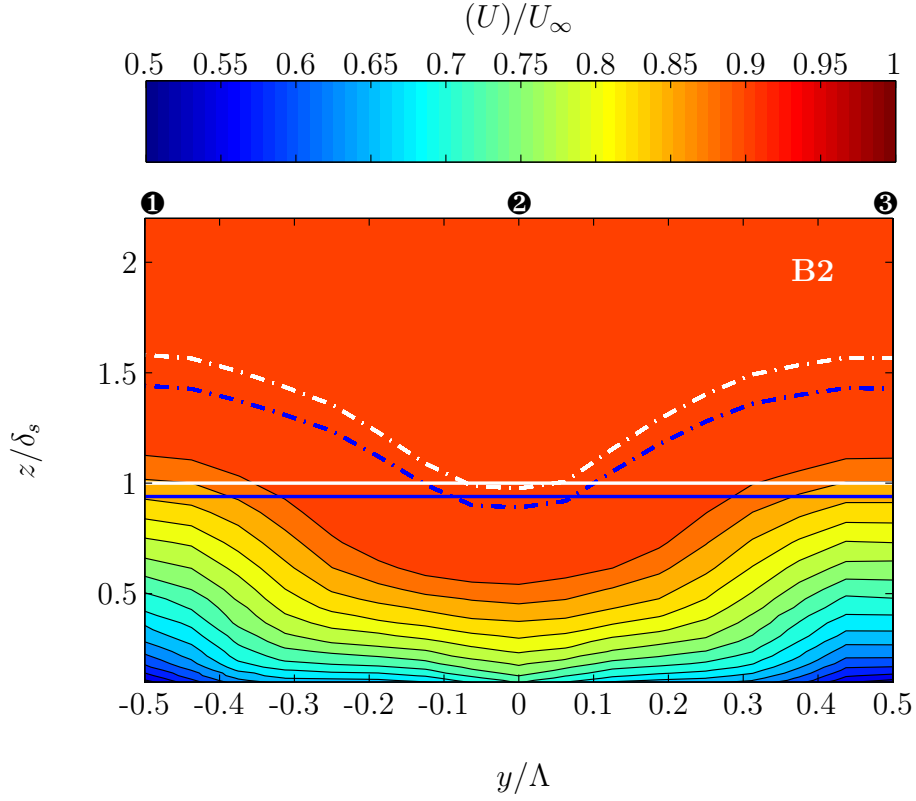
Figure 7.3: Spanwise variation of the streamwise mean velocity for the rough-wall case B2, where $\alpha = 20°$, $h^+ = 20$, $F_x = 4$ m and $x = 4$ m. The mean velocity is normalised by the free-stream U_∞. Wall normal distance is normalised by δ_s, the boundary layer thickness over the smooth-wall, shown here by a white straight horizontal line. The intermittency over the smooth-wall is shown by a blue straight horizontal line. The white dot-dashed line represents the spanwise variation in boundary layer thickness over the rough surface δ_r. The blue dot-dashed line represents the spanwise variation in intermittency over the rough surface.

smooth-wall. The white dot-dashed line represents the spanwise variation in boundary layer thickness over the rough surface δ_r, and the blue dot-dashed line represents the spanwise variation in intermittency over the rough surface. The figure illustrates how the intermittency spanwise variation follows the spanwise variation of the boundary layer thickness. It appears that the large-scale counter rotating vortices, which are generated by the converging and diverging riblet pattern, have modified the intermittency location. Furthermore, the intermittency for these three regions are seem to scaled with their local boundary layer thickness δ.

The variation of the TNTI wall-normal location over the converging and diverging region seems to behave in the same manner as the variation of the turbulent boundary layer thickness δ_r. The TNTI wall normal position above the roughness follows that of the boundary layer thickness (see figure 7.3). One possible explanation of this behaviour is that over the converging region, the near-wall flow is forced to converge towards each other and move vertically upwards (common-flow-up). The common flow up does not only transfer the relatively low speed and highly turbulent near-wall flow vertically upwards, it also forces the TNTI to move further upwards. The opposite occurs over the diverging region, the common-flow-down forces the high speed and low turbulent flow that reside further from the wall to move towards the surface and simultaneously transfer the interface closer to the wall. Finally, the strength of modification seems to depend on the parameters of the converging-diverging surface roughness (i.e h^+, F_x, r_s, and α).

Chapter 8

Conclusion

A series of experiments using a combination of hot-wire (single-wire and cross-wire) and hot-film sensors were conducted to investigate the effect of a new class of riblet-type surface roughness, which has a converging-diverging / herringbone pattern, on zero pressure gradient turbulent boundary layers. The study is inspired by the report of Koeltzsch et al. (2002), who applied a pattern of converging and diverging riblets inside the surface of a pipe. The results from their study show that this unique and unconventional riblet pattern is able to generate a large-scale azimuthal variation in the mean velocity, turbulence intensity, and boundary layer thickness. Our current study seeks to revisit and extend this surface roughness pattern and perform accurate parametric studies for various yaw angle (α), viscous-scaled riblet height (h^+), streamwise fetch (F_x), and relaxation distance (r_s). The results show that the converging and diverging riblet pattern generates a large-scale spanwise variation on the turbulent flow properties (such as mean velocity, turbulence intensity, and boundary layer thickness). Furthermore, the spanwise variation strength and area are sensitive to these experimental parameters. The pronounced spanwise variation over the converging and diverging riblets is surprising and atypical considering the roughness height is $\approx 1\%$ of the boundary layer thickness. The results have raised further questions regarding the turbulent- and non-turbulent interface (TNTI). Our investigation shows that the TNTI properties, such as wall-normal location and length are modified.

Finally, we look into the effect of the converging and diverging riblet-type surface roughness on the large- and very-large-scale structures by analysing the pre-multiplied energy spectra map and the conditional organisation. In addition, we also look into the amplitude modulation of the small-scales due to the large-scale activity within the turbulent boundary layer over the converging and diverging region.

8.1   General results

From the hot-wire measurements (both single- and cross-wire) we observe that the converging and diverging pattern causes a large-scale spanwise variation. Over the converging region, the fluid flow is forced to converge and is transported away from the wall, forming a common-flow-up. This vertically upwards motion carries the relatively high near-wall turbulent fluctuations further from the surface to the outer region of the layer and results in higher local turbulence intensity. The common-flow-up also carries the slow moving near-wall fluid away from the wall, resulting in a low local mean velocity and a thicker boundary layer. Over the diverging region, the opposite situation occurs. Here, the flow is forced to diverge which causes higher speed fluid with low turbulence intensity to move closer towards the surface. The downward motion forms a common-flow-down which confines the turbulent fluctuations closer to the wall, resulting in the reduction of the local turbulence intensity above this area. The common-flow-down also forces the fast moving fluid flow to move much closer to the wall resulting in a higher local mean velocity and thinner boundary layer. The common-flow-up and common-flow-down form large-scale counter rotating vortices that extend from the near-wall location all the way to the wake region. The magnitude of maximum spanwise and wall-normal velocity component (O) are $\approx 2 - 3\%$ of U_∞. A typical vortex generator can generate vortices in the range of $2 - 30\%$ of U_∞

8.2 Parametric studies

For the parametric studies, we have analysed different parameters, namely: yaw angle (α), viscous-scaled riblet height (h^+), streamwise fetch (F_x), and relaxation distance (r_s). Here we look at the effect of these parameters on the spanwise variation strength, spanwise variation area, and vorticity strength. For this study, apart from the parameter under consideration, the others are kept constant.

The mean velocity and turbulence intensity analysis from single-wire and cross-wire measurements show that a lower yaw angle α and shorter viscous scaled riblet height h^+ generates weaker counter-rotating vortices, smaller area/regions of spanwise variation, and a smaller vorticity area. This in turn, results in a weaker spanwise variation in mean velocity, turbulence intensity, and boundary layer thickness δ_r. For different fetch F_x the analysis from the mean velocity and turbulence intensity profiles shows that shorter F_x also results in weaker counter-rotating vortices. These vortices are constrained closer to the surface, leading to more compact regions of spanwise variation in mean velocity and turbulence intensity. Interestingly however, even at the shortest F_x the roughness is still able to generate vortices that produce a near-wall spanwise variation strength that has nominally equal magnitude to that of longer F_x.

The final parametric study is looking at the influence of a reversion from rough to smooth surface r_s. Here we cover the first 3 m of the test section while the remaining 2 m is formed by the smooth-wall. The measurements were performed above the smooth-wall at various r_s locations. The results reveal that the spanwise variation and vorticity strength of the herring-bone patterned riblets diminishes with increasing r_s. Interestingly however, even at the furthest r_s location of $\approx 30\delta_s$ from the rough surface (which is the limit of the tunnel's test section), the roughness is still able to generate considerable spanwise variation in both mean velocity and turbulence intensity. Furthermore, the spanwise variation does not change considerably

8.3   Large- and very-large-scale structures

Here we have compared the three surfaces at similar stream-wise location and free-stream velocity. The pre-multiplied energy spectra map shows that over the diverging region there is an inner peak that is located closer to the wall and lower in magnitude than the smooth-wall case. The lower inner peak magnitude owes its existence to the low turbulence fluctuations that are carried by the common-flow-down from the outer layer. Moreover, the downward fluid flow confines and forces the turbulent fluctuations to move closer to the wall. Lastly, the damping of the small-scale near-wall fluctuations by the riblets seems to be an added factor that leads to the lower energy spectra at the inner peak (see Choi (1989); Karniadakis and Choi (2003)).

The converging region pre-multiplied energy spectra map shows the existence of inner and outer peak. Both peaks are shifted further from the wall when compared to the corresponding smooth-wall peak. The shift may happen due to the common-flow-up that forces the near-wall flow to move further from the surface and transfers the small-scale near-wall structures to a higher location. The inner peak has a smaller magnitude than that of the smooth-wall, which is consistent with the scenario of the damping of the near-wall u fluctuations by riblets. The converging region also has a very pronounced outer-peak, which is consistent with evidence of the existence of superstructures in a boundary layer. It seems that the large-scale counter-rotating vortices induced by the herringbone surface strongly modify the naturally-occurring superstructure events and cause it to be more energetic over the converging region. One interpretation is that the large-scale events, which are generally randomly generated and distributed (both spatially and temporally) in the smooth-wall case, have been preferentially arranged and locked over the converging region and cause the large-scale events to occur more frequently over this particular region.

Finally, when we subtract the pre-multiplied energy spectra of the converging region from the diverging region, we can clearly see that over the converging region, the large-scales are more dominant in the logarithmic region and above. Over the diverging region however, there is a subtle large-scale feature, which is located closer to the wall than that of the converging region and competing with the near-wall small-scale fluctuations.

8.4 Three-dimensional conditional structure

The conditional structure of streamwise velocity fluctuations u shows the existence of an elongated, forward-leaning, large-scale low-speed feature in the streamwise direction. For the converging region, the feature extends a streamwise distance beyond $3\delta_s$ and has a maximum spanwise width of $0.5\delta_s$. Note that here we normalise the length dimension with the boundary layer thickness of the corresponding smooth-wall in order to provide similar direct comparison between the feature over the converging and diverging region. Closer inspection of the $x - z$ plane shows that the low-speed feature detaches from the surface which indicates that the large-scale feature does not extend to the surface. This situation happens possibly due to the common-flow-up over the converging region. Furthermore, we believe that over the converging region the induced secondary flows may preferentially arrange and lock the large-scale structures over this particular location. This event may force several large- or very large-scale features that are generally separated by certain spanwise and wall-normal distances to merge and form an even larger feature. Another possibility is that the large-scale secondary flows may have increased the large-scale's meandering amplitude, which may explain the increase of the large-scale low-speed feature's width.

For the diverging region, the large-scale low-speed feature is elongated and forward leaning, extending a streamwise distance beyond $4\delta_s$ longer than the converging region. This relatively longer feature over the diverging region may be caused by the higher convection velocity than that of the converging region. The maximum spanwise width of the large-scale low-speed feature over the diverging region is approximately $0.4\delta_s$, which is narrower than that of the converging region. The low-speed feature core over the diverging region is also slightly weaker in magnitude than the converging region. Furthermore, the structure extends from the surface to the edge of the boundary layer, which is the opposite of the converging region case where the structure is detached from the surface. We believe that the common-flow-down over the diverging region has pushed the large-scale feature closer to the wall, causing it to reach the surface. Furthermore, based on the spectra analyses, we believe that the large-scale structure over the diverging region is more dominant at the location closer to the wall, competing with the small-scale near-wall structure.

At this stage however, these hypotheses are highly speculative, and further study using multiple spanwise hot-films/hot-wires and PIV may shed more light on this phenomena.

8.5   Amplitude modulation of small-scale events

The amplitude modulation over the converging region shows that the reduction in the conditioned small-scale variance/small-scale energy is much more dominant than the increase. We believe that the captured and locked very-large-scale structure on this region (due to the secondary flow) causes the low-speed very-large-scale features to occur more frequently, resulting in the reduced small-scale energy being detected more often. The common-flow-up around this region may also contribute to the spread of the small-scale attenuation.

Over the diverging region, the increase in small-scale energy is more pronounced than the reduction in small-scale energy. It seems that the behaviour in the conditioned small-scale variance between the converging and diverging region is the opposite of each other. The weak small-scale energy reduction indicates that the low-speed large-scale feature over the diverging region is weaker or occurs less frequently than over the converging region. Furthermore, the low-speed large-scale features may also be confined to much closer to the wall due to the common-flow-down (in which we are unable to detect due to the physical constraint of the hot-wire and hot-film). From the large-scale structure streamwise acceleration and deceleration argument, it seems that over the diverging region the large-scale structure region that produces local streamwise deceleration is more active than the large-scale region that generates local streamwise acceleration. If we look from the hairpin packet concept with the provisio that the packet arrangements are preferential, the dominance of the small-scale energy increase is due to the high vortical activities of the hairpin packet.

8.6   Turbulent and Non-Turbulent Interface (TNTI)

Our analysis of the turbulent and non-turbulent interface (TNTI) over the herringbone pattern reveals that the intermittency between the smooth-wall, and converging and diverging region behaves almost similarly when normalised with their respective boundary layer thickness. The variation of the wall-normal position of the TNTI over the converging and diverging region seems to behave in the same manner as the variation of their respective turbulent boundary layer thickness δ_r. The common-flow-up over the converging region and the common-flow down over the diverging region do not only cause the local velocity and turbulence intensity to move away or towards the wall, they also force the intermittency to move either further or closer to the surface. The spanwise variation of the TNTI seems to depend on the parameters of the herringbone pattern (i.e h^+, F_x, r_s, and α).

8.7   Possible engineering applications

The converging and diverging/herringbone riblet-type surface roughness pattern offers a unique and novel technique of generating large-scale counter-rotating roll-modes or secondary-flows within turbulent boundary layers. Such unique surface pattern may eventually present an interesting addition to the various techniques of controlling boundary layer flows. Some possible applications are:

1. To act as a low-profile device to delay transition from laminar to turbulent flow. Recently Fransson and Talamelli (2012) show that by generating streaks through an array of miniature vortex generators, the streaks can stabilise Tollmien-Schlichting (TS) waves and delay flow transition. Their results suggest the possibility of applying the converging-diverging surface roughness pattern as a technique to delay laminar to turbulent transition. Typical vortex generators have physical height of 2.5 - 18 mm, or more (Lögdberg et al., 2009; Fransson and Talamelli, 2012), which are much higher than our surface pattern.

2. As an alternative for traditional vortex generators in engineering applications, such as aircraft wing.

3. As a method to reduce skin-friction drag. Recently, Chen et al. (2013, 2014) showed that the herringbone surface roughness pattern in a fully developed turbulent pipe flow has the ability to reduce drag by up to 16%, which is much higher than standard riblets that normally reach up to 10%. Furthermore, from the DNS of turbulent channel flow, Schoppa and Hussain (1998) showed that large-scale counter-rotating vortices have the ability to reduce skin-friction drag by up to 20%.

By adjusting the parameters of the surface roughness, such as: yaw angle, viscous scaled height, fetch, and reversion from rough to smooth, it should be possible to produce roll-modes with strengths tailored to specific engineering applications.

8.8   List of publications

8.8.1   Refereed Journals

1. B. Nugroho, N. Hutchins, J.P. Monty (2013) Large-scale spanwise periodicity in a turbulent boundary layer induced by highly ordered and directional surface roughness. International Journal of Heat and Fluid Flow. 41:90 -102.

8.8.2   Refereed Conference

1. Kevin, B. Nugroho, J. P. Monty, N. Hutchins (2014). Wall-Parallel PIV measurements in turbulent boundary layers with highly directional surface roughness. 19th Australasian Fluid Mechanics Conference (AFMC). Melbourne, Australia.

2. Z. Harun, A. A. Abbas, A. Etminan, B. Nugroho, V. Kulandaivelu, M. Khashehchi (2014) Effects of riblet on flow structure around a NACA 0026 Airfoil. 25th International Symposium on Transport Phenomena (ISTP). Krabi, Thailand.

3. B. Nugroho, E. P Gnanamanickam, Kevin, J.P. Monty, N. Hutchins (2014) Roll-modes generated in boundary layers with passive surface

modification. American Institute of Aeronautics and Astronautics (AIAA), SciTech 2014. Maryland, United States.

4. N. Hutchins, B. Nugroho, J.P. Monty (2012) Large-scale secondary flows in a turbulent boundary layer caused by highly ordered and directional surface roughness. 9th International ERCOFTAC Symposium on Engineering Turbulence Modelling and Measurements (ETMM). Thessaloniki, Greece.

5. K.X Oh, B. Nugroho, N. Hutchins, J.P. Monty (2012) Meandering riblets targeting spanwise spatial oscillation of turbulent boundary layer. 18th Australasian Fluid Mechanics Conference (AFMC). Launceston, Australia.

6. B. Nugroho, N. Hutchins, J.P. Monty (2012) Effects of diverging and converging roughness on turbulent boundary layers. 18th Australasian Fluid Mechanics Conference (AFMC). Launceston, Australia.

7. B. Nugroho, V. Kulandaivelu , Z. Harun, N. Hutchins, J.P. Monty (2010) Investigation into the effects of highly directional surface roughness on turbulent boundary layers. 17th Australasian Fluid Mechanics Conference (AFMC). Auckland, New Zealand.

8. Z. Harun, V. Kulandaivelu, B. Nugroho, M. Khashehchi, J.P. Monty, I. Marusic (2010). Large scale structures in an adverse pressure gradient turbulent boundary layer. 8th International ERCOFTAC Symposium on Engineering Turbulence Modelling and Measurements (ETMM). Marseille, France.

Chapter 9

Future work

In the world of scientific research, any current study may raise many more questions that need to be answered. Despite the extended and detailed investigation that we have performed, there are more studies that can be done. Here we have identified five different studies that can be carried out in the future.

9.1 Different wavelength Λ

In this study we have not touched one possible parametric study, different wavelength Λ (see figure 9.1 for schematic diagram). So far we only look into one particular wavelength value, $\Lambda \approx 3\delta_s$, which translates to a distance of $1.5\delta_s$ between a converging and diverging region (or vice versa). The reason we chose this value is to minimise the effect from one region to another. It would be interesting to investigate the effect of increasing or decreasing the wavelength value. We suggest two different values, the first is $\Lambda \approx 1\delta_s$ and the second is $\Lambda \approx 6\delta_s$. We suspect that the shorter wavelength will generate weaker (smaller V and W) and smaller counter-rotating vortices, whereas the longer wavelength may generate a stronger (higher V and W) and larger vortex.
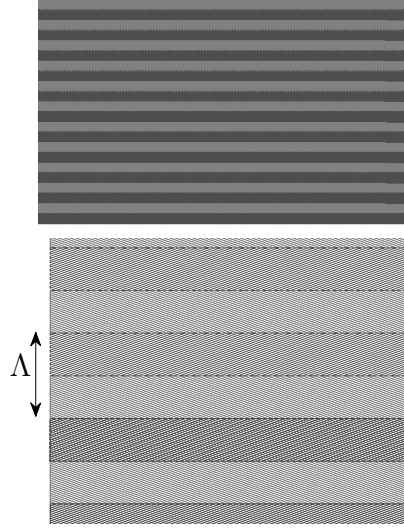
Figure 9.1: Small wavelength for converging and diverging riblets.

9.2   Favourable and adverse pressure gradient

The converging and diverging surface roughness has a potential engineering application as a low-profile vortex generator that can be laid on the fuselage or wings of an aircraft. The curvature of fuselage or wings on an aircraft may modify the performance of the surface roughness. Hence we need to have more information regarding the flow behaviour of the surface roughness under different pressure gradient conditions. Our wind tunnel is designed to have adjustable pressure gradient, and it has been subjected to various pressure gradient studies (Marusic, 1991; Jones, 1999; Jones et al., 2001; Hellstedt, 2003; Monty et al., 2011b; Harun, 2012; Harun et al., 2013). Hence it is an ideal facility to investigate the effect of favourable and adverse pressure gradients on the flow over converging-diverging surface roughness.

9.3   Multiple hot-films

During our conditional structure studies, we noticed the need to have multiple spanwise hot-wire in order to have better understanding of the flow over the converging and diverging surface roughness, particularly the mean-

dering tendency of the large-scale features. Figure 9.2 shows our proposed idea for a future conditional study with multiple hot-films. By combining multiple hot-films in the spanwise direction and the two-dimensional hot-wire traverse covering 1.5Λ we will be able to view the low-speed large-scale features and the amplitude-modulation in more detail. Ideally there should be another set of spanwise hot-films up-stream to obtain more precise convection velocity and to allow us to detect the meandering tendency of the large-scale features. However, the drawback of using two sets of spanwise hot-films located up-stream and down-stream is the possibility that the hot-films that are located up-stream may disturb the flow behind them. The up-stream hot-films may generate an internal layer and create unwanted disturbance.
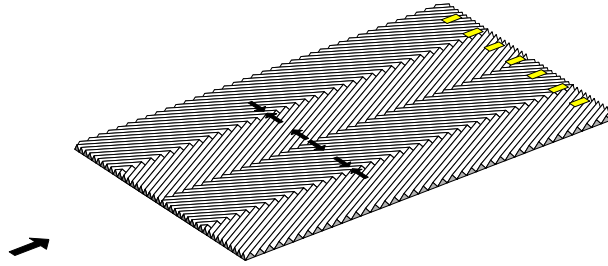
Figure 9.2: Schematic of converging and diverging riblet pattern with multiple hot-films (yellow stripes).

9.4 PIV study

The converging and diverging riblet-type surface roughness produces an unusual turbulent-flow pattern that is very complex and relatively more difficult to analyse when compared to canonical turbulent boundary layers. Although our hot-film and hot-wire sensors manage to capture the flow behaviour, we are unable to fully record the flow pattern, particularly very close to the surface where the hot-film and hot-wire are constrained by their physical dimensions. PIV experiments with high spatial range (de Silva et al., 2014) will allow us to view and study the packets, hairpin vortices, turbulent momentum zones, etc, over the surface roughness.

9.5 Drag-reduction set-up

Recent results from Chen et al. (2013, 2014) show that a surface roughness that has a combination of diverging and smooth surfaces in parallel are able to reduce skin-friction drag in turbulent pipe flow. We are interested to replicate this pattern in a turbulent boundary layer (see figure 9.3). We believe that the diverging proportion of the riblet will generate high local mean velocity and low local turbulence intensity, while the smooth proportion will generate a slightly lower local mean velocity and slightly higher turbulence intensity than the diverging proportion. However, when it is compared with our converging and diverging surface roughness, the diverging and smooth pattern is expected to have an overall lower skin-friction drag. This is possible due to the lack of the converging region, which generates higher skin-friction drag than the smooth surface.
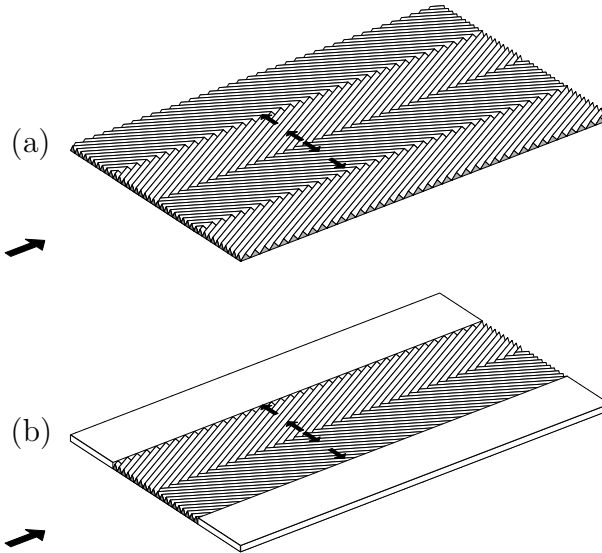
Figure 9.3: Schematic figure of converging and diverging riblet pattern (a) and diverging - smooth pattern (b).

We expect that the diverging and smooth surface may generate weaker counter-rotating vortices than the converging and diverging surface. Hence it is important to balance between the desired strength of the counter rotating vortices and the possible overall lower skin-friction drag.

Appendix A

Manufacturing troubleshoot

Manufacturing the converging-diverging riblets is a challenging process and very prone to errors, that may result in faulty riblets plates. Some of the common errors and possible solutions will be listed in this appendix.

Vibration in CNC-machine thread

Vibrations in the CNC-machine thread are generally caused by dust or dirt on the thread. The thread can be cleaned using high-pressure air and coated by silicone-based lubricant to reduce friction. There are four different threads in the CNC-machine, two for X-axis, one for Y-axis, and one for the Z-axis. The X-axis and Z-axis threads are easily reached and cleaned, however the Y-axis thread is covered by an aluminium panel that is held by four screws. The aluminium panel needs to be removed prior to cleaning and lubrication. Another common cause of vibration is wear of the nuts. The nuts need to be constantly checked and replaced when they are worn out.

Asymmetric master-tile cut

An asymmetric cut occurs if the two X-axis threads of the CNC-machine are not aligned. Prior to each cut it is suggested to move the X-axis location to

the absolute zero position and then switch-off the CNC-machine. When the CNC-machine power is down, use a digital calliper to measure the distance between the X-axis traverse and the ends of both threads. If they are not perfectly aligned, rotate the thread manually until they are both aligned.

Uneven master-tile height

Uneven height commonly occurs on the X-axis direction, although it is generally very small (less than 0.2 mm). The uneven height happens when the raw material is located at the centre base. It seems that the X-axis rail is slightly buckled due to the weight of the traverse. To minimise this, it is suggested to cut closer to the beginning or end of the CNC-machine base (one of the X-axis corner).

Uneven steps on riblets cut

Uneven steps on riblet cut is caused by an error or jump in cut progression. It is recommended to cut the riblets in succession and avoid moving, other than to the next cut inline. The CNC-machine does not have a feedback mechanism, hence it may loose the Z-axis position if it moves too far.

Rough and hairy riblets cut

Rough and hairy cuts can happen due to two possible causes. The first one is due to incorrect cutting speed and feed. To obtain the desirable quality, trial cuts at various cutting speed and feed must be performed for each different cutting material. The second common cause is a blunt drill-bit. It is suggested to use the drill bit once only for each master tile.

Imperfect Mould and cast

There are several methods to ensure proper solution mixing (especially for the first layer that has contact with the riblets) and to prevent a non-uniform result. Firstly, it is important to mix the two part solutions thoroughly. The mixing movement must touch / scrub the side and the bottom of the beaker.

For the best mixing result, use a flat wood spatula (in order to be able to scrub the bottom and side).

Secondly, having a balanced mixing ratio is desirable. To have a balanced mixing ratio it is better to firstly separate both solution parts in two separate beakers (i.e. beaker A and beaker B). Pour solution from beaker A to beaker B and mix thoroughly. It is suggested to regularly clean the solution that is attached to the wooden mixer by scrubbing it on the edge of the beaker. Once part A and part B are mixed, pour the solution back to beaker A and mix thoroughly again by scrubbing the bottom and side of the beaker. By moving the mixture between the two used beakers it ensure a thorough mixing and does not waste any un-mixed materials. Finally pour the mixture to a new and clean beaker, and mix it thoroughly with the wooden spatula again. The use of a clean beaker will ensure that the mixture at the beaker surface is uniform.

Finally, after the solution has been mixed thoroughly, it is imperative to degas the solution using a vacuum chamber. The degassing process will ensure that there is minimum trapped air / bubles in the mixture. Trapped air will result in holes on the hardened mould.

Bubbles on the surface

To prevent bubbles from forming on the riblets surface, the mixed solution for both mould and cast (that contact the riblets) must be degassed prior to pouring. Furthermore, the poured solution must be brushed thoroughly to release bubbles that formed during pouring.

Mould expansion

The type of mould that is used in this experiment does not shrink, however it can expand after being used to make 10 or more casts. It is recommended to replace the mould after making 10 or so casts.

Bibliography

Acarlar, M. S., Smith, C. R., 1987a. A study of hairpin vortices in a laminar boundary layer. Part 1. Hairpin vortices generated by a hemisphere protuberance. J. Fluid Mech. 175, 1–41.

Acarlar, M. S., Smith, C. R., 1987b. A study of hairpin vortices in a laminar boundary layer. Part 2. Hairpin vortices generated by fluid injection. J. Fluid Mech. 175, 43–83.

Adrian, R. J., 2005a. Twenty years of particle image velocimetry. Exp. Fluids. 39, 159–169.

Adrian, R. J., 2005b. Twenty years of particle image velocimetry. Exp. Fluids. 39, 159–169.

Adrian, R. J., 2007. Hairpin vortex organization in wall turbulenc. Phys. Fluids. 19, 041301.

Adrian, R. J., 2010. Particle image velocimetry. Cambridge University Press, Cambridge UK,.

Adrian, R. J., Meinhart, C. D., Tomkins, C. D., 2000. Vortex organization in the outer region of the turbulent boundary layer. J. Fluid Mech. 422, 1–54.

Adrian, R. J., Yao, C. S., 1987. Power spectra of fluid velocities measured by laser doppler velocimetry. Exp. Fluids. 5, 17 – 28.

Antonia, R. A., 1972. Conditionally sampled measurements near the outer edge of a turbulent boundary layer. J. Fluid Mech. 56, 1 –18.

Antonia, R. A., Luxton, R. E., 1971. The response of turbulent boundary layer to a step change in surface roughness. part 1. smooth to rough. J. Fluid Mech. 48, 721–761.

Antonia, R. A., Luxton, R. E., 1972. The response of turbulent boundary layer to a step change in surface roughness. part 2. rough to smooth. J. Fluid Mech. 53, 737–757.

Bacher, E. V., Smith, C. R., 1986. Turbulent boundary-layer modification by surface riblets. AIAA J. 24, 1382–1385.

Balakumar, B. J., Adrian, R. J., 2007. Large- and very-large-scale motions in channel and boundary-layer flows. Phil. Trans. R. Soc. London, Ser. A. 365, 665–681.

Bandyopadhyay, P., 1980. Large structure with a characteristic upstream interface in turbulent boundary layers. Phys. Fluids. 23, 2326.

Barker, M., 1922. On the use of very small pitot-tubes for measuring wind velocity. Phil. Trans. R. Soc. London, Ser. A. 101, 435 – 445.

Bechert, D., Bruse, M., Hage, W., Van Der Hoeven, J. G., Hoppe, G., 1997. Experiments on drag-reducing surfaces and their optimisation with an adjustable geometry. J. Fluid Mech. 338, 59–87.

Bechert, D., Hoppe, G., Reif, W. E., 1985. On the drag reduction of the shark skin. AIAA J. 85-0546.

Bechert, D. W., Bartenwerfer, M., 1989. The viscous flow on surfaces with longitudinal ribs. J. Fluid Mech. 206, 105–129.

Bechert, D. W., Bruse, M., Hage, W., 2000a. Experiments with three-dimensional riblets as an idealized model of shark skin. Exp. Fluids. 28, 403–412.

Bechert, D. W., Bruse, M., Hage, W., Meyer, R., 2000b. Fluid mechanics of biological surfaces and their technological application. Naturwissenschaften 87, 157–171.

Bechert, D. W., Hoppe, G., Van Der Hoeven, J. G., Makris, R., 1992. The berlin oil channel for drag reduction research. Exp. Fluids. 12, 251–260.

Blackwelder, R. F., Kovasznay, L. S. G., 1972. Time scales and correlations in a turbulent boundary layer. Phys. Fluids. 15, 9, 1545–1554.

Bogard, D. G., Tiederman, W. G., 1987. Characteristics of ejections in turbulent channel flow. J. Fluid Mech. 179, 1–19.

Bradshaw, P., 1965. The effect of wind-tunnel screens on nominally two-dimensional boundary layers. J. Fluid Mech. 22, 679–687.

Brown, G. L., Thomas, A. S. W., 1977. Large structure in a turbulent boundary layer. Phys. Fluids. 20, s243.

Bruun, H. H., 1995. Hot-wire anemometry. Oxford University Press, Oxford UK,.

Burdak, V. D., 1969. Function of the etenoid apparatus of fish in the presence of a turbulent boundary layer. Zoologichevskiy Zhurnal 48, 1053–1055.

Buschmann, M. H., Gad-el Hak, M., 2003. Debate concerning the mean-velocity profile of a turbulent boundary layer. AIAA J. 41, 565–572.

Bushnell, D. M., 1983. Turbulent drag reduction for external flows. AIAA 21st Aerospace Sciences Meeting, Reno, Nevada, AIAA Paper. 83-0227.

Cadirci, S., Gunes, H., Rist, U., 2013. Active flow control applications with a jet and vortex actuator in a laminar cross flow. Int. J. Heat Fluid Flow. 39, 146–159.

Chauhan, K., Ng, H. C. H., Marusic, I., 2010. Empirical mode decomposition and hilbert transforms for analysis of oil-lm interferograms. Mes. Sci. Tech. 21, 105405.

Chauhan, K., Philip, J., de Silva, C. M., Hutchins, N., Marusic, I., 2014. The turbulent/non-turbulent interface and entrainment in a boundary layer. J. Fluid Mech. 742, 119–151.

Chen, H., Rao, F., Shang, X., Zhang, D., Hagiwara, I., 2013. Biomimetic drag reduction study on herringbone riblets of bird feather. Journal of Bionic Engineering. 10, 341– 349.

Chen, H., Rao, F., Shang, X., Zhang, D., Hagiwara, I., 2014. Flow over bio-inspired 3d herringbone wall riblets. Exp. Fluids. 55, 1698.

Chernyshov, O. B., Zayets, V. A., 1970. Some peculiarities of the structure of the skin of sharks. In hydrodynamics problems of bionics. Bionica Nr 4, 77–83.

Choi, H., Moin, P., Kim, J., 1993. Direct numerical simulation of turbulent flow over riblets. J. Fluid Mech. 255, 503–539.

Choi, K. S., 1989. Near-wall structure of a turbulent boundary layer with riblets. J. Fluid Mech. 208, 417–458.

Choi, K. S., 2000. European drag-reduction research-recent developments and current status. Fluid Dynamics Research. 26, 325–335.

Choi, K. S., Clayton, B. R., 2001. The mechanism of turbulent drag reduction with wall oscillation. Int. J. Heat Fluid Flow. 22, 1– 9.

Choi, K. S., M, G., 1998. Drag reduction of turbulent pipe flows by circular-wall oscillation. Phys. Fluids. 10, 7– 9.

Choi, K. S., Yang, X., Clayton, B. R., Glover, E. J., Altar, M., Semenov, B. N., Kulik, V. M., 1997. Turbulent drag reduction using compliant surfaces. Phil. Trans. R. Soc. London, Ser. A. 453, 2229–2240.

Christensen, K. T., Adrian, R. J., 2001. Statistical evidence of hairpin vortex packets in wall turbulence. J. Fluid Mech. 431, 433–443.

Chu, D. C., Karniadakis, G. E., 1993. A direct numerical simulation of laminar and turbulent flow over riblet-mounted surfaces. J. Fluid Mech. 255, 1– 42.

Chung, D., McKeon, B. J., 2010a. Large-eddy simulation of large-scale structures in long channel flow. J. Fluid Mech. 661, 341–364.

Chung, D., McKeon, B. J., 2010b. Large-eddy simulation of large-scale structures in long channel flow. J. Fluid Mech. 661, 341–364.

Cimbala, J. M., Park, W. J., 1990. A direct hot-wire calibration technique to account for ambient temperature drift in incompressible flow. Exp. Fluids. 8(5), 299300.

Clauser, F. H., 1954. Turbulent boundary layers in adverse pressure gradients. J. Aeronaut Sci. 21, 91–108.

Clauser, F. H., 1956. The turbulent boundary layers. Adv. Appl. Mech 4, 1–151.

Coles, D. E., 1956. The law of the wake in the turbulent boundary layer. J. Fluid Mech. 1, 191–226.

Collis, S. S., Joslin, R. D., Seifert, A., Theofilis, V., 2004. Issues in active flow control: theory, control, simulation and experiment. Progress in Aerospace Sciences. 40, 237– 289.

Comte-Bellot, G., 1976. Hot-wire anemometry. Annu. Rev. Fluid Mech. 8, 209–231.

Corino, E. R., Brodkey, R. S., 1969. A visual investigation of the wall region in turbulent flow. J. Fluid Mech. 37, 1–30.

Corrsin, S., 1943. Investigation of flow in an axially symmetrical heated jet of air. NACA Report.

Corrsin, S., Kistler, A. L., 1955. The free stream boundaries of turbulent flows. NACA Report.

Cossu, C., Brandt, L., 2002. Stabilization of tollmien-schlichting waves by finite amplitude optimal streaks in the blasius boundary layer. Phys. Fluids. 14:8, 57– 260.

da silva, C. B., Hunt, J. C. R., Eames, I., Westerweel, J., 2014. Interfacial layers between regions of different turbulence intensity. Annu. Rev. Fluid Mech. 46, 567–590.

Davies, M., 2006. Emissions trading for ships- a european perspective. Naval Eng. J. 118:3, 131– 138.

de Silva, C. M., Gnanamanickam, E. P., Atkinson, N. A., Buchmann, N. A., Hutchins, N., Soria, J., Marusic, I., 2014. High spatial range velocity measurements in a high reynolds number. Phys. Fluids. 26(2):025117.

Dean, B., Bhushan, B., 2010. Shark-skin surfaces for fluid-drag reduction in turbulent flow: a review. Phil. Trans. R. Soc. London, Ser. A. 368, 4775–4806.

DeGraaff, D. B., Eaton, J. K., 2000. Reynolds number scaling of the flat-plate turbulent boundary layer. J. Fluid Mech. 422, 319–346.

del Álamo, J. C., Jiménez, J., 2009. Estimation of turbulent convection velocities and correction to taylor's approximation. J. Fluid Mech. 640, 5–26.

Dennis, D. J. C., Nickels, T. B., 2008. On the limitations of taylor's hypothesis in constructing long structures in a turbulent boundary layer. J. Fluid Mech. 614, 197–206.

Dennis, D. J. C., Nickels, T. B., 2011. Experimental measurement of large-scale three-dimensional structures in a turbulent boundary layer. part 2. long structures. J. Fluid Mech. 673, 218–244.

Du, Y., Karniadakis, G. E., 2000. Surpressing wall turbulence by means of a transverse traveling wave. Science. 288, 1230– 1234.

Du, Y., Symeonidis, V., Karniadakis, G. E., 2002. Drag reduction in wall-bounded turbulence via a transverse traveling wave. J. Fluid Mech. 457, 1– 34.

El-Samni, O. A., Chun, H. H., Yoon, H. S., 2007. Drag reduction of turbulent flow over thin rectangular riblets. Int J. Eng Sci. 45, 436–3454.

Ellerman, A. D., Buchner, B. K., 2007. The european unions emissions trading scheme: origins, allocation, and early results. Review of Environmental Economics and Policy. 1, 66– 87.

Erm, L. P., 1988. Low reynolds-number turbulent boundary layeres. Ph.D. thesis, University of Melbourne, Australia.

Erm, L. P., Joubert, P. N., 1991. Low-reynolds-number turbulent boundary layers. J. Fluid Mech. 230, 1–44.

Escuider, M. P., Abdel-Hameed, A., Johnson, M. W., Sutcliffe, C. J., 1998. Laminarisation and re-transition of a turbulent boundary layer subjected to favourable pressure gradient. Exp. Fluids. 25, 491 – 502.

Falco, R. E., 1977. Coherent motions in the outer region of turbulent boundary layers. Phys. Fluids. 20, 124–132.

Falco, R. E., 1991. A coherent structure model of the turbulent boundary layer and its ability to predict reynolds number dependence. Phil. Trans. R. Soc. London, Ser. A. 336, 103–129.

Fernholz, H. H., Finley, P. J., 1996. The incompressible zero-pressure gradient turbulent boundary layer: an assessment of the data. Progress in Aerospace Sciences. 32, 245–311.

Fernholz, H. H., Janke, G., Schobber, M., Wagner, P. M., Warnack, D., 1996. New developments and applications of skin-friction measuring techniques. Mes. Sci. Tech. 7, 1396–1409.

Fiedler, H., Head, M. R., 1966. Intermittency measurements in the turbulent boundary layer. J. Fluid Mech. 25, 719–735.

Flack, K. A., Schultz, M. P., Shapiro, T. A., 2005. Experimental support for townsend's reynolds number similarity hypothesis on rough wall. Phys. Fluids. 17, 035102.

Fox, R. W., McDonald, A. T., 1998. Introduction to fluid mechanics. Wiley and Sons, US,.

Fransson, J. H. M., Talamelli, A., 2012. On the generation of steady streamwise streaks in flat-plate boundary layers. J. Fluid Mech. 698, 211–234.

Fransson, J. H. M., Talamelli, A., Brandt, L., Cossu, C., 2004. Experimental and theoretical investigation of the nonmodal growth of steady streaks in a flat plate boundary layer. Phys. Fluids. 16, 3627.

Fransson, J. H. M., Talamelli, A., Brandt, L., Cossu, C., 2006. Delaying transition to turbulence by a passive mechanism. Phys. Rev. Lett. 96, 064501.

Fransson, J. H. M., Talamelli, A., Cossu, C., 2005. Experimental study of the stabilization of tollmien-schlichting waves by finite amplitude streaks. Phys. Fluids. 17, 054110.

Friederich, T., Kloker, M. J., 2012. Control of the secondary cross-flow instability using localized suction. J. Fluid Mech. 706, 470–495.

Gad-el Hak, M., 1989. Advances in fluid mechanics measurements. Springer, Berlin Germany,.

Ganapathisubramani, B., Hutchins, N., Hambleton, W. T., Longmire, E. K., Marusic, I., 2005. Investigation of large-scale coherence in a turbulent boundary layer using two-point correlations. J. Fluid Mech. 524, 57–80.

Ganapathisubramani, B., Hutchins, N., Monty, J. P., Chung, D., I, M., 2012. Amplitude and frequency modulation in wall turbulence. J. Fluid Mech. 712, 61–91.

Ganapathisubramani, B., Longmire, E. K., Marusic, I., 2003. Characteristics of vortex packets in turbulent boundary layers. J. Fluid Mech. 478, 35–46.

García-Mayoral, R., Jiménez, J., 2011a. Drag reduction by riblets. Phil. Trans. R. Soc. London, Ser. A. 369, 1412–1427.

García-Mayoral, R., Jiménez, J., 2011b. Hydrodynamic stability and breakdown of the viscous regime over riblets. J. Fluid Mech. 678, 317–347.

García-Mayoral, R., Jiménez, J., 2012. Scaling of turbulent structures in riblet channels up to $re_\tau \approx 550$. Phys. Fluids. 24, 105101.

George, W. K., 2007. Is there a universal log law for turbulent wall-bounded flows? Phil. Trans. R. Soc. London, Ser. A. 365, 789 – 806.

Gnanamanickam, E. P., Nottebrock, B., Großbe, S., Sullivan, J. P., Schröder, W., 2013. Measurement of turbulent wall shear-stress using micro-pillars. Mes. Sci. Tech. 24, 124002.

Goldstein, D., Handler, R., Sirovich, L., 1995. Direct numerical simulation of turbulent flow over a modelled riblet covered surface. J. Fluid Mech. 302, 333–376.

Goldstein, D. B., Tuan, T. C., 1998. Secondary flow induced by riblets. J. Fluid Mech. 363, 115–151.

Goldstein, R. J., 1983. Mesurement of wall shear stress. Hemisphere, New York US,.

Grant, H. L., 1958. The large eddies of turbulent motion. J. Fluid Mech. 4, 149–190.

Großbe, S., Schröder, W., 2008. Mean wall-shear stress measurements using the micro-pillar shear-stress sensor mps^3. Mes. Sci. Tech. 19, 015403.

Groth, J., Johansson, A. V., 1988. Turbulence reduction by screens. J. Fluid Mech. 197, 139–155.

Gruneberger, R., Hage, W., 2010. Drag characteristics of longitudinal and transverse riblets at low dimensionless spacings. Exp. Fluids. 50, 363–373.

Guala, M., Hommema, S. E., Adrian, R. J., 2006. Large-scale and very-large-scale motions in turbulent pipe flow. J. Fluid Mech. 554, 521–542.

Guala, M., Metzger, M., McKeon, B. J., 2011. Interactions within the turbulent boundary layer at high reynolds number. J. Fluid Mech. 666, 573–604.

Hage, W., Bechert, D. W., Bruse, M., 2000. Yaw angle effects of optimized riblets. Proceedings of CEAS/DragNet European Drag Reduction Conference, postdam.

Haidari, A. H., Smith, C. R., 1994. The generation and regeneration of single hairpin vortices. J. Fluid Mech. 277, 135–162.

Hall, T., Joseph, D., 2000. Rotating cylinder drag balance with application to riblets. Exp. Fluids. 29, 215–2227.

Harun, Z., 2012. The structure of adverse and favorable pressure gradient turbulent boundary layer. Ph.D. thesis, University of Melbourne, Australia.

Harun, Z., Monty, J. P., Mathis, R., Marusic, I., 2013. Pressure gradient effects on the large-scale structure of turbulent boundary layers. J. Fluid Mech. 715, 477–498.

Head, M. R., Bandyopadhyay, P., 1981. New aspects of turbulent boundary-layer structure. J. Fluid Mech. 107, 297–337.

Head, M. R., Rechenberg, I., 1962. The preston tube as a means of measuring skin friction. J. Fluid Mech. 14, 1 – 17.

Hedley, T. B., Keffer, J. F., 1974a. Some turbulent/non-turbulent properties of the outer intermittent region of a boundary layer. J. Fluid Mech. 64, 645–678.

Hedley, T. B., Keffer, J. F., 1974b. Turbulent/non-turbulent decision in an intermittent flow. J. Fluid Mech. 64, 625–644.

Hellstedt, A. K., 2003. Streamwise evolution of turbulent boundary layers towards equilibrium conditions. Ph.D. thesis, University of Melbourne, Australia.

Herbert, T., 1988. Secondary instability of boundary layers. Annu. Rev. Fluid Mech. 20, 487– 526.

Ho, C. M., Tai, Y. C., 1998. Micro-electro-mechanical systems (mems) and fluid flows. Annu. Rev. Fluid Mech. 30, 579– 612.

Hoyas, S., Jiménez, J., 2006. Scaling of the velocity fluctuations in turbulent channels up to $Re_\tau = 2003$. Phys. Fluids. 18.

Hultmark, M., Smits, A. J., 2010. Temperature corrections for constant temperature and constant current hot-wire anemometers. Mes. Sci. Tech. 21, 1–4.

Hutchins, N., 2014. Large scale structures in high reynolds number wall-bounded turbulence. Progress in Turbulence V., 75 – 83.

Hutchins, N., Chauhan, K., Marusic, I., Monty, J. P., Klewicki, J., 2012. Towards reconciling the large-scale structure of turbulent boundary layers in the atmosphere and laboratory. Boundary Layer Meteorology. 145, 273–306.

Hutchins, N., Hambleton, W. T., Marusic, I., 2005. Inclined cross-stream stereo particle image velocimetry measurements in turbulent boundary layers. J. Fluid Mech. 541, 21-54.

Hutchins, N., Marusic, I., 2007a. Evidence of very long meandering streamwise structures in the logarithmic region of turbulent boundary layers. J. Fluid Mech. 579, 1–28.

Hutchins, N., Marusic, I., 2007b. Large-scale influences in near-wall turbulence. Phil. Trans. R. Soc. London, Ser. A. 365, 647–664.

Hutchins, N., Monty, J., Ganapathisubramani, B., Ng, H., Marusic, I., 2011. Three-dimensional conditional structure of a high-Reynolds-number turbulent boundary layer. J. Fluid Mech. 673, 255–285.

Hutchins, N., Nickels, T. B., Marusic, I., Chong, M. S., 2009. Hot-wire spatial resolution issues in wall-bounded turbulence. J. Fluid Mech. 635, 103–136.

Jiménez, J., 1994. On the structure and control of near wall turbulence. Phys. Fluids. 6, 944–953.

Jiménez, J., 2004. Turbulent flows over rough walls. Annu. Rev. Fluid Mech. 36, 173–196.

Jones, M. B., 1999. Evolution and structure of sink flow turbulent boundary layers. Ph.D. thesis, University of Melbourne, Australia.

Jones, M. B., Marusic, I., Perry, A. E., 2001. Evolution and structure of sink-flow turbulent boundary layers. J. Fluid Mech. 428, 1–27.

Joslin, R. D., 1998. Aircraft laminar flow control. Annu. Rev. Fluid Mech. 30, 1– 29.

Jung, W. J., Mangiavacchi, N., Akhavan, R., 1993. Suppression of turbulence in wall-bounded flows by high frequency spanwise oscillations. Phys. Fluids. 4, 1605– 1607.

Karniadakis, G. E., Choi, K. S., 2003. Mechanism on transverse motions in turbulent wall flows. Annu. Rev. Fluid Mech. 35, 45– 62.

Kasagi, N., Suzuki, Y., Fukagata, K., 2009. Microelectromechanical systems-based feedback control of turbulence for skin friction reduction. Annu. Rev. Fluid Mech. 41, 231– 251.

Kendall, J. M., 1991. Studies on laminar boundary layer receptivity to freestream turbulence near a leading edge. In: Reda, D. C., Reed, H. L., Kobayashi, R. (Eds.), in Boundary Layer Stability and Transition to Turbulence. Vol. 114. ASME FED, pp. 23–30.

Kendall, J. M., 1998. Experiments on boundary-layer receptivity to freestream turbulence. AIAA J. 98-0530.

Kim, H. T., Kline, S. J., Reynolds, 1971. The production of turbulence near a smooth wall in a turbulent boundary layer. J. Fluid Mech. 50, 133–160.

Kim, J., Moin, P., 1986. The structure of the vorticity field in turbulent channel flow. part 1. study of ensemble-averaged fields. J. Fluid Mech. 162, 339–363.

Kim, K. C., Adrian, R., 1999. Very large-scale motion in the outer layer. Phys. Fluids. 11, 417–422.

Klebanoff, P. S., 1971. Effect of free-stream turbulence on a laminar boundary layer. Bull. Am. Phys. Soc. 16.

Klebanoff, P. S., Tidstrom, K., 1959. Evolution of amplified waves leading to transition in a boundary layer with zero pressure gradient. NASA Tech Note D. 195, 1–67.

Kline, S. J., Reynolds, W. C., Schraub, F. A., Rundstadler, P. W., 1967. The structure of turbulent boundary layers. J. Fluid Mech. 30, 741–773.

Kline, S. J., Robinson, S. K., 1989a. Quasi-coherent structures in the turbulent boundary layer. part 1: status report on a community-wide summary of the data. In: Kline, S. J., Afgan, N. H. (Eds.), In Near Wall Turbulence. Proc. Zaric Meml. Conf. Hemisphere, New York.

Kline, S. J., Robinson, S. K., 1989b. Turbulent boundary layer structures. In: Proc. IUTAM Symp. Struct. of Turbul. and Drag Reduct, 2nd, Zurich.

Kodama, Y., Kakugawa, A., Takahashi, T., Kawashima, H., 2000. Experimental study on microbubbles and their applicability to ships for skin friction reduction. Int. J. Heat Fluid Flow. 21, 582–588.

Koeltzsch, K., Dinkelacker, A., Grundmann, R., 2002. Flow over convergent and divergent wall riblets. Exp. Fluids. 33, 346–350.

Kopsch, F., 2012. Aviation and the eu emission trading scheme-lessons learned from previous emissions trading schemes. Energy Policy. 49, 770– 773.

Kovasznay, L. S. G., Kibbens, V., Blackwelder, R. F., 1970. Large-scale motion in the intermittent region of a turbulent boundary layer. J. Fluid Mech. 41, 283–326.

Kulandaivelu, V., 2012. Evolution of zero pressure gradient turbulent boundary layers from different initial conditions. Ph.D. thesis, University of Melbourne, Australia.

Laadhari, F., Skandaji, L., Morel, R., 1994. Turbulence reduction in a boundary layer by a local span wise oscillating surface. Phys. Fluids. 6, 3128– 3220.

Laufer, J., Badri Narayanan, M. A., 1971. Mean period of the turbulent production mechanism in a boundary layer. Phys. Fluids. 14-1, 182–183.

Laws, E., Livesey, J., 1978. Flow through screens. Annu. Rev. Fluid Mech. 10, 247–266.

Lee, J. H., Sung, H. J., Krogstad, P.-A., 2011. Direct numerical simulation of the turbulent boundary layer over a cube-roughened wall. J. Fluid Mech. 669, 397–431.

Lee, S. J., Lee, S. H., 2001. Flow field analysis of a turbulent boundary layer over a riblet surface. Phys. Fluids. 30, 153–166.

Leib, S. J., Wundrow, D. W., Goldstein, M. E., 1999. Effect of free-stream turbulence and other vortical disturbances on a laminar boundary layer. J. Fluid Mech. 380, 169–203.

Ligrani, P. M., Bradshaw, P., 1987. Spatial resolution and measurement of turbulence in the viscous sublayer using subminiature hot-wires probes. Exp. Fluids. 5, 407–417.

Liu, C. K., Kline, S. J., Johnston, J. P., 1966. An experimental study of turbulent boundary layer on rough walls. Stanford University, Dep Mech Eng Rep MD-15, July 1966.

Liu, Z. C., Landreth, C. C., Adrian, R. J., Hanratty, T. J., 1991. High resolution measurement of turbulent structure in a channel wit particle image velocimetry. Exp. Fluids. 10, 301–312.

Lögdberg, O., Fransson, J. H. M., Alfredsson, P. H., 2009. Streamwise evolution of longitudinal vortices in a turbulent boundary layer. J. Fluid Mech. 623, 27 – 58.

Longva, T., Eide, M. S., Skjong, R., 2010. Determining a required energy efficiency design index level for new ships based on a cost-effectiveness criterion. Maritime Policy and Management. 37:2, 129– 143.

Lu, S. S., Willmarth, W. W., 1973. Measurements of the structure of the reynolds stress in a turbulent boundary layer. J. Fluid Mech. 60-3, 481–511.

Lucey, A. D., Carpenter, P. W., 1995. Boundary layer instability over compliant walls: comparison between theory and experiment. Phys. Fluids. 7, 2355–2363.

Luchini, P., Manzo, F., Pozzi, A., 1991. Resistance of a grooved surface to parallel flow and cross-flow. J. Fluid Mech. 228, 87–109.

Malina, R., McConnachie, D., Winchester, N., Wollersheim, C., Paltsev, S., Waitz, I. A., 2012. The impact of the european union emissions trading scheme on us aviation. J. Air Transport Management. 19, 36– 41.

Marusic, I., 1991. The structure of zero and adverse pressure gradient turbulent boundary layer. Ph.D. thesis, University of Melbourne, Australia.

Marusic, I., 2009. Unravelling turbulence near walls. J. Fluid Mech. 630, 1–4.

Marusic, I., Mathis, R., Hutchins, N., 2010a. High reynolds number effects in wall turbulence. Int. J. Heat Fluid Flow. 31, 418–428.

Marusic, I., Mathis, R., Hutchins, N., 2010b. Predictive model for wall-bounded turbulent flow. Science. 329, 193–196.

Marusic, I., McKeon, B. J., Monkewitz, P. A., Nagib, H. M., Smits, A. J., 2010c. Wall-bounded turbulent flows at high reynolds numbers: Recent advances and key issues. Phys. Fluids. 22, 065103.

Marusic, I., Monty, J. P., Hultmark, M., Smits, A. J., 2013. On the logarithmic region in wall turbulence. J. Fluid Mech. 716, R3, 1–11.

Marusic, I., Perry, A. E., 1995. A wall-wake model for the turbulent structure of boundary layers. part 2. further experimental support. J. Fluid Mech. 298, 389–407.

Mathis, R., Hutchins, N., Marusic, I., 2009a. Large-scale amplitude modulation of the small-scale structures in turbulent boundary layers. J. Fluid Mech. 628, 311–337.

Mathis, R., Monty, J. P., Hutchins, N., Marusic, I., 2009b. Comparison of large-scale amplitude modulation in turbulent boundary layers, pipes, and channel flow. Phys. Fluids. 21, 11703.

McKeon, B. J., 2013. Natural logarithms. J. Fluid Mech. 718, 1–4.

Mehta, R. D., Hoffmann, P. H., 1987. Boundary layer two-dimensionality in wind tunnels. Exp. Fluids. 35, 358–360.

Messing, R., Kloker, M. J., 2010. Investigation of suction for laminar flow control of three-dimensional boundary layers. J. Fluid Mech. 648, 117–147.

Metzger, M. M., Klewicki, J. C., 2001. A comparative study of near-wall turbulence in high and low reynolds number boundary layers. Phys. Fluids. 13.

Michaelis, P., Zerle, P., 2006. From acea's voluntary agreement to an emission trading scheme for new passenger cars. J. Environmental Planning and Management. 49:3, 435– 453.

Moin, P., 2009. Revisiting taylor's hypothesis. J. Fluid Mech. 640, 1–4.

Moin, P., Kim, J., 1982. Numerical investigation of turbulent channel flow. J. Fluid Mech. 118, 341– 377.

Moin, P., Kim, J., 1985. The structure of the vorticity field in turbulent channel flow. part 1. analysis of instantaneous fields and statistical correlations. J. Fluid Mech. 155, 441– 464.

Monkewitz, P. A., Chauhan, K. A., Nagib, H. M., 2007. Self-consistent high-reynolds-number asymptotics for zero-pressure-gradient turbulent boundary layers. Phys. Fluids. 19, 115101.

Monty, J. P., Allen, J. J., Lien, K., Chong, M. S., 2011a. Modification of the large-scale features of high reynolds number wall turbulence by passive surface obtrusions. Exp. Fluids. 51, 1755–1763.

Monty, J. P., Harun, Z., Marusic, I., 2011b. A parametric study of adverse pressure gradient turbulent boundary layers. Int. J. Heat Fluid Flow. 32, 575–585.

Monty, J. P., Hutchins, N., Ng, H. C. H., Marusic, I., Chong, M. S., 2009. A comparison of turbulent pipe, channel and boundary layer flows. J. Fluid Mech. 632, 431–442.

Monty, J. P., Stewart, J. A., Williams, R. C., Chong, M. S., 2007. Large-scale features in turbulent pipe and channel flows. J. Fluid Mech. 589, 147–156.

Nagib, H., Chauhan, K., 2008. Variations of von kármán coefficient in canonical flows. Phys. Fluids. 20, 101518.

Nagib, H. M., Chauhan, K. A., Monkewitz, P. A., 2007. Approach to an asymptotic state for zero pressure gradient turbulent boundary layers. Phil. Trans. R. Soc. London, Ser. A. 365, 755–770.

Narahari Rao, K., Narasimha, R., Badri Narayanan, M. A., 1971. The 'bursting' phenomenon in turbulent boundary layer. J. Fluid Mech. 48, 339–352.

Narahimsa, R., Devasia, K. J., Gurunani, G., Narayanan, M. A. B., 1984. Transitional intermittency in boundary layers subjected to pressure gradient. Exp. Fluids. 2, 171 –176.

Naughton, J. W., Sheplak, M., 2002. Modern developments in shear-stress measurement. Progress in Aerospace Sciences. 38, 515–570.

Nychas, S. G., Hershey, H. C., Brodkey, R. S., 1973. A visual study of turbulent shear flow. J. Fluid Mech. 61-3, 513–540.

Offen, G. R., Kline, S. J., 1974. Combined dye-streak and hydrogen-buble visual observations of a turbulent boundary layer. J. Fluid Mech. 62-2, 223–239.

Offen, G. R., Kline, S. J., 1975. A proposed model of the bursting process in turbulent boundary layers. J. Fluid Mech. 70-2, 209–228.

Onsrud, G., Persen, L. N., Saetran, L. R., 1987. On the measurement of wall shear stress. Exp. Fluids. 5, 11–16.

Orlandi, P., Jiménez, J., 1994. On the generation of turbulent wall friction. Phys. Fluids. 6, 634–641.

Österlund, J. M., Johansson, A. V., Nagib, H. M., Hites, M. H., 2003. A note on the overlap region in turbulent boundary layers. Phys. Fluids. 41, 565–572.

Panton, R. L., 2001a. Overview of the self-sustaining mechanisms of wall turbulence. AIAA-paper2001-2911.

Panton, R. L., 2001b. Overview of the self-sustaining mechanisms of wall turbulence. Progress in Aerospace Sciences 37, 341–383.

Park, S. R., Wallace, J. M., 1994. Flow alteration and drag reduction by riblets in a turbulent boundary layer. AIAA J. 32, 31–38.

Perry, A. E., 1982. Hot-wire anemometry. Oxford University Press, Oxford UK,.

Perry, A. E., Chong, M. S., 1982. On the mechanism of wall turbulence. J. Fluid Mech. 119, 173–217.

Perry, A. E., Li, J. D., 1990. Experimental support for the attached-eddy hypothesis in zero-pressure-gradient turbulent boundary layers. J. Fluid Mech. 218, 405–438.

Perry, A. E., Lim, T. T., Teh, E. W., 1981. A visual study of turbulent spots. J. Fluid Mech. 104, 387–405.

Perry, A. E., Morrison, G. L., 1971. A study of the constant temperature hot-wire anemometer. J. Fluid Mech. 47, 577–599.

Praturi, A. K., Brodkey, R. S., 1978. A stereoscopic visual study of coherent structures in turbulent shear flow. J. Fluid Mech. 89-2, 251–272.

Preston, H., Lee, D. S., Hooper, P. D., 2012. The inclusion of the aviation sector within the european union's emissions trading scheme: What are the prospects for a more sustainable aviation industry? Environmental Development. 2, 48– 56.

Pulles, C. J. A., Krishna-Prasad, K., Nieuwstadt, 1989. Turbulence measurements over longitudinal micro-grooved surfaces. Appl. Sci. Res 46, 197–208.

Raffel, M., Willert, C., Kompenhans, J., 1998. Particle image velocimetry, a practical guide. Springer, Berlin Germany,.

Reif, W. E., 1982. Morphogenesis and function of the squamation in sharks. Neues Jahrbuch fuer geologie und palaentologie 164, 172–183.

Reif, W. E., 1985. Squamation and ecology of sharks. Courier Forschungsinstitut Senckenberg, Frankfurt Germany,.

Reif, W. E., Dinkelacker, A., 1982. Hydrodynamics of the squamation in fast swimming sharks. Neues Jahrbuch fuer geologie und palaentologie 164, 184–187.

Robinson, S. K., 1991. Coherent motions in turbulent boundary layers. Annu. Rev. Fluid Mech. 23, 601–639.

Saric, W. S., Carpenter, A. L., Reed, H. L., 2011. Passive control of transition in three-dimensional boundary layers, with emphasis on discrete roughness elements. Phil. Trans. R. Soc. London, Ser. A. 369, 1352–1364.

Schlatter, P., Li, Q., Brethouwer, G., Johansson, A. V., Henningson, D. S., 2009. Turbulent boundary layers up to $re_\theta = 2500$ studied through simulation and experiment. Phys. Fluids. 051702.

Schlatter, P., Örlu, R., Brethouwer, G., Fransson, J. H. M., Johansson, A. V., Alfredsson, P. H., Henningson, D. S., 2010. Simulations of spatially evolving turbulent boundary layers up to $re_\theta = 4300$. Int. J. Heat Fluid Flow. 31, 251 – 261.

Schoppa, W., Hussain, F., 1998. A large-scale control strategy for drag reduction in turbulent boundary layers. Phys. Fluids. 10, 5, 1049 –1051.

Schultz, M. P., 2007. Effects of coating roughness and biofouling on ship resistance and powering. Biofouling. 23(5-6), 331–341.

Schultz, M. P., Flack, K. A., 2005. Outer layer similarity in fully rough turbulent boundary layers. Exp. Fluids. 38, 328–340.

Schultz, M. P., Swain, G. W., 2000. The influence of biofilms on skin friction drag. Biofouling. 15(1-3), 129–139.

Semin, N. V., Golub, V. V., Elsinga, G. E., Westerweel, J., 2011. Laminar superlayer in a turbulent boundary layer. Tech. Phys. Lett. 37 (12), 1154–1157.

Singer, B. A., Joslin, R. D., 1994. Metamorphosis of a hairpin vortex into a young turbulent spot. Phys. Fluids. 6, 3724–3736.

Smith, C. R., Walker, J. D. A., Haidari, A. H., Sobrun, U., 1991. On the dynamics of near-wall turbulence. Phil. Trans. R. Soc. London, Ser. A. 336, 131–175.

Smits, A. J., Marusic, I., 2013. Wall-bounded turbulence. Physics Today. 66, 25–30.

Smits, A. J., McKeon, B. J., Marusic, I., 2011a. High-reynolds number wall turbulence. Annu. Rev. Fluid Mech. 43, 353 –375.

Smits, A. J., McKeon, B. J., Marusic, I., 2011b. High reynolds number wall turbulence. Annu. Rev. Fluid Mech. 43, 353–375.

Smits, A. J., Wood, D. H., 1985. The response of turbulent boundary layers to sudden perturbations. Annu. Rev. Fluid Mech. 17, 321–358.

Spalart, P. R., McLean, J. D., 2011. Drag reduction: enticing turbulence, and then an industry. Phil. Trans. R. Soc. London, Ser. A. 369, 1556–1569.

Stenzel, V., Wilke, Y., Hage, W., 2011. Drag-reducing paints for the reduction of fuel consumption in aviation and shipping. Progress in organic coatings. 70, 224– 229.

Strand, J. S., Goldstein, D. B., 2011. Direct numerical simulations of riblets to constrain the growth of turbulent spots. J. Fluid Mech. 668, 267–292.

Suzuki, Y., Kasagi, N., 1994. Turbulent drag reduction mechanism above a riblet surface. AIAA J. 1781- 1790.

Talluru, K. M., Baidya, R., Hutchins, N., Marusic, I., 2014a. Amplitude modulation of all three velocity components in turbulent boundary layers. J. Fluid Mech. 746, doi:10.1017.

Talluru, K. M., Kulandaivelu, V., Hutchins, N., Marusic, I., 2014b. A calibration technique to correct sensor drift issues in hot-wire anemometry. Mes. Sci. Tech. 25, 105304.

Tan-Atichat, J., Nagib, H. M., Loehrke, R. I., 1982. Interaction of free-stream turbulence with screens and grids: a balance between turbulence scales. J. Fluid Mech. 114, 501–528.

Taylor, G. I., 1938. The spectrum of turbulence. Phil. Trans. R. Soc. London, Ser. A. 164 (919), 476–490.

Tennekes, H., Lumley, J. L., 1972. A first course in turbulence. MIT Press, Massachusetts, US.

Theodorsen, T., 1952. Mechanism of turbulence. In: Proc. Second Midwestern Conference on Fluid Mechanics, Mar. 17-19. Ohio State Univesity, Columbus, Ohio.

Tomkins, C. D., Adrian, R. J., 2003. Spanwise structure and scale growth in turbulent boundary layers. J. Fluid Mech. 490, 37–74.

Townsend, A. A., 1948. Local isotropy in the turbulent wake of a cylinder. Austr. J. Sci. Res. Ser. A.

Townsend, A. A., 1949. The fully developed turbulent wake of a circular cylinder. Austr. J. Sci. Res. Ser. A.

Townsend, A. A., 1956. The structure of turbulent shear Flow. Cambridge University Press.

Townsend, A. A., 1961. Equilibrium layers and wall turbulence. J. Fluid Mech. 11, 97–120.

Townsend, A. A., 1970. The mechanism of entrainment in free turbulent flows. J. Fluid Mech. 41, 327–361.

Townsend, A. A., 1976. The structure of turbulent shear flow, 2nd ed. Cambridge University Press.

Vukoslavcevic, P., Wallace, J. M., Balint, J. L., 1992. Viscous drag-reduction using streamwise-aligned riblets. AIAA J. 30, 1119–1122.

Wallace, J. M., Eckelmann, H, B. R. S., 1972. The wall region in turbulent shear flow. J. Fluid Mech. 54, 38–48.

Wallace, J. M., Eckelmann, H., Brodkey, R. S., 1972. The wall region in turbulent shear flow. J. Fluid Mech. 54-1, 39–48.

Walsh, M. J., 1982. Turbulent boundary layer drag reduction using riblets. AIAA J. 82-0169.

Walsh, M. J., 1983. Riblets as a viscous drag reduction technique. AIAA J. 21, 485–486.

Walsh, M. J., 1990. Riblets in viscous drag reduction in turbulent boundary layers. Progress in astronautics and aeronautics AIAA, Ed: Bushnell, D B and Hefner, J N 203-261.

Walsh, M. J., Lindemann, A. M., 1984. Optimization and application of riblets for turbulent drag reduction. AIAA J. 84-0347.

Walsh, M. J., Weinstein, L. M., 1978. Drag and heat transfer on surfaces with small longitudinal fins. AIAA J. 78- 1161.

Watmuff, J. H., 1998. Detrimental effects of almost immeasurably small freestream generated by wind-tunnel screens. AIAA J. 36, 379–386.

Westerweel, J., Petracci, A., Delfos, R., Hunt, J. C. R., 2011. Characteristics of the turbulent/non-turbulent interface of a non-isothermal jet. Phil. Trans. R. Soc. London, Ser. A. 369, 723–737.

White, C. M., Mungal, M. G., 2008. Mechanics and prediction of turbulent drag reduction with polymer additives. Annu. Rev. Fluid Mech. 40, 235–256.

Winter, K. G., 1977. An outline of the technique available for the measurement of skin friction in turbulent boundary layers. Progress in Aerospace Sciences. 18, 1–57.

Wood, D. H., 1982. Internal boundary layer growth following a step change in surface roughness. Boundary Layer Meteorology. 22, 241–244.

Woodcock, J. D., Sader, J. E., Marusic, I., 2010. On the maximum drag reduction due to added polymers in poiseuille flow. J. Fluid Mech. 659, 473– 483.

Wygnanski, I., Fiedler, H. E., 1970. The two-dimensional mixing region. J. Fluid Mech. 41, 327–361.

Yang, S.-Q., Dou, Y., 2010. Turbulent drag reduction with polymer additive in rough pipes. J. Fluid Mech. 642, 279– 294.

Zagarola, M. V., Smits, A. J., 1998. Mean ow scaling of turbulent pipe ow. J. Fluid Mech. 373, 33–79.

Zaman, K. B. M., Hussain, F., 1981. Taylor hypothesis and large-scale coherent structures. J. Fluid Mech. 112, 379–396.

Zhou, J., Adrian, R. J., Balachandar, S., Kendall, T. M., 1999. Mechanisms for generating coherent packets of hairpin vortices in channel flow. J. Fluid Mech. 387, 353–396.